UNIVERSITÄT ZU LÜBECK
INSTITUT FÜR MEDIZINTECHNIK

From the Institute of Medical Engineering
of the University of Lübeck
Director: Prof. Dr. rer. nat. Thorsten M. Buzug

Integrated Methodology for Enhanced Low-Dose PET Imaging: AI Denoising, Monte Carlo Simulations, and 3D Phantom Printing

Dissertation
for Fulfillment of
Requirements
for the Doctoral Degree
(Dr.-Ing.)
of the University of Lübeck

from the Department of Computer Sciences and Engineering

Submitted by
Ezzat Elmoujarkach
from Florida

Lübeck, 2024

Chairman: Prof. Dr. Philipp Rostalski

First referee: Prof. Dr. rer. nat. Magdalena Rafecas

Second referee: Prof. Dr. phil. Mattias Heinrich

Date of oral examination: 03.06.2025

Approved for printing. Lübeck, 18.06.2025

Dedication

To my parents, for their unwavering support, love, and belief in my potential. To my friends, for their encouragement, understanding, and patience throughout this journey. And to all the mentors and educators who inspired me and guided me along the way, this work is a testament to your dedication and impact.

Abstract

Low-dose positron emission tomography (PET) has been the focus of many recent studies due to its potential to transform PET imaging from a diagnostic tool to a screening process. Low-dose PET imaging and PET imaging with low positron branching ratio isotopes (such as multi-day low-dose imaging using Zirconium-89 (^{89}Zr) for ImmunoPET, and theranostics using Yttrium-90 (^{90}Y)) suffer from high statistical noise levels, hindering the ability to use the PET images for accurate diagnosis. To combat this noise, artificial intelligence (AI) has shown promising results in improving image quality. However, these AI networks often aim to remove noise in a single step, making it difficult to reconstruct images with very low signal-to-noise ratios. Moreover, in phantom studies, ^{89}Zr tends to adhere to the walls of the phantoms. Such adhering affect the scanner's calibration making it more challenging to assess the true uptake in patient studies, especially in low-dose scenarios.

Within the framework of my PhD thesis, I developed a convolutional neural network named *Progressive Elimination of Noise Towards Accurate Ultra Low-Dose PET Images Using 3D U-Nets* (PETAL-3D), aimed at reducing noise levels in the image gradually, similar to diffusion models. Furthermore, a digital twin of a total-body PET scanner was developed to better assess the impact of current methods used for training AI for image denoising on re-framed high-dose images and their application to low-dose imaging. PETAL-3D outperformed three traditional denoising methods within the framework of this PhD thesis; Gaussian filters, conventional artificial neural networks, 3D U-Net, and advanced anatomically guided 3D U-Net. Moreover, it was demonstrated that PETAL-3D, when trained on a variety of noise levels, can be applied to different noise levels, provided the initial noise level in the image is known and similar to what the network was trained on. The results demonstrated that PETAL-3D denoising successfully restored images acquired with 4% of the ^{18}F-FDG standard dose, yielding image quality suitable for routine clinical practice, in contrast to the non-diagnostic quality of the input images.

I utilized 3D printing technology to create a solidified phantom designed to prevent the adherence of ^{89}Zr to the phantom's walls,enabling stable imaging for up to 23 days. Lastly, a PET scan of the AbdoMan phantom using ^{90}Y was used to evaluate PETAL-3D denoising, which improved the coefficient of variation from 33% and 45% in 30-minute and 20-minute equivalent scans, respectively, to 8% and 9% after applying PETAL-3D, despite the model not being trained on ^{90}Y images.

Further improvements to PETAL-3D could also be envisioned to optimize the training parameters more effectively in the aim to reduce the dose below 1%. This progress paves the way for establishing PET imaging as a viable screening tool.

Kurzfassung

Niedrigdosis-Positronen-Emissions-Tomographie (PET) ist der Fokus vieler aktueller Studien, da sie das Potenzial hat, PET-Bildgebung von einem diagnostischen Werkzeug zu einem Screening-Verfahren zu transformieren. Niedrigdosis-PET-Bildgebung und PET-Bildgebung mit Isotopen mit niedrigem Positron-Verzweigungsverhältnis (wie z. B. mehrtägige Niedrigdosis-Bildgebung mit Zirkonium-89 (^{89}Zr) für ImmunoPET und Theranostik mit Yttrium-90 (^{90}Y)) leiden unter hohen statistischen Rauschpegeln, was die genaue Diagnoseeinschätzung der PET-Bilder erschwert. Neuronale Netze hat sich als vielversprechend erwiesen, um das Rauschen zu reduzieren und die Bildqualität zu verbessern. Diese Künstliche Neuronale Netze zielen jedoch oft darauf ab, Rauschen in einem einzigen Schritt zu entfernen, was bei Bildern mit sehr niedrigem Signal-Rausch-Verhältnis nur begrenzte erfolgreich ist. Darüber hinaus neigt ^{89}Zr in Phantomstudien dazu, an den Wänden der Phantome zu haften. Dieses Anhaften beeinflusst die Kalibrierung des Scanners, was die Bewertung der tatsächlichen Aufnahme in Patientenstudien, insbesondere in Niedrigdosisszenarien, erschwert.

Im Rahmen meiner Doktorarbeit habe ich ein Convolutional Neural Network namens *Progressive Elimination of Noise Towards Accurate Ultra Low-Dose PET Images Using 3D U-Nets*(PETAL-3D) entwickelt, das darauf abzielt, die Rauschpegel in den Bildern schrittweise zu reduzieren, ähnlich wie bei Diffusionsmodellen. Darüber hinaus wurde ein digitaler Zwilling eines Total-Body-PET-Scanners entwickelt, um den Einfluss der derzeitigen Methoden zur Schulung von KI zur Rauschunterdrückung auf hochdosierte Bilder und deren Anwendung auf Niedrigdosis-Bildgebung besser zu bewerten. PETAL-3D übertraf im Rahmen dieser Doktorarbeit drei traditionelle Methoden zur Rauschunterdrückung: Gaußsche Filter, konventionelle KI-Netzwerke, 3D U-Net und ein fortgeschrittenes anatomisch geführtes 3D U-Net. Zudem konnte gezeigt werden, dass PETAL-3D, wenn es auf verschiedene Rauschniveaus trainiert wurde, auf unterschiedliche Rauschniveaus anwendbar ist, sofern das anfängliche Rauschniveau im Bild bekannt ist und dem entspricht, worauf das Netzwerk trainiert wurde. Die Ergebnisse zeigten, dass das PETAL-3D-Denoising erfolgreich Bilder wiederherstellte, die mit 4% der Standarddosis von ^{18}F-FDG aufgenommen wurden, und eine Bildqualität lieferte, die für die routinemäßige klinische Praxis geeignet ist, im Gegensatz zur nicht-diagnostischen Qualität der Ausgangsbilder.

Ich nutzte 3D-Drucktechnologie, um ein verfestigtes Phantom zu erstellen, das darauf ausgelegt ist, das Anhaften von ^{89}Zr an den Wänden des Phantoms zu verhindern und so eine stabile Bildgebung für bis zu 23 Tage zu ermöglichen. Abschließend wurde ein PET-Scan des AbdoMan-Phantoms mit ^{90}Y verwendet, um die Rauschunterdrückung durch PETAL-3D zu bewerten. Dabei verbesserte sich der Variationskoeffizient von 33% und 45% in 30-minütigen bzw. 20-minütigen äquivalenten Scans auf 8% bzw.

9% nach Anwendung von PETAL-3D, obwohl das Modell nicht auf ^{90}Y-Bildern trainiert war.
Weitere Verbesserungen von PETAL-3D könnten ebenfalls angestrebt werden, um die Trainingsparameter effektiver zu optimieren und das Ziel zu erreichen, die Dosis auf unter 1% zu reduzieren. Dieser Fortschritt ebnet den Weg, um die PET-Bildgebung als ein praktikables Screening-Werkzeug zu etablieren.

Contents

List of Acronyms

ABS	Acrylonitrile Butadiene Styrene
ACF	Attenuation Correction Factors
AFOV	Axial Field Of View
AG	Anatomically Guided
AI	Artificial Intelligence
APD	Avalanche Photodiodes
BG	Background
BGO	Bismuth Germanate
BMI	Body Mass Index
CAD	Computer-Aided Design
CERN	Conseil Européen pour la Recherche Nucléaire
CNN	Convolutional Neural Network
COR	Coefficient Of Range
CPU	Central Processing Unit
CRC	Contrast Recovery Coefficients
CT	Computed Tomography
CV	Coefficient Of Variation
DAE	Denoising Autoencoder
DDM	Denoising Diffusion Models
DEA	Detector Electronics Assembly
DLP	Digital Light Processing
DNN	Deep Neural Network
DOI	Depth-Of-Interaction
DRF	Dose Reduction Factor
EANM	European Association Of Nuclear Medicine
EM	Expectation-Maximization
FBP	Filtered Back Projection
FDG	Fludeoxyglucose
FDM	Fused Deposition Modeling
FEE	Front End Electronics
FOV	Field Of View
FWHM	Full-Width Of Half-Maximum
GAMOS	GEANT4-based Architecture for Medicine-Oriented Simulations
GAN	Generative Adversarial Networks
GATE	GEANT4 Application for Emission Tomography
GPU	Graphics Processing Unit
HVL	Half Value Layer
HYPR	HighlY constrained backPRojection

IEC	International Electrotechnical Commission
IEEE	Institute Of Electrical And Electronics Engineers
immuno-PET	Immuno-Positron Emission Tomography
IQ	Image Quality
LAFOV	Long Axial Field Of View
LCD	Liquid-Crystal Display
LDR	Lesion Detectability Rate
LOR	Axial Field Of View
LSO	Lutetium Oxyorthosilicate
LYSO	Lutetium Oxyorthosilicate
MAP	Maximum-A-Posteriori
MC	Monte Carlo
MCNP	Monte Carlo Nuclear Particle Transport
MERMAID	Multi-Emission Radioisotopes - Marine Animal Imaging Device
MIC	Medical Imaging Conference
ML	Maximum Likelihood
MLEM	Maximum Likelihood Estimation Method
MR	Magnetic Resonance Imaging
MRD	Maximum Full-Ring Difference
MRI	Magnetic Resonance Imaging
MSE	Mean Squared Error
NDPVR	Normalized Delta Peak To Valley Ratio
NEC	Noise Equivalent Counts
NECR	Noise-Equivalent Count Rate
NEMA	National Electrical Manufacturers Association
NLM	Non-Local Means
NN	Neural Networks
NRMSE	Normalized Root Mean Square Error
NSS	Nuclear Science Symposium
NURBS	Utilizing Non-Uniform Rational B-Splines
OP	Ordinary Poisson
OS	Ordered Subset
OSEM	Ordered Subset Expectation Maximization
PET	Positron Emission Tomography
PETAL-3D	Progressive Elimination of Noise Towards Accurate Ultra Low-Dose PET Images Using 3D U-Net
PMMA	Polymethyl Methacrylate
PMT	Photomultiplier Tubes
PSF	Point Spread Function
PSFTOF	Point Spread Function-Time-Of-Flight

PSMA	Prostate-Specific Membrane Antigen
PSMR	PET, SPECT, and MR
PSNR	Peak Signal-to-Noise Ratio
PVR	Peak To Valley Ratio
QA	Quality Assurance
QC	Quality Control
RAM	Random Access Memory
RC	Recovery Coefficients
RDPI	Relative Difference Between The Peak Intensities
ROI	Region-Of-Interrest
RP	Replication Padding
RTSD	Room-Temperature Semiconductor Detectors
SBR	Sphere-To-Background Ratios
SF	Scatter Fraction
SLA	Stereolithography
SNR	Real-Time Ray Tracing
SOR	Spill-Over Ratio
SPECT	Tomographic Single Photon Emission Computed Tomography
SR	Singles Rate
SSIM	Structural Similarity Index Measure
SSRB	Single-Slice Rebinning
SSS	Single Scatter Simulation
STL	Standard Tessellation Language
SUV	Standardized Uptake Value
TBPET	Total Body Pet
TBR	Tumor-To-Background Ratio
TOF	Time-Of-Flight
TRPMS	Transactions On Radiation And Plasma Medical Sciences
UDPET	Ultra-Low Dose Pet Imaging
UHS	Ultra-High Sensitivity
ULDPET	Ultra-Low Dose PET
UNN	Unified Noise-Aware Network
UV	Ultraviolet
VOI	Volume-Of-Interest
VOR	Volume Of Response
VRAM	Video-RAM
XCAT	4D Extended Cardiac-Torso

1 Introduction

Contents

1.1 Background and Context

Positron Emission Tomography (PET) is a well-established tool in nuclear medicine, widely used in oncology, cardiology, neurology, and treatment monitoring. Several developments over the years have significantly improved the outcomes of PET imaging and expanded its applications.

The first PET systems consisted of two rotating heads similar to those used in earlier gamma cameras. Eventually, PET was introduced into clinical practice as a full ring system with a limited axial field of view (AFOV), thanks to advances in computational systems for data processing and image reconstruction. The addition of Computed Tomography (CT) and Magnetic Resonance Imaging (MRI) to PET systems greatly improved image quality by enabling attenuation correction and scatter estimation for PET/CT systems. The development of new detector technologies enabled PET scanners to be compatible with MRI machines, introducing PET/MRI scanners to new applications and establishing PET as one of the most reliable tools for brain studies. The advent of new scintillation crystals and the adoption of time-of-flight

(TOF) technology further enhanced image reconstruction quality and temporal resolution [1].
In recent years, the introduction of total body PET (TBPET) systems has markedly improved PET scan sensitivity by a factor of 2.8. This improvement has reduced both the scanning time and the required administered dose for clinical PET routines, expanding the range of PET applications to include total-body dynamic scans and low-dose PET imaging [2]. The increased sensitivity has also enhanced the viability of immuno-positron emission tomography (immuno-PET) and radioembolization studies using TBPET scanners [3, 4].
Reducing the administered activity to levels comparable to the dose of a chest radiography is highly desirable. The dose reduction would also help make PET safer pediatric imaging applications and could transform PET from a diagnostic tool into a screening tool, such as breast cancer screening.

1.2 Problem Statement

Reducing the dose in PET imaging leads to an increase in statistical noise levels due to the low counts, which compromises the diagnostic quality of the images. Traditional noise reduction methods, such as Gaussian filters, have been widely used but are limited in their ability to retain detailed information as they tend to blur edges.
With the advancement of artificial intelligence, numerous deep learning algorithms have been developed to address statistical noise at the data level, image level, and within the reconstruction process outperforming traditional noise reduction methods. However, these AI-based approaches often face challenges, including high computational costs due to the complexity of the algorithms and limited performance on data that falls outside the training set's scope.
Additionally, multi-day studies using immuno-PET face calibration and quantification challenges, particularly with Zirconium-89 (^{89}Zr). ^{89}Zr tends to adhere to the walls of the phantoms over time, impacting the accuracy of quantification and calibration.

1.3 Research Objectives

The aim of this dissertation is to address the challenges in low-dose PET imaging by developing innovative methods utilizing three technologies: Monte Carlo (MC) simulations, 3D printing, and deep learning for image denoising.

- **Objective 1:** Developing a digital twin of a total body PET scanner to simulate low-dose/high-dose scans. The digital twin will also provide valuable insights, such as ground truth information that cannot be obtained during actual measurements.

- **Objective 2:** Utilizing 3D Printing technology to create high-resolution, solid, customizable wall-less phantoms for PET imaging. This will improve immuno-PET ^{89}Zr quantification by addressing the issue of the isotope adhering to the walls of phantoms.
- **Objective 3:** Developing a series of neural networks trained on varying noise levels to improve image denoising compared to traditional denoising methods and AI approaches. These networks will denoise PET images with different noise levels using various isotopes. Additionally, the digital twin will be used to produce downsampled low-dose images from high-dose injected PET images for AI training and generate low-dose images resembling clinical settings. Moreover, the wall-less 3D-printed radioactive phantoms will be utilized to further evaluate the performance and limitations of the developed AI algorithms. Lastly, with the success of the developed AI approach, a new application was investigate of applying the AI algorithms to denoise theragnostic images obtained when utilizing ^{90}Y.

1.4 Hypothesis

For image denoising, I propose that a series of neural networks trained at different noise levels can be constructed with lower computational costs compared to current state-of-the-art AI applications. By gradually reducing noise through multiple networks, rather than a single-step denoising process, these networks will be both more efficient and effective, contributing to the achievement of the third objective. The data provided by the digital twin will be used to evaluate the performance of these neural networks, as it offers ground truth data that is otherwise unobtainable during actual measurements, aligning with the first objective.
The issue of ^{89}Zr adhering to the walls of phantoms is a result of the radioisotope being in liquid form. Mixing ^{89}Zr with a UV-curable resin will cause the resin to solidify, preventing the migration of the isotope to the phantom walls. This will result in a stable phantom suitable for multi-day studies. These phantoms would be the first of their kind for ^{89}Zr, enabling calibration and characterization of the scanner for multi-day studies with this isotope. Additionally, the phantoms would serve as a valuable dataset for AI algorithms used in image denoising, providing better means to evaluate their limitations, and contributing to the achievement of the second objective.

1.5 Structure of the Thesis

The thesis is structured as follows: The next chapter provides the foundational information necessary to understand the subsequent work presented in the thesis.

Chapter 3 covers the development and validation of the digital twin, including simulations of various simple phantoms, patient-like phantoms, and phantoms for radioembolization studies. Chapter 4 focuses on the development of methods for 3D printing radioactive phantoms, starting with the use of Fluorine-18 (^{18}F) for small animal PET scanners, before translating the application to TBPET scanners and using ^{89}Zr. Chapter 5 discusses the application of AI for image denoising, including patient data, phantom data, and 3D printed phantoms using ^{89}Zr. It also covers the simulation of different methods for generating low-dose data and their implications on the quality of the output images. The final chapter, Chapter 6 summarizes the key findings of the research and suggests directions for future work.

1.6 Thesis contributions

Several conference contributions have resulted from the work developed in this thesis.

Conference proceedings as first author:

- **E. Elmoujarkach**, C. Pommranz, J. Cabello, F. Schmidt, and M. Rafecas, "Impact of Re-framing High-Dose Scans for the Training of Neural Networks for Denoising Low-Dose PET" 2024 IEEE Nuclear Science Symposium, Medical Imaging Conference and Room Temperature Semiconductor Detector (IEEE NSS/MIC RTSD) Conference, 2024. https://doi.org/10.1109/NSS/MIC/RTSD57108.2024.10657465.

- **E. Elmoujarkach**, F. Schmidt, and M. Rafecas "PETAL-3D: A Novel 3D U-Net Approach for Ultra-Low-Dose PET Image Denoising" MODE2024 4th MODE Workshop on Differentiable Programming for Experiment Design, Valencia, Spain, 2024, pp. 23. https://indico.cern.ch/event/1380163/book-of-abstracts.pdf.

- **E. Elmoujarkach**, F. Schmidt, and M. Rafecas "PETAL-3D: Progressive Elimination of Noise Towards Accurate Ultra Low-Dose PET Images Using 3D U-Net" PSMR2024 10th Conference on PET, SPECT, and MR Multimodal Technologies, Total Body and Fast Timing in Medical Imaging, Elba, Italy, 2024, pp. 10. https://agenda.infn.it/event/36860/book-of-abstracts.pdf.

- **E. Elmoujarkach**, S. Seeger, C. Schmidt, J. Mannheim, F. Schmidt, and M. Rafecas, "First 3D Printed Radioactive ^{89}Zr Phantoms for Positron Emission Tomography", Transactions on Additive Manufacturing Meets Medicine, vol. 5, pp. 833–833, 9 2023. https://doi.org/10.18416/AMMM.2023.2309833.

- **E. Elmoujarkach**, S. Seeger, N. Möller, C. Schmidt, and M. Rafecas, "Development and Characterization of 3D Printed Radioactive Phantoms for High Resolution PET", 2022 IEEE NSS/MIC RTSD - IEEE Nuclear Science Symposium, Medical Imaging Conference and Room Temperature Semiconductor Detector Conference, 2022. https://doi.org/10.1109/NSS/MIC44845.2022.10399242.

- S. Seeger*, **E. Elmoujarkach***, N. Möller, C. Schmidt, and M. Rafecas, "3D Printed Radioactive Phantoms for Positron Emission Tomography", Transactions on Additive Manufacturing Meets Medicine, vol. 4, pp. 640–640, 9 2022. https://doi.org/10.18416/AMMM.2022.2209640.

- **E. Elmoujarkach**, S. Seeger, C. Schareck, L. de Graaf, J. Barkhausen, and M. Rafecas, "Characterization of Using Infused PLA for 3D Printed Radiation Shielding", Current Directions in Biomedical Engineering, vol. 8, pp. 576–579, 8 2022. https://doi.org/10.1515/cdbme-2022-1147.

Conference proceedings as Co-Author:

- S. Seeger, **E. Elmoujarkach**, H. Vo, C. Schmidt, and M. Rafecas, "Feasibility of Zirconium-89 Imaging with MERMAID, a Small-Fish PET Scanner Prototype", 2024 IEEE NSS/MIC RTSD - IEEE Nuclear Science Symposium, Medical Imaging Conference and Room Temperature Semiconductor Detector Conference, 2024. https://doi.org/10.1109/NSS/MIC/RTSD57108.2024.10656767.

- W. Lan, H. Vo, C. Pommranz, **E. Elmoujarkach**, J. Cabello, N. Birge, P. Schleyer, M. Rafecas, C. la fougère, and F. Schmidt, "A Simulation Framework to Establish Ground Truth for Motion Correction in Total-Body PET: Initial Evaluation for Complex Respiratory Motion" 2024 IEEE NSS/MIC RTSD - IEEE Nuclear Science Symposium, Medical Imaging Conference and Room Temperature Semiconductor Detector Conference, 2024. https://doi.org/10.1109/NSS/MIC/RTSD57108.2024.10656116.

- S. Seeger, **E. Elmoujarkach**, F. Schmidt, G. Nachimuthu, C. Schmidt, J. Mannheim, and M. Rafecas, "Fabrication of Zirconium-89 Solid Phantoms for PET Using 3D Printing", 37th Annual Congress of the European Association of Nuclear Medicine, Hamburg, Germany, 2024. pp. S707. https://doi.org/10.1007/s00259-024-06838-z.

- P. Linder, **E. Elmoujarkach**, J. Schwenck, L. Köhnlein, M. Rafecas, C. la fougère, and F. Schmidt, "Feasibility Study on Late ^{89}Zr-Immuno Total-Body PET based

on Patient Simulation and a Customized Longterm-stable Phantom" 3rd edition of the Total Body PET (TBPET) Groningen, The Netherlands, 2024.

- S. Weigel, **E. Elmoujarkach**, L. Rauscher, W. Lan, E. Calder´on, P. Linder, M. Rafecas, C. la Foug'ere, and F. Schmidt, "A moveable 3-D Printed Phantom Setup for Evaluation of Motion Induced Artefacts in a Total-Body PET/CT", Nuklearmedizin - Nuclear Medicine, vol. 63, p. V69, 2024. https://doi.org/10.1055/s-0044-1782396.

- C. M. Pommranz, **E. Elmoujarkach**, J. Cabello, M. Rafecas, J. Mannheim, A. Santangelo, C. la Foug'ere, B. Pichler, and F. Schmidt, "Simulation Studies and Experimental Model Validation of the Biograph Vision Quadra", Nuklearmedizin - Nuclear Medicine, vol. 62, p. V8, 4 2023. https://doi.org/10.1055/s-0043-1766212.

- C. Pommranz, **E. Elmoujarkach**, J. Cabello, W. Lan, M. Rafecas, J. Mannheim, P.Linder, A. Santangelo, C. Fougére, B. Pichler, and F. Schmidt, "Development and Validation of a Monte Carlo Simulation Workflow for a Total-Body PET Scanner", 36th Annual Congress of the European Association of Nuclear Medicine 2023, 690–691, 2023, https://doi.org/10.1007/s00259-023-06333-x.

- C. Pommranz, **E. Elmoujarkach**, J. Cabello, W. Lan, M. Rafecas, J. Mannheim, A. Santangelo, C. L. Foug'ere, B. Pichler, and F. Schmidt, "Development and Initial Validation of Two Simulation Workflows Using GATE for a Total-Body PET/CT Scanner", pp. 1–1, 12 2023. https://doi.org/10.1109/NSS/MIC44845.2022.10399242.

Peer review papers

- **E. Elmoujarkach**, S. Seeger, L. Morgner, F. Schmidt, J. Mannheim, C. Schmidt, and M. Rafecas, "Dedicated 3D Printed Radioactive Phantoms with ^{18}F-FDG for Small Animal PET", Accpeted, to be published in IEEE Transactions on Radiation and Plasma Medical Sciences 2024.

Peer review papers - under review:

- **E. Elmoujarkach**, F. Schmidt, E. Calderón, W. Lan, P. Linder, L. Kiefer, C. la fougère, and M. Rafecas, "PETAL-3D: Progressive Elimination of Noise Towards Accurate Ultra Low-Dose PET Images Using 3D U-Nets", under review at IEEE

Transactions on Radiation and Plasma Medical Sciences, PSMR 2024 special issue.

- C. Pommranz*, **E. Elmoujarkach***, W. Lan, J. Cabello, P. Linder, H. Vo, J. Mannheim, A. Santangelo, A. Conti, M. Rafecas, C. la fougère, and F. Schmidt, "A Digital Twin of the Biograph Vision Quadra Long Axial Field of View PET/CT: Monte Carlo Simulation and Image Reconstruction Framework", under review at European Journal of Nuclear Medicine and Molecular Imaging, Physics 2024.

2 Basics

Contents

2.1 Imaging in nuclear medicine

Imaging in nuclear medicine is a medical technique that uses small amounts of radioactive substances, known as radiotracers, to visualize physiological functions within the body. This technique relies on the detection of gamma rays emitted by these radiotracers as they concentrate in specific organs or tissues. Specialized detectors are used to capture the emitted photons, typically in the energy range of 50 to 1000 keV, allowing detailed images of internal organs and structures to be produced. This non-invasive method provides valuable insights into metabolic processes, as well as other processes such as infections, tumors, and the overall health of various organs, aiding in the diagnosis and management of diseases.
A radiopharmaceutical, which is a tracer tagged with a radionuclide, decays to produce photons either directly or indirectly. These photons are then detected by specialized detectors. Two main imaging modalities have been developed: single photon emission imaging, which includes planar and tomographic single photon emission computed tomography (SPECT) scans, and positron emission tomography (PET). Unlike imaging modalities such as X-ray Computed Tomography (CT) and Magnetic Resonance Imaging (MRI), imaging in nuclear medicine is particularly useful for tracking the metabolism of tracers [5].
Clinical PET scanners are equipped with a ring of detectors surrounding the patient. When two correlated annihilation photons reach the detectors, they are either detected almost simultaneously or penetrate the detector, escaping the detection chain. The scanner uses coincidence electronics to identify that these two photons are correlated, a process known as coincidence detection.
When the first photon is detected by a crystal in the scanner, the electronics are triggered, and a coincidence circuit is opened. If the second photon is detected by another crystal within a very short time window (usually a few nanoseconds), the system records this event as a coincidence. The path between the two detectors that registered the photons is referred to as a 'line of response' (LOR). By recording information about the interactions, such as detector ID, time of detection, and energy of detection throughout the measurement,the data is stored in a format known as a list-mode file. Additional information, such as blood flow, motion, and data from physiological monitors, can also be coupled to the list-mode data outside the PET scanner to aid in the image reconstruction process [6, 7].
Once the predefined scan time is over, an image reconstruction algorithms is used to process the collected data and create a three-dimensional image of the radiotracer distribution within the body. This process allows clinicians to visualize the metabolic or functional activity of tissues and organs, which is crucial for diagnosing and monitoring various diseases, including cancer, neurological disorders, and cardiovascular conditions [8].

2.1.1 Radioactive Decay

Radioactive decay is the spontaneous nuclear transformation of an unstable nucleus into a stable one, resulting in the emission of particles, photons, or both. This transformation can occur in one or multiple steps. The process is driven by nuclear instability and is characterized by various modes of decay, including alpha decay, beta decay, gamma emission, internal conversion, internal pair production, nuclear fission, and spontaneous fission. Each type of decay has its own characteristic properties, such as the type of emissions, the transition energy, and the average lifetime of the radionuclide before it undergoes radioactive decay.

Beta-minus decay (β^- decay) occurs when a neutron in the nucleus is converted into a proton, emitting an electron (beta particle) and an antineutrino. In contrast, beta-plus decay (β^+ decay) involves the conversion of a proton into a neutron, accompanied by the emission of a positron and a neutrino. A related process is electron capture, in which an unstable nucleus captures one of its own orbital electrons, typically from the innermost shell. This process also converts a proton into a neutron and results in the emission of a neutrino, without the production of a positron.

Internal pair production is a process in which an excited nucleus releases energy by directly creating an electron-positron pair, provided that the nuclear energy exceeds the threshold of 1.022 MeV, which is the combined rest mass energy of the electron and positron [8, 9].

All three types of decay—β^- decay,β^+ decay, and electron capture—involve changes in the proton-neutron ratio within the nucleus. This process increases the atomic number by one, resulting in the formation of a different element with the same mass number. These processes can result in the emission of high-energy particles or radiation, leading to further ionizations within the tissue. In PET, the radionuclides used for imaging are primarily positron emitters.

In β^+ decay, the emitted positron travels a certain distance through a medium, depending on its energy. As it moves, it collides with electrons and atoms, gradually losing energy. The energy of the emitted positron follows a continuous spectrum, with the mean energy being approximately one-third of the maximum energy. Higher-energy positrons travel farther within the medium, which can degrade spatial resolution in imaging. For ^{18}F, the positron range in water is typically less than 0.5 mm, whereas for other radionuclides, it can reach several millimeters. Once the positron loses all its kinetic energy and comes to rest, it annihilates upon colliding with an electron, producing two 511 keV gamma photons, which correspond to the rest mass energy of the electron and positron. Due to the conservation of momentum, these photons are not emitted in perfectly opposite directions, a phenomenon known as acollinearity (or non-collinearity). Acollinearity arises from the residual momentum of the positron and electron at the moment of annihilation, resulting in a deviation

that follows a Gaussian distribution with a Full-Width at Half-Maximum (FWHM) of approximately 0.25°. This effect becomes more pronounced with larger scanner diameters and represents a fundamental physical limitation in PET imaging. For a PET scanner with a 90 cm diameter, acollinearity limits the spatial resolution to approximately 2.5–3 mm [10, 11].
The radioactive decay of a parent atom to its daughter atom can occur through a single decay process or through multiple decay steps before reaching the daughter. Since decay is a random process, the probability of each possible decay pathway is described by the branching ratio.
For instance, a radionuclide with a branching ratio of 80% for positron emission implies that 80% of its decays produce positrons, while the remaining 20% may proceed through different decay routes. High branching ratios are desirable in PET imaging because they result in a greater number of detectable annihilation photons, thus improving image quality and diagnostic accuracy. Radionuclides such as fluorine-18 and carbon-11, which exhibit high branching ratios for positron emission (approximately 97% and near 100%, respectively), are preferred for their effectiveness as tracers in PET scans, enhancing the precision and resolution of metabolic and functional imaging.

2.1.2 PET radioisotopes

Various isotopes are used in nuclear imaging. The following section provides brief descriptions of the isotopes relevant to this thesis, which are listed in Table 2.1. A simplified decay scheme for each source is shown in Figure 2.1.

Table 2.1: Properties of various positron emitters isotopes used in PET imaging [12, 13]

Source	Production	Positron Maximum Energy (MeV)	Mean Positron Range in Water	Positron Branching Ratio	Gamma Energy (MeV)	Half life
F-18	Cyclotron	0.635	0.6 mm	96.7 %	0.511	109.8 min
Na-22	Cyclotron	0.545	2.4 mm	90.4 %	0.511, 1.275	2.6 years
Ga-68	Ge-68 decay	1.899	3.5 mm	87.7 %	0.511	68 min
Zr-89	Cyclotron	0.902	1.3 mm	22.3 %	0.511, 0.909	78.4 hours

2.1.2.1 Fluorine-18

Fluorine-18 (^{18}F) is most commonly used in radiopharmaceutical form as fluorodeoxyglucose (^{18}F-FDG), which is used to detect metabolic activity in tissues, often to identify cancer, assess brain function, and evaluate cardiac function. ^{18}F has a relatively short half-life of approximately 110 minutes, which is long enough

to conduct imaging procedures but short enough to minimize radiation exposure to patients. Its high positron branching ratio and relative low positron energy makes it highly effective for PET imaging for high resolution systems [14]. The decay scheme of ^{18}F is shown in Figure 2.1a.

2.1.2.2 Sodium-22

Sodium-22 (^{22}Na) is used as a positron source in PET scanner calibration and for studying the behavior of sodium in biological systems. ^{22}Na has a relatively long half-life of 2.6 years, making it suitable for long-term studies and calibration sources. ^{22}Na emits both positrons and a high-energy gamma photon (1.275 MeV), making it useful for coincidence detection in dual-modality PET imaging. The decay scheme of ^{22}Na is shown in Figure 2.1b.

2.1.2.3 Gallium-68

Gallium-68 (^{68}Ga) is often obtained from a germanium-68/gallium-68 generator. ^{68}Ge decays to ^{68}Ga, which can then be eluted from the generator and used immediately for medical imaging. ^{68}Ga is widely used in PET imaging, especially for calibration and detecting neuroendocrine tumors using ^{68}Ga-labeled somatostatin analogs. It is also used in other radiopharmaceuticals for imaging infection, inflammation, and other diseases. ^{68}Ga has a very short half-life of about 68 minutes, allowing for rapid imaging after administration and reducing the radiation dose to the patient. Its production via generators allows hospitals without a cyclotron to utilize PET imaging effectively [15]. The decay scheme of ^{68}Ga is shown in Figure 2.1c.

2.1.2.4 Zirconium-89

Zirconium-89 (^{89}Zr) is used in PET imaging, particularly in immuno-PET for imaging the biodistribution of monoclonal antibodies. This allows for the visualization of specific molecular targets and is valuable in oncology for assessing the presence and spread of tumors. ^{89}Zr has a relatively long half-life of 78.41 hours, making it suitable for imaging over extended periods. This is particularly useful for tracking biological processes and the distribution of therapeutic antibodies [16, 17]. The decay scheme of ^{89}Zr is shown in Figure 2.1d.

2.1.3 Interaction of Radiation with Matter

In this thesis, two types of interactions between radiation and matter are relevant: the interaction of light charged particles with matter and the interaction of photons with matter.

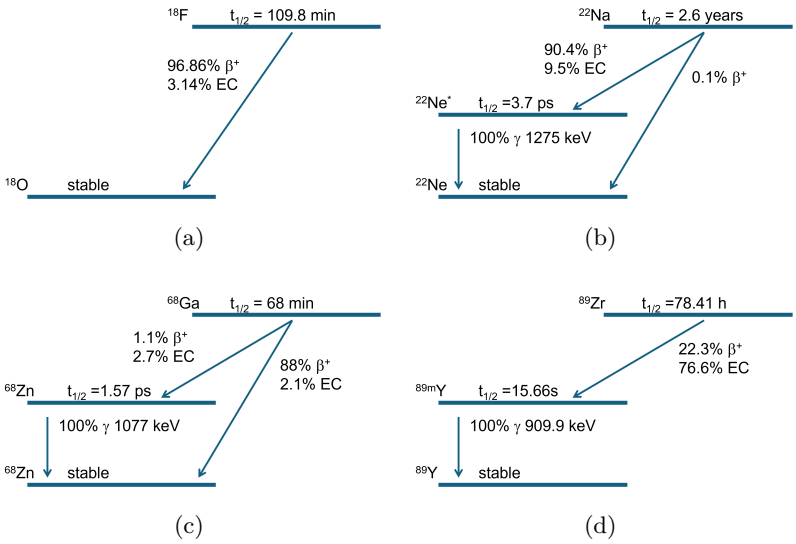

Fig. 2.1: A simplified decay scheme of: a) ^{18}F [18], b) ^{22}Na [19], c) ^{68}Ga [20], and d) ^{89}Zr [17].

2.1.3.1 Interactions of light charge particles with matter

Charged particles, such as electrons particles, interact with matter primarily through Coulomb forces. These forces arise from the interaction between the positive charge of the particles and the negative charge of the orbital electrons in the atoms of the absorbing material. As charged particles traverse a medium, they experience changes in energy and direction, leading to ionizations and excitations of the atoms in the medium. This interaction process results in the loss of kinetic energy of the charged particles and the production of ion pairs, consisting of positively charged ions and free electrons.

The most significant interaction process for charged particles in matter is inelastic collisions with atomic electrons. During these collisions, a substantial portion of the kinetic energy of the charged particle is transferred to the atomic electron, resulting in the excitation or ejection of the electron. The latter process creates ion pairs.

Ionization occurs when the energy transferred to an atomic electron is sufficient to overcome the binding energy holding the electron in the atom, resulting in the ejection of the electron from the atom. The liberated electron can further cause additional excitations and ionizations as it moves through the medium, contributing to the overall ionization process.

Excitation involves the transfer of energy to an atomic electron, elevating it to a higher energy state without ejecting it from the atom. This excited state is temporary, and the electron will eventually return to its ground state, often releasing energy in the form of electromagnetic radiation.

In regions where multiple ionizations occur within a small volume, a cluster of ion pairs is formed. When an orbital electron gains sufficient energy, the liberated electron can further cause additional excitation and ionization as it moves through the medium. Moreover, it can cause multiple ionizations, creating what is known as a delta particle. These clusters and delta particles play a crucial role in the localized energy deposition in the absorbing material, significantly affecting the radiation damage and the subsequent physical and chemical changes in the medium [21, 22]. When high-energy electrons are decelerated by the electric field of another charged particle and subsequently collide with atoms in a material, they produce bremsstrahlung radiation. Bremsstrahlung radiation is characterized by its broad spectrum, with the maximum energy being the energy of the incident electrons. Bremsstrahlung radiation can be detected using various types of radiation detectors, each optimized for different energy ranges and applications [16]. In diagnostic PET imaging, bremsstrahlung radiation does not play a significant role.

2.1.3.2 Interaction of photons with matter

Photon interactions with matter involve several key processes, each affecting the photon's energy and direction differently. These interactions play a crucial role in various applications, including medical imaging and radiation therapy. These interactions include photoelectric effect, Compton scattering, and pair production. Figure 2.2 illustrates the dominant photon interactions as a function of photon energy and material composition.

The photoelectric effect is a process in which an atom absorbs the energy of an incoming photon. This energy is transferred to an electron, most commonly in the K-shell, ejecting it from the material if the energy exceeds the material's work function. This process result in the creation of a vacancy. An electron from an outer shell then fills this vacancy, and the residual excess energy is emitted as characteristic X-ray photons or Auger electrons. This effect is more pronounced in materials with higher atomic numbers and is a critical mechanism in X-ray and gamma-ray detection.

In Compton scattering, a photon interacts with an electron, resulting in the photon being scattered in a new direction. During this interaction, the photon transfers a portion of its energy to the electron, which causes the electron to be ejected from the atom. The scattered photon continues its path with reduced energy (and different direction), while the ejected electron carries away the energy difference as kinetic energy. The energy and angle of the scattered photon are related by the Compton Equation below:

$$\Delta E = E' - E = \frac{h}{m_e c}(1 - \cos\theta), \tag{2.1}$$

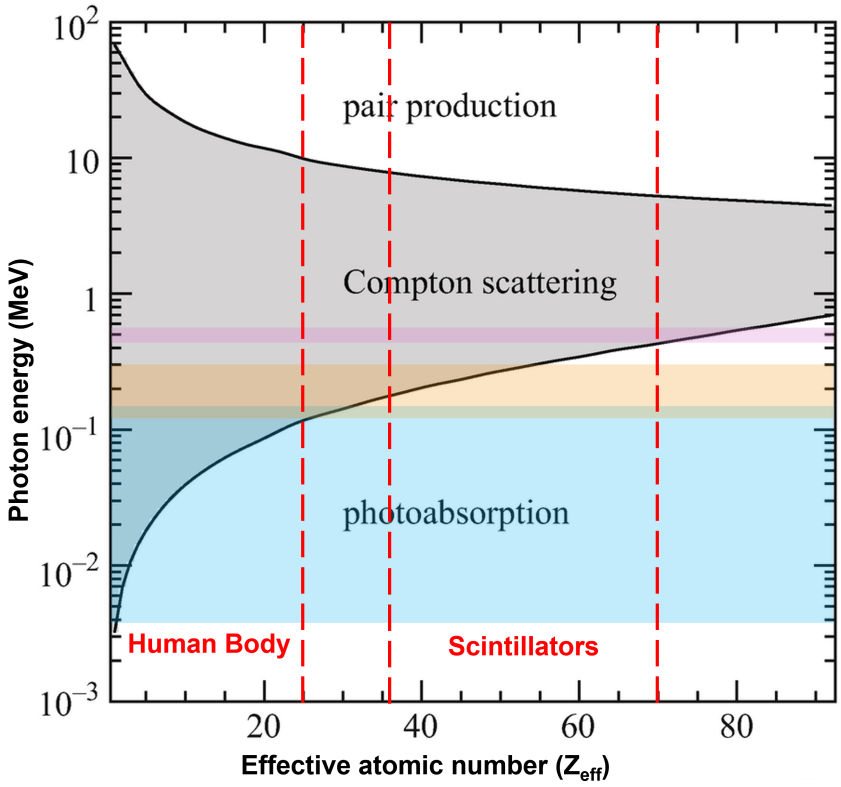

Fig. 2.2: The various interactions of photons with matter based on their energies. The blue region highlights the energy range for medical X-rays, while the orange region indicates the energy range for SPECT, and the pink region marks the PET energy range (511 keV). The typical effective atomic number for human tissue is below 22, whereas for scintillator materials it ranges between 35 and 70. This figure is modified from C. Fabjan's *The Interaction of Radiation with Matter*, licensed under CC BY 4.0 (https://creativecommons.org/licenses/by/4.0/), source: [23].

where ΔE is the change in energy, E' is the scattered photon energy, E is the incident photon energy, h is Planck's constant, (m_e) is the electron rest mass, c is the speed of light, and θ is the scattering angle.
Compton scattering affects PET imaging by contributing to the attenuation of gamma rays in tissues, which influences image formation and contrast, and by altering the trajectory of annihilation photons, leading to the incorrect assignment of detector pairs. Distinguishing single events from Compton scattering is essential for optimizing image quality and accurately quantifying the distribution of radionuclides within the body. Additionally, understanding Compton scattering is important for radiation protection considerations, as it influences dose deposition within tissues.
Pair production occurs when a high-energy photon, with energy exceeding 1.022 MeV, interacts with the nucleus or an electron, converting its energy into a positron-electron

pair. The excess energy from this interaction is shared as kinetic energy between the positron and electron. In diagnostic PET imaging, pair production does not play a significant role.

The interaction of photons with matter is significantly influenced by the effective atomic number of the material. Materials with higher atomic numbers exhibit greater probability for photoelectric absorption. Conversely, Compton scattering predominates in materials with lower atomic numbers, where photon energies are more likely to be sufficient to induce this type of interaction. This relationship is critical in PET imaging, where the attenuation of photons is a key consideration.

When photons traverse a material, such as the patient's body or detector components, their probability of being attenuated depends on several factors: the photon's energy, the composition of the material, and the thickness of the material. Attenuation is particularly significant because it directly impacts the accuracy of the imaging process by affecting the number of photons that reach the detectors.

In a narrow-beam geometry, the transmission of a monoenergetic photon beam through an absorber is governed by an exponential attenuation law, described mathematically by the following equation:

$$I(x) = I_0 e^{-\int_0^x \mu(s)\,ds}, \tag{2.2}$$

where $I(x)$ is the intensity of the transmitted photon beam after passing through a thickness x of the absorber, I_0 is the initial intensity of the photon beam, and $\mu(s)$ is the linear attenuation coefficient, which depends on the energy of the photons and the properties of the absorber material at position s along the path through the absorber. The total linear attenuation coefficient of 511 keV gamma rays in tissue is 0.096 cm^{-1}; this corresponds to 7 cm half value layer (HVL). HVL is the thickness of a material required to reduce the number of photons passing through it by half. It can be calculated as follows:

$$\text{HVL} = \frac{\ln 2}{\mu}. \tag{2.3}$$

More information about attenuation coefficient for different materials can be found at the National Institute of Standards and Technology website[1]. Figure 2.3 illustrates the concept of photon attenuation as photons transmit through a medium.

2.1.4 Radiation detectors

Various types of detectors are commonly employed for radiation detection, including ionization detectors, proportional counters, scintillation detectors, liquid scintillation detectors, and semiconductor detectors. In PET imaging, scintillation detectors are

[1] `https://www.nist.gov/pml/x-ray-mass-attenuation-coefficients/`

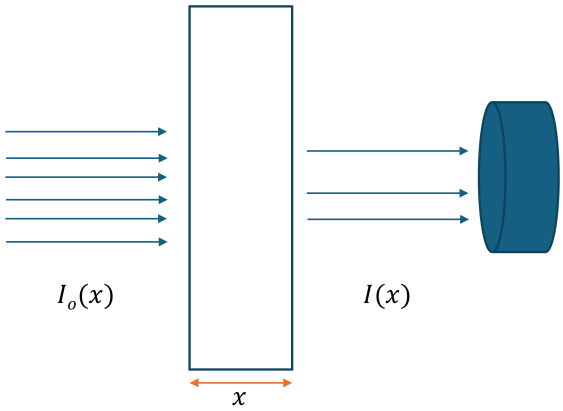

Fig. 2.3: The initial number of photons ($I_0(x)$) passing through a uniform medium of thickness x, resulting in a reduced number of photons ($I(x)$) reaching a detector (indicated in blue).

used to detect the annihilation photons generated from positron annihilations. These detectors are made of scintillation crystals, which produce light emissions upon exposure to radiation. The emitted light is then captured by photomultiplier tubes or other light-sensitive devices [24].
Scintillation crystals (typically have a cuboid structure), chosen as they are rugged, not readily effected by moisture, and have efficient stopping power. These crystals are paired with sensitive photodetectors, such as photomultiplier tubes (PMTs) or silicon photomultipliers (SiPMs), which convert visible light into electronic signals. PMTs and SiPMs differ in their underlying physics, structure, and performance characteristics. PMTs are vacuum tubes that use a photocathode to convert light photons into electrons, which are then multiplied through a series of dynodes to produce a measurable current. In contrast, SiPMs are solid-state devices composed of an array of avalanche photodiodes (APDs) operating in Geiger mode, with each APD coupled to a quenching resistor to control the avalanche process. PMTs offer high sensitivity, and lower noise. However, in recent years, there has been a shift towards using SiPMs due to their compatibility with magnetic fields (essential for PET/MRI systems), compact design, and higher timing resolution [11]. Figure 2.4 shows an example of PMT and SiPM.

2.2 PET

PET is a well-established imaging modality utilized for routine clinical diagnostic imaging, basic human research, and clinical and preclinical research. It is also employed in translational imaging, with the development and use of pre-clinical scanners for imaging small animals (e.g., mice, rats) and large animals (e.g., dogs,

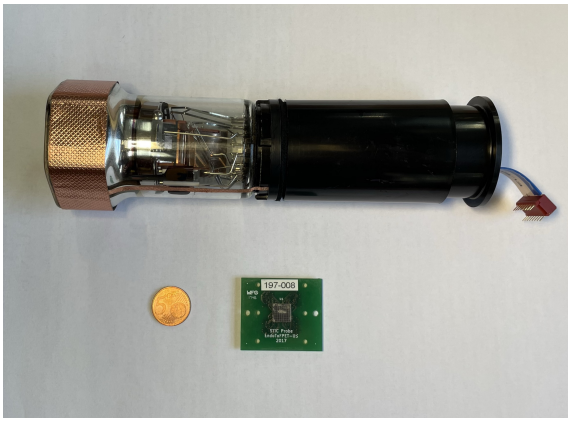

Fig. 2.4: A picture of a PMT (top) and a SiPM (bottom). The SiPM is significantly more compact, highlighting its advantage in size and integration for modern PET detector applications.

nonhuman primates). The anatomical data from CT and MRI can often be used to provide estimates for quantitative corrections needed for accurate PET imaging.
To enhance the diagnostic quality of a PET scan, it can be combined with either MRI (PET/MRI) or CT (PET/CT) to provide anatomical information as a reference for the PET data. This combination provides detailed anatomical information that complements the physiological data obtained from the PET scan, resulting in more accurate and comprehensive imaging. By integrating the structural details from MRI or CT with the functional insights from PET, clinicians can achieve better localization of abnormalities, enhance diagnostic accuracy, and improve overall patient outcomes. With MRI, there is no additional ionizing radiation dose, unlike with CT. However, MRI does not offer total body imaging in a single bed position, and the procedure takes longer, reducing patient throughput and increasing the risk of motion artifacts. Additionally, MRI is not as effective for imaging bones. In contrast, a full-body CT scan takes only a few minutes, and the images can be used for attenuation correction in PET imaging, thereby improving the image quality of the PET compared to a standalone PET image [25].
Advances in PET technologies have created a fertile ground for the development of new imaging methods and applications such as theranostics (therapeutics and diagnostics). PET imaging has also attracted the interest of pharmaceutical companies as a valuable tool for accelerating and reducing the costs associated with traditional drug discovery efforts. Numerous initiatives are currently focused on developing novel diagnostic imaging agents for routine use in cardiology, oncology, neurology, inflammation, and other medical applications [11, 26].

2.2.1 PET Systems

A typical clinical PET system consists of a ring of detectors surrounding an inner bore where the patient bed is placed. The PET system is attached to a computational unit for data processing and image reconstruction. The ring of detectors are made of scintillation crystals coupled with photodetectors, which are connected to a readout circuit. In PET systems, there are several factors that can influence the detection, including the crystal material, depth-of-interaction (DOI), dead time, and pileup [1]. Figure 2.5 shows a commercial PET/CT system.

Fig. 2.5: A commercial PET/CT system showing the system's bore (yellow), patient bed (green), CT component (blue), and PET component (pink).

2.2.1.1 Detection

Recent advancements in PET technology have achieved submillimeter resolution in preclinical scanners while maintaining high sensitivity, making PET indispensable for imaging small-molecule drugs [27]. PET imaging operates on the principle that when a positron emitted by a β^+ radiotracer in the body encounters an electron, they annihilate each other, producing two photons that travel in opposite directions. These photons are 511 keV gamma rays, which correspond to the rest mass energy of electrons (and positrons).
PET detectors are used to identify annihilation photons resulting from positron annihilation. The detection process in a PET scanner begins by placing a positron-

emitting source, such as a phantom or a patient, within the scanner's field of view (FOV). Assuming no attenuation medium, the annihilation photons travel until they interact with a scintillation crystal. Upon interaction with the scintillation crystal, an annihilation photon deposits some or all of its energy, generating a brief flash of visible light that lasts for a duration defined by the scintillator's decay time (in the order of nanoseconds) [24]. This light is then converted into electrons by a photodetector, resulting in an electronic output pulse that signals the detection of an event. Here, front-end electronics are used to process and digitize the signals from the photodetectors. The front-end electronics are responsible for amplifying the signals from the photodetectors, digitizing these signals for further processing, and sending the digitized signals to the data acquisition system (DAQ), which then transmits them to a workstation for image reconstruction and analysis. When two events are detected within a specific coincidence timing window (typically 2-6 nanoseconds), they are assumed to originate from the same positron annihilation and are recorded as a coincidence event [28]. By analyzing the timing and location of these coincidence events, the origin of the annihilation photons can be determined wihtin a specific volume within the FOV called volume of response (VOR) (also LOR). PET scans rely on reconstruction algorithms to convert the detected events into a quantitative image, where the image intensity represents the radiotracer activity per unit tissue volume (kBq/cm^3, or MBq/mL).

In PET imaging, there are three types of coincidences of interest: true, random, and scatter coincidences. True coincidences are the primary contributors to the PET image signal, occurring when annihilation photons reach the detectors without undergoing any interactions before being absorbed by the detectors. Scatter coincidences occur when one or both annihilation photons undergo Compton scattering before detection, resulting in a false LOR and leading to inaccurate localization of the annihilation event. The rate of scatter coincidences is proportional to the size of the object being imaged, as larger objects increase the probability of photon attenuation before reaching the detector. Random coincidences, on the other hand, occur when two unrelated annihilation photons are detected that do not originate from the same annihilation event, again resulting in an incorrect LOR. The number of random coincidences detected (R) is related to the count rate (S) following the equation below:

$$R_{ij}^{SR} = 2\tau S_i S_j, \tag{2.4}$$

where S_i and S_j are the count rate in detector i and j, repetitively. R_{ij}^{SR} represents the estimated randoms rate for the LOR between detectors i and j , and τ denotes a predefined time coincidence window [29, 30]. Consequently, the randoms rate R is quadratically related to the activity, as increased activity leads to a propor-

tional increase in both S_i and S_j. Figure 2.6 illustrates an example of each type of coincidence.

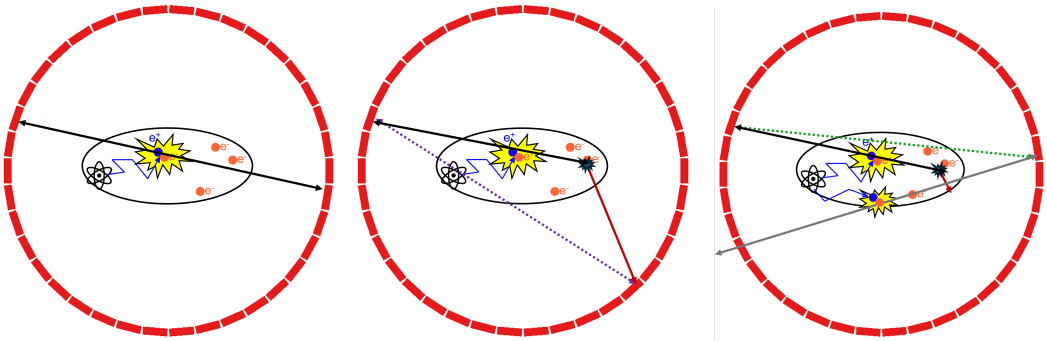

(a) (b) (c)

Fig. 2.6: a) A true coincidence event (black) in a ring of detectors (red), b) a scatter coincidence event where the original LOR is replaced by the dashed false LOR (purple) due to scattering of the second annihilation photon (dark red), and c) a random coincidence event where the scattered photon is absorbed in the tissue while, in a separate coincidence event (gray), one annihilation photon escapes the detector ring, resulting in a new false LOR (green).

When an attenuation medium is present in the scanner's FOV, the two annihilation photons may interact with the object before escaping. This could result in the attenuation and scattering of the photons. Such scatter causes the arrival points of the annihilation photons to be mislocated, leading to a loss in spatial resolution. To minimize the effect of scattered photons, an energy window is used to reject photons with energies below 511 keV, as scattered photons typically have energies lower than this threshold.

2.2.1.2 Scintillation Crystals

The crystal material used in PET detectors is an important factor that can affect the sensitivity, spatial resolution, and energy resolution of the system. The crystal size also contributes to determine the detector spatial resolution, sensitivity, and light output. The PET detectors of a clincal PET scanner typically are consist of crystals that are 3-5 mm wide and 18-25 mm thick. Moreover, the interaction probability of an annihilation photon within the scintillator depends on multiple factors, including the scintillator thickness. Increasing the length of the crystals can increase the detection probability and sensitivity, but it also has two main disadvantages: degraded timing resolution and increase of parallax error. The crystal size influences the detector's spatial resolution (determined by its cross-sectional

area) and sensitivity (determined by its thickness), as well as the light output, which subsequently impacts the detector's energy and timing resolution [11]. Light output is the amount of visible light produced by a scintillation crystal when it absorbs the annihilation photon. When a photon interacts with the scintillator material, it excites the electrons within the crystal, causing them to emit light as they return to their ground state. The quantity of light emitted is a critical parameter, as it directly influences several key performance characteristics of the detector.
The energy of the detected photon is proportional to the number of light photons generated in the scintillator. A stronger light signal leads to a better distinction between different energy levels, enhancing the ability to accurately reconstruct the energy spectrum of the detected photons. Moreover, a higher light yield enables faster and more accurate detection of the scintillation event's timing, which is essential for determining the exact location of the annihilation event along the LOR [31].
A good scintillator crystal for PET detectors must efficiently absorb 511 keV annihilation photons and convert them into visible light detectable by subsequent photodetectors. An overview of different scintillator crystals used in PET can be found here [32]. The scintillation light generated should be proportional to the energy of the incident photons and have a short decay time within the crystal. It is crucial to ensure that the crystal is transparent to the emitted visible light to prevent self-attenuation. Additionally, the photodetector's index of refraction should match that of the crystal. Applying optical grease or glue can help prevent air pockets, which could alter the index of refraction. Moreover, the crystal must be mechanically robust to withstand the manufacturing process without breaking or cracking [25, 33].
The two most commonly used crystals in PET systems are Bismuth Germanate (BGO) and Lutetium Oxyorthosilicate (LSO). BGO was one of the first crystals used due to its good absorption of 511 keV gamma photons. It can be manufactured as pixelated crystals coupled with photodetectors or as a monolithic crystal, resulting in light sharing between the photodetectors. LSO was developed as an alternative and became widely used due to its higher timing resolution, improving the TOF resolution from around 500-600 ps to about 250-400 ps (further details regarding TOF are provided in Section 2.2.1.5). A variant of LSO, doped with Yttrium, is LYSO, which shares similar properties and TOF timing characteristics with LSO [32, 34]. In this thesis, LSO is the scintillator crystal used in the Siemens Biograph Vision Quadra, while both the Multi-Emission Radioisotopes – Marine Animal Imaging Device (MERMAID), developed at the Institute of Medical Engineering, Universität zu Lübeck, and the United Imaging uEXPLORER use LYSO crystals.
One characteristic of LSO (and LYSO) is their inherent background radiation introduced by the Lutetium-176. ^{176}Lu decays by β^- emission, along with gamma rays with energies of 88 keV (6.2% abundance), 202 keV (10.3% abundance), and 307 keV (1.1% abundance) [35, 36]. Even though the branching ratio of the ^{176}Lu is

low and would have a negligible effect for a routine clinical PET scan, for low-dose PET studies it would have a noticeable impact [37].

2.2.1.3 Spatial Resolution

The dominant factor affecting spatial resolution in current PET scanners is the detector design. Monolithic crystals, which are generally larger, may encounter challenges such as edge distortion and parallax effects. In contrast, pixelated detectors can have very small detector elements and, with one-to-one readout, can achieve high resolution. However, this increases the system cost due to the greater number of crystals and readout channels.
Within the crystal, Compton scatter and light spread can cause mispositioning (wrong crystal is identified) and further degrade the spatial resolution. The parallax effect also degrades the spatial resolution due to the fact that the DOI in the crystal cannot be measured. The DOI refers to the distance from the surface of the scintillation crystal to the exact point where the interaction occurs along its longitudinal axis [11]. Light sharing occurs when scintillation light generated by a single event within the scintillator crystal is read out by multiple photodetector elements. Instead of being confined to a single photodetector, the light spreads out and is detected by several adjacent photodetectors. This effect can enhance spatial resolution by allowing the precise localization of the event through analysis of the light distribution across multiple detectors. However, light sharing can reduce energy resolution, as the signal is divided among several detectors, potentially leading to less accurate measurements of the total deposited energy. This issue can be mitigated through careful scanner calibration prior to measurement.

2.2.1.4 Dead Time and Pileup

Dead time is another important factor that can affect the detection in PET systems. It is the time period during which a detector is unable to respond to a signal due to previous activity. This can result in the loss of photon events and can affect the accuracy of the measurements. On the other hand, pileup occurs when multiple photon events occur close in time, resulting in the superposition of signals and distortion of pulse shapes. This can lead to inaccurate information about the height and time of the pulse. Dead time typically ranges from tens to hundreds of nanoseconds, while pileup can extend up to a few microseconds, depending on the specific characteristics of the crystals and the readout electronics used [38]. To overcome these issues, PET systems use various techniques such as shaping the pulse to reduce the duration of the trailing edge, using block detector designs with individual crystal readout to reduce pileup effects, and using dedicated front-end electronics to digitize and decode the photodetector signals. These techniques can

help improve the sensitivity, spatial resolution, and time-of-flight reconstruction in PET systems. Dead time and pileup have a noticeable effect on PET measurements when using high activity. However, for low-dose PET studies, their impact is negligible [39].

2.2.1.5 Time-of-Flight

Each photon detected by the PET scanner has an associated arrival time. The time difference between the arrival of the two photons is used to estimate the position along the LOR where the annihilation occurred. This technique is referred to as Time-of-Flight (TOF). TOF helps to localize the emission point along the LOR within a smaller region of the object following a Gaussian model, leading to an improvement in the image signal-to-noise ratio (SNR). This improvement is proportional to the square root of the object size divided by the system's timing resolution. Figure 2.7 illustrates how a TOF PET system compares to a non-TOF system.

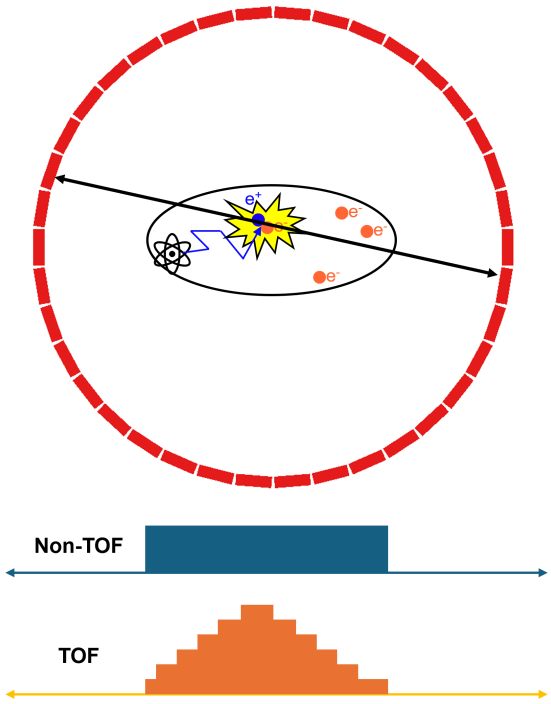

Fig. 2.7: A PET ring with an object in the center. In blue, a non-TOF PET system yields a homogeneous probability of detection along the LOR. In orange, a TOF PET system provides a higher probability of detection along the LOR, with the detection probability slightly shifted to the left.

TOF PET systems require high-performance detectors with precise timing capabilities. Advances in detector technology, such as scintillators with fast decay times and

high-resolution photodetectors, are essential for effective TOF PET. Modern PET systems typically achieve timing resolutions in the range of 250 to 600 picoseconds (ps), which enhances image quality [1]. TOF resolution of 250-600 ps corresponds to a 35-90 mm uncertainty in the position of the annihilation event. The current goal is to achieve a 10 ps TOF resolution, which would allow direct image reconstruction with only 1.5 mm uncertainty in the annihilation position [40, 41].

2.2.1.6 Data Processing

PET data can be organized in different ways, such as list-mode, or sinograms. List-mode data is a sequential record of detected events, allowing for the storage of additional information such as the energy, arrival time, and detector ID of both photons. Consequently, the storage space required for a list-mode file depends on the number of recorded events.
Sinograms are an alternate data structure in PET imaging, organized according to the geometry of the PET scanner. Each detected event is categorized by its angular orientation θ and its orthogonal distance s from the center of the FOV along the detector. For a point source, this results in a sinusoidal pattern in the sinogram.
The 2D sinogram can be represented using rotated coordinates r and θ, where these coordinates are defined in relation to the original Cartesian coordinates (x, y) rotated by the angle θ. For oblique angles ϕ (which account for LORs spanning multiple transaxial slices along the patient bed direction z), the axial position z is also considered. This extends the sinogram into a 3D representation $S(\theta, r, z, \phi)$, where four parameters are required to fully describe the lines in 3D space. Visual presentation of the axis are shown in Figure 2.8.
Oblique angles are crucial for systems with multiple detector rings. The value of ϕ controls the maximum ring difference (MRD) in such systems, where oblique angles can enhance the sensitivity of the scanner but come with the trade-off of higher data transfer rates and increased computational demand [43]. Adding the TOF information t to the sinogram creates a 4D dataset, denoted as $(S(\theta, r, z, \phi), t)$. The TOF information t can be incorporated by considering a bin segment value c, which corresponds to the coincidence window and the TOF resolution.
The number of sinogram bins can increase with a longer axial FOV (increasing the ϕ value), improved TOF resolution (increasing the t value), smaller detector crystals (increasing the s and r values), DOI detection, and the potential use of photon energy. However, unlike list-mode data, the maximum size of the sinogram is independent of the number of recorded events. Since most sinogram bins are empty, it is possible to further reduce the size of the sinogram by storing it as a sparse matrix. Moreover, a Michelogram offers a method to organize and interpret sinograms across multiple planes, capturing their relationships within the entire 3D volume [44]. A Michelogram is a graphical representation particularly valuable in systems with

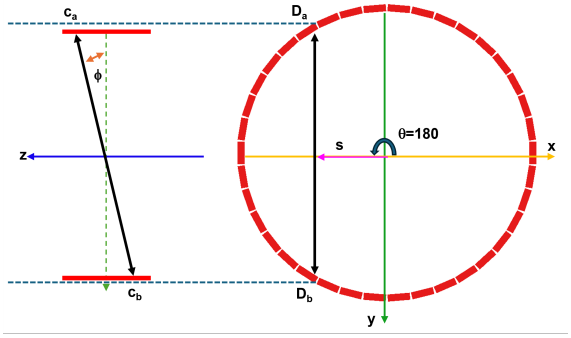

Fig. 2.8: Illustration of a transverse and longitudinal views of a PET system highlighting the principles of sinogram formation. The black line represents the LOR between detectors D_a and D_b (red blocks) which registers coincident events. c_a and c_b represent the crystals in different detector rings along the Z-axis.The angle ϕ and distance s describe the positioning of the LOR in relation to the sinogram coordinates, where $\theta = 180°$ denotes a direct back-to-back coincidence [42].

multiple detector rings, helping to organize and visualize the arrangement of sinogram data. By identifying symmetries and redundancies in the data, the Michelogram facilitates data reduction, segmenting the sinogram data into manageable parts and clarifying which sinogram bins correspond to specific detector pairs. Each point on the Michelogram corresponds to a particular detector pair, linking it directly to the relevant sinogram bins.
To accurately measure the count between two detector pairs, single-slice rebinning (SSRB) is performed, wherein oblique angle slices are remapped to the central slice. SSRB is most accurate when the activity is concentrated near the scanner's axis. However, for extended activity distributions, such as in whole-body scans, SSRB can introduce distortions and reduce accuracy. Therefore, SSRB is not used for imaging patients but is employed for measuring the sensitivity of PET systems [45].

2.2.2 Image Reconstruction

Image reconstruction is the process of estimating the radiotracer distribution from a set of projections. Image reconstruction is inherently an inverse problem, complicated by noise and incomplete data. Two main categories of image reconstruction methods, i.e. analytical and statistical iterative, were used in this thesis. In particular, only image reconstruction algorithms developed by the PET scanner manufacturers were used. Filtered back projection (FBP), an analytical image reconstruction method, was employed for CT image reconstruction and for determining the spatial resolution of the digital twin and the 3D printed phantoms (more details are provided in Section 3.2.3.2 and Section 4, respectively). Additionally, statistical iterative image reconstruction methods such as Maximum Likelihood Expectation Maximization

(MLEM) and Ordered Subset Expectation Maximization (OSEM) were used for the 3D printed phantoms and the digital twin image reconstruction. These algorithms functioned as a 'black box,' with no information or details provided about their exact implementation. However, the flexibility to adjust parameters and select the type of algorithm was allowed.

2.2.2.1 Analytical image reconstruction

Analytical image reconstruction in PET imaging involves mathematical methods that directly compute the radiotracer distribution within the body from the measured projection data. However, these methods do not fully account for the statistical nature of the data, such as noise and variance inherent in the PET measurements. Analytical image reconstruction in PET imaging is grounded in the concept of line integrals and the Radon transform, where PET imaging represent possibility weighted line integrals of the radiotracer distribution. The primary objective of analytical reconstruction is to invert the Radon transform to retrieve the original image from the projection data. FBP is the most common analytical reconstruction method used in medical imaging, particularly in CT and PET.
FBP is a common analytical reconstruction technique. It consists of two main steps: filtering and back projection. In the filtering step, projection data are transformed into the Fourier domain, where specific filters are applied to reduce blurring and enhance image quality. These filters often emphasize high-frequency components to preserve edges, but this can also amplify noise, which is typically high-frequency in PET images. The filtered projections are then transformed back into the spatial domain and 'smeared' across the image space at the angles they were originally acquired. This process, known as back projection, reconstructs the original distribution of the imaged object. The cumulative sum of these projections provides an approximation of the object's original structure. FBP is favored for its computational efficiency and ease of implementation. It is straightforward to apply and has been extensively validated, making it a standard choice in clinical CT imaging. However, its applications in PET are limited, being primarily used for quantification studies and spatial resolution determination [46].

2.2.2.2 Statistical iterative image reconstruction

Analytical image reconstruction methods have limitations as they often neglect several factors that affect PET spatial resolution. These factors include positron range, photon non-collinearity, penetration and scattering (both in the detector and within the patient), and random coincidences. Neglecting these factors can reduce image accuracy and quality, thereby impacting the diagnostic effectiveness of PET imaging. Statistical iterative approaches, such as methods like Origin Ensembles (OE)

and criteria like Maximum A Posteriori (MAP) and Maximum Likelihood (ML), are often employed to address these challenges. Hence, model-based statistical iterative reconstruction methods have replaced analytical image reconstruction methods for routine clinical studies. ML is the criterion used within this thesis work. For this section, the following references has been used [8, 46, 47, 48].
Statistical iterative reconstruction methods utilize comprehensive system models to describe the scanner geometry and the physics of data acquisition. By incorporating statistical iterative noise models, they effectively account for noise present in the data. Iterative image reconstruction methods offer several advantages over traditional analytical approaches. One significant benefit is their ability to enhance PET images by incorporating prior information about the scanned object or the imaging process. These methods also model the characteristics of the imaging system, which are encoded in the system matrix. By doing so, they can achieve higher image quality and resolution, reduce artifacts, and improve quantitative accuracy.
The foundation of statistical iterative methods lies in the discrete-discrete linear model of the imaging process, which relates the measured data $\boldsymbol{y}$ to the object of interest $\boldsymbol{f}$ through the equation:

$$\boldsymbol{y} = \boldsymbol{A}\boldsymbol{f} + \boldsymbol{r} + \boldsymbol{\sigma}, \tag{2.5}$$

where $\boldsymbol{f}$ is a vector representing the discretized object of interest, such as pixel or voxel values in an image, $\boldsymbol{A}$ is a system matrix that encodes the physics of the detection process, including how the object $\boldsymbol{f}$ contributes to the measurements $\boldsymbol{y}$, and $\boldsymbol{y}$ is a vector of measured data, $\boldsymbol{r}$ is the contribution of random coincidences, and $\boldsymbol{\sigma}$ represents the contribution of scattered coincidences.
In this model, the observed data $\boldsymbol{y}$ is inherently stochastic, meaning it is subject to random variations due to the physical process of measurement, such as gamma-ray emission and detection. The expectation value $E[\boldsymbol{y}]$ represents the average or expected measurement for a given object distribution $\boldsymbol{f}$, and is given by:

$$E[\boldsymbol{y}] = \boldsymbol{A}\boldsymbol{f} + \boldsymbol{r} + \boldsymbol{\sigma}. \tag{2.6}$$

This recognition is fundamental to the iterative approach: given only the observed data $\boldsymbol{y}$, the aim is to estimate the underlying object $\boldsymbol{f}$.
To do so, a probability distribution function is formulated $P(\boldsymbol{f}|\boldsymbol{y})$, which represents the likelihood that a particular object distribution $\boldsymbol{f}$ could have produced the observed measurements $\boldsymbol{y}$. Using this distribution, a selected estimate of $\boldsymbol{f}$ can be obtained based on a chosen criterion, such as ML estimation, which seeks to maximize $P(\boldsymbol{f}|\boldsymbol{y})$, or MAP estimation, which includes prior information about $\boldsymbol{f}$ in the estimation process. The probability distribution used in the thesis work is assumed to be a product of independent Posisson distributions.

The MLEM algorithm iteratively updates the image by comparing the measured data to the current estimate's forward-projection and adjusting the estimate accordingly. The attenuation correction factor c_{ij} is used during the iterative update to account for the reduced detection probability caused by photon attenuation. The MLEM algorithm is shown below:

$$f_j^{(k+1)} = \frac{f_j^{(k)}}{s_j} \cdot \sum_{i=1}^{I} \frac{y_i}{\sum_{m=1}^{J} a_{im} f_m^{(k)} + r_i + \sigma_i} a_{ij} c_{ij}, \quad \text{with} \quad s_j = \sum_{i=1}^{I} a_{ij} c_{ij}, \tag{2.7}$$

where k is the iteration number, $f_j^{(k)}$ is the reconstructed image value at voxel j in the k-th iteration, s_j is the sensitivity for voxel j, y_i corresponds to the number of measured events in LOR i (with $i = \{1, \ldots, I\}$), a_{ij} is the element of the system matrix that represents the probability that an event from voxel j is detected along LOR i, $\sum_{m=1}^{J} a_{im} f_m^{(k)}$ is the estimated projection value along LOR i based on the current image estimate, summing the contributions of all voxels m to the detected signal in LOR i as weighted by a_{im}, and c_{ij} is the attenuation correction factor for LOR i, applied during the iterative update. r_i and σ_i are the contributions of random coincidences and scattered coincidences, respectively, in LOR i.
A known limitation of MLEM is its slow convergence, which can lead to long reconstruction times, especially for high-resolution images and long measurements. To accelerate MLEM, the OSEM algorithm was developed [49]. OSEM (also called Ordinary Poisson OSEM (OP-OSEM)) accelerates MLEM by dividing the data into subsets and applying the update step to each subset in sequence during each iteration. By doing this, OSEM achieves faster convergence because it processes smaller portions of the data at a time, allowing for more frequent updates to the image estimate. OSEM can be described as follows:

$$f_j^{(k+1,s)} = \frac{f_j^{(k,s)}}{s_j^{(s)}} \cdot \sum_{i \in S_s} \frac{y_i}{\sum_{m=1}^{J} a_{im} f_m^{(k,s)} + r_i + \sigma_i} a_{ij} c_{ij}, \quad \text{with} \quad s_j^{(s)} = \sum_{i \in S_s} a_{ij} c_{ij}, \tag{2.8}$$

where k is the iteration number, s is the subset index, $f_j^{(k+1,s)}$ is the updated image value in voxel j after processing subset s in iteration $k+1$, and $f_j^{(k,s)}$ is the image value in voxel j after processing subset s in iteration k. The set S_s denotes the subset of LORs used in the s-th subset.
This method provides a significant improvement in computation speed, making it widely used in clinical PET reconstruction. However, while OSEM converges faster, it may not always converge to the exact MLEM solution unless carefully tuned.
In addition to scatter, attenuation, and random corrections, normalization correction is also essential for accurate PET image reconstruction [50]. Normalization accounts for variations in detector sensitivity across the PET scanner, which can arise from

differences in detector geometry, crystal efficiency, and electronic discrepancies among detector channels. Without normalization correction, the reconstructed image would display non-uniformities that do not reflect true variations in the distribution of the radiotracer. By applying normalization correction, these sensitivity variations are equalized, ensuring that the final image accurately represents the true activity distribution within the scanned object. This correction is critical for achieving quantitative accuracy in PET imaging, as it allows for reliable comparison of tracer uptake across different regions [51].
In this thesis, the PET image reconstruction algorithms provided by the vendor were used, including corrections such as scatter correction, random correction, and attenuation correction, as well as normalization and resolution improvement through PSF (Point Spread Function) modeling and TOF reconstruction. Detailed information about the exact methods used for these corrections is not available. For a comprehensive discussion of these corrections, please refer to [50, 52, 53, 54, 55, 56, 57, 58].

2.2.2.3 Noise amplification in PET reconstructed images

PET images exhibit two main types of noise: statistical noise and signal noise. Statistical noise arises due to the low count rates typical of PET images (compared to CT), along with the inherent randomness of radioactive decay, which follows a Poisson distribution. Signal noise refers to noise generated during the detection process, including scattering, and random coincidences, such as gamma emissions from non-pure positron emitters (such as ^{89}Zr). This noise is more pronounced in low-count regions. Noise often contains high-frequency components, which can make it challenging to distinguish from edges and textures in an image. This is why noise reduction techniques need to be carefully designed to preserve important details while removing unwanted noise.
After image reconstruction with algorithms such as MLEM, the statistical noise characteristics change. While MLEM iteratively refines the image to better fit the measured data, it can also amplify noise, particularly with increased iterations. After reconstruction, noise often appears spatially correlated, with higher noise in areas of low activity. Though MLEM sharpens the image, excessive iterations can overemphasize noise, leading to streaks and localized variations, commonly referred to as 'night sky noise'. This makes post-reconstruction noise more structured compared to the pre-reconstruction Poisson noise.
Since PET data include both true signals and noise, without regularization, image reconstruction algorithms tend to process the image in a way that amplifies the noise. Several regularization methods have been developed that introduces additional constraints to limit the impact of noise on the reconstructed image. These include early stopping of iterations, post-reconstruction denoising, smoothing basis functions,

and incorporating penalized likelihood functions into the ML criterion. One limitation of MLEM is that it converges faster for low spatial frequencies (signal) than for high frequencies (noise), making early stopping a potential source of error in quantitative PET when using too few iterations.
In high-iteration images, strong negative correlations between neighboring pixels make post-reconstruction denoising feasible. The most effective method for noise reduction is often applying a Gaussian filter with an appropriate FWHM and kernel size, producing images with reduced noise suitable for quantitative analysis. Rather than reducing iterations, post-reconstruction filtering is generally preferred for noise suppression. Another approach involves using smooth, overlapping basis functions, such as spherical (blobs) or Gaussian basis functions, to enhance image quality [59, 60]. More details regarding post-reconstruction denoising will follow in Section 2.3.2.

2.2.3 PET applications

PET imaging is most commonly used for diagnostic purposes. It is used to detect and monitor various cancers for oncology, helps during the cardiology exams to evaluates heart conditions and blood flow, and diagnoses neurological disorders and brain function. The second application relevant to the work presented in the thesis is theranostics, particularly with ^{90}Y, where it is measuring the distribution and dose of radiation delivered to the tumor.

2.2.3.1 Diagnostics

During a diagnostic PET scan, the patient receives an injection of a radiotracer. Following this, there is a waiting period of approximately one hour. This allows the radiotracer to circulate and be absorbed by the body's tissues. The scanning procedure itself typically spans a duration of 30 to 60 minutes [61]. The most widely employed isotope for PET imaging is ^{18}F, which is used for total body imaging, brain imaging, and cancer detection. ^{18}F-FDG is a glucose analog taken up by cells with high metabolic activity, such as cancer cells. ^{18}F-FDG scans are used to detect and monitor various types of cancers. For bone imaging, sodium ^{18}F-fluoride (^{18}F-NaF) is used. It is taken up by areas of increased bone turnover, which can indicate metastatic bone disease. ^{68}Ga-PSMA is used for prostate-specific membrane antigen (PSMA) is a protein overexpressed in prostate cancer cells and is used to detect prostate cancer and its metastases. For imaging neuroendocrine tumors, ^{68}Ga-DOTATATE is used as it binds to somatostatin receptors, which are overexpressed in many neuroendocrine tumors [62].
Moreover, immuno-PET is a form of molecular imaging that combines the high specificity of antibodies with the sensitivity of PET, enabling precise tumor detection

and aiding in the planning of antibody-based therapies. It uses radiolabeled antibodies to target specific antigens on cancer cells, allowing for precise imaging of tumors. The long-lived positron emitter ^{89}Zr is often used for this purpose, enabling non-invasive tracking of monoclonal antibodies, supporting longitudinal studies. ^{89}Zr is also being investigated as a tool for cancer imaging [3, 63].

2.2.3.2 Theranostics

Theranostics is a term derived from two words: therapeutics and diagnostics. The concept involves using a radioactive source to both treat tumors and obtain diagnostic information without the need for additional sources. This ensures that the treatment is administered effectively and allows for adjustments if necessary. Theranostics is particularly useful in personalized medicine, as it allows for tailored treatment plans based on the specific characteristics of a patient's disease.
Theranostics can be achieved through methods such as in-beam PET during particle therapy or following radioembolization, also known as Selective Internal Radiotherapy (SIRT). SIRT is a minimally invasive treatment primarily used for liver tumors, where tiny beads containing a radioactive substance (Yttrium-90 (^{90}Y)) are injected into the blood vessels supplying the tumor. This targeted approach allows for high doses of radiation to be administered to the tumor while minimizing exposure to surrounding healthy tissues [64].
SIRT is predominantly used to treat liver cancers, such as hepatocellular carcinoma and metastatic liver tumors from other primary cancers like colorectal cancer. This treatment is especially beneficial for patients who are not candidates for surgery due to the size, number, or location of the tumors, or other underlying health conditions. The procedure is conducted during an angiogram. A catheter is inserted into an artery, typically through the groin or wrist, and is carefully guided to the blood vessels supplying the tumor. Once the catheter is in place, ^{90}Y particles are injected. These particles lodge in the tumor's blood vessels, emitting radiation that destroys cancer cells over time by delivering high doses of radiation directly to the tumor, effectively sparing the surrounding healthy tissue from unnecessary radiation exposure.
^{90}Y is a nearlly a pure β^- emitter with a high-energy beta particle emission (2.186 MeV) and almost no gamma radiation. Due to the absence of gamma radiation, ^{90}Y is ideal for therapeutic applications where the goal is to deliver a high dose of radiation to a localized area while minimizing exposure to surrounding tissues. ^{90}Y half-life of 64.1 hours allows for effective treatment duration [65].
The decay scheme of ^{90}Y is shown in Figure 2.9. As shown, ^{90}Y does not emit positrons, making it unsuitable for direct PET imaging. However, positrons can be generated through internal pair production due to the high-energy beta particles emitted by ^{90}Y. Nevertheless, the branching ratio for pair production is extremely

low (approximately $3.2 \times 10^{-5}\%$), resulting in minimal positron counts to produce the PET image. Additionally, the high-energy electrons produced by ^{90}Y leads to significant bremsstrahlung radiation, which further degrades image quality.

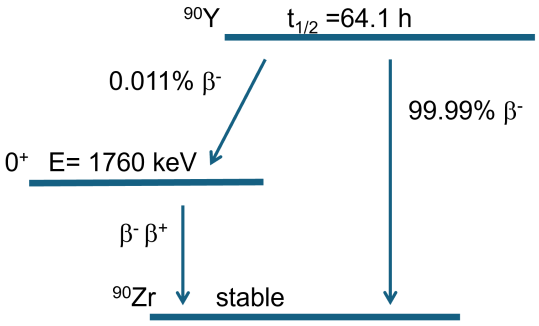

Fig. 2.9: Simplified decay scheme of ^{90}Y [66].

^{90}Y low branching ratio for positrons can still produce a PET image due to the use of high activity (typically in the range of GBq). However, the reconstructed PET images have high level of noise. However, long scan times are utilized to combat the noise (more details will follow in Chapter 5).
PET scans are instrumental in identifying the exact location and size of tumors before and after treatment. This precision ensures that the radioactive particles are delivered accurately to the target area, enhancing the treatment's effectiveness. PET imaging is also used to monitor the effectiveness of radioembolization over time. By evaluating the metabolic activity of the tumor, healthcare providers can calculate the dose delivered to the tumors and determine the treatment's success or make necessary adjustments to the patient's treatment plan [4, 67]. Hence, In Chapter 3, I aim to leverage the Quadra digital twin to evaluate the performance of the image reconstruction tools for scatter scaling used for dose estimation from the PET image.

2.3 Low Dose PET

Higher administered doses would help to reduce the noise level, but at the cost of increasing the radiation dose delivered to the patient. The alternative of increasing the scan time is often unfeasible due to the defined daily patient throughput, the degradation of image quality due to motion artifacts, and the limited availability of radiotracer signal due to its decay over time.
Furthermore, achieving low-dose imaging could expand the use of PET in a wide range of applications that prioritize reduced radiation exposure. These applications include parametric imaging, dynamic imaging, theranostics, and immunology with

low branching ratio isotopes. In addition, a reduction of the administered dose is desirable for pediatrics and low-dose PET could enable its use as a screening procedure [25].
Noise in PET images degrades both quantitative accuracy and lesion detectability, potentially leading to missed lesions. Consequently, there is a strong demand for noise reduction techniques that improve image quality without increasing the injected dose. To address this issue, researchers have developed various methods to enhance the imaging quality and accuracy of low-dose PET scans, including improvements in image reconstruction algorithms (as illustrated previously), the development of new detectors and scanners (such as TBPET scanners), and post-reconstruction filtering (using both classical methods and AI implementations) [1, 68, 69].

2.3.1 Total Body PET

The idea for TBPET has been around since the 1990s. However, due to limited detector technology and computational power, none were implemented in clinical settings. Typically, whole-body PET scanners have an AFOV of 15 to 26 cm long, requiring multiple bed positions to obtain a whole body image. This results in long scan times and low patient throughput (20 to 40 minutes per patient for whole-body PET scan). These issues were solved by the introduction of TBPET scanner making it possible to obtain a whole body image in a single bed position [1]. Figure 2.10 shows an example of a conventional PET scanner and a TBPET scanner.

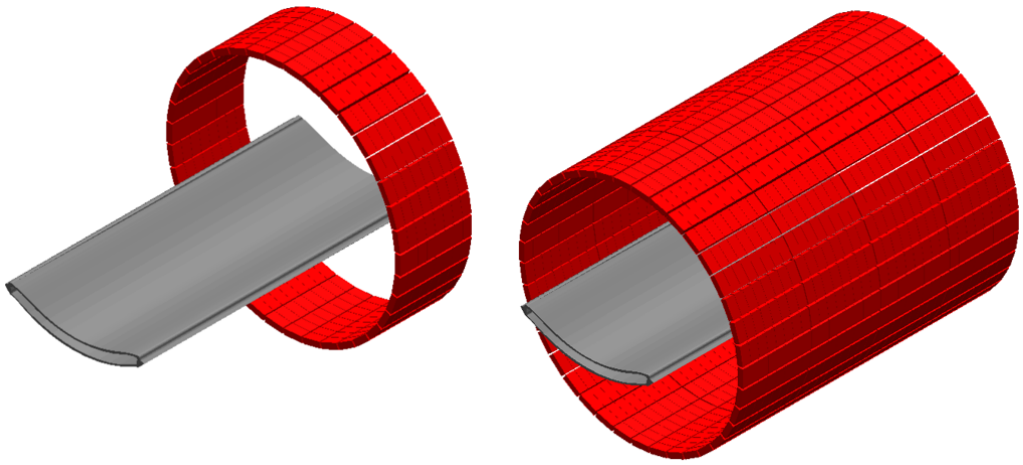

(a) (b)

Fig. 2.10: a) 3D rendering of a conventional 26 cm AFOV PET scanner (Siemens Biograph Vision) and b) a 106 cm AFOV TBPET scanner (Siemens Biograph Vision Quadra) with the patient bed (gray).

With the advancement of faster TOF timing resolution crystals and the introduction of SiPMs, the pathway was paved for bringing TBPET to the market, with the only limitation being the higher cost. This higher cost can be justified by increased patient throughput due to reduced scanning procedures, lower required injected activity, and the introduction of new applications for PET imaging. These applications include kinetic modeling, where TBPET provides superior quality for kinetic data across the entire body, pharmacokinetic modeling, drug development, the development of new radiotracers, and the reintroduction of some radiotracers that were previously discarded due to poor energy resolution or low signal-to-noise ratio with older systems. There are several TBPET scanners currently in development or being simulated for future use. However, as of now, only two TBPET scanners are widely actively used for clinical diagnostics: United Imaging uEXPLORER, and Biograph Vision Quadra [1, 43]. A summary of each system is shown in Table 2.2.

The Siemens Biograph Vision Quadra PET/CT scanner is a state-of-the-art TBPET system. Biograph Vision Quadra is composed of four Biograph Vision, where both scanners are utilizing silicon SiPM as an alternative of PMT to obtain a higher sensitivity and TOF resolution. The scanner has an AFOV of 106 cm, a transaxial FOV of 70 cm, and a bore size of 80 cm. It consists of 243000 LSO crystals ($3.2 \times 3.2 \times 20$ mm) coupled to SiPM detectors. The crystals are arranged in 760 radial rings and 320 axial rings. During image reconstruction, Biograph Vision Quadra can operate in two sensitivity modes: high sensitivity (HS) mode with MRD of 85 with acceptance angle of 18 degrees (such as Biograph Vision), and ultra-high sensitivity (UHS) mode MRD322 with acceptance angle of 52 degrees encompassing all oblique coincidences throughout the scanner's rings. MRD322 boosts the sensitivity of Quadra by 2.75 compared to Biograph Vision [43]. As of 2024, only the UHS mode is being used due to its superior preference in the clinical setting [2]. The Biograph Vision Quadra will be the imaging system utilized in Chapter 3 for developing the digital twin, Chapter 4 for imaging 3D printed phantoms, and Chapter 5 for the application of AI for image denoising.

Despite the advantages mentioned above, there are still some drawbacks to these systems. The most notable one is the higher cost. Additionally, there is a need for dedicated image reconstruction and storage units due to the high volume of data generated, especially for dynamic scans. Lastly, with the increased number of measured LORs-more than 100 billion possible LORs in the Quadra scanner, for example—there would also be more noise-equivalent count-rate (NECR) observed (NECR of 1613 kcps for MRD 85 and of 2956 kcps for MRD 322 for Biograph Vision Quadra [43]).

Recently, Calderón et al. conducted a study utilizing the Siemens Biograph Vision Quadra PET/CT scanner to investigate the feasibility of reducing the injected activity to obtain a low-dose PET image while maintaining image quality and

Table 2.2: Specifications of the three total body PET systems [43, 70, 71]

System	**uEXPLORER**	**Biograph Vision Quadra**
Scintillator	LYSO	LSO
Readout	SiPM	SiPM
Scintillator size (mm^3)	2.76 × 2.76 × 18.1	3.2 × 3.2 × 20
Total number of detector pixels	564,480	243,200
Bore/detector diameter (cm)	68.6/78.6	82
Axial length (cm)	194.8	106
Transaxial res. (FWHM in mm)	3.0	3.4
Axial res. (FWHM in mm)	3.0–3.5	3.8
Energy res. @ 511 keV (%)	11.7	10.1
Energy window (keV)	430–645	435–585
Coincidence window (ns)	4.5–6.9	4.7
TOF resolution (ps)	505	228
NU2-2018 sensitivity (kcps/MBq)	191.5	176
NU2-2018 scatter fraction (%)	35.8	37
NU2-2018 peak NEC (kcps)	1435 @ 16.8 kBq/cc	2956 @ 27.49 kBq/cc

lesion detectability. This was accomplished by rebinning the PET raw data into shorter frame durations to simulate 5-minute scans with reduced activities in the ultra-high sensitivity mode. Their findings revealed that it is possible to obtain diagnostically adequate images using an injected activity as low as 0.5 MBq/kg, a significant reduction compared to the conventional injected activity of 3 MBq/kg. This represents a dose reduction factor (DRF) of approximately 17% relative to full-dose imaging [2]. The DRF value can be calculated by dividing the desired lower dose to the full dose, in this case, $0.5(MBq/kg)/3\ (MBq/kg) = 17\%$. In recent years, there has been a growing interest in achieving even lower DRF values in PET imaging. Xue et al. have proposed the application of ultra-low dose PET (ULDPET) for a DRF of 100 (1% of the full dose) [72].

2.3.2 Denoising at PET Image Reconstruction Level

The primary source of noise in PET data is Poisson noise (though scatter and random coincidences also contribute significantly), arising from the stochastic nature of radioactive decay, photon detection, and related processes. However, in the reconstructed PET image, the noise is influenced by both the Poisson characteristics of the data and the reconstruction algorithm applied.
PET scanners overall sensitivity can be affected by factors such as scanner design, detector efficiency, and patient characteristics. The inherent noise due to the stochastic nature of the detected events remains Poisson-distributed irrespective of the sensitivity levels.
Image noise could be mitigated by regularizing the reconstruction (e.g. Bayesian approaches [73]); however, throughout the work presented in the thesis, the reconstruction software used for the commercial PET scanners relies on OSEM algorithm.

Noise reduction is performed through post-reconstruction filtering and early stopping of the iteration process. This section will cover some of the classical image denoising methods used in PET and new approaches with AI for image denoising.

2.3.2.1 Post-reconstruction filtering methods

To enhance PET image quality, various approaches have been explored, including post-denoising techniques. Post-reconstruction filters include, non-local mean filter [74], HighlY constrained backPRojection (HYPR) filter [75], guided image filter [76] and the application of post-reconstruction Gaussian filter [77]. It has been a standard clinical practice to use a Gaussian filter with $\sigma = 4$ mm for denoising PET images [78]. Moreover, recent studies with the TBPET Biograph Vision Quadra have shown that a 2-6 mm is sufficient to improve the coefficient of variation (CV) and image metrics without degrading image quality even at the edges of the FOV [79]. Hence, only Gaussian filter will be considered in Chapter 5 for image denoising. Gaussian filtering has been widely used in commercial PET scanners. Despite causing some blurring of images during noise reduction, Gaussian filters are popular due to their linearity and robustness. Gaussian filtering is often applied during image reconstruction, but it can lead to signal loss [80, 81]. The kernel of the 3D Gaussian filter is defined as follows:

$$G(x, y, z) = \frac{1}{(2\pi\sigma^2)^{3/2}} \exp\left(-\frac{x^2 + y^2 + z^2}{2\sigma^2}\right), \tag{2.9}$$

where σ is the standard deviation, which controls the extent of smoothing, and x, y, and z correspond to the spatial location in the image relative to the center of the kernel. In practice, the Gaussian kernel is truncated at a distance of 3σ or 4σ from the mean to limit the extent of the filter. This means that the kernel size is chosen such that it covers the range where the Gaussian function has significant values, while values beyond this range are considered negligible and ignored. The image support, therefore, refers to the region of the image that is influenced by the filter, which is approximately $8\sigma \times 8\sigma \times 8\sigma$ in size for 3D images.
The advantage of using a post-reconstruction filter lies in its ability to be generalized across data from different scanners without requiring access to the raw data or the image reconstruction algorithm, which are often proprietary of the vendor. Additionally, various approaches have been developed to anonymize patient images, enabling their sharing across different research sites. However, sharing of raw PET data still faces significant challenges, primarily due to its large size (0.5 GB per image compared to 30 GB for five minutes of list-mode data).

2.3.2.2 Image denoising using AI

With the advancements in deep learning in recent years, AI applications in PET imaging have expanded to include enhancing radiation detection, developing quantitative image reconstruction algorithms, and supporting decision-making processes. This section will focus on the use of post-processing techniques for image denoising. A detailed overview of other applications can be found in the referenced literature [28, 82].

AI-based denoising techniques have shown promising results in improving the PET image quality, and ongoing research continues to explore new approaches and improve existing ones. The advantage of AI-based denoising approaches over traditional methods is their ability to generalize more effectively to a wide variety of noise patterns and image features. This is because AI models can learn complex mappings from noisy to clean images, utilizing millions of parameters for optimization, compared to the handful or few dozen parameters typically used by classical denoising methods. Additionally, AI-based approaches can adapt to different types of noise when trained on diverse datasets. However, these methods require significant computational resources and large training datasets. For a recent comprehensive overview, refer to [69, 83].

Several methods have been investigated for using different AI deep learning models at both the data level and the image level for image denoising. The advantage of using AI at the data level, as compared to the image level, is that it ensures no noise or bias from the reconstruction algorithms is amplified. Any bias or noise amplification caused by the reconstruction algorithm would be present in the image to be denoised. However, the biggest limitation of the data-level approach is the enormous size of the data to be denoised, especially when investigating TBPET sinograms. For example, a Biograph Vision Quadra 3D volume image ($440 \times 440 \times 645$ pixels) would be about 0.5 GB of data, while the 4D sinogram used for the reconstruction would be approximately 40 GB for one patient.

PET denoising applications aim to improve the image quality of PET scans by removing noise and enhancing the resolution of the images. Some of the popular AI-based denoising techniques for PET imaging include supervised learning, unsupervised learning, and generative models. Supervised learning involves training a model on a labeled dataset of high-dose and low-dose image pairs [84, 85, 86], while unsupervised learning involves training a model on an unlabeled dataset [87, 88]. In addition, Schramm et al. [89] introduced an innovative method of anatomically guided image denoising. By leveraging MRI images in conjunction with low-dose PET images, they were able to significantly enhance the output of their network. This method underscores the importance of integrating anatomical information to improve denoising performance. Onishi et al. [90] adopted a similar strategy by training an unsupervised network, further demonstrating the efficacy of using

additional anatomical data for denoising purposes. Xie et al. [91] extended this concept by incorporating CT data to further refine the network output. Their work illustrates the versatility of using different types of anatomical images to aid in the denoising process. The advantage of using anatomically guided networks is that MRI and CT images are already acquired and used within the reconstruction algorithm, as mentioned earlier. This approach adds more information to the network without delivering additional dose to the patient.
Generative models, on the other hand, aim to learn the underlying statistical distribution of PET images and generate noise-free images based on this distribution [92, 93].
A very recent approach proposed has been the use of diffusion models for image denosing. Diffusion models are a type of neural network that learns the target data distribution by iteratively refining the data distribution based on a Markov chain. The forward diffusion process gradually adds noise to the input image, while the learned reverse diffusion process removes noise from it gradually over many steps. The goal of diffusion models is to transform a normal distribution into a specific data distribution based on iterative refinements [94]. Diffusion models have shown promising results in various computer vision tasks, such as image generation, super resolution, image in-painting, and MR image reconstruction. In PET imaging, diffusion models serve as effective tools for denoising, aiming to eliminate noise from the image while retaining its underlying structure and intricate details as demonstrated by Gong et al. [95]. However, a notable drawback of diffusion models lies in their inherent highly complex and computationally expensive during the training phase, coupled with the necessity for large-scale datasets containing both clean and noisy pairs, as highlighted by Kim et al. [96]. Furthermore, there is ongoing research to deconstruct Denoising Diffusion Models (DDMs) for self-supervised learning. This approach gradually transforms a DDM into a classical Denoising Autoencoder (DAE), exploring how various components of modern DDMs influence self-supervised representation learning [97]. A disadvantage of such networks is the need for a large pool of training data to generalize effectively, resulting in high computational time. Moreover, since these networks generate images from noise or random signals within the image, there is a higher chance of hallucination, where the network may produce elements that were not actually present in the original image [98, 99].
For supervised learning, training pairs are typically generated through two approaches: the addition of noise, primarily Gaussian noise, to the target image (full-dose) to create the network input (low-dose), thus introducing additional noise, or through re-framing the data of the full-dose image to generate a low-dose reconstructed image. The primary issue with adding Gaussian noise to full-dose PET images is that models trained on such data may not generalize well to real-world

scenarios where noise is more complex and influenced by factors such as patient size, scan time, and medical history. Gaussian noise does not accurately represent the noise characteristics of actual low-dose PET images. As a result, training with Gaussian noise can lead to unrealistic training data and potential overfitting to the specific type of noise introduced. Furthermore, Gaussian noise may obscure fine details and small lesions in the images, increasing the risk of missing these critical features in the denoised output [100].

One issue concerning the utilization of denoising networks trained with a specific noise level is their limited generalization to other noise levels, as demonstrated by Xie et al. [101]. To address this limitation, Xie et al. introduced a Unified Noise-aware Network (UNN) for low-count PET denoising, which combine various denoising networks to consistently yield promising denoised outcomes irrespective of the input noise level. This network primarily targets dynamic imaging scenarios wherein the noise levels may differ across different frames.

Currently, in the re-framing method, the input is assumed to be a low-dose image obtained by injecting the patient with lower activity. However, the initial activity remains the same; the scan duration is shortened to reduce the prompt events in the data. Since the lengths of these scans are typically much shorter than the radiotracer's half-life (e.g., 5-10 minutes for ^{18}F-FDG, which has a half-life of 109 minutes), obtaining shorter frames at the start, middle, or end would not significantly affect the reconstructed image. This approach allows for the generation of more training data points from a single scan. Nevertheless, even for high timing resolution, the use of high activity leads to a higher number of random coincidences in the sinogram data, and the data can be affected by pile-up and dead-time effects. With higher activity levels, the random and scatter fractions escalate further, especially in the context of TBPET scanners with a broader acceptance angle compared to traditional scanners [43, 102]. Statistical modeling and regularization help minimize the impact of random events within the reconstructed image, while methods such as single scatter simulation are used to estimate scatter noise. Despite the aforementioned limitations, the re-framing method remains widely utilized for the training of neural networks. Obtaining genuine low-dose high-dose pairs for training poses a significant challenge due to several factors. Firstly, it necessitates scanning the same patient or a healthy volunteer twice: once after administering the high activity, and again after the initial injected activity decays, reaching the desired DRF. This process introduces alignment challenges to ensure minimal gross motion artifacts, as it involves two separate scans. Secondly, as demonstrated in the literature [103], the metabolism of the radiotracer alters its distribution within the body during PET imaging over a span of hours, rendering it unsuitable to compare the two scans, as the tracer distribution within the body might have changed.

As the low-dose scans from the re-framing method maintain the same random-to-true ratio as the high-dose scans, the data used for training the AI-based denoising model consist of images with a higher level of randoms compared to the actual low-dose images that will be denoised in a clinical setting. Hence, I aimed to address this issue in Chapter 5 by utilizing the Quadra digital twin. Moreover, in low-dose PET, the injected activity corresponding to the DRF is known in advance. I have made use of this fact to propose a new network for an image-denoising of low-dose PET data, inspired by the architecture of the diffusion model during network training, namely *Progressive Elimination of Noise Towards Accurate Ultra Low-Dose PET Images Using 3D U-Nets* (PETAL-3D). Instead of adding noise to the image during the forward process, and later gradually remove noise in thousands of denoising steps, we generate few training images with various noise levels, from low noise to ultra high noise levels, to be used later as network training pairs.

2.4 Monte Carlo Simulation

Monte Carlo (MC) methods are a class of computational algorithms that utilize random sampling to solve problems involving uncertainty or complexity. The core idea is to use randomness to approximate solutions to problems that are often deterministic in nature but difficult to solve directly. MC methods are widely used in optimization, numerical integration, and sampling from probability distributions across various fields. The name derives from Monte Carlo in Monaco, famous for its casinos and the randomness associated with gambling. Monte Carlo simulations, a specific application of MC methods, are used to simulate complex systems or processes by generating random samples and analyzing the outcomes.
MC simulations involve running the algorithm multiple times to model the probability distribution of an uncertain variable or system. They are particularly useful for predicting the behavior of systems over time or under varying conditions by averaging results from random sampling. These simulations can handle complex problems with many uncertain parameters, providing approximate solutions when traditional methods are impractical [104].
MC simulations are a crucial tool in PET imaging, as they enable the optimization of complex systems without the need for costly manufacturing and equipment testing. MC simulations have been used to investigate problems that are analytically intractable and for which experimentation is too time-consuming, costly, or impractical. Moreover, MC simulations can be used to investigate initial approaches in silico to determine the most suitable methods before implementing them in the lab.
MC simulations are commonly used to study the effects of variations in individual parameters, such as crystal thickness, detector orientation, phantom size, and other system-specific factors. They are also used to investigate physical phenomena that are

difficult or impossible to measure directly in experiments, such as scatter correction in imaging or dose estimation in radiation therapy. MC simulations serve as a valuable complement to experimental studies and should always be validated and compared against experimental measurements to ensure their accuracy and reliability [105, 106].
However, MC simulations have some drawbacks. One major drawback is that they can be computationally intensive and time-consuming, especially for large-scale simulations. Additionally, MC simulations may not always provide accurate results, as the accuracy depends on the precision of the models used and the number of events simulated. Finally, Monte Carlo simulations may not always capture all the complexities of a system or process, which can limit their usefulness in certain cases.

2.4.1 Monte Carlo simulations toolkits in PET imaging

Over the years, several MC simulation toolkits have been developed for PET imaging. The most commonly used are the Monte Carlo Nuclear Particle Transport (MCNP), a Monte Carlo PET simulation tool based on PENELOPE (PeneloPET), and the GEometry ANd Tracking toolkit (Geant4) [107, 108, 109]. Each was developed for specific use cases and applications, with Geant4 being the most widely used in PET MC simulations. MCNP offers capabilities to simulate diverse radiation transport scenarios and evaluate parameter impacts on image quality while validating PET system performance, but it demands substantial computational resources and exhibits limited modeling flexibility. Similarly, PENELOPE can simulate a wide range of radiation transport scenarios and assess the impact of different parameters on PET image quality, also serving to validate PET system performance. Nevertheless, it shares the drawback of high computational resource demands and limited flexibility. Moreover, PENELOPE and MCNP have the additional disadvantage of being closed-source toolkits, making them harder to access.
Geant4 is a simulation toolkit developed by the *Conseil Européen pour la Recherche Nucléaire* (CERN) that accurately simulates the passage of particles through matter. It has a diverse range of applications, from modeling the interactions of cosmic radiation with materials on the International Space Station to studying the interactions of photons with DNA molecules. Geant4 excels in tracking various types of radiation interactions with matter due to its robust and flexible architecture. It employs comprehensive physics lists that encompass electromagnetic, hadronic, and optical processes, allowing for precise simulation of particle interactions across a broad energy spectrum. The $emstandard_{opt4}$ physics list is optimized for precise calculations of electromagnetic interactions. It includes multiple scattering, ionization, bremsstrahlung, and pair production for electrons and positrons, as well as Compton scattering, photoelectric effect, and Rayleigh scattering for photons, making it a suitable candidate for PET systems simulations.

The toolkit's versatility extends to fields such as medical physics, where it is used for radiation therapy planning and imaging [108, 110]. In recent years, several simulation toolkits have been developed based on Geant4, eliminating the necessity of C++ programming by utilizing macro languages. Among the most widely used toolkits in PET imaging are the GEANT4-based Architecture for Medicine-Oriented Simulations (GAMOS) [111] and the GEANT4 Application for Emission Tomography (GATE) [112, 113, 114]. Both GAMOS and GATE are open-source and benefit from the extensive validation and reliability of the Geant4 toolkit while providing higher-level interfaces that simplify the simulation setup. These toolkits help researchers and clinicians to focus on their specific applications and scientific inquiries without the steep learning curve associated with C++ programming.
GATE extends the capabilities of Geant4 by focusing on emission tomography, including PET and SPECT. GATE incorporates dedicated models for detector response, time-of-flight measurements, and accurate simulation of the physics involved in emission tomography.
GATE has been used to simulate a variety of PET scanners. This includes preclinical systems such as the Siemens Inveon [115], the Siemens Inveon Trimodal Imaging Platform (which includes PET, SPECT, and CT) [116], the X-PET subsystem [117], and the Mediso AnyScan [118]. GATE has also been used to validate clinical PET scanners, such as the GE Discovery MI 4-ring model [119] and the Siemens Biograph mMR [120], which was additionally employed to simulate a breast PET insert that integrates with the Siemens Biograph mMR scanner [121]. Furthermore, GATE has been utilized for the validation of TBPET scanners, including uEXPLORER [122, 123], PennPET Explorer [124], and, more recently, the Siemens Biograph Vision Quadra [125]. In addition, GATE has been applied to simulate and validate novel PET scanners, such as J-PET, a TBPET systems using plastic scintillators [126], TBPET systems employing monolithic LYSO detectors [127], and the newly developed walk-through PET scanner [128]. Moreover, it has been used to simulate dedicated scanners such as Positrigo's NeuroLF, brain PET scanner [129] and the MERMAID scanner, dedicated to small-fish imaging [130]. Hence, throughout the work of the thesis, the GATE simulation toolkit will be used for developing the digital twin, as detailed in Chapter 3.

2.4.2 GATE

GATE can simulate a wide range of applications, provided the minimum required parameters are specified to run the simulation. Users can perform simulations using predefined systems for SPECT, PET, and CT, or they can customize their simulation setup by defining each layer of the system. When preparing simulations, it is essential to define the system, source, and physics list. The physics list controls the types of

interactions between radiation and matter and the energy range that the simulation will track, ensuring accurate and relevant results.
GATE also provide a module called 'Digitizer'. The primary purpose of the module is to model the Front End Electronics (FEE) signal-processing chain in the detectors. This involves a two-step process. In the first step, the geometric elements that compose the detector are described in detail. The second step involves detailing the process used to convert particle interactions in the scintillator into a recorded signal. The digitizer module is constructed by selecting a set of processing submodules that perform operations on the list of interaction events ('hits') occurring in the detector elements. This process chain is capable of modeling spatial, energetic, and temporal uncertainties, calculating various energy or position thresholds, and creating the output signal. The results of these simulations can be stored in various formats, such as list-mode, sinograms, or projection images, depending on the requirements of the study. Additionally, the timing elements of the module include TOF, dead-time, and coincidence windows, all of which can be user-parameterized to tailor the simulation to specific experimental conditions. The output can be stored as raw data format, American Standard Code for Information Interchange (ASCII), or an Object-Oriented Data Analysis Framework (*ROOT*) file [131] for subsequent processing. This comprehensive approach ensures that the module can accurately replicate the complex processes involved in detecting and recording particle interactions, thereby enhancing the reliability and applicability of the simulations. Figure 2.11 presents a visual representation of the workflow from simulation to image reconstruction using GATE.
Additionally, GATE provides interactive tools known as 'Actors' that track the simulations and can provide a variety of output information. Actors are employed to extract specific data from the simulations, such as simulation statistics, absorbed dose, 3D images, particle filtering, and more. The actors used throughout this thesis are the *SimulationStatisticActor* and *MuMapActor*. The *SimulationStatisticActor* is used to count the number of steps, tracks, events, and runs in the simulation. This is a crucial tool for monitoring simulation performance, especially when the goal is to optimize the simulation or ensure that it is not stuck. The *MuMapActor* is used by attaching it to the 'world' (the environment where the simulation occurs, ensuring that no particle tracking takes place outside this boundary) to produce the attenuation map (MuMap) of all simlated geometries. This actor is essential for obtaining an accurate attenuation map, which is critical for PET simulations. Additionally, it can generate a 3D image of the source emission (sourceMap). The MuMap can serve as ground truth for the attenuation map, eliminating the need for a CT simulation to obtain the attenuation map, while the sourceMap can be used as the ground truth for the emitted data points of the source. The actor can be set for any energy (ideally 511 keV for PET) and with any resolution. However, it is

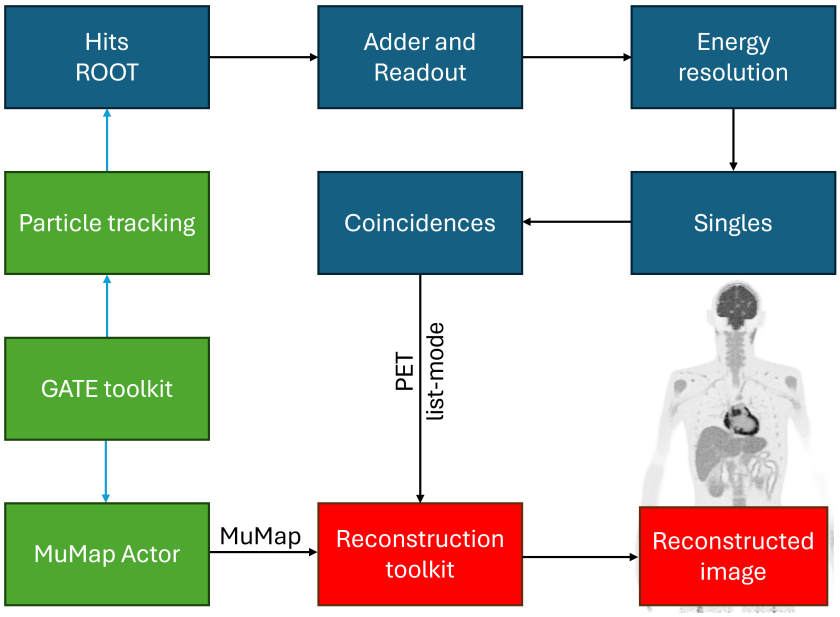

Fig. 2.11: A sequence diagram of the steps involved in a GATE simulation, leading to a reconstructed image. Green boxes indicate GATE process, blue boxes are processes through ROOT files, and red boxes is the image reconstruction toolkit process. This figure is a reproduction from [132].

most appropriate to ensure that the size and resolution of the image match those used for the attenuation map during image reconstruction.
As the focus in many applications in recent years requires the assistance of a digital twin, MC simulations have been used for simulating and validating PET scanners for both preclinical and clinical systems. GATE simulation toolkit has been essential for validating variety of PET scanners [110, 112, 113, 114]. These validations helped improve our understanding and characterization of the scanners to obtain better designs for achieving TBPET scanners.
Most recently, Peña-Acosta et al. [125] simulated both the Biograph Vision and Quadra scanners using GATE. Their objective was to validate the simulation results of each scanner against the previously published measured values by Sluis et al. and Prenosil et al. [43, 102]. Their simulation outputs exhibited a high degree of agreement with the measured data. This close alignment was achieved by leveraging the open-source CASToR for image reconstruction and calculating normalization factors for the scanners as outlined in Pépin et al. [133]. In addressing dead-time and pile-up effects, an empirical approach was adopted, involving multiple simulations executed iteratively until the values converged with the measured data. Their study's scope is constrained by the utilization of open-source tools, which may differ from those employed in clinical settings. To address this limitation, we devised a simulation workflow that mirrors the image reconstruction and single event processing methods

utilized in the clinical scanner with the tools provided by the Siemens Medical Solutions (Siemens Healthineers, Knoxville, TN, USA) as detailed in Chapter 3.

2.5 Artificial Intelligence

Artificial Intelligence (AI) is a field of computer science that involves creating systems capable of performing tasks that typically require human intelligence. These tasks include learning, reasoning, problem-solving, perception, and decision-making. In the field of nuclear imaging, the main focus of AI is the use of neural networks (NN) and deep neural network (DNN) algorithms developed in recent years to improve imaging systems. These applications include enhancing the detection chain, refining quantitative reconstruction algorithms, and improving decision-making for lesion detectability and patient care.

2.5.1 Neural Networks

The simplest form of an artificial NN, a single neuron, operates by having an input x and a weight w to obtain the target value Y. Each neuron with a weight can be associated with multiple inputs (or features) [134, 135]. As the number of weights increases, the number of neurons used also increases, adding more complexity to the algorithm. Equation 2.10 presents the general concept of a neural network:

$$y = f\left(\sum_{i=1}^{n} w_i x_i + b\right), \tag{2.10}$$

where x_i represents the input features, w_i denotes the corresponding weights, b is the bias term, f is the activation function, and y is the output. The weights of the network are updated to align the values of y and Y using different loss functions such as the mean absolute error (L1) or the mean squared error (MSE). To ensure that the neural network can converge to the required solution without becoming stuck or diverging, an optimizer such as gradient descent is employed, with a parameter known as the learning rate. The learning rate is a critical parameter that needs to be adjusted according to the specific application and the data used. To ensure that the network output values are within an acceptable range (e.g., avoiding negative numbers), activation functions such as the sigmoid function or the absolute value function are applied on a per-neuron basis.
NN have many applications and, with a limited number of layers, do not require vast amounts of computational power. However, with the introduction of DNN containing many hidden layers, the number of training parameters increased drastically, thus requiring significantly higher computational power.

2.5.2 Deep Neural Networks

A DNN is a type of artificial neural network that consists of multiple layers of neurons between the input and output layers. DNN has at least three layers: an input layer, one or more hidden layers, and an output layer. The presence of multiple hidden layers is what distinguishes a DNN from a shallow NN. The depth of a DNN is defined by the number of hidden layers. Increasing the depth allows the network to learn more complex patterns and representations [136, 137]. The mathematical representation of a DNN can be expressed as:

$$y = f_L\left(W_L\left(f_{L-1}\left(W_{L-1}\left(\ldots f_1\left(W_1 x + b_1\right)\ldots\right) + b_{L-1}\right)\right) + b_L\right), \tag{2.11}$$

where y represents the output of the DNN, while $\mathbf{x}$ is the input vector. The network consists of L layers, where each layer applies a linear transformation followed by a non-linear activation function. Specifically, W_l and b_l represent the weight matrix and bias vector for the l-th layer, respectively, with $l = 1, 2, \ldots, L$. The function f_l is the activation function applied at the l-th layer, such as a Rectified Linear Unit (ReLU) or sigmoid. The input passes through each layer sequentially, with each layer's output feeding into the next, until the final layer L, where the output y is produced.

2.5.2.1 Convolutional Neural Networks

Convolutional Neural Networks (CNNs) are a class of deep learning algorithms designed for processing structured grid data, such as images. They are particularly effective for tasks related to computer vision, including image classification, object detection, and segmentation. CNNs have also demonstrated their feasibility for image denoising. These algorithms have been successfully adapted for use on single-channel images (i.e., images containing data from only one source, such as the intensity of PET signals) in PET imaging. The key components include convolutional layers, ReLU activation functions, and pooling layers [138, 139]. The following equation is used to calculate the convolutional operation for each spatial position (x, y, z) in the output tensor by summing over all input channels c and kernel positions (i, j, k):

$$\text{Convolution}(I, K)_{(x,y,z)} = \sum_{c=1}^{C_i} \sum_{i=0}^{F-1} \sum_{j=0}^{F-1} \sum_{k=0}^{F-1} I_{(x+i,y+j,z+k,c)} \cdot K_{(i,j,k,c)}, \tag{2.12}$$

where I represent the input tensor with dimensions $H_i \times W_i \times D_i \times C_i$, H_i, W_i, and D_i represent the height, width, and depth respectively, and C_i represents the number of input channels. When using only PET images as input, the input channel is set to 1, reflecting the fact that PET images do not employ the RGB format, which typically consists of 3 channels. If CT or MRI images used as a prior in a network, the input channel would be 2.

K represents the convolutional kernel with dimensions $F \times F \times F \times C_i \times C_o$, where F is the filter size, C_o represents the number of output channels, and (x, y, z) represents the spatial position in the output tensor. Padding is utilized to ensure that the spatial dimensions of the tensor remained unchanged after convolution operations. The padding option could be zeros, ones, mirror, or replication. The padding is symmetrically applied on both sides of each dimension.

ReLU activation function is used to avoid negative values in the neural network input x by replacing them with zeros, while leaving positive values unchanged as follows:

$$\text{ReLU}(x) = \max(0, x). \tag{2.13}$$

ReLU activation function is commonly used in deep learning to introduce non-linearity and improve the model's ability to learn complex patterns in the data.

Pooling layers in CNNs serve to improve performance and efficiency through dimensionality reduction, translational invariance, and controlling overfitting by reducing the complexity of the features. There are three major pooling operations: global pooling, average pooling, and max pooling. Global pooling, applies pooling over the entire dimensions of the input at the end of the network, resulting in a single value for the feature map. Average pooling, unlike global pooling, takes the average over a window (such as 2×2 or 3×3). Lastly, max pooling where it takes the maximum value within a defined window. For image segmentation and image denoising tasks, max pooling has been the dominate use pooling method.

For calculating the max pooling operation for each spatial position (x, y, z) in the output tensor is done by taking the maximum value over a $(F \times F \times F)$ region in the input tensor, where F is the size of the pooling window. The stride for the max pooling operation is typically set to 2, which leads to downsampling the input tensor following the equation below:

$$\text{Max pooling}(I)_{(x,y,z)} = \max_{i=0}^{F-1} \max_{j=0}^{F-1} \max_{k=0}^{F-1} I_{(2x+i,2y+j,2z+k)}. \tag{2.14}$$

For regularization during training and to prevent overfitting, the dropout operation is used. Each element of the input tensor is set to zero with probability p, and the remaining elements are scaled by $\dfrac{1}{1-p}$ to maintain the expected value of the tensor, i.e.,

$$\text{Dropout}(I, p) = \begin{cases} 0 & \text{with probability } p \\ \frac{I}{1-p} & \text{otherwise,} \end{cases} \tag{2.15}$$

where p represents the probability of dropping out a neuron, and $Dropout(I, p)$ represents the output of the dropout operation applied to the input tensor I.

The last layer of the network is typically a softmax layer. The aim of the softmax layer is to convert logits (unnormalized scores) to a probability distribution where

the probabilities of all classes sum to 1. This in turn helps in making clear and interpretable predictions for classification tasks. The convolutional operation performed by the final convolutional layer in the CNN can be describes as follows:

$$\text{Final Convolution}(I,K)_{(x,y,z)} = \sum_{c=1}^{C_i}\sum_{i=0}^{F-1}\sum_{j=0}^{F-1}\sum_{k=0}^{F-1} I_{(x+i,y+j,z+k,c)} \cdot K_{(i,j,k,c)}. \tag{2.16}$$

For image denoising applications, the softmax layer is not used as the goal is to predict continuous intensity values for each pixel rather than discrete classes or probabilities preserving the pixel intensity values. The softmax can be represented as follows:

$$\sigma(z_i) = \frac{e^{z_i}}{\sum_{j=1}^{K} e^{z_j}}, \tag{2.17}$$

where z_i are the logits and K is the number of classes. The final convolutional layer in the denoising CNN is responsible for generating the denoised image, serving as the culmination of the network's processing.

Adam optimizer [140] is the most robust optimizer used for a variety of CNN. The optimizer is used for updating the parameters θ of the neural network based on the gradients of the loss function. The moments m_t and v_t are exponentially decaying averages of past gradients and squared gradients, respectively. The bias-corrected estimates m^t and v^t adjust for the initial bias towards zero in the moments. Finally, the parameters θ are updated based on the scaled and normalized moments as follows:

$$m_t = \beta_1 m_{t-1} + (1-\beta_1) g_t \tag{2.18}$$

$$v_t = \beta_2 v_{t-1} + (1-\beta_2) g_t^2 \tag{2.19}$$

$$\hat{m}_t = \frac{m_t}{1-\beta_1^t} \tag{2.20}$$

$$\hat{v}_t = \frac{v_t}{1-\beta_2^t} \tag{2.21}$$

$$\theta_{t+1} = \theta_t - \frac{\alpha}{\sqrt{\hat{v}_t}+\epsilon}\hat{m}_t, \tag{2.22}$$

where θ_t represents the parameters of the neural network at iteration t; g_t represents the gradient of the loss function with respect to the parameters at iteration t; m_t and v_t are the first and second moments of the gradients, respectively, with decay rates β_1 and β_2, and $\hat{m}^t$ and $\hat{v}^t$ are bias-corrected estimates of the moments; α is the learning rate, and ϵ is a small constant added to prevent division by zero. The value of the learning rate is usually selected empirically between 0.01 and 0.00001. There are several loss functions that can be implemented [141]. For image denoising applications, the mean absolute error (L1) and the mean squared error (MSE) are widely used. Both loss functions are calculated as follows:

$$L1(y, \hat{y}) = \sum_{i=1}^{n} |y_i - \hat{y}_i|, \tag{2.23}$$

$$MSE(y, \hat{y}) = \frac{1}{n} \sum_{i=1}^{n} (y_i - \hat{y}_i)^2, \tag{2.24}$$

where y_i is the actual value, $\hat{y}_i$ is the predicted value, and n is the number of observations.

2.5.2.2 U-Net

The U-Net is a convolutional neural network architecture that was first designed and used for volumetric image segmentation tasks in three-dimensional space. It was first introduced by Ronnenberger et al. [142, 143]. It has demonstrated effectiveness in various applications, showcasing its ability to accurately segment structures within volumetric data and contributing to advancements in medical imaging and computer vision. It can be applied as a 2D or 3D network where it is an extension of the 2D U-Net architecture, adapted to handle three-dimensional data. It includes several key components that are not typically found in a standard CNN. The distinctive layers and features of a U-Net that differentiate it from a traditional CNN are the deconvolution layers for up-sampling, skip connections, and concatenation layer. The skip connections pass feature maps from the encoder to the decoder, which helps the network learn to reconstruct the fine-grained details of the input. In the encoder segment of the model, the input volume undergoes a systematic reduction in size through the application of convolutional and pooling layers, leading to the extraction of hierarchical features. This architecture aids in preserving spatial information and mitigates the vanishing gradient problem.
The skip connection in the 3D U-net is defined as follows:

$$\text{Skip Connection}(E, D) = \text{concat}(E, D), \tag{2.25}$$

where E represents the feature map from the encoder; D represents the upsampled feature map from the decoder, and *concat* represents the concatenation operation. The feature map from the encoder and the up-sampled feature map from the decoder are concatenated along the channel dimension. This helps in preserving spatial information during upsampling.
Following this, the decoder segment enlarges the feature maps through an upsampling process to reconstruct the segmentation mask. During this process, it merges information from earlier stages via skip connections. Although skip connections are not essential for the network's operation, they act as shortcuts, allowing the network to map the output to the same dimensions and size as the input without requiring numerous iterations to determine the shape independently.

The deconvolutional operation for each spatial position (x, y, z) in the output tensor by summing over all input channels c and kernel positions (i, j, k) as follows:

$$\text{Deconvolution}(I, K, S)_{(x,y,z)} = \sum_{c=1}^{C_i} \sum_{i=0}^{F-1} \sum_{j=0}^{F-1} \sum_{k=0}^{F-1} I_{(Sx+i,Sy+j,Sz+k,c)} \cdot K_{(i,j,k,c)}, \quad (2.26)$$

where S represents the stride of the deconvolution operation that determines the upsampling factor.
With the development of network architectures like U-Net, more advanced algorithms have emerged, such as GANs and diffusion models utilizing transformers. The U-Net architecture, with its encoder-decoder structure and skip connections, is well-suited for image processing tasks as it preserves fine details while progressively refining the image. Diffusion models often employ a U-Net architecture, especially for image generation tasks. Additionally, transformers can be integrated to enhance the model's capabilities. The specific combination of these components depends on the requirements of the task and the desired properties of the generative model.

2.6 Additive Manufacturing Technologies

To fabricate phantoms for PET scanner quality assurance (QA) and quality control (QC) studies, blocks of polymethyl methacrylate (PMMA) are utilized. The process involves either drilling holes into a single block to create cavities that are subsequently filled with radioactive materials, or fusing multiple blocks together to produce the desired phantom, as specified in the NEMA NU 2-2018 protocol [45, 144]. The subtractive manufacturing process involves drilling, sanding, and cutting, among other techniques, to remove parts of the main block until the desired shape of the phantom is achieved. The primary issues with subtractive manufacturing are the generation of a large amount of waste and the necessity to start with a substantial block of material to reach the desired geometry.
Using casting molds is another effective method for fabricating phantoms for PET QA and QC studies. This technique involves creating a mold of the desired shape and then filling it with a suitable material, such as a resin or gel, that can solidify to form the phantom. Common materials include silicone, gelatin, and various resins. This method can be cost-effective and efficient, especially for producing multiple phantoms with the same design. Once the mold is created, it can be reused to produce additional phantoms. Howoever, casting molds can struggle to accurately replicate complex geometries and intricate details, which are often required for realistic phantoms. Moreover, while molds can be reused, the process of creating each phantom can be time-consuming and labor-intensive where there can be variations in the final product due to inconsistencies in the casting process, such as air bubbles or uneven material distribution [145].

In contrast, additive manufacturing has been gaining more attention due to its ability to reduce material waste and fabricate geometries that are not possible with traditional subtractive manufacturing or casting mold methods. Three-dimensional printing technology (also referred to as additive manufacturing) has advanced by incorporating various materials and printing methods.
There are eight primary methods of 3D printing: Fused Deposition Modeling (FDM), Stereolithography (SLA), Selective Laser Melting, Selective Laser Sintering, Direct Metal Laser Sintering, Electron Beam Melting, Multi Jet Fusion, and PolyJet. Despite their differences, these methods share the fundamental principle of additive manufacturing, which involves constructing objects by adding material layer by layer, with each layer fusing to the one beneath it. This layer-by-layer approach enables the precise creation of complex geometries, which is central to the versatility and effectiveness of additive manufacturing [146, 147]. In this thesis, the 3D printing methods employed are FDM and SLA.

2.6.1 Fused Deposition Modeling

FDM stands out as a widely adopted 3D printing technique renowned for its versatility and accessibility across industries. In FDM, objects are built layer by layer through the extrusion of thermoplastic filament, which is heated to its melting point and deposited onto a build platform in a cross-hatching pattern. This additive manufacturing process results in robust structures suitable for rapid prototyping and production needs. FDM printers offer advantages such as affordability, ease of use, and versatility in material selection. However, drawbacks include limited print quality resolution, noticeable layer lines on finished parts, potential warping of large flat surfaces due to material cooling, and slower print speeds compared to alternative technologies [148].
Various types of filaments are utilized in 3D printing, each offering distinct properties suitable for diverse applications. Common materials include Polylactic Acid, Acrylonitrile Butadiene Styrene, Polyethylene Terephthalate Glycol, Thermoplastic Polyurethane, and Acrylonitrile Styrene Acrylate. These filaments differ in their mechanical characteristics, heat resistance, and flexibility, making them suitable for a wide range of uses from prototyping to functional parts production. In the field of radiation detection, filaments are infused with high-density materials to enhance their effectiveness in attenuating ionizing radiation. This process enables the filaments to be used in shielding applications [149].
FDM printers have lower resolution compared to SLA printers (0.1 mm vs. 0.05 mm), primarily due to the limitations of nozzle size. As a result, FDM-printed parts are typically not used for nuclear imaging phantoms, as they may leak radioactive solutions. Instead, FDM-printed parts are mainly utilized for mechanical support [150]. Figure 2.12 shows an example of a FDM 3D printer.

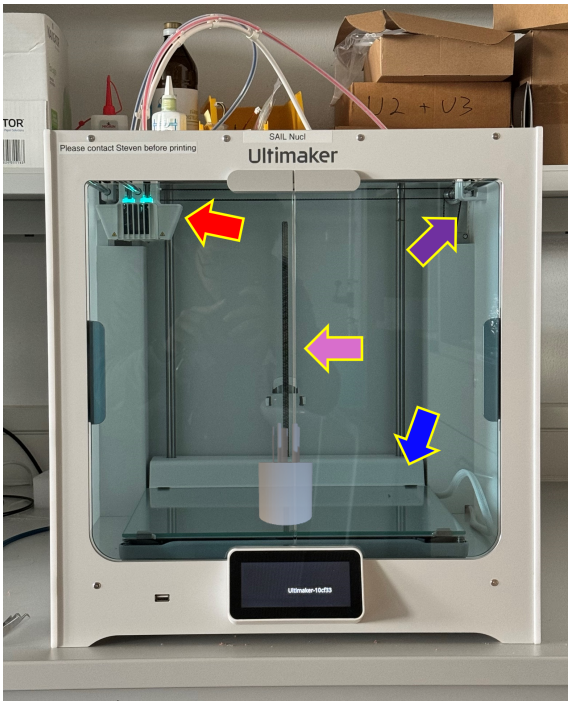

Fig. 2.12: An FDM 3D printer, Ultimaker S5, showing the printer bed (blue), the nozzle head (red), the XY-axis for moving the print head (purple), and the Z-axis for lifting the print bed towards the nozzle head.

2.6.2 Stereolithography

SLA is the most widely known and utilized vat photo-polymerization process in the field of 3D printing. SLA's prominence in additive manufacturing is due to its ability to create highly detailed and precise 3D models by selectively curing liquid resin with UV light [151].
SLA 3D printing employs the principle of photo-polymerization to produce three-dimensional objects. The process involves curing a liquid photopolymer resin contained in a vat using a UV light source. This curing process solidifies the resin in a layer-by-layer manner, closely resembling the method used in FDM. In SLA, the liquid resin serves as the primary printing material, analogous to the filaments used in FDM printers. The curing is executed by a laser, which is precisely controlled and aimed using mirrors, known as galvanometers. These mirrors guide the laser beam to trace the cross-sectional geometry of the model, layer by layer, until the entire object is constructed [147].
Resin 3D printers consist of several key components include: the resin tray, which holds the UV-sensitive resin used for printing and is also referred to as the vat or tank; the mobile platform (Z-axis), which moves vertically and is lowered into the resin tank as each new layer is cured; the scraping system (X-axis), which ensures a

smooth and even layer of resin for each subsequent layer of printing; the UV laser, responsible for curing the resin; the focusing optics, which focus the laser beam to ensure precise curing of the resin; and lastly, the mirrors (galvanometers), situated on the X and Y axes to control the direction and aiming of the laser beam, allowing for accurate layer formation.

There are two types of stereolithography (SLA) 3D printers [150]: bottom-up and top-down. Most SLA 3D printers use the top-down method. Each has its advantages and disadvantages. Bottom-up advantages include requiring less resin since the part is pulled out of the vat, which also allows for smaller machine sizes. It facilitates easier control of layer thickness. However, frequent replacement of the resin vat is necessary to maintain print quality, and the weight of the part can increase the risk of print failure. Additionally, the 3D printed part must be angled to prevent air bubble trapping, necessitating support structures that complicate post-processing steps. Top-down advantages are primarily speed-related, as there is no need to separate the build plate from the vat after each layer, enabling continuous resin flow. It also reduces stress on the 3D part, minimizing the risk of print failure, and requires fewer supports since the part is not printed at an angle. Top-down disadvantages include the need for a larger machine footprint and higher resin consumption. Changing and replacing resin tanks is both difficult and costly. Careful control of resin thickness between the surface and the top of the 3D model is crucial.

After the initial printing process, post-processing involves cleaning the printed object with alcohol to remove any residual resin. This is followed by an additional round of UV curing to ensure the material achieves its final properties and full strength. A significant limitation of the printing method used is the restriction to a single material for both the object and its support structures. Consequently, this necessitates the use of the same material for the supports as for the printed object. This constraint complicates the post-processing phase, as removing the support structures becomes more challenging. The material adherence and the precision required to avoid damaging the printed object while eliminating supports necessitate careful and often time-consuming techniques.

Over the years, SLA printers were further developed, following the same concept of curing UV resin. Two other types of printers, Digital Light Processing (DLP) and Liquid Crystal Display (LCD), were developed based on similar principles but differ in their UV light sources [152].

SLA utilizes a UV laser to trace the dimensions of each layer, curing the resin precisely along the path of the laser. This method allows for high accuracy and detail but can be time-consuming as the laser must individually trace every part of the layer. Moreover, this results in different print speeds according to the orientation of the object. For example, a $2\times4\times1$ box would not require the same amount of time to print as a $4\times2\times1$ box.

In contrast, DLP and LCD technologies employ a different approach. DLP uses either a projector (while LCD screen for LCD printers) to project an image of the entire layer onto the resin, curing the entire layer simultaneously. This method significantly speeds up the printing process compared to SLA, as it eliminates the need for layer-by-layer tracing with a laser. DLP's ability to cure whole layers at once makes it faster than SLA. The efficiency of DLP is particularly advantageous for producing larger prints or multiple objects simultaneously, as the printing time is not dependent on the complexity of the individual layers. Furthermore, it solves the previously mentioned issue with object orientation, resulting in the same speed for both cases [150]. For instance, our LCD printer took 27 minutes to print a 25 mm long phantom, whereas an SLA *Form 2* printer (Formlabs, USA) using the same printing parameters, such as layer height and exposure time, took 6 hours for the same task.
Resin 3D printing, encompassing SLA, DLP, and LCD technologies, is renowned for its accuracy and precision. Even low-cost DLP printers can produce complex geometries with high detail, which is often unattainable with technologies such as FDM. The print quality of SLA and DLP is generally comparable, with higher-end printers offering superior resolution. LCD printers, for instance, can achieve up to 12K resolution in their LCD screens, providing exceptional detail and surface finish. Figure 2.13 shows an example of a LCD 3D printer. Throughout this thesis, an LCD printer will be used for printing phantoms, as detailed in Chapter 4.

2.6.3 Standard Tessellation Language

Standard Tessellation Language (STL) is a widely used file format within the field of 3D printing and additive manufacturing. This file format plays a critical role in the translation of digital 3D models into physical objects by describing the surface geometry of the model. Specifically, STL files utilize a raw, unstructured triangulated surface to represent the three-dimensional structure of an object [153]. STL files are designed to approximate the surfaces of a solid model using a series of triangles, also known as facets. Each triangle is defined by three vertices in three-dimensional space, along with a normal vector that indicates the outward-facing direction of the surface. This method of representation allows for the detailed capture of the object's external geometry without including any internal structure or color information. The resolution and complexity of an STL file are directly related to the number of triangles used to approximate the surfaces of the model. For simple geometric shapes, such as a box, the surface can be adequately represented using a relatively low number of triangles. A box, or a cuboid, is a three-dimensional shape with six faces. In an STL file, each face of the box can be represented by two triangles (since a square can be divided into two triangles). Therefore, a box would typically need 12 triangles to be represented in an STL fil. Conversely, more complex surfaces, such

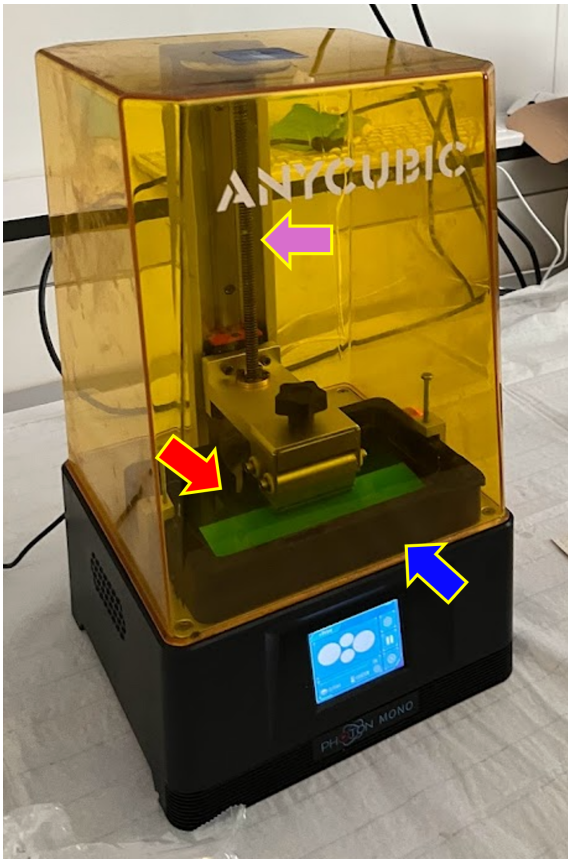

Fig. 2.13: An DLP 3D printer, Anycubic mono, showing the resin tank (blue), the build plate immersed in green resin (red), and the Z-axis for lifting the build plate outward the resin tank.

as those found in human organs or highly detailed models, require a significantly larger number of triangles to achieve an accurate approximation.
The granularity of the triangulated surface in an STL file determines the resolution of the resulting 3D print. A higher number of triangles results in a finer resolution, allowing for more precise and smoother surface details in the object. However, this increase in resolution also leads to larger file sizes and potentially longer processing times [154].
For 3D printing, STL files are processed using slicer software to generate the necessary G-code. G-code is a programming language utilized by 3D printers and Computerised Numerical Control machines, providing step-by-step instructions that control the machine's movements, temperatures, fan speeds, and other operational parameters. Essentially, G-code directs the 3D printer on how to construct the object layer by layer based on the encoded instructions in the file [155].
This conversion is pivotal as the slicer software translates the 3D model into a set of instructions comprehensible to the 3D printer. The slicer software effectively 'slices'

the 3D model into thin, sequential layers, producing the G-code required for the printing process. Slicer software serves as a critical intermediary, bridging the gap between the digital 3D design and the physical printed object. It offers users control over various printing parameters such as layer height, infill density, print speed, and support structures. By adjusting these settings, users can optimize the quality and efficiency of the printing process to suit specific needs and constraints. Without the use of slicer software, manually creating G-code would be an exceptionally time-consuming and error-prone task. Slicer software automates this process, ensuring precision and consistency in the generated instructions, thereby enhancing the reliability and quality of the 3D printing process. All major 3D printing technologies rely on slicer software to generate a G-code file, which initiates the printing process. Regardless of the specific 3D printing method employed, slicer software remains an indispensable tool in converting digital designs into tangible objects [156].
STL files were used throughout this thesis when utilizing 3D printing applications (as detailed in Chapter 4). Additionally, since the GATE simulation toolkit supports the use of STL files to construct geometries, STL files were employed in Chapter 3.

2.6.4 3D printing fillable phantoms for PET imaging

A prominent area of application of 3D printing in the field of biomedical engineering, for instance, the manufacture of phantoms imitating mechanical properties of the human body [157], as well as other phantoms for quality assurance or evaluation of medical imaging systems were developed for the use in medical imaging that involved various types of imaging techniques including X-ray, CT, SPECT and PET [158, 159].
For PET, a large variety of phantoms are usually employed for QA and system performance evaluation. These phantoms are either solid or consist of various empty cavities that can be filled with radiotracers or solutions containing specific radioisotopes. The design can follow certain standards, such as the National Electrical Manufacturers Association (NEMA) NU 2-2018 [160], and NEMA NU 4-2008 [144], for clinical and preclinical PET, respectively. To ensure that the 3D-printed phantoms perform as well as conventional ones and to detect possible deviations from the standards, a careful analysis of the phantom imaging properties is required. It is essential that the 3D-printing material is not porous to prevent the radiotracer from leaking out and to avoid chemical binding of the radiotracer to the phantom. If multimodal systems are employed, e.g., PET combined with CT or MRI, compatibility with the other imaging modalities is also required.
Bieniosek et al. [161] fabricate multi-modality imaging phantoms for a PET system. The 3D printed phantoms were imaged using CT, MRI and PET modalities. Moreover, Zell et al. [162] at the Institute of Medical Engineering, Universität zu Lübeck, utilized SLA 3D printing technology to develop cost-effective phantoms for quality control of

imaging devices. They constructed a fillable micro-PET IQ phantom for small animal PET that was MRI-compatible. In PET imaging, low-density materials should be preferred to reduce the attenuation of gamma rays. Additionally, the density of the 3D-printed material affects the positron range. Without positron-range correction, the reconstructed image displays the distribution of annihilation points. The density of the material surrounding the radionuclides determines the average distance the positron travels before annihilating with an electron. Incorrect estimation of the volume occupied by radiotracers, whether by overestimation or underestimation, may result from the use of air or low-density materials [162]. In addition to system performance evaluation, 3D printed fillable phantoms have also been proposed to improve SPECT-based activity calibration in the field of radiotherapy dosimetry [163].

2.6.5 3D printing radioactive phantoms

As SPECT and PET often use liquid radioactive sources for calibration and testing, typically requiring filling cavities with radioactive liquids, this process is time-consuming and error-prone. In recent years, a novel approach utilizing liquid photopolymer resin-based 3D printing technology has been explored. This approach allows the 3D printing of radioactive phantoms as solid objects, eliminating the need to fill cavities with radioactive liquids [164, 165].
Compared to fillable phantoms, 3D printed phantoms (as sealed solid sources) are easier and safer to handle than radioactive solutions. Furthermore, they eliminate artifacts due to the trapping or formation of air bubbles in small cavities and are easier to handle, requiring no special training to prepare the phantom. In particular, correctly filling small cavities and thin vessels might be time-consuming and difficult. For calibration and QA, 3D printed phantoms containing long-lived radioisotopes would be desired. However, using radioisotopes with long half-lives also creates problems when testing the procedures, such as long-lived radioactive waste.
Drawing on this methodology, Laeppchen et al. [164] and Gear et al. [165] demonstrated the feasibility of mixing ^{99m}Tc with liquid resin to 3D print various simple geometric objects, such as uniform cubes and spheres. The results showed a uniform distribution of activity within their 3D printed phantoms, while the resulting images were consistent with those of established SPECT calibration phantoms. Moreover, Gillet et al. extended the procedure to PET by mixing ^{18}F-Fluorodeoxyglucose (^{18}F-FDG) with liquid resin to 3D print phantoms where the test objects had a uniform distribution of activity [166]. Lastly, Meier et al. [167] developed a method for directly mixing ^{68}Ge, a long-lived isotope that decays by electron capture within the phantom, to ^{68}Ga which, in turn, also decays within the phantom emitting positrons. The printed phantom was used for calibration of clinical PET systems and a study of the wall effect of the phantom. Moreover, 3D printing allows us to

obtain images using wall-less phantoms. The aim of a wall-less phantom is to better mimic the accumulation of activity within an organ and the surrounding tissues, unlike the situation when using phantoms with cold walls.

The advancements in 3D printing of radioactive phantoms have motivated us to further explore the applications of 3D-printed radioactive phantoms, extending their use to high-resolution scanners and addressing the issue of ^{89}Zr sticking to the walls of fillable phantoms, as detailed in Chapter 4.In immuno-PET and radio-immunotherapy, accurate knowledge of the underlying activity distribution is essential. However, the adsorption of metallic radionuclides into the walls of phantoms leads to a nonuniform activity distribution, affecting imaging studies and absorbed dose calculations during the development of phantom validation studies. Several challenges need to be addressed when printing with ^{89}Zr compared to ^{18}F-FDG, including differences in energy, half-life, and branching ratio (909 keV vs 633 keV, 78.4 hours vs 1.83 hours, and 0.22% vs 0.963%, respectively) [168, 169]. Further information about each source can be found in Section 2.1.2.

3 Monte Carlo Simulation

This section is an extension of submitted abstracts to the 36th Annual Congress of the European Association of Nuclear Medicine (EANM) 2023 Vienna, Austria [170], IEEE Nuclear Science Symposium, Medical Imaging Conference and International Symposium on Room-Temperature Semiconductor Detectors (NSS/MIC/RTSD) 2023, Vanccover, Canada [171], and the 61st Annual Meeting of the German Society for Nuclear Medicine, Leipzig, Germany 2023 [172]. Moreover, a paper titled "A Digital Twin of the Biograph Vision Quadra Long Axial Field of View PET/CT: Monte Carlo Simulation and Image Reconstruction Framework" is under review at the European Journal of Nuclear Medicine and Molecular Imaging - Physics.
The work presented here is a result of a collaboration with Department of Preclinical Imaging and Radiopharmacy, Institute for Astronomy and Astrophysics, and Cluster of Excellence iFIT (EXC 2180) at Eberhard Karls University Tübingen, Tübingen, Germany, Department of Nuclear Medicine and Clinical Molecular Imaging, University hospital Tübingen, Tübingen and Siemens Medical Solutions USA, Inc., Knoxville, USA.
The simulation code and reconstruction tools were provided by Siemens Medical Solutions. Christian Pommranz (Werner Siemens Imaging Center, University Tübingen), and the author of this dissertation were responsible for developing the simulation code, debugging, and running the simulations. Fabian Schmidt and Wenhong Lan (Department of Nuclear Medicine, University hospital Tuebingen) developed the analysis script for the NEMA NU 2-2018 measurements.

Contents

3.1 Introduction

The objective of the work presented in this section was to develop and validate a digital twin for the Biograph Vision Quadra TBPET scanner based on comprehensive MC simulations. In this work, Biograph Vision Quadra will be referred to as 'Quadra'. The digital twin encompassed modeling the physical properties of events and their detection. The simulations underwent validation against scanner measurements, with a focus on quantification, spatial resolution, sensitivity, Noise-Equivalent Count Rate (NECR), and image quality, adhering to the NEMA NU 2-2018 protocols [45]. Next, I applied the model for two distinct tasks. The first involves simulating ^{90}Y-filled phantoms to investigate the impact of Bremsstrahlung radiation on PET image quality. This was achieved by evaluating the performance of the image reconstruction tools for scatter scaling used for dose estimation from the PET image. The second study focuses on evaluating the current method employed in re-framing PET images to generate low-dose/high-dose pairs for AI training (more details to follow in Section 5).

3.2 Materials and Methods

3.2.1 Quadra Simulation model

The MC simulations were performed by employing GATE version 9.1 using the Geant4 toolkit [108] version 10.7.2. The GATE simulation was aimed to model the PET aspects of the Quadra scanner. The Quadra digital twin was implemented with the same specifications as the scanner using $3.2 \times 3.2 \times 20$ mm^3 LSO crystals. The scanner consisted of 320 rings divided into four blocks, each ring had 760 crystals in the axial direction amounting to a total of 243,200 crystals. The segments are separated by a gap of a single crystal width in size. The scanner has an 82 cm bore diameter and an AFOV of 106 cm. Figure 3.1 represents the simulated scanner.
The patient bed geometry was replicated by extracting data from a CT phantom scan stored as a DICOM file. Subsequently, the DICOM file was converted into

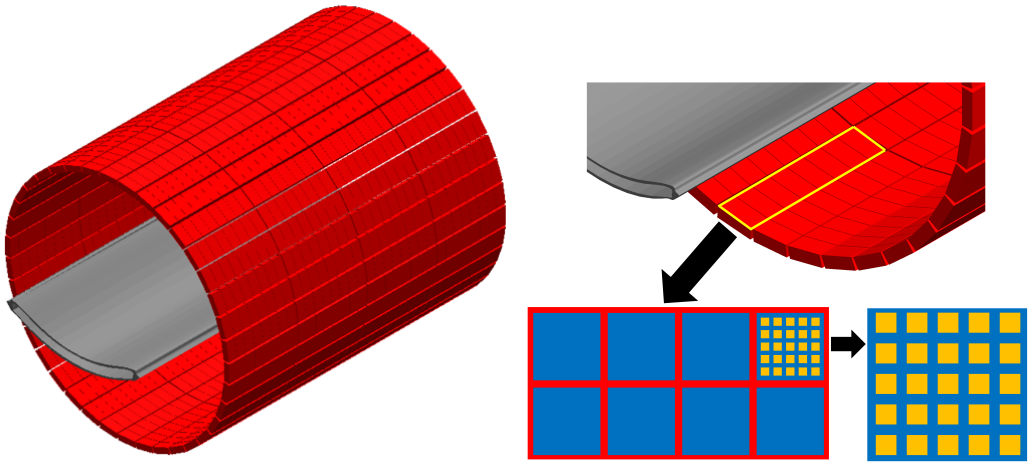

(a) (b)

Fig. 3.1: a) 3D rendering of the simulated Quadra detector blocks (red) alongside the patient bed (gray), and b) a close-up of the detector block (red). The first Detector Electronics Assembly (DEA) is highlighted in yellow and consists of eight detector blocks. Each detector block contains 2×4 mini-blocks (blue), with each mini-block composed of a 5×5 crystal array. Each crystal (orange) measures 3.2×3.2 mm.

an STL model compatible with GATE simulation software. Alternative considered methods included simulating a simplistic box positioned beneath the simulated patient or implementing the bed as a voxelized phantom. However, the former would have oversimplified the bed's structure, rendering it inaccurately modeled, while the latter would have resulted in higher simulation time due to voxelization. Utilizing an STL volume for the bed incurred a negligible reduction in simulation speed (less than 0.001%) compared to omitting the bed model entirely. In GATE, tessellated volumes can be created from STL files, enabling the simulation of complex geometries imported from CAD software. This functionality is facilitated by the Geant4 *G4TessellatedSolid* class, which constructs a volume in GATE by adding facets to the tessellated solid, thereby defining the surface of the three-dimensional object. Figure 3.2 illustrates the STL representation of the bed. The material selected for the bed was plastic, leading to similar attenuation values observed between the CT attenuation image (0.095 mm^{-1}) and the simulation attenuation map (0.105 mm^{-1}). The physics list used in GATE for modeling the interactions of charged particles and photons with matter was $emstandard_{opt4}$. $emstandard_{opt4}$ was the best trade off between the simulation accuracy and computational efficiency [132, 173]. The digitizer used for converting hits to singles (using policy winner takes all) applied an energy resolution blurring of 9%, chosen to match the resolution acquired by the Quadra's readout system. This digitalizer was utilized in the blurring module preceding the addition of hits within single crystals to form single-crystal events

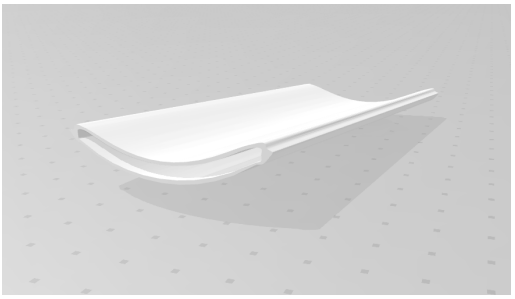

Fig. 3.2: The STL bed used in the simulation. The length of the bed was set to 106 cm to cover the complete axial FOV.

via the adder module. Subsequently, these events were combined into single events using the readout module. No upper or lower energy threshold was applied to retain low-energy signals, as they would be processed in the subsequent stage when creating the coincidences. The resulting events were stored in a *ROOT* file for subsequent processing.
Utilizing the GATE *MuMapActor*, we acquired the attenuation map employed for attenuation correction of the simulated phantoms, with a voxel size of $0.4\times0.4\times0.4$ mm^3. For normalization correction of the simulated data, a normalization matrix obtained from the real scanner was utilized. However, the normalization file was adjusted to prevent over-correction for scanner calibration and crystal efficiency, which are idealized in the simulation.

The validation simulations were conducted on a Linux computational cluster node running Ubuntu 22.04 LTS, equipped with an AMD 96-core CPU and 512 GB of RAM (Institute of Medical Engineering, Universität zu Lübeck). The simulation speed varied depending on factors such as phantom geometry complexity, activity utilized, and the type of source employed in the simulation (back-to-back gamma source, positron source, or ion source). The work presented in this chapter required over 250000 CPU-hours for simulation. As for the XCAT and ^{90}Y simulations, the *Nationales Hochleistungsrechnen at Zuse Institut Berlin (NHR@ZIB)* as part of computing project shb00004, CPU clusters were used[1].

3.2.2 Image Reconstruction

Our initial work [171, 172], along with other published studies [125], demonstrated the effectiveness of using standard open-source tools. Specifically, the GATE built-in digitizer for coincidence sorting and CASToR for image reconstruction can produce reconstructed images that closely match published measurement results according to the NEMA NU 2-2018 protocols. However, the lack of accurate normalization of the

[1] `https://nhr.zib.de/`

scanner poses a limitation for image quantification in the simulation workflow. To address these limitations, we adopted two tools from the vendor for post-simulation processing in this study: *root-to-listmode* tool and *e7 tools*.

3.2.2.1 root-to-listmode tool

In GATE simulations, it is feasible to include an extra processing stage aimed at converting the singles list to coincidences. This entails the algorithm scanning through the list to identify groups of singles occurring within a defined time window, termed as 'coincident events'. Furthermore, the coincidence data may undergo filtering to simulate potential data loss that could occur within the coincidence logic circuit or during data transfer (dead-time losses). Similar to singles processing, this stage involves designating a list of general modules to be applied to the flow of coincidence data. The simulation output is stored as a ROOT file using ROOT version 6.24/06 [131]. ROOT files record information related to the interaction of radiation with matter during simulations. This information includes timestamps, event IDs, particle IDs, parent IDs, and position coordinates. These data can be stored as hits, singles, or coincidences To conserve storage space, neither hits nor coincidences were stored within the ROOT file.

For our approach, the singles were processed using a custom scanner-tailored software prototype called *root-to-listmode*[2] that will be referred to as 'R2LM'. R2LM is a proprietary executable program in which we provide input files and specify relevant parameters (flags) to generate the desired output. However, we do not have access to, nor interact with, the internal processes or operations that occur within the software, as these are the intellectual property of the vendor. R2LM accurately models PET detectors response in terms of time resolution, dead time, intercrystal scatter, and crystal background radiation. The dead time and crystal background modeling can be toggled on or off depending on the type of study being simulated. Additionally, the tool provides the capability to merge multiple ROOT files and offers the option to provide an offset for the ROOT file time tag. This functionality is crucial as the GATE toolkit lacks the ability to utilize multiple CPU cores, operating only on a single CPU of the machine. With the time tag offset, we are able to run long simulations (1800 seconds scan in the case of ^{90}Y simulations) with low simulation scan time (typically between 1 and 0.05 seconds per run). Furthermore, R2LM applies the same coincidence sorter as in the real system, transferring the output ROOT file to a new file following the same PETLINK data format [174] used for the Quadra raw data.

[2] Siemens Healthineers, Knoxville, TN, USA

3.2.2.2 e7 tools

The Siemens *e7 tools*[3] are part of Siemens Healthineers' digital solutions suite. This software is capable of performing tomographic image reconstruction for Siemens mCT, mMR, Vision, and Quadra PET scanners. The *e7 tools* facilitate the processing and reconstruction of PET emission data acquired by Siemens scanners. When integrated with a Siemens PET scanner's user interface, images reconstructed by *e7 tools* are approved for clinical use, as the software functions in a tested and validated manner. However, when used in research settings—interacting directly with the program executables—*e7 tools* are intended solely for research purposes, not for clinical diagnostics. Furthermore, the tool offers the advantage of handling anonymized raw data from the Quadra scanner, enabling reconstruction in a research environment while ensuring patient information remains confidential.
The typical steps employed for reconstruction using the *e7 tools* are as follows: Histogramming the listmode data, generating the attenuation map, performing image reconstruction, and finally converting the interfile to DICOM images. In the histogramming step, the listmode file is converted to a sinogram. During this process, the *e7 tools* provide the capability to perform gating or re-framing on the data. Figure 3.3 shows the workflow of using the *e7 tools* with both measured data and simulated data.
The subsequent step involves generating attenuation maps from the CT scan or LSO transmission scan [175] accompanying the PET acquisition. Additionally, the *umapBedRemoval* application is employed at this stage to remove the patient bed from the attenuation map. This is done to reconstruct the PET image without the patient bed. For image reconstruction processing, users have access to a wide range of different reconstruction algorithms with various corrections. Users can opt for analytical methods such as FBP or iterative reconstruction algorithms such as MLEM or OP-OSEM with different iterations and subsets, while also applying TOF and PSF corrections. The corrections available include normalization, attenuation correction, decay correction, scatter correction, absolute scatter scaling (ABS), and the application of filters to the reconstructed image such as Gaussian filters. A new feature introduced in the Quadra version of the *e7 tools* is the ability to select the MRD for the acceptance angle. Users can choose between the standard MRD322 of 52° angle or the limited MRD85 angle of 18°. This functionality is enabled by the fact that the Quadra always acquires events within the MRD322 range.
For the image reconstruction of the simple geometric phantoms and the NEMA IQ phantom, the OP-OSEM-TOF-PSF reconstruction algorithm was implemented using the *e7 tools* with four iterations and five subsets. The reconstructed images were of dimensions $440 \times 440 \times 645$ voxels with a voxel size of $1.65 \times 1.65 \times 1.65$ mm^3. These

[3] Siemens Healthineers, Knoxville, TN, USA

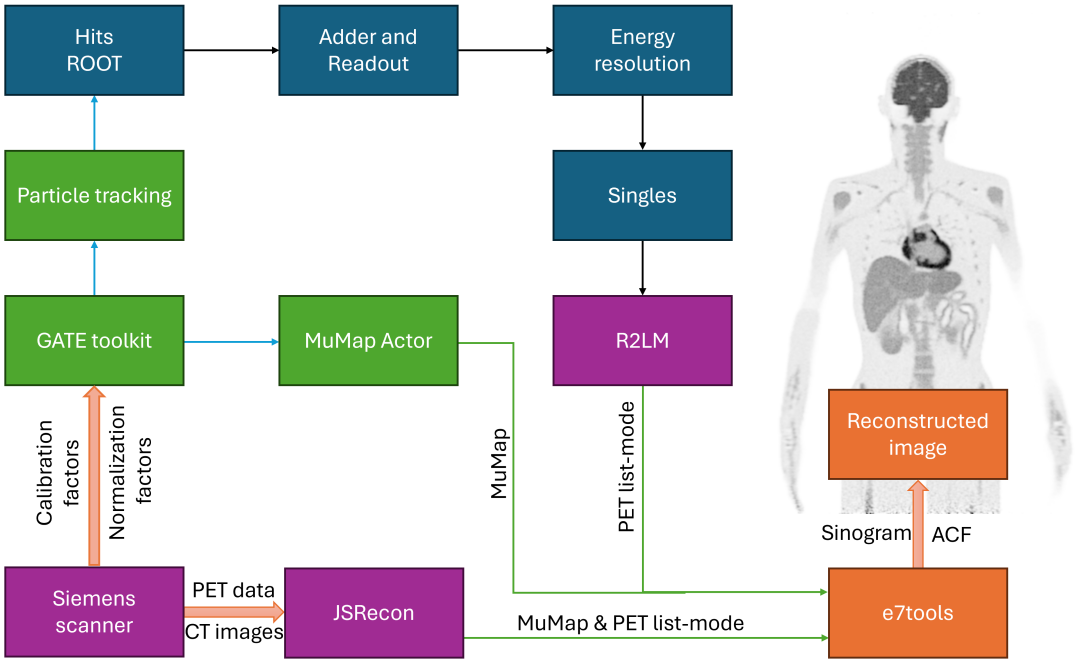

Fig. 3.3: A sequence diagram of the steps involved in a GATE simulation and the scanner measurement, leading to a reconstructed image. Green boxes indicate GATE process, blue boxes are processes through ROOT files, purple boxes are Siemens tools, and orange boxes is the *e7 tools* image reconstruction toolkit process.

are the same parameters that are being used for the clinical scanner [2]. Only for ^{90}Y image reconstruction different parameters were used with OP-OSEM algorithm with two iterations instead of four [4].
The reconstruction was performed using a Windows 10 workstation equipped with an Intel Core i7-13700K Processor and 128 GB of DDR5 RAM (Institute of Medical Engineering, Universität zu Lübeck).

3.2.3 Simulation Validation

The GATE model and image reconstruction algorithm were evaluated using various phantom studies. Initially, simple geometric uniform phantoms were simulated and validated against simulation ground truth, followed by the use of phantoms based on the NEMA NU 2-2018 protocol [45]. The output of the NEMA simulations were validated against Quadra measurements obtained from the initial performance assessment of the Quadra, as published by Prenosil et al. [43]. Additionally, a voxelized anthropomorphic phantom, the 4D Extended Cardiac-Torso (XCAT) phantom [176], was simulated to showcase the potential of the simulation in investigating realistic patient scan scenarios.

The initial tests were conducted using an isotropic back-to-back gamma source with an energy of 511 keV. Such a source simulates the gamma rays produced by the annihilation of a positron-electron pair without explicitly simulating the positron interaction within the phantom and thus neglecting positron range. This approach significantly reduces the computational burden of the simulation, thus drastically increasing simulation speed. Subsequently, to enhance realism, the validation process progressed to using an isotropic positron source before eventually incorporating an ^{18}F ion source. Throughout the validation stage presented in this work, all simulation results were obtained using the ^{18}F ion source.

3.2.3.1 Validation of Simple Geometric Phantom Simulations

The first step involved validating the GATE simulation and *e7 tools* using simple uniform phantoms. These phantoms were utilized to detect any inconsistencies or defects in the scanner simulation model. The initial uniform phantom consisted of a tube measuring 140 cm in length, filled with water of 5.5 cm in diameter, and enclosed with a 0.8 cm PMMA wall. The 140 cm tube exceeds the scanner AFOV (106 cm). Additionally, this phantom underwent scanning using the Quadra scanner, providing both simulation ground truth via the emission source map from the MuMap actor and measurement ground truth. Here, only the simulation values are reported. Subsequently, two shorter phantoms were employed, one with a length of 100 cm and 5.5 cm in diameter followed by another with a length of 10 cm and 10 cm in diameter, both are within the AFOV. The activity concentration of 3 kBq/mL was used for the first two tubes, while the 10 cm tube was 6 kBq/mL. Figure 3.4 visually depicts the simulated 140 cm tube within the scanner.

3.2.3.2 NEMA NU 2-2018 Validation

The first step in validating the simulation model following the NEMA NU 2-2018 protocol was to determine the sensitivity. The scanner sensitivity and axial sensitivity profiles were determined by simulating a 680 mm long line source with a diameter of 3 mm. This line source comprised ^{18}F mixed with water, injected into a polyethylene tube with an inner diameter of 3 mm and an outer diameter of 3.1 mm, with a total activity of 4.56 MBq. Figure 3.5 shows the CAD drawing of the sensitivity phantom. The line source simulation was repeated five times, each time with an aluminum sleeve added, with each sleeve being 1.25 mm thick. The simulations were then repeated with a 100 mm radial offset, adhering to the NEMA NU 2-2018 protocol. A SSRB was performed on the histogram derived from the list-mode data, converting the 3D sinograms into 2D sinograms using a self developed python script. This step is necessary to calculate the total count rate with no attenuation in accordance

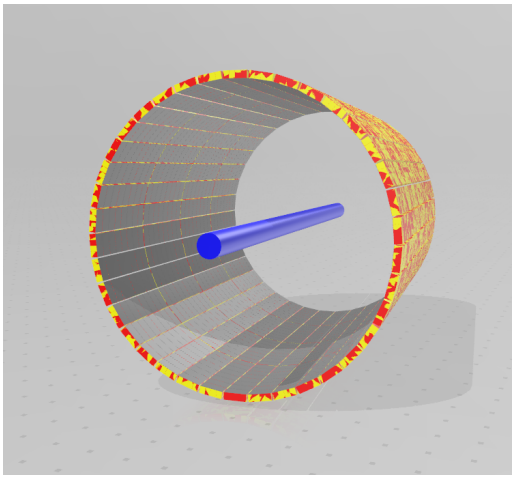

Fig. 3.4: A 140 cm tube within the Quadra scanner. The simulation was conducted without the addition of the patient bed.

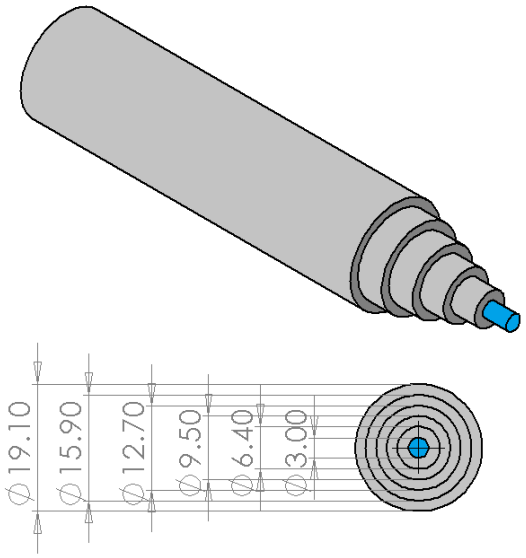

Fig. 3.5: A CAD drawing of the sensitivity phantom used in GATE simulation showing the water mixed with activity is (blue) and the five sleeves (gray). Dimensions are in millimeters.

with the NEMA NU 2-2018 protocol. The scanner sensitivities and axial sensitivity profiles for each simulation are reported for MRD85 and MRD322. The system sensitivity (S_{TOT}) is computed as a ratio, as shown below:

$$S_{TOT} = \frac{R_{CORR,0}}{A}; \tag{3.1}$$

where A denotes the source activity in Bq, and $R_{CORR,0}$ is the attenuated corrected count rate. The five simulations with the sleeves are used to estimate the detected count rate ($R_{CORR,0}$) through data fitting interpolation.
As for the sensitivity profile (S_i) for slice i, it was calculated by acquiring the count rate of the simulation with only one sleeve ($R_{CORR,1}$):

$$S_i = \frac{R_{CORR,1,i}}{R_{CORR,1}} S_{TOT}. \tag{3.2}$$

The simulation output was processed utilizing the R2LM tool and subsequently SSRB using the *e7 tools* to derive the 3D sinograms.
The next step, in accordance with the NEMA NU 2-2018 protocol was to ascertain the scatter fraction (SF) and noise equivalent counts (NEC). A polyethylene cylinder block measuring 700 mm in length and 203 mm in diameter was simulated, featuring a 6.4 mm cavity positioned at a radial distance of 45 mm towards the direction of the patient bed. Within this cavity, an 800 mm long polyethylene tube with an inner diameter of 3.2 mm was installed. Similar to the sensitivity simulations, the source material for these simulations comprised ^{18}F mixed with water, injected into the tube. The patient bed was simulated beneath the phantom to replicate the measurement scenario. Following the methodology outlined by Prenosil et al. [43], the source activity at the beginning of the measurement was 894 MBq. Data acquisition was conducted every 1200 seconds for a duration of 240 seconds each time. However, for the simulation of source activity, the approach described in the NEMA NU 2-2018 protocol, as well as that followed by Prenosil et al., was not adopted as it was computational expense to simulate the decay of 894 MBq to 0.01 MBq over time. This approach would require a continuous simulation of more than 100000 seconds, resulting in more than one billion computational hours. Instead, we simulated a total of 21 activity points ranging from 800 MBq to 0.01 MBq, to match the measurement points of Prenosil et al. [43]. Each activity point was simulated for 4 seconds. For activity points between 1 MBq and 0.01 MBq, simulations were continued until a total of 500000 prompts were accumulated in the list-mode file, as required by the NEMA NU 2-2018 protocol. To validate this approach, a simulation of the 100 MBq activity point was conducted for 240 seconds, resulting in less than 0.1% difference for prompt and random rates between the 240 seconds simulation and the 4 seconds simulation. The simulation output was processed using the R2LM tool and re-binned using the *e7 tools* to extract trues, randoms, and scatter counts. The SF and noise

equivalent counts NEC were computed using the equations provided by the NEMA NU 2-2018 protocol:

$$SF = \frac{S}{S+T}; \tag{3.3}$$

$$NEC = \frac{T^2}{T+S+R}; \tag{3.4}$$

where T represents the true coincidences rate, S denotes the scatter coincidences rate, and R stands for the random coincidences rate. Since deadtime and pileup were not integrated into the GATE simulations, the deadtime flag was utilized when employing the R2LM tool when processing the ROOT files.

The validation of spatial resolution was not included in the thesis work. Additional details can be found in references [43, 171, 172], where it was determined following the NEMA NU 2-2018 protocol. TOF resolution validation was beyond the scope of this study, as the TOF resolution was already implemented within the R2LM tool. The image quality of the simulation model was evaluated by simulating the standard NEMA International Electrotechnical Commission (IEC) phantom according to the NEMA NU 2-2018 protocol [45]. This phantom consists of six hot spheres with diameters of 37, 28, 22, 17, 13, and 10 mm, submerged in water mixed with activity (warm background) with a hollow insert representing the lungs positioned at the transaxial center of the FOV. A background activity of 5.7 kBq/mL was utilized for the warm background. Two different activity concentrations were simulated for the hot spheres to achieve sphere-to-background ratios (SBR) of 4:1 and 8:1, respectively. The centers of the spheres were aligned with the axial center of the FOV. Additionally, the scatter phantom with an activity of 100 MBq was placed at a distance of 50 mm from the IEC phantom. Each configuration was scanned and simulated for 300 seconds. The phantom material used was PMMA, and the simulated source was mixed with water filling the phantom.
The IQ was determined by calculating the Contrast Recovery Coefficients (CRC), as per the NEMA NU 2-2018 protocol. To obtain the CRC, the mean of the maximum values of the slices for each sphere was calculated, along with the standard deviation (SD), using the following equations:

$$CRC = \frac{\frac{S_{avg}}{B_{avg}} - 1}{\frac{S_{act}}{B_{act}} - 1} \times 100\%; \tag{3.5}$$

where S_{avg} represents the average value measured within the sphere using a VOIs, while B_{avg} denotes the average value measured in the background utilizing VOIs; S_{act} is the activity concentration within the spheres, and B_{act} indicates the activity concentration in the background. The mean voxel values were determined for spherical

inserts with diameters of 10, 13, 17, 22, 28, and 37 mm, representing the average values for the spheres. To assess quantification accuracy, the background activity concentration was determined using the mean voxel value within a cube VOI measuring $150 \times 15 \times 170$ mm^3 in the background region. Additionally, a cylindrical VOI, measuring 30 mm in diameter and 160 mm in length, was positioned within the lung insert (empty cavity within the phantom). Lung residual error was calculated by dividing the mean value of the lung VOI by the value of the total background VOI. Lastly, the sum of the sixty VOIs in the background (K) was drawn to calculate the SD using the following equation:

$$SD = \sqrt{\sum_{k=1}^{K} \frac{(B_{avg,k} - B_{avg})^2}{K-1}}. \tag{3.6}$$

3.2.3.3 XCAT Phantom

Following the validation of the NEMA simulation model, a static XCAT phantom [176] was simulated with a voxel size of $3.1 \times 3.1 \times 3.1$ mm^3. The XCAT Phantom is a sophisticated tool designed for medical imaging research applications, offering detailed anatomies for both male and female. The anatomies are based on the weight, height, and organ volumes of the 50th percentile. Utilizing non-uniform rational b-splines (NURBS), it includes thousands of defined structures and parameterized models for respiratory motions and heart beat. This allows to simulate a wide range of normal and abnormal anatomical and motion variations, creating a comprehensive virtual patient population.
A female XCAT phantom was simulated with a total activity of 160 MBq distributed within the phantom following the typical mean organ-specific SUV [177]. The static simulated scan time was 300 seconds to replicate a typical scan duration for a ^{18}F-FDG scan using the Quadra [2]. This simulation will provide the ground truth data for the reframing study in Chapter 5. Figure 3.6 shows the ground truth of the XCAT simulation obtained by using the MuMap actor from GATE.

3.2.4 ^{90}Y Spheres Simulation

The high-energy electrons emitted from a ^{90}Y source produce bremsstrahlung radiation, which contributes to the dose delivered to the patient. The *e7 tools* offer an ABS flag used to correct for scatter scaling. To assess the ABS functionality of the reconstruction tool, I simulated a warm spherical phantom containing four hot spheres. This was a simplified version of the Abdomen phantom used ^{90}Y in studies. The total activity of the ^{90}Y ion source for the background was 530.1 MBq, while it was 78.5, 40.2, 16.9, and 4.19 MBq for the 50, 40, 30, and 20 mm hot spheres, respectively. The goal was to reach a SBR of 4:1 with the spheres having an activity

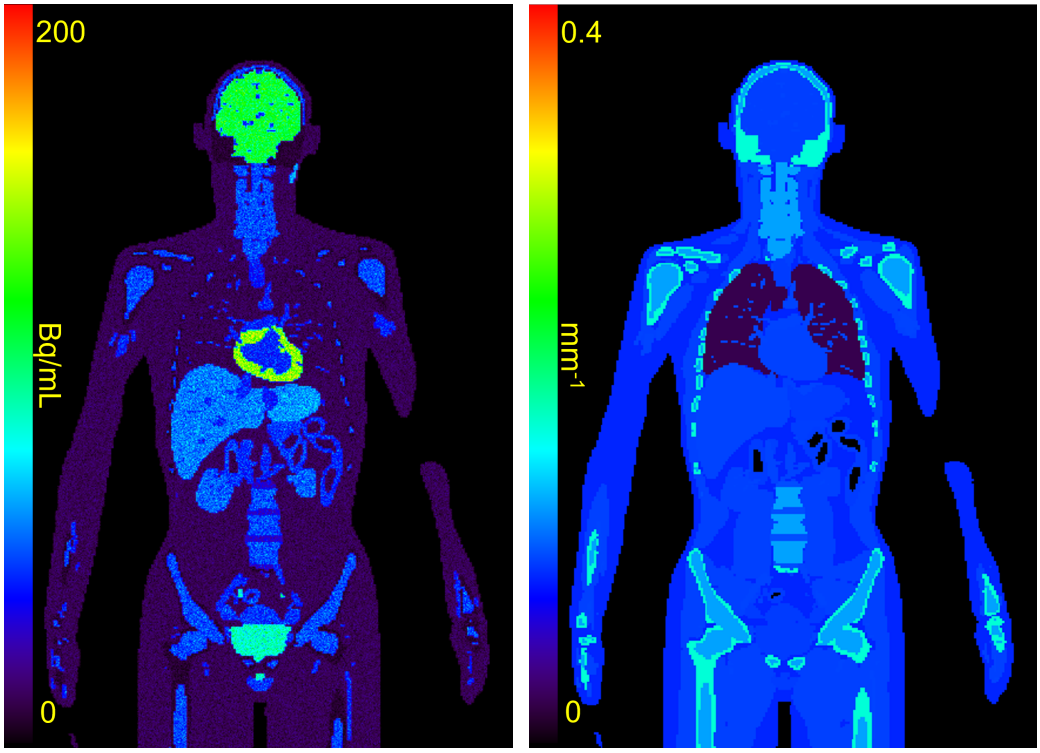

(a) (b)

Fig. 3.6: Coronal view of the XCAT phantom: a) Source emission map obtained from a simulation of 2 seconds scan, b) coronal view of the XCAT phantom attenuation map.

concentration of 1200 kBq/mL while the background was 400 kBq/mL. Figure 3.7 depicts a CAD image of the simulated phantom.

Initial tests, revealed that GATE and Geant4 cannot model the positrons generated from the pair production of the ^{90}Y ion source. To address this issue, the ^{90}Y source was simulated as a positron source with a continuous energy spectrum matching that of the positron energy spectrum that is the by product of the pair production [178]. Additionally, another approach was pursued by simulating a ^{18}F ion source to serve as ground truth for comparison with the ^{90}Y ion source.
For the positron (e^+) and ^{18}F simulations, the activity used corresponded to the activity after correcting for the branching ratio of the positron generated from the ^{90}Y ion source (0.04 and 0.01 kBq/mL for the spheres and background, respectively. Each source was used to simulate a scan time of 1800 seconds, corresponding to the typical clinical scanning duration of the ^{90}Y imaging protocol [4]. Since these are low-count, long scans, the LSO background would play a significant role in the

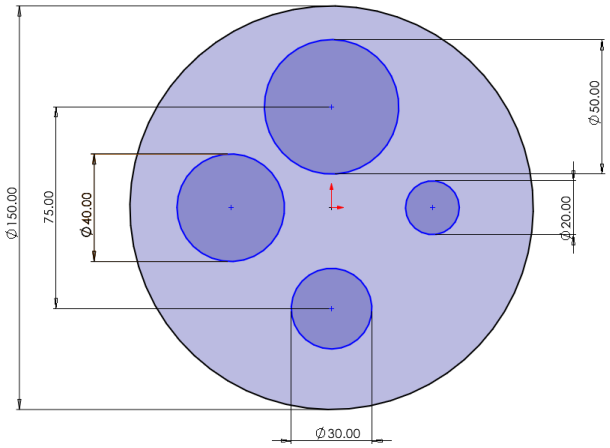

Fig. 3.7: A CAD design of the ^{90}Y phantom hot spheres (middle purple) in a warm background (pale blue). Dimensions are in millimeters.

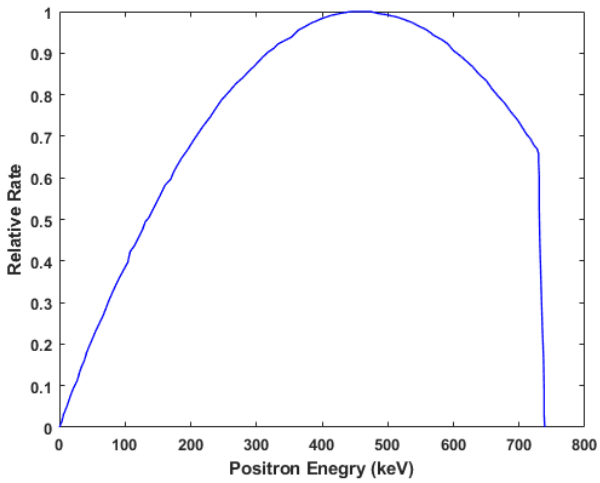

Fig. 3.8: a) Spectrum of positron energy emitted at the positron-electron pair creation of the energy level of 1760.7 keV to the base level of the ^{90}Zr nucleus at the ^{90}Y decay [178].

imaging process. Hence, for each simulation output, R2LM was utilized twice: once with LSO background and once without enabling the Quadra LSO background.
The OP-OSEM-TOF-PSF reconstruction algorithm was implemented using the *e7 tools* with two iterations and five subsets. The parameters for the decay rate correction and the source half-life were adjusted to match those of ^{90}Y imaging [4]. To further investigate the ABS correction capability of the *e7 tools*, each simulation output was reconstructed twice: once with the ABS flag enabled and once without.

3.3 Results

3.3.1 Quadra Validation

3.3.1.1 Simple geometric phantom simulation

Table 3.1 summarizes the mean activity concentration values obtained from the VOI for each tube image. Figure 3.9a presents the reconstructed image of the simulated tube (100 cm). Moreover, Figure 3.9b shows a line profile through both the 140 cm and 100 cm simulated tube showing a uniform activity distribution within the phantom even when having activity outside the FOV. The values obtained from the reconstructed images differed by less than 1% compared to the reference activity used in the simulation. This difference is smaller than the expected Poisson statistical fluctuation of 1.83%, indicating that the observed deviation is within the range of statistical noise and can therefore be considered negligible.

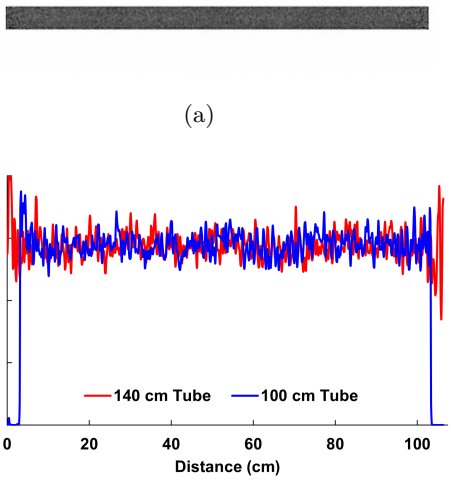

(a)

(b)

Fig. 3.9: a) Coronal view of reconstruction image of the 100 cm tube showing a homogeneous activity distribution, b) line profile through both the 140 cm (red) and 100 cm tube (blue).

3.3.1.2 NEMA Simulations

The results obtained from the NEMA IQ simulation, as reported in [171], are shown in Figure 3.10. These results shows a good agreement in the CRC values between the simulated and measured IEC phantoms for both SBRs. The lung residual error for

Table 3.1: Comparison of mean and reference activity concentration values for different tube lengths

Tube length (cm)	Mean (Bq/mL)	Reference (Bq/mL)	Difference (%)
140	2997±155	3000	0.1
100	3005±149	3000	0.2
10	5958±182	6000	0.7

the 4:1 SBR was 4.7% and 4.8% for the simulation and measurement, respectively. As for the 8:1 SBR, it was 6.3% and 5.1% for the simulation and measurement, respectively. The image-derived mean activity concentration was 5.73±0.4 kBq/mL (relative difference of 2.4% compared to the simulated concentration). Figure 3.11 shows the reconstructed images for a 300 seconds simulation of the IEC phantom for both activity concentrations. The MRD85 reconstruction took approximately 4 minutes each, while MRD322 reconstruction required about 38 minutes due to the larger data volume to be processed resulting from the wider acceptance angle.

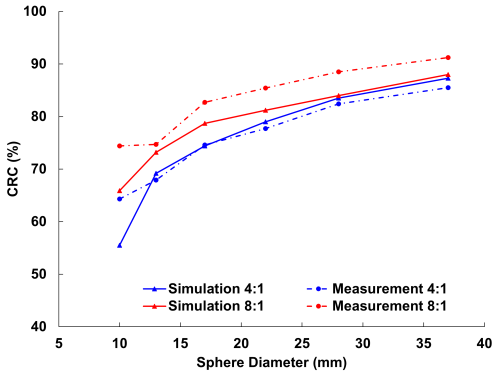

Fig. 3.10: The CRC (%) of the IEC phantom with SBR of 4:1 and 8:1 for both the measurement and simulation. Data reported in [43, 171].

The system sensitivity for the simulation and the measurement as reported by [43] was 83.6 cps/kBq and 82.6 cps/kBq for MRD85, and 176.7 cps/kBq and 175.3 cps/kBq for MRD322, respectively. A strong agreement was found between the simulated and measured value with relative differences of 0.1% and 0.4%, for MRD85 and MRD322 respectively. Moreover, both axial sensitivity profiles of the simulation with and without the offset, as shown in 3.12.
Figure 3.13 shows the NECR plots for MRD85 and MRD322. In the low activity region, below 10 kBq/mL, the simulated data closely agrees with the measurement data, with relative differences in NECRs of less than 8% for MRD85 and 9% for MRD322, respectively. However, as the activity and count rate increase, the difference becomes larger.

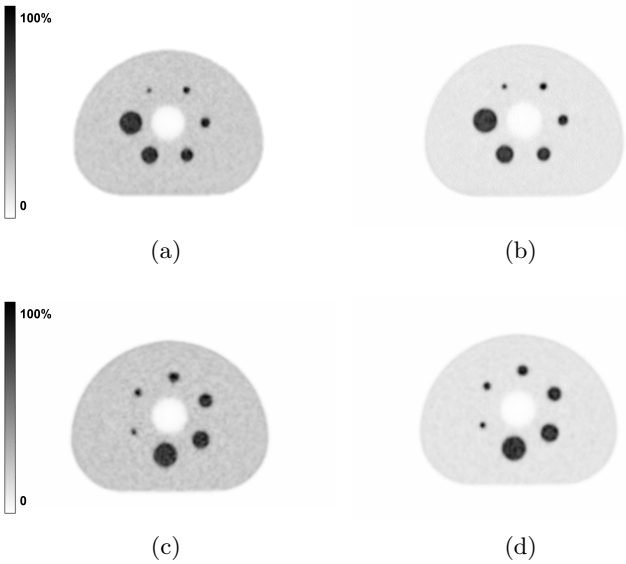

(a) (b)

(c) (d)

Fig. 3.11: A 2D transverse slice of the IQ IEC simulated phantom is shown for a) simulated phantom with SBR 4:1, b) simulated phantom with SBR 8:1, c) measured phantom with SBR 4:1, and d) measured phantom with SBR 8:1 [79, 171].

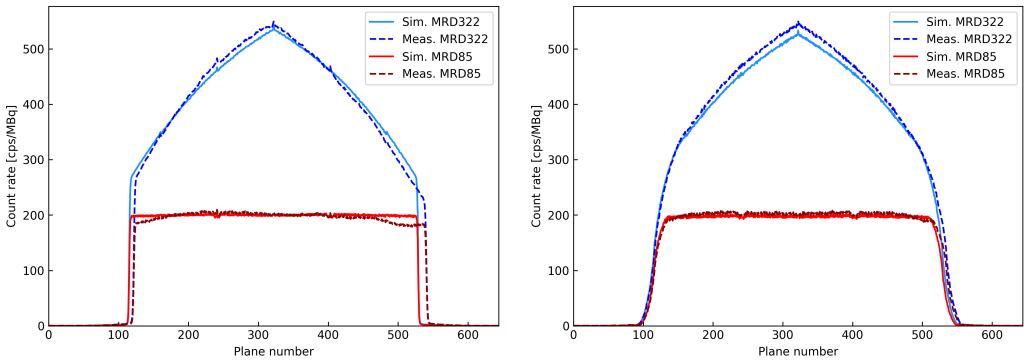

(a) (b)

Fig. 3.12: a) Sensitivity profiles for MRD85 and MRD322, showing both simulated and measured data at a 0 cm offset, and b) at a 10 cm offset. Data reported in [43, 171].

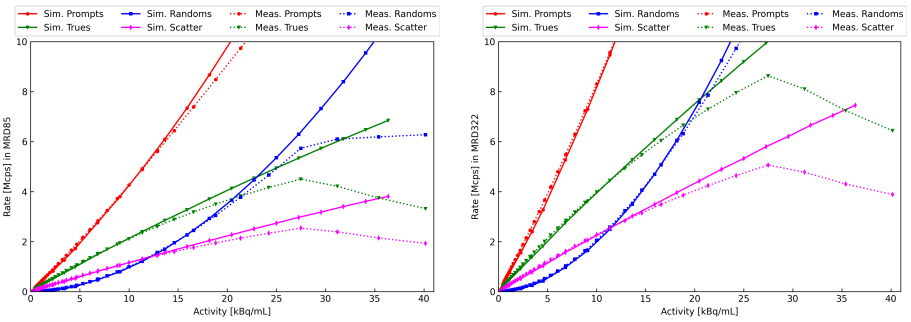

(a) (b)

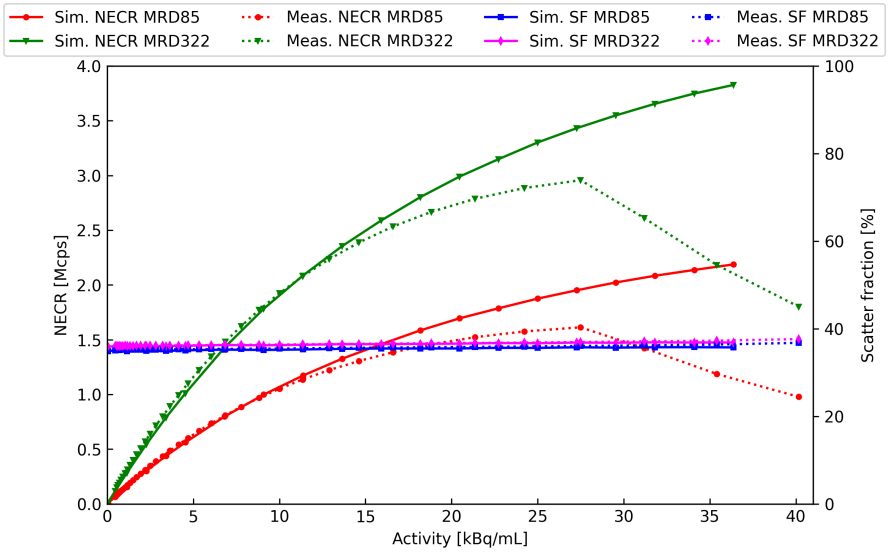

(c)

Fig. 3.13: Simulated and measured count rates for different activity concentrations for a) MRD85 and b) MRD322. c) NECRs and scatter fractions for both MRDs. Plots adapted from [43, 171].

3.3.2 XCAT Phantom

Figure 3.14 presents the reconstructed image of the simulated XCAT phantom, accurately depicting the distribution of radioactive activity across various regions of the body, including specific organs. This demonstrates the ability to simulate patient-like phantoms, rather than just simple geometries.

3.3.3 ^{90}Y Simulation

Figure 3.15 shows the simulated sphere phantom using ^{90}Y ion, e^+, and ^{18}F sources. Visually, the images of all the ^{90}Y phantoms look similar.

Fig. 3.14: Reconstructed image of the XCAT phantom. The image was obtained for 300 seconds simulation with ^{18}F.

Table 3.2 presents the mean VOR for each source, both with and without the LSO background and ABS flag enabled. It can be observed that both ^{18}F and e^+ sources yielded values closer to the simulated activity when the LSO background was disabled, compared to those obtained with it. This can be attributed to the low simulated activity making the LSO background more dominate. As expected, the ^{90}Y ion source was not affected by the LSO background due to the higher prompt rates, which result from increased random events caused by the high activity of the ^{90}Y ion source.
Moreover, the difference between applying the ABS flag and disabling it for all cases resulted in difference of less than 1.5%. However, it is noticeable that the background had a larger difference of 4.6%. It was expected to have higher difference for the ^{90}Y ion and e^+ sources as they have higher positron energies compared to the ^{18}F ion source.

3.4 Discussion

The Quadra validation simulations shows accurate results when using simple geometrical phantoms. The activity concentration had less than a 1% error, which is acceptable as the error falls within the normal levels of uncertainty for MC simulations. One reason the simulation may differ from the measured values is the idealized

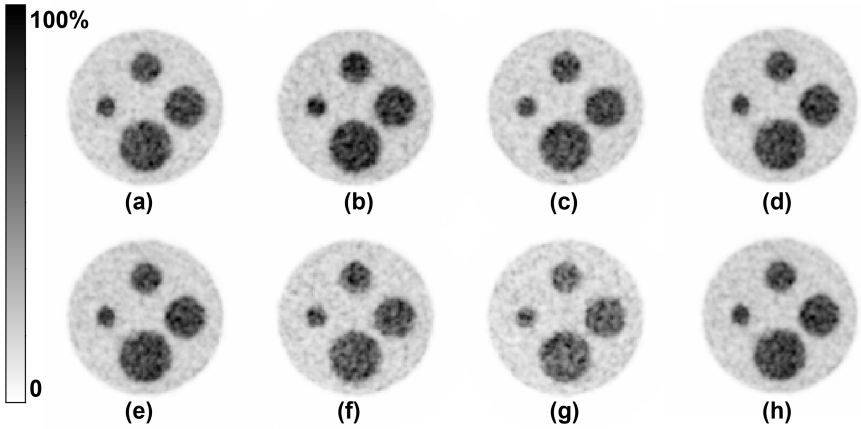

Fig. 3.15: Reconstructed images of a) the ^{90}Y ion source, b) the e^+ positron source, and c) the ^{18}F ion source, without LSO background, e) the ^{90}Y ion source, f) the e^+ positron source, and g) the ^{18}F ion source, with LSO background. d) ^{90}Y ion source with LSO background but ABS off (same as (e)), and h) with ABS on.

Table 3.2: Comparison of the mean ROI values for the ^{90}Y sphere phantom simulations with ^{90}Y ion source (Y-90 ion), only the positron of the ^{90}Y pair production (Y-90 e+) positron, and ^{18}F ion source (F-18 ion). **ΔABS** represents the difference in mean ROI values with and without the ABS flag, while **ΔLSO** denotes the difference between mean ROI values with and without the LSO background. The ROIs were calculated for each individual hot sphere and as the average of five background ROIs. The standard deviation was approximately 10% for the hot spheres and 20% for the background across all simulation scenarios.

		With LSO (kBq/mL)		Without LSO (kBq/mL)			
ROI	**Source**	With ABS	Without ABS	With ABS	Without ABS	**ΔABS**	**ΔLSO**
Background	Y-90 ion	297	284	299	287	4.1%	0.7%
	Y-90 e^+	187	179	303	290	4.4%	38.3%
	F-18 ion	159	152	266	254	4.6%	40.3%
5 cm sphere	Y-90 ion	1210	1193	1207	1191	1.3%	-0.3%
	Y-90 e+	759	749	1213	1195	1.5%	37.4%
	F-18 ion	641	631	1090	1074	1.5%	41.2%
4 cm sphere	Y-90 ion	1207	1193	1215	1201	1.2%	-0.1%
	Y-90 e+	744	735	1235	1220	1.4%	37.6%
	F-18 ion	634	626	1081	1068	1.4%	39.9%
3 cm sphere	Y-90 ion	1207	1193	1215	1201	1.1%	0.6%
	Y-90 e+	744	735	1235	1220	1.2%	39.8%
	F-18 ion	634	626	1081	1068	1.2%	41.4%
2 cm sphere	Y-90 ion	1207	1191	1219	1204	1.2%	0.9%
	Y-90 e+	736	726	1199	1182	1.4%	38.6%
	F-18 ion	633	625	1066	1051	1.4%	40.6%

conditions in the GATE simulation. In the simulation, all crystals have the same efficiency, no dead time, no pile-up, and perfect positioning within the scanner.
The presented work utilized ion sources when employing ^{18}F. The ion source includes the branching ratio, decay scheme, and mean free path of the positron, which helps mimic the radionuclide processes during the measurement. Despite their accuracy, ion sources are computationally intensive, particularly when using sources with multiple energy decays, as they require simulating emissions that are not relevant to PET imaging. Using the same simulation setup, a simulation with a back-to-back gamma source was 60% faster than one using an ion source.
For simulating the patient bed, the bed's geometry was extracted from one of the UMapSeries images from the scanner. The bed material was chosen as plastic so that the simulation MuMap values would match those from the UMapSeries of the *e7 tools*. Since we are not interested in, nor can we test, the mechanical properties of the bed in GATE, and because the attenuation correction is for 511 keV, the exact material composition is not a major issue as long as the attenuation values match. In the future, a new material can be defined in GATE to match exactly the material of the bed when the information becomes available.
It is noteworthy that the CT component of the PET/CT was not modeled in the simulations. Instead, the attenuation map was produced by the GATE MuMap actor with a configurable voxel size. Consequently, the simulation results always contain ground truth information about the initial source configuration and attenuation of the imaged medium. This approach provides highly accurate ground truth data, which is ideal for use with machine learning algorithms for training and validation, as well as for image-based dosimetry approaches.
Simulating a simple uniform phantom helped us examine the simulation environment and the R2LM toolkit. The first versions of the R2LM toolkit resulted in an overestimation of counts when the source was simulated outside the AFOV. This issue was resolved by the vendor updated codes, as evidenced by the results of the 140 cm tube. Additionally, no abnormalities were detected in the reconstructed images.
The simulation output from the NEMA protocol showed good agreement with the measured values for the sensitivity, and image quality with a limited agreement for the NEC simulations. The sensitivity values were in close agreement when using both MRD85 and MRD322 with deviations of less than 0.1% and 0.4%, respectively. This consistency was further shown by the matching sensitivity profile plots for both measurements and simulations. Moreover, the NEC values showed an overestimation of the counts by maximum absolute difference of 11% while below the NEC peak measured by the scanner at 27 kBq/mL. This discrepancy results from the electronics saturation of the Quadra scanner, reaching the limits of its data transfer bandwidth. This effect cannot be modeled in the GATE simulation and was not included as

a parameter within the R2LM tool. This indicates that the simulation would be less accurate when using values above 600 MBq (27 kBq/mL), reflected in an overestimation in the reconstructed image. However, the majority of clinical scans are performed with activities below 10 kBq/mL, providing ample applications for the Quadra digital twin. The IEC phantom sphere results indicate that the detection of simulated lesions within a warm background is achievable with an error of 13% for tumors less than 10 mm and 2% for larger tumors of 37 mm compared to the Quadra measurements. The lung residual error was also in good agreement with the measurements for the 4:1 SBR, but was 1.2% higher for the 8:1 SBR.

One drawback of our technique is its decreased flexibility compared to other GATE models, as the R2LM tool is a black box for the user, which does not allow for modifications to detectors or scanner geometry. While GATE uses more generic (and consequently simplified) models in the digitizer chain, the R2LM tool enables the accurate modeling of detector and readout effects specific to the Quadra.

Another limitation of the workflow is the inherent limitations of GATE MC simulation in modeling deadtime, pile-up effects, and data transfer rate. While the current version of R2LM allows for highly accurate simulation in the low-activity range, discrepancies emerge as the activity levels increase. This causes the simulated NEC curves to deviate from the measured values. Further development is needed for the R2LM to handle high activity simulations, which can correct for deadtime, pile-up effects, and data transfer rate in a post simulation step. In a recent publication [125], the GATE digitizer chain was used to validate the Quadra scanner. They were only able to model the NEC curves by empirically changing the digitizer values until the NEC curves matched the published results by Prenosil et al. [43]. Although the NEC curves match the measurements, this empirical approach does not guarantee consistent agreement in other cases. The conditions used differ from those typically encountered in clinical settings, where more variability and complexity could challenge the generalizability of results derived from controlled phantom measurements.

The ^{90}Y spheres simulation was another application of the Quadra digital twin. The simulation used a high activity level, amounting to a total of 640 MBq for the ^{90}Y ion source simulation. Even though this value is higher than what was earlier demonstrated for the NEC curve, it is worth mentioning that this was the activity of the beta decay. The actual annihilation photon activity, when calculated from the ^{90}Y decay scheme, would be much lower than the NEC validated activity value (less than 20 kBq). Moreover, for the positron source and ^{18}F source, a fraction of the activity was used (about 20 kBq), making the simulated values within the validated activity for the digital twin of the Quadra.

When activating the ABS flag of the *e7 tools* reconstruction using ^{90}Y simulations showed only a 1.5% increase in the counts for the hot spheres, while the background

had an increase of 4.5%. The difference between the hot spheres and the background could be attributed to the lower counts in the background region. For both cases, the SBR achieved was 4:1. The R2LM LSO flag had minimal effect when simulating the ^{90}Y ion source as the total activity was higher than the LSO background rate. However, for both the positron and ^{18}F ion sources, the LSO flag generated images with quantitative values 40% less compared to the ground truth, underestimating the injected activity. This could be a side effect of the low activities used that made the LSO background more dominant. Simulations with such low activity (0.01 kBq/mL) would not be feasible to verify through measurements on the scanner due to the low activity and long scan times required.

3.5 Conclusion

Following the above discussion, a comprehensive MC simulation digital twin for the Biograph Vision Quadra total body PET scanner was validated. The digital twin demonstrated agreement with less than a 1% difference compared to the measured phantom and ground truth for simple geometries. It also aligned closely with the published results from the NEMA NU 2-2018 protocol. The validation was conducted using an ^{18}F ion source, with further applications involving an ^{90}Y ion source.
With the aid of the digital twin, low-dose studies can be examined in-silico with access to the ground truth data. This allows for the optimization of study parameters before conducting measurements at the scanner site. A potential future application of the Quadra digital twin is the study of low-dose, long scans to optimize the scanning procedure and reconstruction parameters before implementing them in clinics. Another potential application involves investigating the impact of the LSO background in extended or low-dose scans. Unlike a real scan, where the LSO background can be removed by filtering, the R2LM tool allows for two sets of simulations: one with and one without the inclusion of the LSO background in the post-simulation phase. Moreover, this work can serve as a stepping stone for simulating other radionuclides and ions used in therapy. This involves acquiring PET images of the scan, complemented by the crucial ground truth information detailing the delivered dose to the target organ.
The simulated XCAT phantom produces images that resemble those obtained from patient scans. This provides us with the opportunity to simulate scenarios with complex geometries and abnormalities where the ground truth is known. This is pivotal in evaluating the precision of reconstruction algorithms or applied corrections for different imaging studies, such as motion correction studies where the *MuMapActor* data would serve as the ground truth. In addition, various image segmentation tasks could benefit from the ground truth images for validating the segmentation masks. Moreover, the Quadra digital twin can also be used in the future to simulate a

voxelized phantom generated from a patient PET scan. This would help to simulate scans of healthy patients and study the effect of motion or the addition of tumors using more accurate data than the standard XCAT phantom. However, it should be noted that such an application would carry with it the inherent limitations and uncertainty from the original PET image that is used for generating the voxelized phantom.

In the following chapters, the Quadra digital twin will be utilized for low-dose applications mainly, to simulate the XCAT phantom to generate accurate low-dose high-dose pairs for evaluating the training of AI models for image denoising. Moreover, it will be used to investigate the current methods used for re-framing high-dose scans to obtain low-dose scans for AI training (more details will follow in Chapter 5).

4 3D Printing Radioactive Phantoms

This section is an extension of abstracts submitted to 37th Annual Congress of the EANM, Hamburg, Germany, 2024, IEEE NSS/MIC/RTSD 2022, Milan, Italy [179], Transactions on Additive Manufacturing Meets Medicine 2022, and 2023, Lübeck, Germany [180, 181], Nuclear Medicine 2023, 62st Annual Meeting of the German Society for Nuclear Medicine, Leipzig, Germany 2024 [182], and The Total Body PET (TBPET) 2024 conference 3rd edition, Groningen, The Netherlands 2024 [183]. In addition, a paper titled 'Dedicated 3D printed radioactive phantoms with ^{18}F-FDG for ultra-high resolution PET' was published at the IEEE Transactions on Radiation and Plasma Medical Sciences journal.
The presented work in this section is a result of a collaborative work with Isotope Laboratory of the Natural Sciences Section, Universität zu Lübeck, Lübeck, Germany, Werner Siemens Imaging Center (WSIC), University of Tübingen, Tübingen, Germany, and Department of Preclinical Imaging and Radiopharmacy, University of Tübingen, Tübingen, Germany. The developing of 3D printing resin with radioactive material was done in collaboration with Steven Seeger (Institute of Medical Engineering, Universität zu Lübeck) and Prof. Dr.Christian Schmidt (Isotope Laboratory of the Natural Sciences Section, Universität zu Lübeck). Steven Seeger handled the first 3D prints with the 2D imager and help with developing the new method of mixing with ^{89}Zr.

Contents

4.1 Introduction

The objective of the work presented in this section was to develop procedures for printing radioactive phantoms for low-dose PET imaging using ^{18}F-FDG, ^{18}F, and the non-pure positron emitter ^{89}Zr. These phantoms included submillimeter structures and regions with different activity concentrations. A conventional 3D desktop printer was utilized to create these phantoms, which should serve as surrogates for fillable phantoms used in motion correction and low-dose imaging studies. Throughout the work of the thesis, three main applications of employing 3D printing technology in PET imaging were investigated: development of high-resolution dedicated 3D printed radioactive phantoms for small animal PET, development of wall-less phantoms for clinical PET scanners, and utilization of 3D printing technology to solve the issue of adsorption of metallic radionuclides into the walls of phantoms. The first application aimed to develop the method within the framework of preclinical scanners before translating it into printing larger phantoms for clinical scanners. This would pave the way for further development of the method for low-dose PET scans using ^{89}Zr. To our knowledge, the full exploration of 3D printing with ^{89}Zr has not yet been accomplished. Our aim is to address the issue of ^{89}Zr adsorption onto phantom walls and support the characterization of imaging performance and optimization of imaging protocols for low-dose PET imaging of the Quadra scanner.

The development of high-resolution dedicated 3D printed radioactive phantoms was a part of the MERMAID project, for the developing of a high-resolution PET prototype system [130, 184, 185]. The MERMAID concept is dedicated to small-fish imaging, including the development of water-filled imaging chambers using

3D-printing technology [186], as well as dedicated radiotracer administration procedures. To test the MERMAID prototype, dedicated phantoms with submillimeter radioactive structures are necessary. Preliminary studies have shown that printing hollow phantoms to be filled with activity often leads to incomplete filling and air bubbles due to the small size of the structures [162].

The second application involved using 3D printing to create customizable wall-less spheres. These spheres were used to validate motion correction when applying AI algorithms. The process entailed generating data with respiratory motion and ground truth information, which were then utilized to test different AI algorithms for motion correction. The effectiveness of the applied correction was quantified based on the ground truth. This work focused solely on the 3D printing process and the generation of ground truth simulated data. The development of the motion correction algorithm was beyond the scope of this thesis. More details can be found in [182], where the study aimed to investigate various effects associated with motion correction and low-dose imaging using wall-less phantoms.

4.2 Materials and Methods

4.2.1 3D Printer and Printing Setup

A LCD *Photon Mono* (Anycubic, China), an affordable desktop printer (Figure 2.13), was used for 3D printing. LCD printers utilize a liquid resin placed in a tank above a UV light-emitting screen. In this setup, the transverse plane of the tank defines the X and Y directions. A printing plate attached to a platform moves along the Z-axis, immersing in the resin. UV light is directed onto defined positions on the X and Y axes, polymerizing the resin into a solid structure attached to the printing plate. Stepwise upward movement of the printing plate creates stacked layers, forming the 3D object. The printer's resolution is 0.051 mm, 0.051 mm, and 0.01 mm in the X, Y, and Z directions, respectively. Printing parameters include 2 seconds of UV irradiation per layer with a layer height of 0.05 mm.
We made several modifications to customize the commercial 3D printer for our study. These changes were aimed at reducing the size of the printing plate and resin tank. This step is crucial when using radioactive substances to minimize the required activity mixed with the resin and to reduce surface contamination when using longer-lived isotopes. The resin tank now has a volume of 31 mL, with a printing plate measuring 60×30 mm^2. Figure 4.1 shows the printer used and the size of one of the phantoms we aim to print, showcasing the unused space on the printing plate without the modified parts. The original size is sufficient for printing

phantoms for the preclinical scanners. The original tank had a volume of 250 mL, with a printing plate measuring 130×80 mm^2, and was used for printing larger phantoms. (For more details regarding the phantoms, refer to Section 4.2.3.)

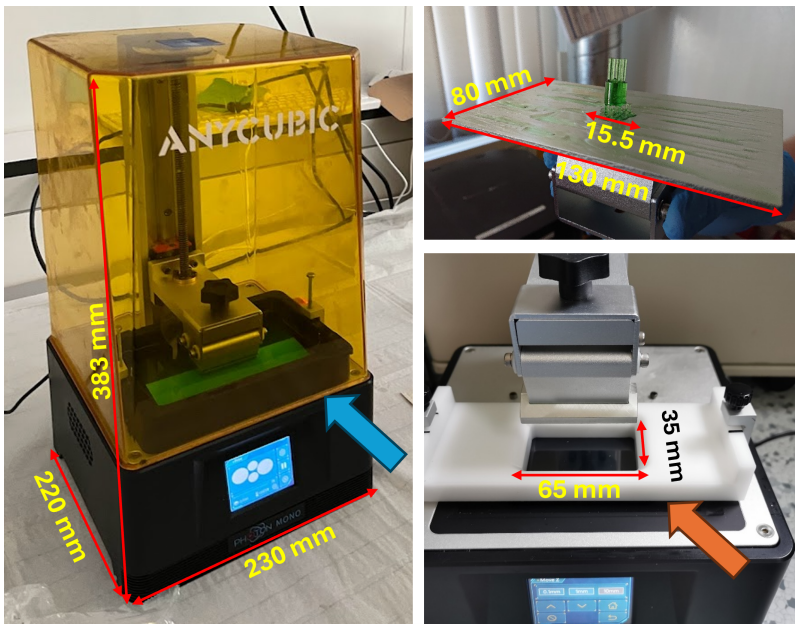

Fig. 4.1: Anycubic Mono LCD printer (left) with the blue arrow showing the original resin tank; on the top right, the original printing plate, and the bottom image shows the modified printing plate, and the orange arrow showing the resin tank.

4.2.2 Mixing and Printing

Two mixing approaches were developed throughout the project as new information was obtained from the results. The first mixing method worked well when ^{18}F-FDG and ^{18}F were used. The second method, developed for ^{89}Zr, also proved to work with ^{18}F-FDG and ^{18}F. An overview of the process of generating the phantoms is shown in Figure 4.2.

4.2.2.1 Methods of mixing resin with ^{18}F-FDG

Anycubic Green Bio resin (1.1 g/cm^3), was mixed with a radioactive solution containing ^{18}F-FDG, referred to as 'mixture$_{FDG}$'. Firstly, the desired amount of resin required to achieve the activity concentration (see Section 4.2.3) with ^{18}F-FDG was calculated using Anycubic Photon Workshop software. The mixture was stirred using a magnetic stirrer for 5 minutes to ensure uniform distribution of the radiotracer within the resin. To remove any air bubbles before printing, the mixture was heated for 5 minutes at 70°C. After printing was completed, the phantoms were immersed

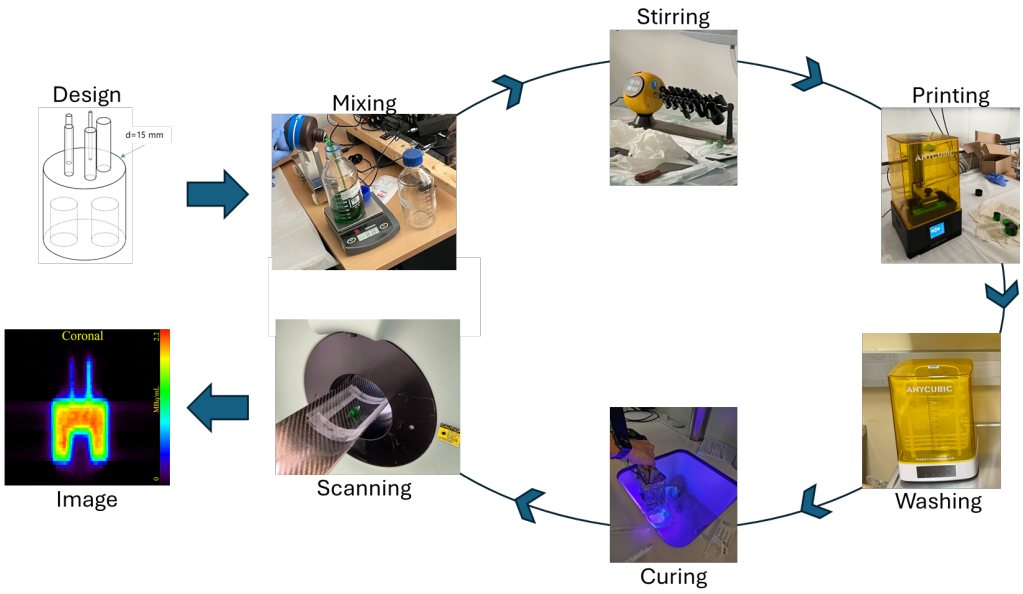

Fig. 4.2: The procedure for printing the phantom begins with designing it in a CAD software. Subsequently, the radiotracer is blended with the photoresin and stirred using either a rotary or magnetic stirrer before heating it. The phantom is then printed, followed by a process of washing and curing under UV light. Finally, the phantom is imaged.

twice in a 2-propanol solution and washed for 5 minutes each time to remove any uncured resin. This step was necessary to ensure the cleaning of the phantom's surface and removal of any uncured resin to prevent artifacts on the phantom's surface. Lastly, the phantoms were placed within a UV chamber for 30-40 seconds to completely cure the surface of the print and minimize the release of activity from the phantom's surface. Several phantoms were printed with this mixture, including a flood phantom, two-point phantom, a single sphere phantom, NEMA IQ phantom, and ^{18}F 3D printed IEC spheres as presented in Table 4.1. Using the same mixing method, ^{89}Zr was added to the resin instead of ^{18}F-FDG. However, PET images showed some hot spots and inhomogeneities, prompting us to scan the liquid resin. The remaining resin was loaded into a 15-mL syringe to study the effect of mixing the radioactive source with the liquid resin. Additionally, the remaining resin mixed with ^{18}F-FDG was loaded into a 50 mL Falcon tube to compare both sources. Figure 4.3 shows the homogeneous distribution of ^{18}F-FDG radiotracer in the resin. However, it was noticed that ^{89}Zr was precipitating. Despite attempts to shake the syringe again and measure it after rotating it at a 90-degree angle, the issue persisted. Consequently, a second mixing method was developed for using ^{89}Zr.

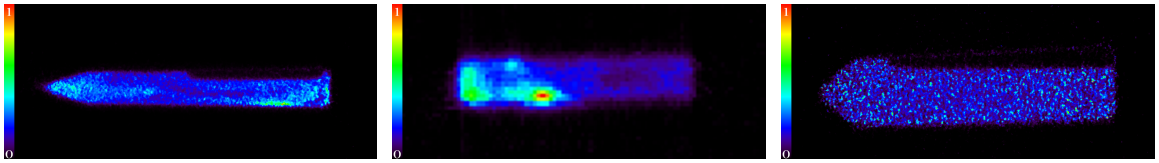

(a) (b) (c)

Fig. 4.3: a) Uncured ^{18}F-FDG resin with mixture$_{FDG}$ imaged using the Inveon scanner, b) uncured ^{89}Zr using mixture$_{FDG}$ method imaged using the Inveon scanner, and c) uncured ^{89}Zr using mixture$_{Zr}$ imaged using the MEDISO nanoPET/CT scanner.

4.2.2.2 Methods of mixing resin with ^{89}Zr

Anycubic water washable resin (1.1 g/cm^3), was used while mixing it with cold Zirconium diluted in hydrochloric acid (HCl), referred to as 'mixture$_{Zr}$'. Furthermore, the mixing method was changed to shaking the resin by hand vigorously to ensure adequate mixing while in a sealed container. The step of heating the resin was removed as the heat was causing the plastic film in the resin tank to warp and deform, resulting in failed prints. The remaining steps, including printing, cleaning, and curing, remained unchanged. The radioactive resin was filled into a 50 mL Falcon tube and scanned for 5 minutes, as shown in Figure 4.3c. With mixture$_{Zr}$, additional phantoms were printed, including a single-point phantom, an IQ phantom, an IQ$_{mermaid}$ phantom, and IEC Spheres as presented in Table 4.1.

4.2.3 Phantoms

The first printed phantom was a rectangular cuboid measuring $44 \times 22 \times 2$ mm^3. This phantom was printed and imaged at Isotope Laboratory of the Natural Sciences Section, University of Lübeck, Lübeck, Germany. More information of this phantom can be found at [179, 185].

4.2.3.1 Point source phantoms

The two-point phantom consisted of two radioactive cylinders with a diameter of 1 mm and a height of 1 mm printed onto a non-radioactive plate (cold background) measuring $5 \times 30 \times 2$ mm^3 (Figure 4.4). The two cylinders were separated by a gap of 5 mm. The main purpose of this phantom was to test printing a phantom using both radioactive and non-radioactive resins. In the long term, we aim to produce grids of point sources to estimate the spatial resolution of the MERMAID scanner prototype.
The printing of active and nonactive regions was carried out in three stages: First, the cold background was printed using non-radioactive resin. In the next step, the

Table 4.1: Summary of the phantoms used, including details on activity concentration at the start of printing, print time, volume, radionuclide, and the intended application of the 3D-printed phantom. For phantoms containing both a sphere (S) and background (BG), information is provided separately for each.

Phantom	Activity concentration (MBq/mL)	Printing time (min)	Volume (mL)	Radionuclide	Application
Two-point phantom	3.54	15	0.03	^{89}Zr & ^{18}F-FDG	Resolution test
Single point phantom	9.8	15	0.01	^{89}Zr	Single seed source
Fish-like phantom (S)	3.54	15	0.06	^{18}F-FDG	Activity concentration feasibility
Fish-like phantom (BG)	1.66	30	1.82	^{18}F-FDG	Activity concentration feasibility
Single sphere phantom (S)	21.2	15	0.52	^{89}Zr	^{89}Zr walls adherence
Single sphere phantom (BG)	2.66	45	10.3	^{89}Zr	^{89}Zr walls adherence
IQ Phantom	0.2	120	19.70	^{89}Zr & ^{18}F-FDG	NEMA walles phantom
IQ$_{mermaid}$ phantom	1.97	45	2.45	^{89}Zr & ^{18}F-FDG	NEMA walles phantom
IEC sphere (BG)	0.0004	150	63-200	^{89}Zr & ^{18}F	Clinical scanner imaging
IEC sphere (S)	0.003	45	65	^{89}Zr & ^{18}F	Clinical scanner imaging

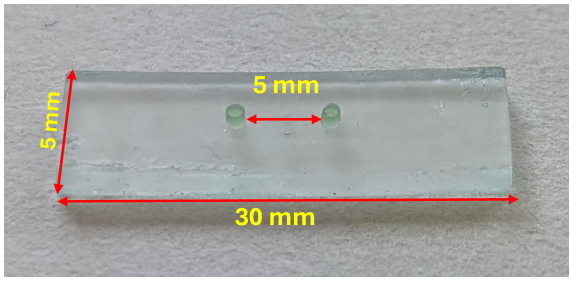

Fig. 4.4: The two-point phantom: Two radioactive point sources (green) that are 1-mm each on top of a non-active background (transparent).

printer was paused before switching to the radioactive resin mixture and cleaning the printer plate. The printed part and printing plate were wiped to remove any uncured resin from the surface. The nonactive resin in the tank was then replaced with the ^{18}F-FDG mixed resin. It was crucial not to remove the printing plate or turn off the printer during this step to allow for resuming the print at the same layer where it was paused. The final step involved resuming the print job to produce the two radioactive cylinders. The entire printing process took 15 minutes, including the time required for resin changing and the two print steps. To evaluate the print quality of the two-point source, we aimed to compare it against a commercially available ^{22}Na point source. This phantom was printed using mixture$_{FDG}$ with ^{18}F-FDG initially and later with ^{89}Zr. This phantom was printed and imaged first at Isotope

Laboratory of the Natural Sciences Section, and later a new print was performed at WSIC, Department of Preclinical Imaging and Radiopharmacy, Tübingen, Germany. Additionally, a single-point phantom was printed, in which the cold rectangular background was replaced with a cone as showin in Figure 4.5b. The purpose of the cones is to limit the contamination of the cold background with the radioactive resin. Additionally, the cone helped reduce the amount of resin needed when printing the point sources, as we were able to place a droplet of high activity mixed resin using a pipette just above the screen where the points would be printed, instead of filling the minimum amount of resin in the tank to ensure a successful print. The aim of this phantom was to compare the printed point source with the seed of few commercially available ^{22}Na single point sealed sources. The 3D printed single-point phantom and the point sources are shown in Figure 4.5. The single-point phantom was printed with only using mixture$_{Zr}$. This phantom was printed and imaged at WSIC, Department of Preclinical Imaging and Radiopharmacy, Tübingen, Germany.

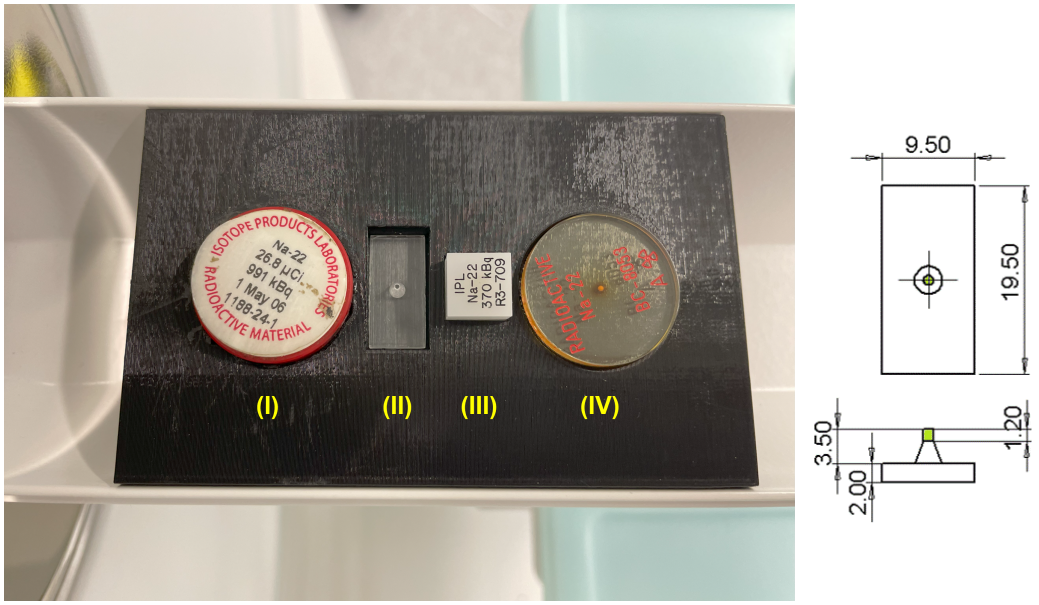

(a) (b)

Fig. 4.5: a) The commercial ^{22}Na single-point sealed sources (I,III, and IV) utilized in this study were positioned in the center of the PET scanner, with the 3D-printed ^{89}Zr single-point phantom (II), b) the CAD design of the 3D-printed ^{89}Zr single-point phantom (point source green) includes a larger rectangular structure to stabilize it during scanning.

4.2.3.2 Fish-like phantom

The fish-like phantom has a spindle shape and consists of three regions: a radioactive body ('warm background') with a length of 40 mm, a radioactive sphere ('hot') with a diameter of 5 mm, and an air-filled, non-radioactive spherical cavity ('cold') with a diameter of 5 mm (Figure 4.6). The goal was to investigate the feasibility of including different activity concentration levels in the same phantom. The ratio of activity concentration between the warm body and the hot sphere was 1:2, with no activity in the air cavity.

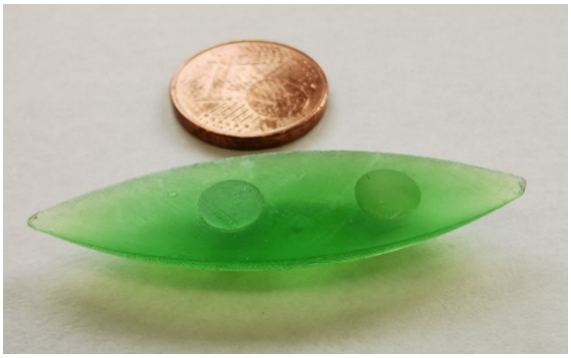

Fig. 4.6: One half of the spindled shape printed fish-like phantom with the two cavities [179] © 2024 IEEE.

This phantom was designed to mimic a zebrafish after administration of ^{18}F-FDG. The three areas and activity concentrations mimic the body ('warm background'), heart ('hot') and swim bladder ('cold') [187, 188]. The location of the spheres with respect to the phantom body follows the anatomical position of the organs in a living fish. To produce regions of different activities, the phantom was printed in two steps, in a similar manner as the two-point phantom. Firstly, the radioactive mixture with the highest activity (3.54 MBq/mL) to print the two hemi-spheres was prepared. To reduce the amount of radioactive waste, we avoided using a support structure. Next, two hemispheres were printed and then fused together after cleaning and curing. They were fused by adding resin from the printer tank between the flat surface of the hemispheres and curing them again forming the sphere. The next stage focused on printing the radioactive body. To achieve a 1:2 ratio, we added the required amount of resin to the one remaining from the last print, and mixed them as described before. The two halves of the body were printed separately, both including two hemispherical cavities as shown in Figure 4.6. The hot sphere was inserted in one of the cavities and the two halves were fused together in the same way as the two hot hemispheres mentioned above. The total print time and preparation of the phantom was 30 min. This phantom was printed with only using mixture$_{FDG}$.

This phantom was printed and imaged at WSIC, Department of Preclinical Imaging and Radiopharmacy.

4.2.3.3 Single sphere phantom

The single sphere phantom comprised a hot spherical source of 1 cm diameter placed within a warm cylindrical background with a diameter of 2 cm, and height of 3.5 cm, as shown in Figure 4.7. The design of the sphere was inspired by the IQ phantom of the NEMA NU 2–2018 standards [160]. This phantom was printed using the same steps as the fish-like phantom. Its purpose was to test the mixing of ^{89}Zr using the same process as mixture$_{FDG}$. Additionally, this served as the initial test to examine our hypothesis that 3D printing the phantom would resolve the issue of ^{89}Zr sticking to the walls of the phantom after a rescan a few days later. This phantom was printed and imaged at WSIC, Department of Preclinical Imaging and Radiopharmacy.

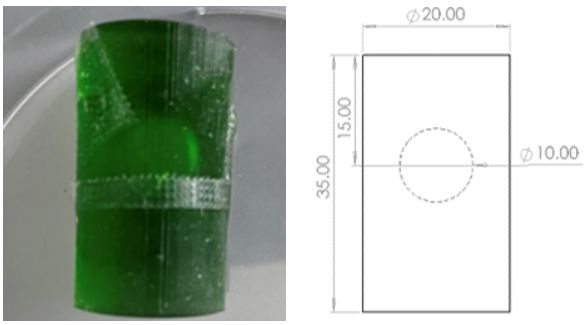

(a) (b)

Fig. 4.7: a) The single sphere phantom, b) the corresponding CAD design. Dimensions are in millimeters.

4.2.3.4 3D printed NEMA NU 4-2008 phantoms

In this section, a total of four IQ phantoms were printed using ^{18}F-FDG and ^{89}Zr. Two phantoms were of the standard size, while the other two were downscaled versions. Additionally, the ^{18}F-FDG phantoms included a non-active wall. This phantom was printed and imaged at WSIC, Department of Preclinical Imaging and Radiopharmacy.

The 3D printed NEMA NU 4-2008 phantoms are based on the IQ phantom described in the NEMA standards for evaluating the image quality of small animal PET scanners [144]. It consists of three regions: a 'rod region' comprising five rods, each 20 mm long with diameters of 1, 2, 3, 4, and 5 mm (Figure 4.9), a 'uniform region' consisting of a 15 mm long radioactive cylinder with a diameter of 30 mm, and

a 'cavity region' with two 15 mm long cylindrical air cavities with a diameter of 5 mm. This phantom was printed twice, once using mixture$_{FDG}$ with ^{18}F-FDG and later mixture$_{Zr}$ with ^{89}Zr. Additionally, a cover with a wall thickness of 2.5 mm was produced through subtractive manufacturing of a PMMA block, as it was feasible and accurate due to its relatively large size. While the printed phantom is solid and does not require a cover to contain the radiotracer, the cover serves to reduce radiation exposure from the short-range β^+ radiation emitted from the phantom, enhancing its safety during handling. Furthermore, the cover reduces the range of positrons, similar to the walls enclosing the cavities of standard fillable IQ phantoms, typically made of PMMA material. As positrons penetrating the cover and their subsequent annihilation also affect the PET imaging properties of the phantom, we scanned the IQ phantom with and without the cover and compared the reconstructed images. Additionally, a standard NEMA fillable IQ phantom was used to evaluate the quality of the printed phantom with and without the cover. The volume of the printed phantom was 19.7 mL, while the volume injected into the fillable phantoms was 20 mL. The slight difference can be attributed to a 1.5% shrinkage in the printed phantom. The fillable phantom had an activity of 3.7 MBq, following the NEMA 2008 guidelines, resulting in an activity concentration of 0.185 MBq/mL. The printed phantom had an activity concentration of 0.2 MBq/mL due to human error while preparing the mixture.

Since MERMAID is designed for small fish rather than rodents, the original size of the micro-PET IQ phantom does not fit within its FOV. Therefore, we developed a downscaled version of the micro-PET IQ phantom, which is 50% smaller in size compared to the original design. It is important to note that this is a volumetric downscaling in three dimensions (H/2 and r/2), resulting in a new volume that is actually 12.5% of the original, rather than just 50% smaller. The new volume is approximately 2.46 mL. The downscaled version will be referred to as IQ*mermaid*. IQ*mermaid* preserves the ratios between the various regions and structures of the phantom, which is an advantage of using STL files. Additionally, a cover with a wall thickness of 2.5 mm and a clearance of 0.25 mm was printed using non-radioactive resin. The cover was produced with an SLA printer, specifically the *Form 2* (Formlabs, USA), as SLA printers are better suited for printing halo structures compared to LCD printers. Figure 4.8 shows the CAD designs for the IQ phantom while Figure 4.9 shows the CAD designs for the IQ$_{mermaid}$ and its cover.

To mimic the attenuation of radiation by PMMA (with a density of 1.18 g/cc and an electron density of 0.639 [189]), clear resin was used as the printing material. The clear resin is composed of 60% epoxy resins, 35% diacrylate compound ((1-methyl-1,2-ethanediyl)bis[oxy(methyl-2,1-ethanediyl)]), and 5% hydroxycyclohexyl phenyl ketone with a density of 1.17 g/cc. The electron density of the resin (ρ_e^{resin}) can be calculated with the following equation [190]:

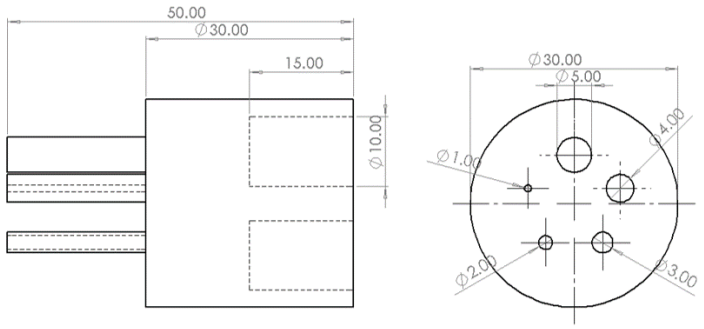

Fig. 4.8: The IQ phantom CAD designs. Dimensions are in millimeters.

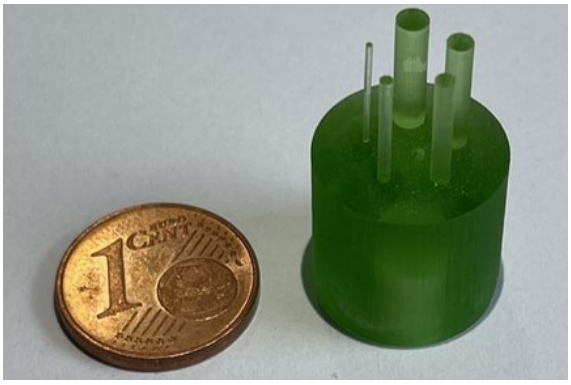

(a)

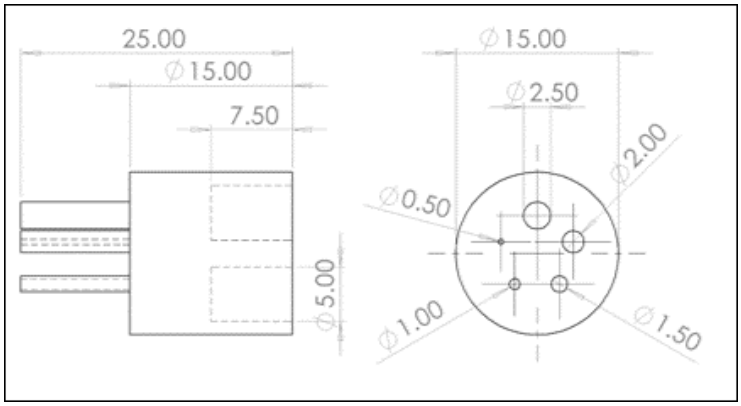

(b)

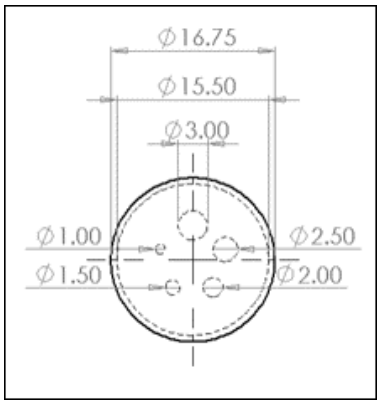

(c)

Fig. 4.9: a) IQ*mermaid* phantom, b) the corresponding CAD design, and c) the CAD design for the phantom cover. Dimensions are in millimeters [179] © 2024 IEEE.

$$\rho_e^{resin} = \rho \times \left(f_{\text{epoxy}} \times \frac{A_{\text{epoxy}}}{Z_{\text{epoxy}}} + f_{\text{diacrylate}} \times \frac{A_{\text{diacrylate}}}{Z_{\text{diacrylate}}} + f_{\text{ketone}} \times \frac{A_{\text{ketone}}}{Z_{\text{ketone}}} \right), \quad (4.1)$$

where Z is the atomic number, A is the atomic weight, ρ is the density, and f is the fractional composition of each material in the compound. To calculate the Z to A ratio for each compound as a whole, we need to take into account the number of each type of atom in the compound. Assuming a basic structure of epoxy resin as $C_{21}H_{25}ClO_5$, the total atomic number would be 208 and the total atomic weight 392.45 g/mol. Therefore, the atomic number to atomic weight ratio would be 0.53. The molecular formula for the diacrylate compound is $C_{20}H_{22}O_6$. The total atomic number would be 190 and the total atomic weight 358 g/mol. Therefore, the atomic number to atomic weight ratio would be 0.53. Lastly, for the ketone compound, the molecular formula is $C_{13}H_{16}O_2$. The total atomic number would be 110 and the total atomic weight would be 204 g/mol. Therefore, the atomic number to atomic weight ratio would be 0.54. Hence, the calculated electron density is 0.652.

4.2.3.5 3D printed IEC spheres

The aim of this phantom was to test different AI-based motion correction algorithms where a static scan of the printed spheres would serve as the ground truth image. The application of the motion correction was carried out by W. Lan and S. Weigel (University of Tübingen, Tübingen, Germany), which was outside the scope of this thesis work. More details of the step and motion parameters can be found in [182]. The phantom used comprised a 10 mm sphere with a warm background and a 28 mm sphere with a cold background, which are the smallest two sphere of the NEMA IEC phantom [45]. The background dimensions are illustrated in the CAD drawing in Figure 4.10. The activity ratio between the hot sphere and the warm background was 4:1. The sizes of the spheres were chosen to closely match the smallest two spheres in the NEMA NU 2–2018 standards [160]. The spheres and background were printed using the same method as the fish-like phantom. However, a few changes were made regarding the printing plate and the radiotracer. For the printing plate, as we were printing larger phantoms in this step, we exchanged the modified printed bed with the original bed to accommodate the large background. As for the radiotracer, we used ^{18}F instead of ^{18}F-FDG for the mixture$_{^{18}F}$ as we aimed to expand our trials by mixing the resin with a radioisotope without the FDG kit. The FDG kit is essential when injecting patients with ^{18}F, as it enhances the stability, safety, and effectiveness of radiotracer uptake in cells and tumors during PET scans. However, in a phantom study, the use of the FDG kit provided no added benefit. Thus, it was omitted, reducing both the cost and preparation time for the radiotracer.
As these were the first prints we performed with such large volumes, we initially conducted a cold print without radioactive resin to optimize the parameters before

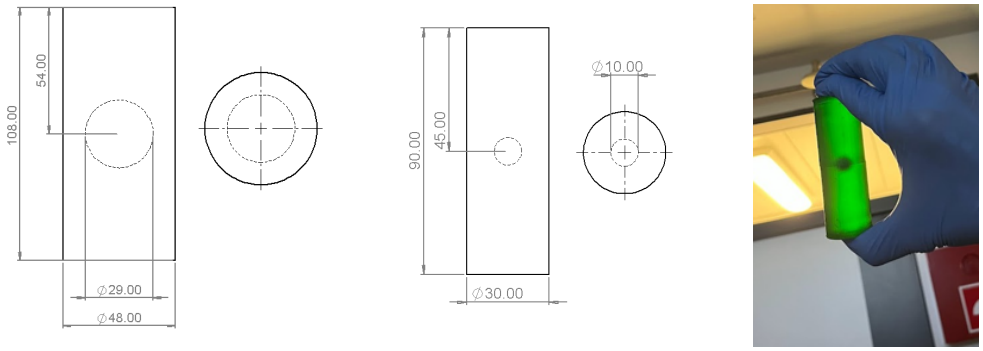

(a) (b) (c)

Fig. 4.10: a) CAD design of the big sphere of the ^{18}F 3D printed IEC spheres, b) the small spheres CAD design, and c) an example of the printed small sphere phantom. Dimensions are in millimeters.

printing the phantoms again with radioactive resin. The only parameter we had to modify was adding eight base layers that were exposed for 60 seconds each. None of the phantoms mentioned above had base layers. The base layers were necessary to ensure the adhesion of the phantom to the printing plate and to prevent warping or falling off the printing plate during the print. We were able to successfully print the phantoms by first printing all four hemispheres, then printing the small background as two halves, and lastly, printing the big background following the same process. While printing with the radioactive resin, we encountered an issue where the printer overheated due to the contentious printing using the full volume of the print plate over several hours. This resulted in the warping of the phantom during the production of the large warm background. Consequently, we opted to place the larger active sphere in the cold background that was printed during the initial cold test, rather than in the warm background as originally planned. This phantom was printed only with mixture$_{^{18}F}$ at University hospital Tübingen, Tübingen, Germany.
The two IEC spheres were reprinted using ^{89}Zr. Additionally, half of the 28 mm sphere was placed in a 1 cm cold background, leaving the other half exposed without any surrounding attenuation medium. Alongside the two spheres, a warm cylindrical background with a diameter of 50 mm and a height of 40 mm was printed. This cylindrical background contained a hollow sphere that accommodates the 28 mm sphere (without placing any sphere or medium within it). This phantom represented the hollow section of the IEC phantom, simulating the imaging conditions for the lungs.
Furthermore, the sphere phantoms were used to study the effect of ^{89}Zr sticking to the walls of the phantom, similar to the single sphere phantom. The sphere phantoms had an 8:1 sphere-to-background activity ratio, a ratio typically present in

the NEMA NU 2–2018 IQ phantom [160], mimicking the activity disruption between a tumor and an organ. The sphere and cylinder were printed as two halves and later fused together following the method elaborated for the fish-like phantom in Section 4.2.3.2. The CAD drawings were similar to what was shown in Figure 4.10. Figure 4.11 shows the addition of the hollow sphere and images of the phantom. This phantom was printed with only using mixture$_{Zr}$ at University hospital Tübingen.

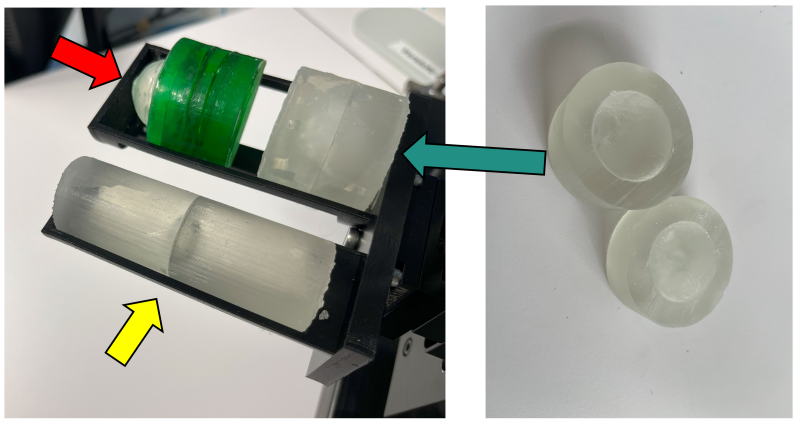

Fig. 4.11: a) The printed IEC spheres: the 28 mm sphere (red arrow) with one half covered by a non-active background (green resin) and the other half exposed without any attenuation medium, the 10 mm spheres within the active cylindrical background (yellow arrow), and the warm cylinder with a hollow 28 mm sphere (teal arrow). b) The two cylinder halves with a hollow sphere before fusion. The printed spheres are mounted on a stage to ensure consistent positioning during multi-day scans within the scanner.

4.2.4 Low dose imaging of 3D printed ^{89}Zr spheres

The last application performed with 3D printing phantoms involved using IEC ^{89}Zr spheres to study low-dose PET imaging using the Quadra. The phantom underwent scanning for 23 days, analyzing sinogram count rates and activity concentration within the phantom. As for the ^{89}Zr IEC spheres, they were scanned five times: on day 1 for 12 minutes, day 4 for 15 minutes, day 12 for 23 minutes, day 16 for 128 minutes, and lastly on day 23 for 1440 minutes. This study marked the first of its kind performed with the Quadra, as previous attempts to image a ^{89}Zr phantom longitudinally had failed due to the adherence of ^{89}Zr to the phantom walls. For low-dose imaging studies, the LSO background from the scanner affects quantification, an effect that is unavoidable due to the intrinsic nature of the scanner.

4.2.5 Contamination tests

During the initial development stage we conducted several contamination tests. After printing the flood source, a contamination test was conducted using a handheld survey meter for all printer's parts that were not in direct contact with the radioactive resin. Additionally, wipe tests were performed on the radioactive printed phantoms after washing and curing using a Gamma Counter to measure the amount of activity not firmly attached to the surface, thus indicating possible contamination upon contact with the printed phantoms. Moreover, a sample of the cleaning solution was measured using the same Gamma Counter to quantify the level of contamination. The resin tank and the printing plate were removed and stored for 10 half-lives (approximately 20 hours for ^{18}F prints and 30 days for ^{89}Zr prints) with the cleaning solutions before the activity level was below the allowed limits for discharge. As an additional precaution against surface contamination from the printed phantoms, a thin plastic sheet was placed on the scanner bed underneath the phantom.

4.2.6 Imaging procedures

Initial evaluation of the flood phantoms and the two-point phantom was performed using a 2D phosphor imager, the Typhoon FLA 7000 (GE Healthcare, UK), at the Isotope Laboratory of the Natural Sciences Section, as a substitute for the lack of a small-animal PET scanner. This provides projection images of the activity distribution with a resolution of 50×50 µm^2 per pixel. The phosphor imager is commonly utilized for phosphor imaging of radioisotopes, including ^{18}F-FDG [191]. Our initial results indicated that the phosphor imager screen is more sensitive to the β^+ emissions from the radioisotope compared to the 511 keV photons. The exposure time was two minutes per phantom. Additionally, the two-point phantom was compared against a commercially available phantom consisting of an arrangement of two ^{22}Na point-like sources. The nominal distance between the two point sources of the commercial phantom was 5 mm.
For 3D imaging of the printed phantoms using a PET scanner, another measurement campaign took place at the WSIC and within the University Hospital Tübingen, employing both a preclinical scanner and a clinical scanner. The two-point phantom, point phantom, single sphere phantom, fish-like phantom, and IQ phantoms were scanned using a small animal PET scanner, Inveon (Siemens, USA). The acquisition time was 30 minutes per phantom. In the case of the IQ phantom, the first scan was carried out without the cover. To compensate for the activity loss during preparation, the PET scan with the phantom and the cover was extended to 60 minutes to ensure comparable event statistics. The single sphere phantom was scanned twice, once for 30 minutes on day 0 and then for 9 hours on day 21. The PET data were reconstructed using the OSEM 2D method with 4 iterations and 16 subsets, employing a matrix

size of $256 \times 256 \times 159$ voxels and a voxel size of $0.388192 \times 0.388192 \times 0.796$ mm^3. Attenuation correction was performed using a transmission scan.
The IQ phantom, both printed and filled, was scanned using the *MEDISO nanoPET/CT* (Mediso Kft., Hungary) for 20 minutes, while the IQ$_{mermaid}$ phantom was scanned for 40 minutes due to its lower total activity resulting from the difference in volume compared to the IQ phantom. Additionally, we acquired high-resolution CT images to be used for attenuation correction during PET image reconstruction, and to inspect the quality of the printed phantom to ensure no cracks or air bubbles were present. Finally, CT images were obtained for commercial point sources and compared to the printed point source in terms of the size of the source seeds. *MEDISO nanoPET* reconstruction was using OSEM-3D method with 4 iterations and 16 subsets employing a matrix size of $225 \times 225 \times 235$ voxels and voxel size of $0.4 \times 0.4 \times 0.4$ mm^3. The CT images were reconstructed using *Tera-Tomo^{TM} 3D*, a reconstruction algorithm based on OSEM. The CT resolution matrix size was $244 \times 244 \times 408$ voxels with a voxel size of $0.25 \times 0.25 \times 0.25$ mm^3, while the high-resolution CT matrix size was $1090 \times 1090 \times 935$ voxels with a voxel size of $0.03936 \times 0.03936 \times 0.03936$ mm^3.
The IEC phantoms were scanned using a clinical scanner, the Quadra. The ^{18}F IEC spheres were scanned for 600 seconds to obtain a static image. As for the ^{89}Zr IEC spheres, they were scanned five times: on day 1 for 12 minutes, day 4 for 15 minutes, day 12 for 23 minutes, day 16 for 128 minutes, and lastly on day 23 for 1440 minutes. Quadra reconstruction used 3D OSEM with PSFTOF with 3 iterations and 5 subsets with an image size of $440 \times 440 \times 645$ vocels and voxel size of $1.65 \times 1.65 \times 1.645$ mm^3.
Lastly, a high-resolution micro-CT scan of the IQ$_{mermaid}$ phantom with the cover was performed using a Bruker Skyscan 1172, available at the Institute of Medical Engineering, University of Lübeck, to inspect the quality and integrity of the printed phantom and to investigate the presence of air bubbles or damage within the phantom. The data were reconstructed using the filtered back projection algorithm with a Hamming filter, and the image pixel size was (16.96 µm)^2.

4.2.7 Image analysis and evaluation

The planar image of the flood-source was analyzed quantitatively in terms of uniformity. For the latter, a 2D ROI covering 75% of the actual surface of the source was drawn, and the standard deviation σ_{ROI} as well as the mean intensity μ_{ROI} were extracted. The relative standard deviation was calculated as the ratio between the two values. The higher the relative standard deviation, the lower the uniformity. Additionally, projection profiles were extracted for visual analysis.
For the two-point phantom, we calculated the peak-to-valley ratio (PVR) and the relative difference between the peak intensities ($RDPI$) as follows:

$$PVR = \frac{\bar{P}}{V}, \qquad \text{and} \qquad RDPI = \frac{|P_1 - P_2|}{\bar{P}}, \tag{4.2}$$

where P_1, and P_2 are the maximum intensities, $\bar{P}$ their average, and V is the minimum value reached in the region between the two maxima. Ideally, $P_1 = P_2$ and $V = 0$. $RDPI$ is a measure of how similar the maximum intensities are. In addition to the extension of the sources and the spatial resolution of the imaging system, positron range effects and scatter in the materials can contribute to $V > 0$. High PVR and low $RDPI$ values are thus desirable.

Moreover, since the image of the source has two hot points separated by a cold valley, we have introduced a new metric, the *Normalized Delta Peak to Valley Ratio* (NDPVR):

$$\text{NDPVR} = \frac{|P_1 - P_2|}{\frac{\min(P_1, P_2)}{V}} \quad \text{when } P_1 \neq P_2. \tag{4.3}$$

The $NDPVR$ considers the absolute difference between the two peaks, P_1 and P_2; this value is divided by the relative difference between the smaller peak and the valley (V). By combining the two measures, this new metric yields a low value when the peak-to-valley ratio is large (which is desirable) and the difference between the two peak intensities is small (also desirable).

To evaluate the PET images of both IQ phantoms, we adapted the NEMA NU 4-2008 protocol and calculated the uniformity and recovery coefficients (RC) [144]. For the uniform region, the mean value (μ_{uni}) was obtained using a ROI that was 75% of the uniform region's size. The RC for the rods was calculated by drawing an ROI over each rod to measure the average maximum value of each slice (μ_{R_i}) along the length of the rod. The size of the ROI was twice the diameter of the rod. The RC value was then obtained by dividing (μ_{R_i}) by (μ_{uni}), where i represents the rod size.

For the fish-like phantom, spherical ROIs were drawn within the fish body, as well as within the hot and cold spheres. The ROIs were set to 75% of the spheres' diameters. The mean, median, standard deviation, and coefficient of range (COR) were calculated for each ROI (as shown in Equation 4.4), along with the ratio of the mean values between the hot sphere and the background ROI.

$$COR = \frac{ROI_{\max} - ROI_{\min}}{ROI_{\min} + ROI_{\max}}. \tag{4.4}$$

For evaluating the single sphere phantom and the IEC spheres, spill-over ratio (SOR), CV, and uniformity were calculated following the NEMA NU 2–2018 protocol [160]. Regarding the SOR, the ROI was set to 75% of the air-filled region (μ_{air}) and was divided by the uniform region (μ_{uni}). The CV was determined by the ratio of the standard deviation (σ) to the mean value (μ) within the ROI, as follows:

$$CV = \frac{\sigma}{\mu}. \tag{4.5}$$

4.3 Results

4.3.1 Contamination tests

After the flood phantom was printed, cured, and completely dried with no liquid drippings, a wipe test was performed on its surfaces. The wipe test showed activity levels twice that of the ambient background. The first and second wash solutions measured in a Gamma Counter exhibited 20 times and twice the activity of the natural background, respectively.
All printer parts were cleared of contamination after a wipe test and a survey scan with a Geiger-Müller counter. However, the resin tank and the printing plate showed high levels of contamination because they were in contact with active resin during the printing process. After cleaning the resin tank, new non-active resin was added to print a 2-cm cylinder. A sample of the resin was measured (Resin after cleaning) to assess any remaining contamination. The results of the contamination test are presented in Table 4.2. For reference, the counts from the active resin were also reported.

Table 4.2: Results of the contamination test (wipe test).

Part	Counts per minute (cpm)
Ambient background	244
Printer	262
Phantom Surface	832
Washing solution 1	5415
Washing solution 2	729
Resin after cleaning	831
Active resin	1.88×10^6

4.3.2 Planar imaging

The two-point phantom using the Mixture$_{FDG}$, were imaged with the planar imager. Mixture$_{Zr}$ phantoms were also imaged during the development stage. The study on developing the mixing process for ^{89}Zr is beyond the scope of this thesis, as it was conducted by S. Seeger and C. Schmidt [185].

4.3.2.1 ^{18}F-FDG two-point phantom

The intensity profiles for the 3D printed two-point phantom (^{18}F-FDG) and the commercial one (^{22}Na) are shown in Figure 4.12.

The relative difference between the two maxima was $RDPI = 6\%$ for our 3D-printed phantom, which is much smaller than $RDPI = 72\%$ for the commercial one. The peak-to-valley ratios were 75.32 and 14.1 for the 3D-printed and the commercial phantoms, respectively. $NDPVR$ values were 6.6 and 633.2 for the 3D-printed and the commercial sources, respectively. It is also worth noting that the cold background did not contain any activity, even though it was submerged within the radioactive resin mixture during the printing process of the point sources.

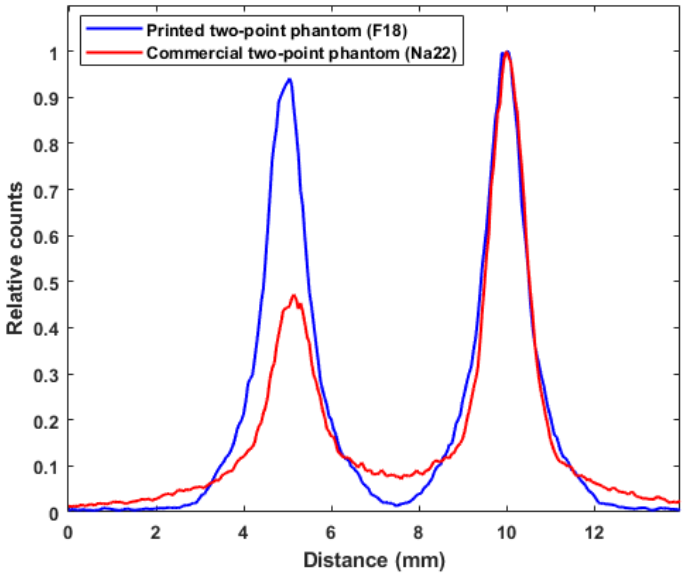

Fig. 4.12: Normalized line profiles for the two 3D printed $^{18}F - FDG$ two-point phantom (blue) and the commercial two ^{22}Na two-point phantom (red) [179] © 2024 IEEE.

4.3.3 ^{18}F-FDG two-point phantom vs ^{89}Zr two-point phantom

Figure 4.13 presents intensity profiles derived from PET images for both the 3D-printed two-point phantom with ^{18}F-FDG and the two-point phantom with ^{89}Zr. The PVR values were 7.4 and 4 for the ^{18}F-FDG phantom and ^{89}Zr phantom, respectively. Upon visual inspection of the images and analysis of the profile line of the ^{89}Zr phantom, we observed some activity within the cold background. This phenomenon is attributed to the effect of positron range, resulting in radioactive emissions escaping from the radioactive points and annihilating within the cold background. For ^{18}F, the maximum range of positrons in water is 2.4 mm, with a mean range of 0.6 mm, while for ^{89}Zr, the positron maximum range is 4.2 mm, with a mean range of 1.2 mm [16]. Moreover, the positron range in air could be over a meter [192].

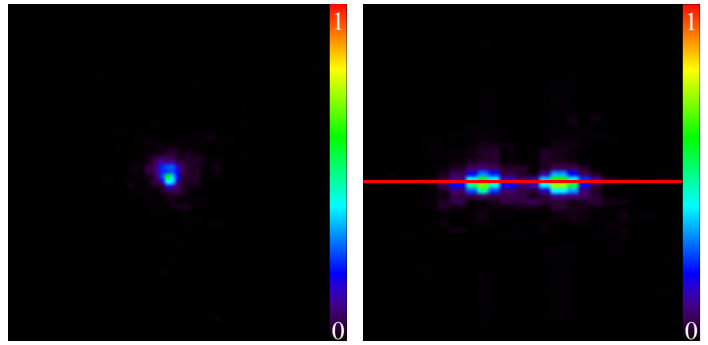

(a)

(b)

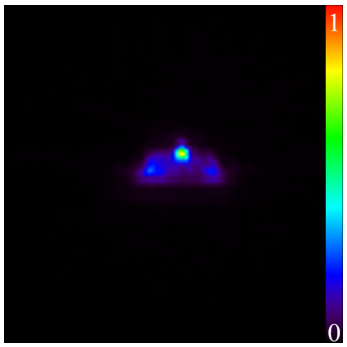

(c)

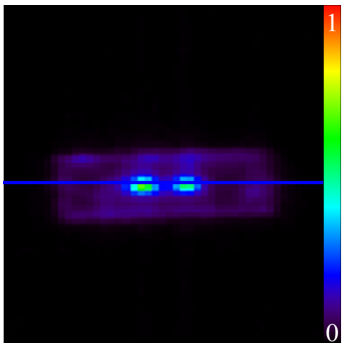

(d)

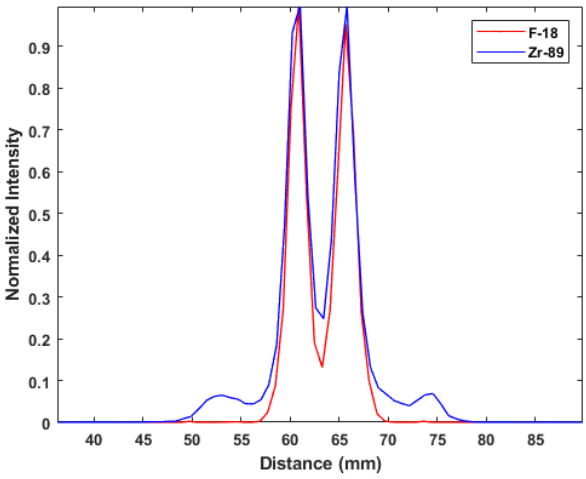

(e)

Fig. 4.13: PET scans: a) Transverse view of the PET image of ^{18}F-FDG two-point phantom while b) shows the coronal view; c) transverse view of the PET image of ^{89}Zr two-point phantom while d) shows the coronal view; e) shows a line profile through the coronal view.

Table 4.3 presents the PVR, RDPI, and NDPVR values obtained from the planar images of the ^{18}F-FDG two-point phantom and the commercial ^{22}Na two-point phantom, as well as from the PET images of the ^{18}F-FDG two-point phantom and the ^{89}Zr two-point phantom.

Table 4.3: The values of PVR, RDPI, and NDPVR for the two-point phantoms.

Phantom	PVR	RDPI(%)	NDPVR
^{18}F-FDG two-point	75.3	6.2	6.6
^{22}Na two-point	14.3	72.3	633.2
^{18}F-FDG two-point PET scan	7.4	4.7	712.9
^{89}Zr two-point PET scan	4.0	0.4	415.9

4.3.4 Single point phantom

Figure 4.14 displays PET and CT images of the 3D-printed single point alongside four other point sources. Due to differences in activity between the 3D-printed ^{89}Zr source (less than 2 kBq when accounting for the branching ratio) and the ^{22}Na commercial sources (about 18 kBq), when imaged together, the point source was not visible. Consequently, the printed point source was subsequently scanned separately, and its image was overlaid onto the original scan for enchanted visualization of the sources. Additionally, the CT image was used to compare the size of the seed in the 3D-printed phantom with that of commercially available point sources.
Three seeds were detected in the commercial disk source (Figure 4.14b), each housed within a 20 mm diameter area. Each seed had a diameter of approximately 0.8 mm and was skewed to the right of the disk. This indicates that if the source were used in a scanner with a resolution lower than 1 mm, rotating the source by 180 degrees could result in different measurements due to the altered positioning of the seeds in the two measurements. In contrast, the 3D-printed source contains a single centered seed (as shown in CAD design in Figure 4.5b).

4.3.5 Fish-like phantom

Figure 4.15 shows the central slices of the reconstructed transverse, coronal and sagittal views for the fish-like phantom. The corresponding quantitative analysis is presented in Table 4.4. The images show a uniform distribution of the activity in the various regions. An artefact is also visible at the top of the coronal and sagittal slices. The calculated ratio for the hot sphere to the fish body was 1.7:1.

4.3.6 Single sphere phantom

Figure 4.16 displays a slice of the reconstructed PET images for the ^{89}Zr single sphere phantom on Day 0 and Day 21. The corresponding quantitative analysis

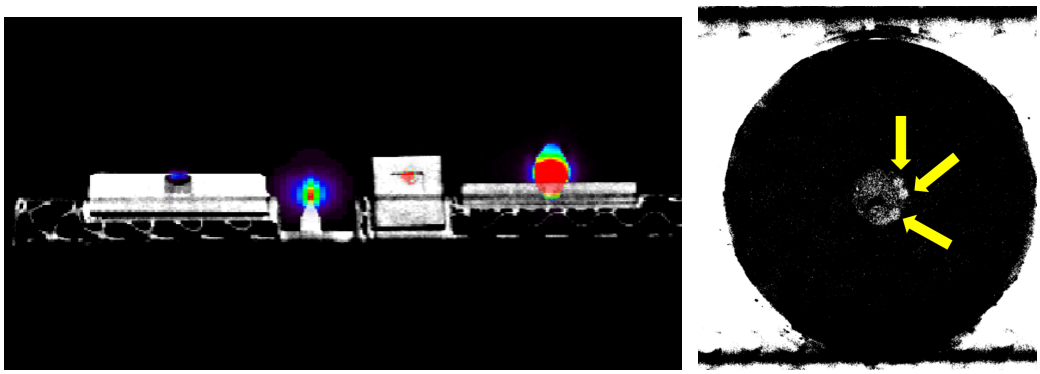

(a) (b)

Fig. 4.14: a) 2D slice of the PET of the point sources overlayed on the high-resolution CT image obtained using the MEDISO scanner. b) The CT slice of a disk sources (first disk from left in 4.14a) showing the radioactive seeds (yellow arrows).

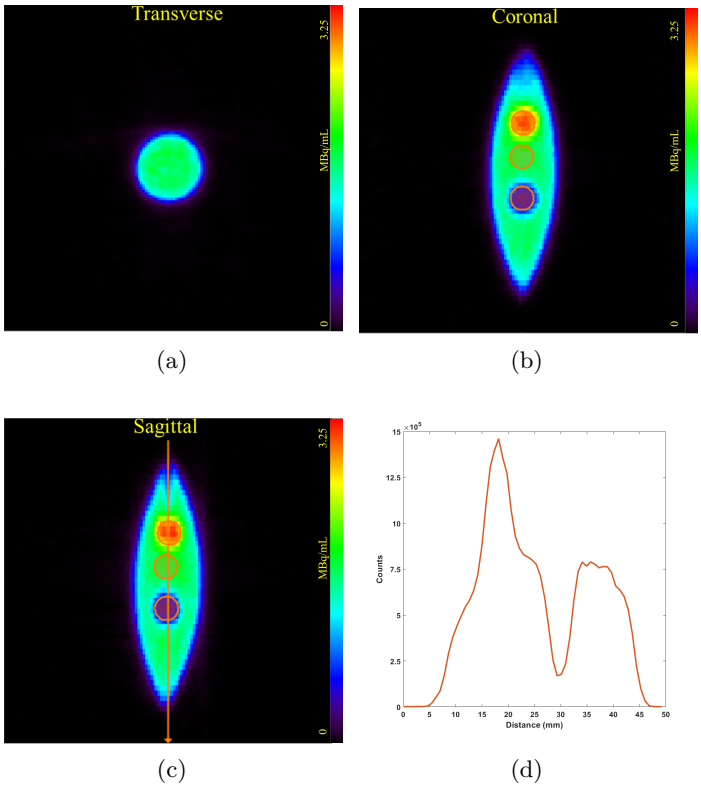

(a) (b)

(c) (d)

Fig. 4.15: ^{18}F-FDG fish-like phantom: (a) Transverse, (b) coronal, and (c) transverse views with ROI contours onto both the hot sphere (top circle) and the empty cavity (bottom circle). The circle in the middle corresponds to the ROI used to calculate the values of Table 4.4. (d) Line profile through the sagittal view [179] © 2024 IEEE.

Table 4.4: Image metrics for the fish-like phantom. The values are in MBq/mL after being corrected for decay.

ROI	Median	Mean ± Std. Dev.	COR
Fish body	1.77	1.76 ±0.06	0.11
Hot sphere	2.90	2.94 ±0.18	0.18
Cold sphere	0.66	0.58 ±0.13	0.50

is presented in Table 4.5. The SBR was 7.3:1 compared to the target of 8:1. The images reveal a nonuniform distribution of activity in certain regions of the phantom background and the presence of hot spots within the inner sphere, which affected the hot sphere to background ratio. The SBR on Day 21 showed a lower SBR of 5.8:1. However, this can be attributed to the low counts, as the scan time was doubled but seven half-lives had passed compared to Day 0. This was not an issue since we were not aiming for a quantitative measurement on Day 21.

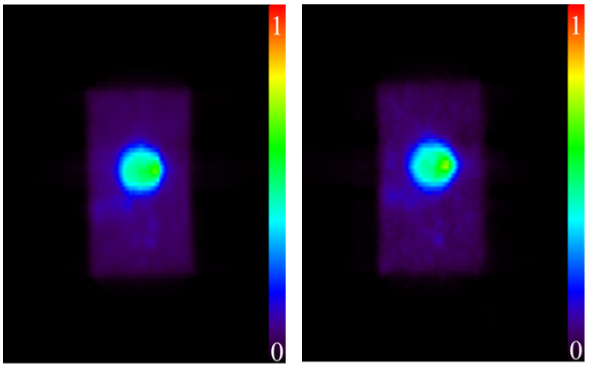

(a) (b)

Fig. 4.16: a) First scan of the ^{89}Zr single sphere phantom, and b) second scan after 21 days.

Table 4.5: Image metrics for the ^{89}Zr single sphere phantom. The values are in MBq/mL after being corrected for decay during measurement.

	Day 0 (4 hours)			Day 21 (9 hours)		
ROI	Median	Mean ± Std. Dev.	COR	Median	Mean ± Std. Dev.	COR
Background	2.64	2.70 ±0.3	0.32	0.36	0.37 ±0.05	0.45
Hot sphere	18.70	19.60 ±0.2	0.39	2.09	2.15 ±0.2	0.36

4.3.7 3D printed NEMA NU 4-2008 IQ phantom

The $IQ_{mermaid}$ phantom was printed without any detectable defects, or damage including the smallest rod (0.5 mm diameter). However, the smallest rod was not visible in the reconstructed PET images as it was smaller than the 1.8 mm spatial resolution of the scanner [193]. Representative slices of the PET image are shown in Figure 4.17.

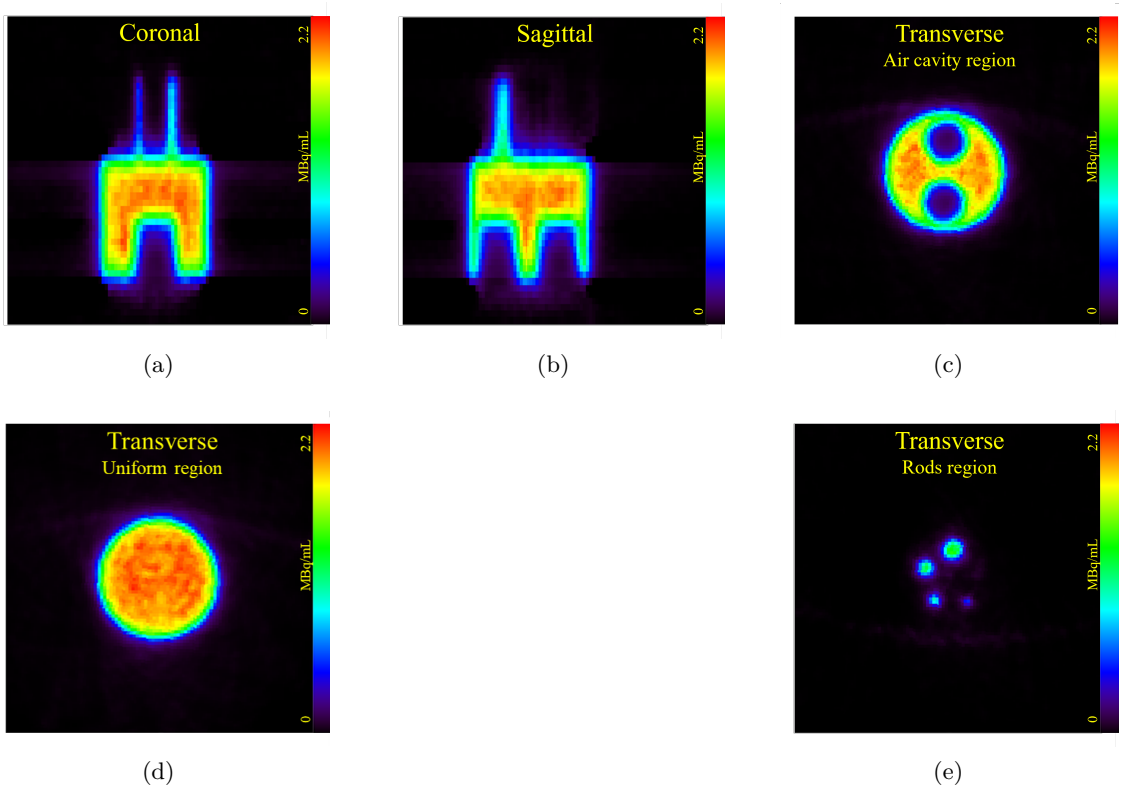

(a) (b) (c)

(d) (e)

Fig. 4.17: ^{18}F-FDG PET images of the $IQ_{mermaid}$ phantom without cover. (a) and (b) show two views of the whole phantom; (c), (d) and (e) correspond to transaxial slices of the cavity region, the uniform region, and the rod region, respectively [179] © 2024 IEEE.

Figure 4.18 depicts PET scans of the $IQ_{mermaid}$ phantom with and without a cover. The cover material, in contrast to air, increases the probability of positron-electron annihilation in regions near the radioactive rods. Given that the total activity in the thin rods is very low, the relative increase in annihilation events within the walls is higher, highlighting the impact of positron range on the detection of smaller objects, as shown by the line profile. Notably, when applying a low image threshold, reconstructed images with and without the cover exhibit relevant differences. In the latter case, the annihilation of positrons escaping from the IQ phantom is observable

within the surface of the scanner bed. Additionally, the visibility of the 1-mm rod is enhanced compared to images without the cover. However, the recovery coefficients of the active rods do not show significant improvement, as illustrated in Figure 4.19. However, The standard deviation is higher for the phantom without a cover. A similar behavior is observed in the uniformity region, where no significant improvement—or degradation—was achieved with the addition of the cover, as shown in Table 4.6. The standard deviation differed by less than 1%.
By comparing the activity within the printed phantom to the activity in the mixture prior to printing, it was found that the mean activity concentration in the uniform region of the $IQ_{mermaid}$ phantom was 7.6% lower than the activity level in the mixture prior to printing.

Table 4.6: Image metrics for the uniformity of the different IQ phantoms. The values are in MBq/mL after being corrected for decay.

Scan	Mean	Max	Min	%STD
^{18}F-FDG $IQ_{mermaid}$ phantom with cover	1.8	2.1	1.5	5.4
^{18}F-FDG $IQ_{mermaid}$ phantom without cover	1.8	2.1	1.5	6.0
^{18}F-FDG printed IQ phantom	1.7	1.9	1.5	4.6
^{89}Zr printed IQ phantom	0.2	0.5	0.1	3.4
^{89}Zr filled IQ phantom	0.2	0.2	0.1	1.5

The $IQ_{mermaid}$ phantom printed with ^{18}F-FDG was compared to a ^{89}Zr printed phantom without a cover, as illustrated in Figure 4.20. Both phantoms exhibit a uniform distribution of activity. The effect observed earlier by scanning the phantom without a cover is now visible through the images of the ^{89}Zr phantom. This phenomenon is attributed to the higher mean positron energy of ^{89}Zr compared to ^{18}F as was observed earlier with the ^{89}Zr two-point phantom.
Figure 4.21 presents the PET scans obtained using the MEDISO scanner of the IQ phantom printed with ^{18}F-FDG and ^{89}Zr. Both printed phantoms were scanned without a cover. Additionally, an official ^{89}Zr-filled NEMA IQ phantom was also scanned. The values of the ROIs in the uniformity region are provided in Table 4.6. The values for the printed ^{89}Zr IQ phantom and the filled phantom were similar (mean value of 0.2 MBq/mL), with the only notable difference being the reported maximum value, where the printed phantom exhibited nearly double the value of the filled one (0.5 and 0.2 for the printed and filled one, respectively). This discrepancy can be attributed to the presence of walls (cover) in the filled phantom, which the printed phantom lacked. This effect was also observed in the RC values shown in Figure 4.22, where the 1 mm rod had a higher recovery (approximately 3%), similar to what was observed with the $IQ_{mermaid}$ phantom with and without the cover. Moreover, both printed phantoms showed higher RC values compared to the filled one. However, the slight differences in RC values are not statistically significant.

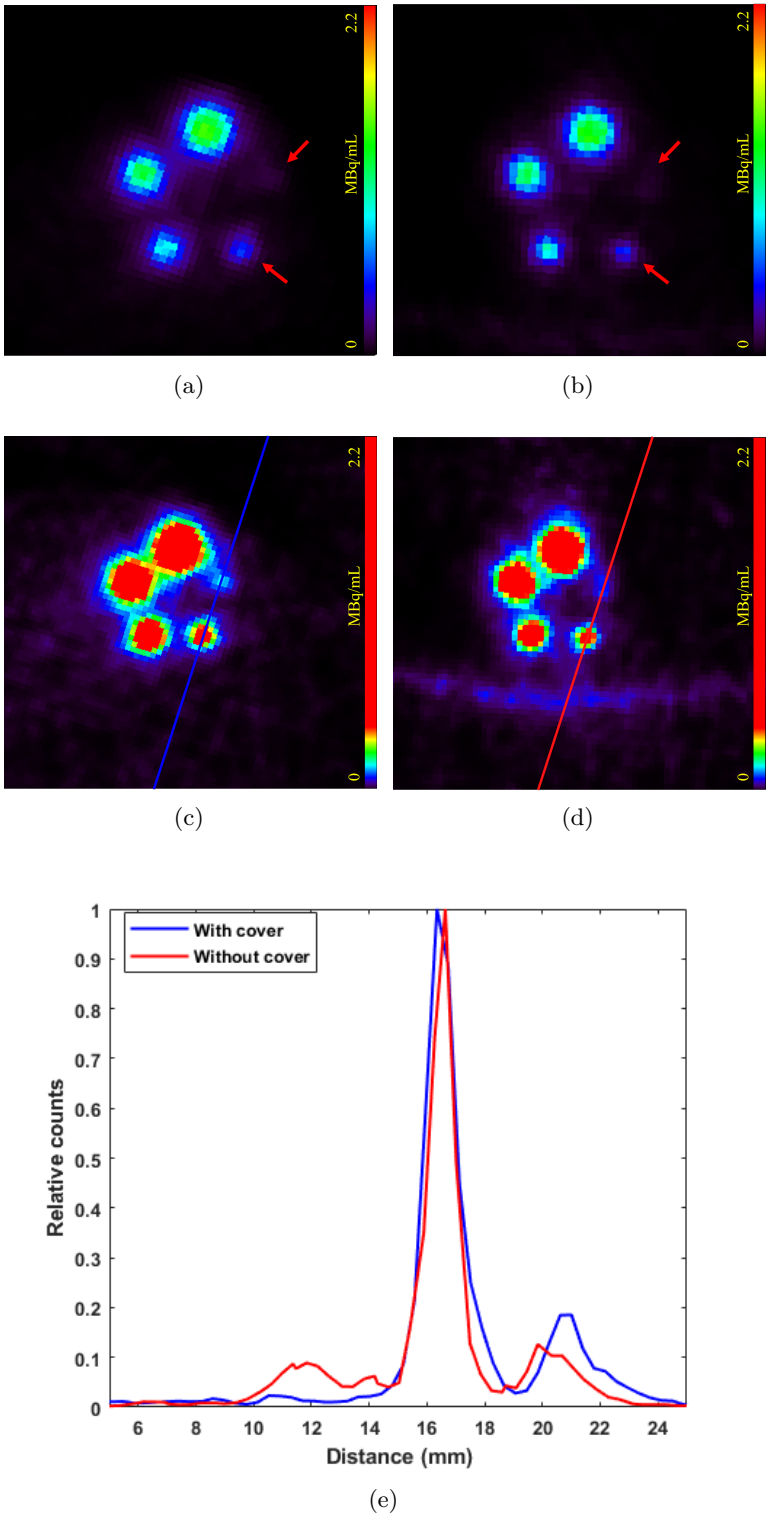

Fig. 4.18: Reconstructed images of the ^{18}F-FDG IQ$_{mermaid}$ phantom with (a) and without (b) cover; (c) and (d) represent the same slices with an upper threshold set to 18% of the intensity maximum to highlight the effects of using the cover. (e) Line profile through the 0.5-mm and 1-mm rods. For better visual comparison, the original images behind (a) and (c) have been rotated to show the same orientation as (b) and (d) [179] © 2024 IEEE.

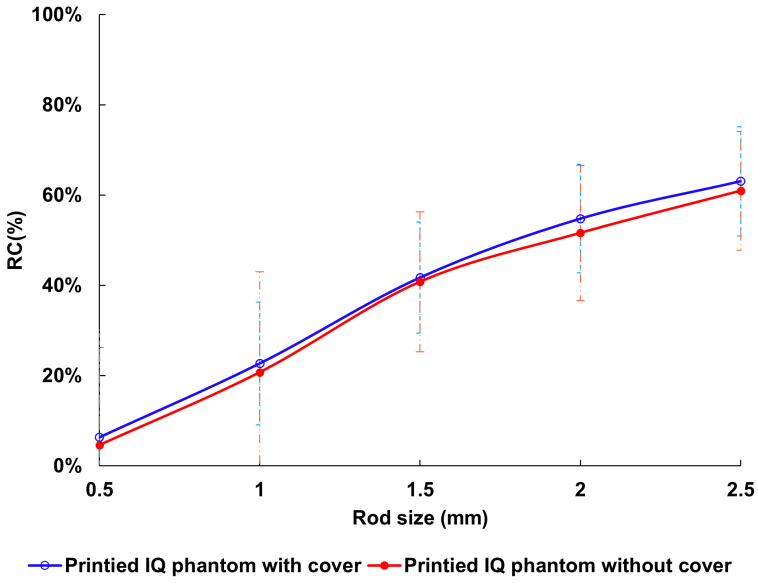

Fig. 4.19: Recovery coefficients for the rods of the $IQ_{mermaid}$ phantom with and without using a cover.

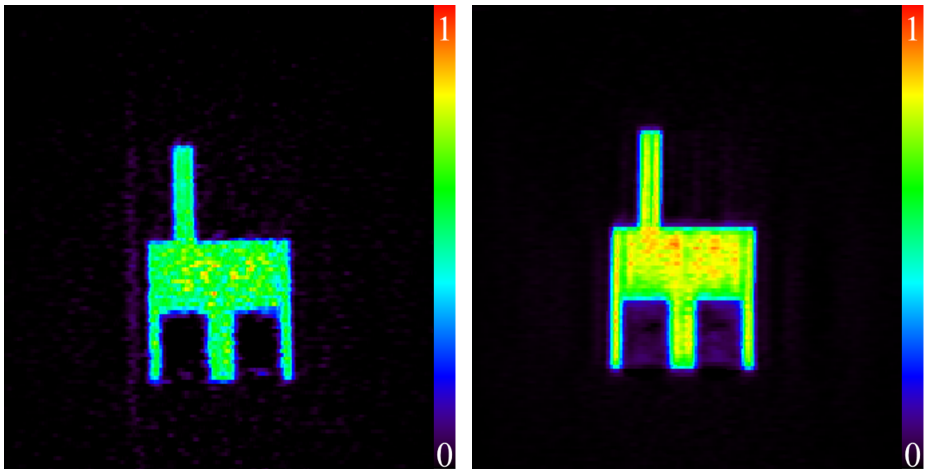

(a) (b)

Fig. 4.20: PET image of the $IQ_{mermaid}$ phantom when: a) Printed with ^{89}Zr, and b) printed with ^{18}F-FDG .

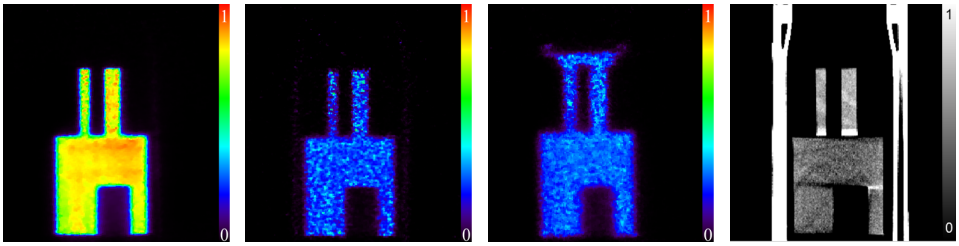

(a) (b) (c) (d)

Fig. 4.21: Comparison of three IQ phantoms; a) 3D prints with ^{18}F-FDG and b) 3D prints with ^{89}Zr, c) the offical NEMA filled with ^{89}Zr, and d) shows a high-resolution CT slice of b). The PET images are normalized to the shown slice of the ^{18}F-FDG phantom.

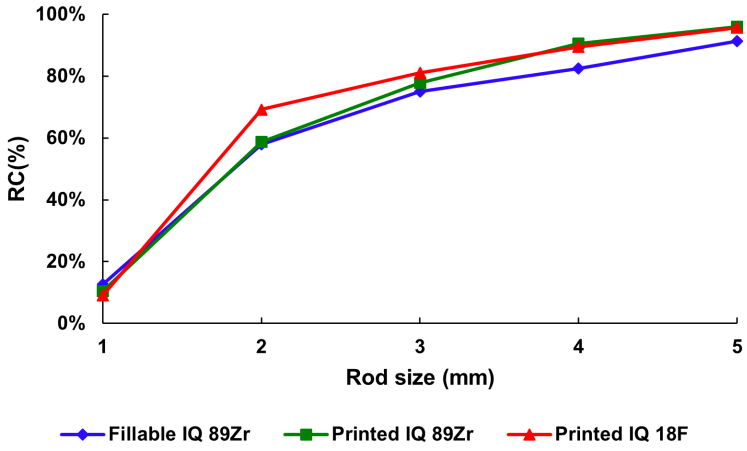

Fig. 4.22: Recovery coefficients for the rods of the IQ phantom for the printed phantom using ^{89}Zr and ^{18}F-FDG and fillable phantom using ^{89}Zr.

The CT scan of the $IQ_{mermaid}$ phantom with a cover revealed three air bubbles with a diameter of 0.68 mm and four with a diameter below 0.068 mm within the uniform region of the phantom (refer to Figure 4.23). The bubbles were manually counted throughout the entire volume scan of the phantom.

4.3.8 3D printed IEC spheres

The switch from ^{18}F-FDG to ^{18}F did not affect the print quality or the mixing process; we were still able to achieve homogeneous phantom prints, as shown in Figure 4.24. The 600-second static scan of the spheres demonstrates uniformity in the background, with no accumulation or hotspots. The measured ratio of the hot sphere to background in the static scan was approximately 3.9:1. The calculated CV for the spheres was 7%.

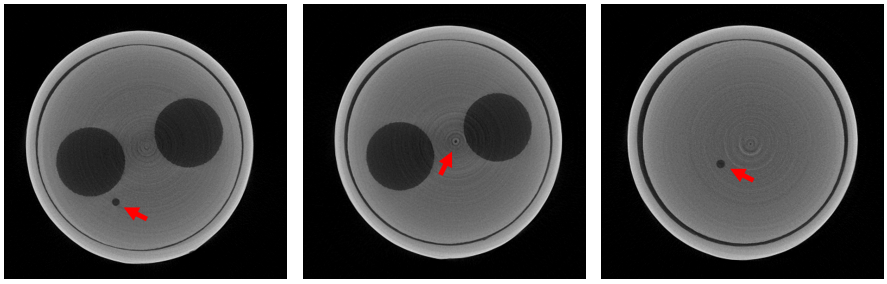

(a) (b) (c)

Fig. 4.23: Selected slices of the reconstructed CT images showing the air cavity (a and b), and the uniform region (c) of the IQ phantom placed within the cover. The first ring is the phantom cover while the second ring (thin black circle) is the air gap required for the tolerance. The red arrows show the air bubbles [179] © 2024 IEEE.

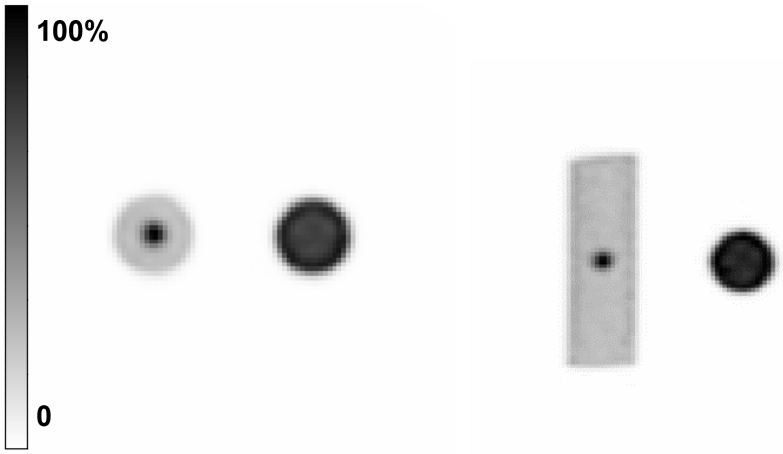

(a) (b)

Fig. 4.24: PET scans: a) Transverse view of the PET image of ^{18}F IEC spheres, while b) shows the coronal view.

Figure 4.25 shows the 3D-printed ^{89}Zr spheres scanned on days 1, 4, 12, 16, and 23, with scan durations of 12, 15, 23, 128, and 1440 minutes (a full day), respectively. Quantitative analysis of the images reveals no significant change in the distribution of ^{89}Zr over time, as evidenced by the consistent image quality from day 1 to day 23. The absence of ^{89}Zr accumulation on the phantom walls is indicating stable and uniform activity distribution within the phantom. Table 4.7 presents evaluation metrics for the background, 1 mm sphere, 28 mm sphere, and the 28 mm halo sphere. The hot SBR consistently measured at 7.4:1 across all time points, reflecting the high stability of the printed phantoms. Quantitatively, the lung error values were within 1.5% from day 1 to day 16, demonstrating minimal variation, with a notable increase to 11% on day 23. This increase in the error value corresponds to a decrease in

^{89}Zr activity, suggesting that lower activity levels contribute to higher measurement variability even when offseted by a longer scan.
Further analysis was conducted for the Quadra across all time points, including calculations of randoms and prompts, as well as an investigation into the impact of the LSO background on the measurements. This was carried out by P. Linder (University of Tübingen, Tübingen, Germany) and is beyond the scope of this thesis.

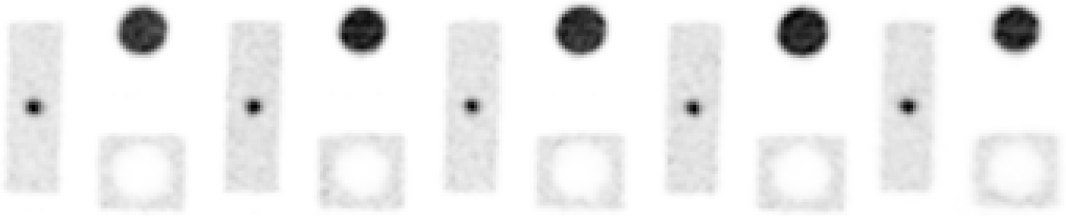

(a) (b) (c) (d) (e)

Fig. 4.25: From left to right, the static PET scan of the 3D printed ^{89}Zr spheres for day 1, day 4, day 12, day 16, and day 23.

Table 4.7: Image metrics for the 3D printed ^{89}Zr spheres phantom.

Scan day	SBR	Lung error	CV
1	7.4	6.3%	0.14
4	7.4	6.5%	0.15
12	7.5	7.0%	0.15
16	7.3	7.8%	0.13
23	7.4	11%	0.13

4.4 Discussion

The procedures outlined in this study have enabled the manufacturing of IQ phantoms suitable for high-resolution PET imaging using both ^{18}F-FDG and ^{89}Zr, applicable for both preclinical and clinical PET scanners.
The ^{18}F-FDG 3D printed two-point phantom outperformed the commercial one according to the two metrics used here. The latter presented an increased intensity in the valley region compared to the 3D printed one. This might be caused by the housing material surrounding the commercial sources in which the positrons might also annihilate, or the annihilation radiation might scatter. The variance in intensities observed between the two points in the commercial one can be attributed to differences in the manufacturing of the sources. This is supported by the source

data-sheet, which indicates an activity error of approximately ±20%. As the phosphor imager can directly detect positrons, the planar images of the 3D printed two-point phantom has a better agrrement of activity compared to the commercial available source (1% and 5% respectively).

It is also worth noting that the cold plate was not sufficiently radioactive to be seen despite being immersed in the radioactive resin mixture during the radioactive source printing process. This was verified through a visual inspection of the PET image of the point source. Furthermore, the absence of broad tails in the line profile of the two-point phantom suggests that there are no hot spots along the line. However, from the PET images of the ^{89}Zr two-point phantom, broad shoulders are shown on both images of the line profile. Furthermore, upon visual inspection of the PET image, the baseplate is detectable. Initially, results suggested that this could indicate contamination of the cold background. However, further investigation of other PET images indicated that this could be a result of positrons annihilating in the cold background region of the phantom, causing it to be visible in the PET image.

The 3D printing of the single-point phantom demonstrated accuracy in locating the source seed at the center of the phantom, compared to commercial point sources. Notably, the source contained a single 1 mm seed, in contrast to commercial sources, which often include multiple seeds that are not centrally positioned within the phantom. For clinical scanners, this discrepancy is negligible since the source size is still smaller than the scanner's resolution. However, for high-resolution preclinical and dedicated scanners, aligning the center of the source phantom with the center of the field of view could pose a challenge.

One limitation of printing point sources is the need for high activity concentration when mixing the radioactive compound with the resin due to the small volume of a point source (1 μL per point in this work). On the other hand, when printing a grid of point sources the increased total volume would be beneficial. The minimum required resin for the Anycubic Photon Mono printer tank to ensure a successful print is 110 mL. However, by modifying the print plate and the resin tank we achieved a minimum of about 180 μL. Moreover, the method of using a pipette to place a single high-activity drop in the tank at the position of the source to be printed, as opposed to filling the minimum volume required for the tank, yielded promising results. This approach produced a relatively high-activity point source within a very small volume (approximately 1 μL) when printing the single point phantom.

The process of pausing the printer demanded our continuous attention and presence to ensure the pause occurred at the correct layer, thereby achieving the desired size of the point source in the design. To streamline this process in the future, we propose modifying the G-code of the printer to automatically halt at the desired layer. This modification would help mitigate human error, preventing the printer from pausing a layer too quickly (resulting in an active layer on the cold background

before printing the point source) or too late (resulting in a smaller active region of the point source).
The method used to print the two point sources onto a cold background was also effective for printing a phantom with regions of different activity concentrations, as shown from the initial results of the fish-like and single sphere phantoms. This approach opens the door to more complex phantoms designed for specific studies, such as 1-3 cm tumors (represented as hot spheres) within the lung (cold background). This method was also extended to clinical scanners with larger spheres, as demonstrated with the IEC phantom spheres. Additionally, it could be used to replace fillable phantoms, such as the Abdo-Man 3D-printed anthropomorphic phantom [194].
For the fish-like phantom, the preparation time was approximately one quarter of the half-life of ^{18}F. In subsequent experiments, we modified the heating step to decrease preparation time by pre-heating the resin before mixing. Eventually, we eliminated resin heating altogether. These adjustments were motivated by observations of resin-induced warping of the printer tank foil, particularly relevant when working with radioisotopes of shorter half-life, although less critical when utilizing ^{89}Zr or other long-lived radioisotopes. An alternative approach to reduce print time involves minimizing the duration of washing phantoms with the 2-propanol solution. Contamination test results underscored the necessity of a second wash solution to maintain surface contamination below acceptable limits, defined as a maximum of three times the ambient background. These findings are pertinent to long-lived radioisotope 3D printing planning, particularly concerning radioactive waste management. However, a preliminary test revealed that equivalent surface decontamination of the uncured surface can be achieved by increasing the stirring speed, thereby reducing the duration of the first wash to three minutes and the second wash to two minutes. Further studies are required to optimize the washing parameters to achieve the most efficient timing. With these adjustments, phantom manufacturing time can be decreased from 30 minutes to 20 minutes.
The single sphere phantom showcased the feasibility of 3D printing radioactive phantoms using ^{89}Zr, as it effectively prevented the adherence of ^{89}Zr to the phantom walls. This was evidenced by a re-scan of the phantom, which showed no changes in the activity distribution even after three weeks. However, a non-homogeneity was observed within the printed phantom. The average ratio of the hot sphere to the background was 7.3:1, while the mixture was 8:1. This discrepancy was attributed to the precipitation of ^{89}Zr from the liquid resin during the printing process. This issue served as the impetus to explore a new method of mixture, which was subsequently adopted in later prints with ^{89}Zr.
Utilizing Mixture$_{Zr}$, we successfully 3D printed the IQ phantom with ^{89}Zr and compared the print quality to both the fillable phantom and the 3D printed phantom with ^{18}F-FDG. Both printed phantoms were produced without covers. The RC

values of the 5 mm rods closely matched those of the fillable phantom, with relative differences of 4% for the ^{18}F-FDG and 5% for the ^{89}Zr, respectively. Images of the fillable phantom revealed a hot spot near one of the screws of the IQ phantom, attributed to an error made during the filling process. This supports our earlier assertion regarding the potential for human error in the preparation of fillable phantoms, even by trained personnel.

As for the current method of hand-shaking the mixture, to ensure a homogeneous activity distribution without exposing the hand to absorbed radiation dose, alternative methods should be considered. One possible solution is the use of a high-speed magnetic stirrer to ensure proper mixing. Another approach could be high shear mixing combined with ultrasonics [195].

Furthermore, we successfully printed the $IQ_{mermaid}$ phantom, which contains a submillimeter region with uniform activity. This achievement is notable as the smallest 3D printed structures reported in the literature were 2 mm [166] and 7 mm [167]. This outcome addresses the challenging issue of filling very thin rods. The smallest rod (0.5 mm) was not visible in the images due to the limited resolution of the PET scanner. Additionally, the low activity level (3.7 kBq in 0.98 mm^3 compare to the 106 kBq in 0.03 mL of the two-point phantom) within the rod makes it difficult to detect without the use of high-sensitivity scanners or extended scan durations. The activity concentration determined from the reconstructed image of the IQ phantom differed from the activity concentration of the resin by 7.6% after applying decay correction for the time between the measurement in the activimeter and the scan time.

The $IQ_{mermaid}$ phantom utilized in our study was a scaled-down replica of the NEMA IQ phantom, inclusive of the two smallest rods measuring 1 mm and 2 mm, akin to the official NEMA phantom. Measurements obtained from the printed IQ phantom closely aligned with those from the official NEMA phantom, as documented in [193]. Specifically, for the 1 mm rod, measurements were 0.23 for the printed IQ phantom with a cover and 0.17 for the fillable official NEMA phantom. Correspondingly, for the 2 mm rod, measurements were 0.55 and 0.48, respectively.

In addition, alongside the limitations inherent in the PET scanner, another potential source of error stems from the activimeter utilized to measure activity in the syringe. This procedure demands precise positioning of the syringe within the bore. In our measurements, we were obliged to employ a non-standard syringe due to the high viscosity of the resin, rendering the use of a standard syringe impractical. These factors collectively have the potential to introduce errors, thereby impacting the accuracy of the reference measurement.

In this study, we filled both cylindrical cavities of the IQ phantom with air, diverging from the NEMA NU 4-2008 protocol [144] which stipulates that one cavity should contain water. While it was feasible to add a 3D-printed solid cylinder or a water-

filled cylinder, this would have escalated the radiation exposure due to the need to handle the radioactive component for cylinder insertion. This was carried out with our primary objective being the investigation of the printing process, rather than characterizing the printed phantom for scatter correction.
The PET scans of $IQ_{mermaid}$ without and with cover show similar metrics, with slightly higher RC values (4.9%) and smaller standard deviation (0.1%) when using a cover. Compared to air, the cover material increases the probability of positron-electron annihilation in the regions close to the radioactive rods. As in the thin rods the total amount of activity is very low, the relative increase is much more significant.
The slightly higher RC values are not statistically relevant as they can be a consequence of the longer scan time required when using the cover aimed to compensate for the decay time between the two measurements. Another factor that could affect the results is positron range, as without the cover positrons emitted from the surface of the active regions can travel up to 1 meter in air [192]. This effect is observed in the case of the smallest rod, where it becomes more apparent when the cover is used. Also the scanner bed was faintly visible in the PET reconstructed image without the cover. The annihilation of positrons escaping from the IQ phantom can be observed within the surface of the scanner bed. This conclusion was reinforced when we scanned the IQ phantom and the fillable phantom with ^{89}Zr, given that ^{89}Zr positrons exhibit a higher energy and positron range. This so-called shine-through effect has been observed in clinical PET mainly for high-energy positron emitters [196, 197], but also for ^{18}F-FDG [198].
The ability to produce nuclear imaging phantoms with and without walls can help to better understand the role of the non-radioactive walls in conventional phantom measurements. Additionally, 3D printing phantoms allows for a more accurate simulation of in vivo imaging conditions, as the activity distribution within an organ accounts for radionuclide deposition along the organ walls. This contrasts with current fillable phantoms, which have non-active walls [167].
Air bubbles within the $IQ_{mermaid}$ phantom were visible in the CT images. These bubbles were excluded from the Region of Interest (ROI) owing to their proximity to the air cavity region and the last slices of the homogeneous region. Furthermore, their diminutive size rendered them undetectable in the PET image. The air bubbles formed during the print as the printing plate was moving in the Z-axis where air pockets are trapped between the printer screen and the phantom. One well-established method when using SLA or LCD technology is tilting the phantom during printing by 30 degrees while using support structures. This will help avoid air pockets during the print especially when printing large phantoms. Support structures are small rods that connect the printing plate to the surface of the overhang phantom, i.e., part of the phantom not placed on the printing plate. However, air bubbles with

a volume of significantly less than 1 μL in a viscous medium do not move even when the structure is tilted by 30 degrees as they remain stuck. If these bubbles pose a problem, we could try degassing the resin under reduced pressure. Additionally, the support structures must be removed from the phantom before scanning, which would increase print time, require more post-processing, generate more waste, and, most importantly, lead to higher radiation exposure. Another method that can reduce the air bubbles is to reduce the speed along the Z-axis during the print and increase the retraction distance (the distance the printing plate is moved upwards after printing each layer); however, this will increase the print time by a factor of three or more, so it is not suitable for short-lived radioisotopes such as ^{18}F.

The image of the fish-like phantom body revealed a defect caused by warping. This occurred due to printing the phantom without support structures while the printer temperature was elevated, likely due to UV irradiation during the print process. This problem was particularly noticeable when printing the relatively large IEC phantoms. Even with the implementation of support structures, the printed parts experienced warping and detachment from the printing plate due to excessive heat. To mitigate this issue in the future, we propose either cooling down the printer between print jobs or enhancing continuous cooling and ventilation of the printer.

We used the Quadra to examine the 3D-printed IEC spheres, demonstrating a uniform activity distribution with ^{18}F, consistent with our results from previous phantoms prepared with ^{18}F-FDG. Since ^{18}F was mixed with saline water instead of FDG, this may have affected the mixing and chemical bonding with the resin used in the study, as it might not interact with the resin in the same way. Consequently, the water-washable resin was not used. However, this did not pose an issue, as we were still able to achieve a uniform activity distribution within the mixture. This highlights our capability to produce phantoms without the need for an expensive FDG kit, significantly reducing the costs associated with preparing 3D-printed phantoms. The printed phantoms further demonstrated the feasibility of employing a wall-less phantom for clinical scanning studies. Notably, we observed a 4:1 activity ratio between the hot sphere and the warm background. These were the first printed phantoms we measured in a clinical scanner.

Lastly, the ^{89}Zr IEC spheres demonstrated the Quadra's capability to acquire high-quality images using a low-activity source. A scan with such a low dose could not have been performed previously using ^{18}F, as a few hours of measurement would already include the half-life of ^{18}F. Additionally, utilizing ^{89}Zr in a fillable phantom would result in variations in images over different days due to the adherence of ^{89}Zr to the phantom walls. The printed spheres exhibited uniform activity distribution, and delayed scans revealed no evidence of ^{89}Zr adherence to the walls of the phantoms, even after 23 days. The adherence of the metastatic radioactive source to the walls of the phantom was prevented due to the solid nature of the printed phantom,

hindering the movement of liquid particles within the phantom. Increasing the scan duration improved image quality, particularly when the activity decreased to as low as 0.02 kBq/mL, making it challenging to obtain measurable image quality within a 24-hour scan.
Future work can focus on integrating the low-dose images obtained from the ^{89}Zr IEC spheres with the Quadra digital twin developed in Section 3. As the LSO background from the scanner affects quantification, by utilizing the same STL files used for printing the phantom, we can simulate the scan with the digital twin. This approach offers the advantage of adding or disabling the LSO background using the R2LM tool, allowing us to study the effect of the LSO background on low-dose imaging studies.
One issue not addressed in the presented work is the positron range in the 3D-printed point source. The imaging of the printed point sources was done without a medium (surrounded by air), unlike the commercial source, which was placed within PMMA or plastic. This results in positrons having a longer range in the printed point source before annihilation, leading to higher PVR values. Future studies should replicate the presented work while placing the printed point source in a medium, such as water or PMMA.

4.5 Conclusion

Utilizing an affordable desktop 3D printer, we have successfully achieved uniform activity distributions in our 3D printed radioactive phantoms. Additionally, we manufactured not only standardized phantoms, but also customized phantoms featuring distinct regions with varying activity concentrations. These customizations would otherwise be difficult to reproduce using fillable phantoms. Moreover, we were able to produce phantoms ranging from submillimeter to 9 cm in size, suitable for both clinical and preclinical applications.
Furthermore, 3D printing phantoms have demonstrated effectiveness in preventing the adherence of ^{89}Zr to the phantom walls, as evidenced by delayed scans even after 23 days. These findings contribute to enhancing current calibration methods for low-dose immuno-PET, enabling stable phantom scans over several days. The use of both ^{18}F and ^{89}Zr provided a half-life that was short enough to prevent long-term contamination, yet long enough to accommodate the necessary mixing and printing procedures.
Building upon our results, our next steps will involve 3D printing using longer-lived radionuclides, such as ^{22}Na or ^{68}Ge, which are commonly used isotopes for PET quality control phantoms. Our ultimate goal is to develop durable radioactive phantoms that can be utilized over extended periods, ranging from several days to months, or even years with the use of ^{22}Na (with a half-life of 2.6 years). This

longevity will enhance the reliability and consistency of calibration and evaluation studies. Leveraging the advantages of 3D printing technology, these phantoms could encompass a wide range of designs, from simple geometries to intricate and realistic models mimicking blood vessels, organs, etc., applicable to both human and small animal studies. In particular, specific phantoms reproducing non-standard small laboratory animals (e.g., zebrafish).

Another approach would be to extend this technology to other nuclear imaging modalities, such as 3D printing radioactive phantoms for PET dosimetry of ^{90}Y, and for SPECT imaging and dosimetry with ^{177}Lu. Additionally, future studies may explore the utilization of new types of flexible resin. This would enable the 3D printing of phantoms with not only reduced rigidity but also a degree of flexibility. These flexible phantoms could be deformed under pressure to produce images with different shapes. This capability could serve as a tool for generating data for AI training. While current rigid phantoms may be easily learned by AI, using a single 3D printed phantom to produce multiple images with deformation would pose a greater challenge for AI networks, encouraging the network to focus on learning the properties of the phantom rather than specific image characteristics.

In conclusion, our study demonstrates the successful application of 3D printing technology, particularly in low-dose PET imaging for both high-resolution preclinical systems and clinical scanners. While this technology has shown great promise, there are still numerous opportunities for further advancement, including its integration with AI. In the next section, we will utilize the low-dose ^{89}Zr IEC sphere data to implement an AI-based image denoising application, with the goal of enhancing image quality in delayed scans.

5 PETAL-3D

This section is an extension of the work presented at the Ultra-Low Dose PET Imaging (UDPET) Challenge, 2023 IEEE NSS/MIC/RTSD 2023, Vancouver, Canada and an abstract at the 10th Conference on PET, SPECT, and MR Multimodal Technologies, Total Body and Fast Timing in Medical Imaging (PSMR2024), 2024, Isola d'Elba, Italy. Moreover, the work has been submitted to IEEE Transactions on Radiation and Plasma Medical Sciences journal.
Mohammad Tanzil Idrisi from Beloit College, USA, contributed to the development of the anatomically guided 3D U-Net (AG-UNet) during a summer internship as part of the German Academic Exchange Service (DAAD) Research Internships in Science and Engineering (RISE) program 2024, in which I served as the principal investigator (PI) for the project (Luebeck EN CS 4796).

Contents

5.1 Introduction

In this section, our objective was to implement PETAL-3D for image denoising at the image level for several low-dose imaging applications. PETAL-3D had undergo training and application using two datasets with varying DRF levels. Following the network's training, its performance was evaluated through ^{90}Y imaging and low-dose ^{89}Zr imaging. Lastly, we aimed to investigate the current re-framing method as well as the influence of utilizing high-activity scans for generating neural network training pairs by employing the developed Quadra digital twin introduced in Chapter 3.

5.2 Materials and Methods

5.2.1 Training PET data

Two datasets with varying DRF levels, namely the *Ultra Low Dose PET (ULDPET) challenge* training dataset ($Dataset_{ULD}$)[1] [72] and a low-dose dataset ($Dataset_{LD}$) [2], were employed for training and testing the proposed neural network. To assess the network's performance, images from these datasets, as well as from ^{90}Y phantom and ^{89}Zr 3D printed phantom scans were used. A list of the data used is shown in 5.1. All patient data used in this study were anonymized by the provider of the data to ensure the confidentiality and privacy of the individuals or entities associated with the patients.

Table 5.1: List of data used for training and testing PETAL-3D

Data	Scanner	Training	Testing
ULD	Quadra and uEXPLORER	X	X
LD	Quadra	X	X
^{90}Y phantom	Quadra	-	X
^{89}Zr IEC Spheres	Quadra	-	X
Sampling study	Quadra Digital Twin	-	X

5.2.1.1 Ultra low dose PET challenge training dataset

$\text{Dataset}_{\text{ULD}}$ were provided by the University of Bern, Dept. of Nuclear Medicine and School of Medicine, Ruijin Hospital [72]. $\text{Dataset}_{\text{ULD}}$ had 1447 subjects of whole-body

[1] `https://udpet-challenge-2024.github.io/`

PET imaging, acquired from Quadra (total number of subjects is 387) and United Imaging uEXPLORER (total number of subjects is 1060), will be referred to as uEXPLORER. The dataset included ^{18}F-FDG, ^{18}F-PSMA, ^{68}Ga-DOTA-TOC, and ^{68}Ga-DOTA-TATE PET examinations. Only the reconstructed images corresponding to low-dose PET with specific DRF levels were provided to us. These images were obtained from the full-dose data through re-framing. The DRF level used in the training were 1, 2, 4, 10, 20, 50, 100 corresponding to the full dose image 100%, 50%, 25%, 10%, 5%, 2% and 1% of the data respectively. No information was provided regarding the reconstruction parameters for the dataset. Given the large image volume ($440 \times 440 \times 645$ with a $1.65 \times 1.65 \times 1.65$ mm^3 voxel size, and $360 \times 360 \times 673$ with a $2.73 \times 2.73 \times 2.73$ mm^3 voxel size for Quadra and uEXPLORER, respectively) and limited GPU computational power, only a subset of the 1447 subjects was utilized for training and evaluating the network. Specifically, for training the network, data from 200 patients were randomly selected, with 100 subjects from each scanner. Figure 5.1 shows an example of both Quadra and uEXPLORER dataset with different DRF levels.

5.2.1.2 Low dose PET training data

Dataset$_{\text{LD}}$ corresponds to Quadra scans of patients who received a dose of 3 MBq/kg of ^{18}F-FDG. The re-framed dataset was provided to us as images of DRF 6, 12, and 24, corresponding to 17%, 8%, and 4% of the full dose [2]. The re-framed dataset was created by selecting an initial portion of the list-mode data, corresponding to an activity level equivalent to the low-dose image, while accounting for radiotracer decay. Calderón et al. highlighted that even with the use of UHS mode (MRD322), the quality of DRF24 images remained poor, impacting diagnostic reliability. The data was reconstructed using the *e7 tools* software employing the OP-OSEM algorithm with four iterations and five subsets. PSF modeling, TOF information; attenuation correction using the diagnostic CT was also incorporated. Only data reconstructed using the UHS mode were included for training and evaluating the neural network. No post-reconstruction filters were applied. Further details regarding the dataset and the reconstruction parameters can be found in [2]. The dataset comprised of only 27 patients. To train the network, we randomly selected data from 20 patients. Figure 5.2 shows an example of a dataset with different DRF levels.

5.2.2 Test PET data

The network's performance was assessed in the following scenarios: (A) Dataset$_{\text{ULD}}$: A separate group of 30 patients examined with each scanner, unseen during training, subdataset was employed; (B) Dataset$_{\text{LD}}$: the remaining 7 patients were reserved for testing, ensuring that the network had not been exposed to the testing data during the

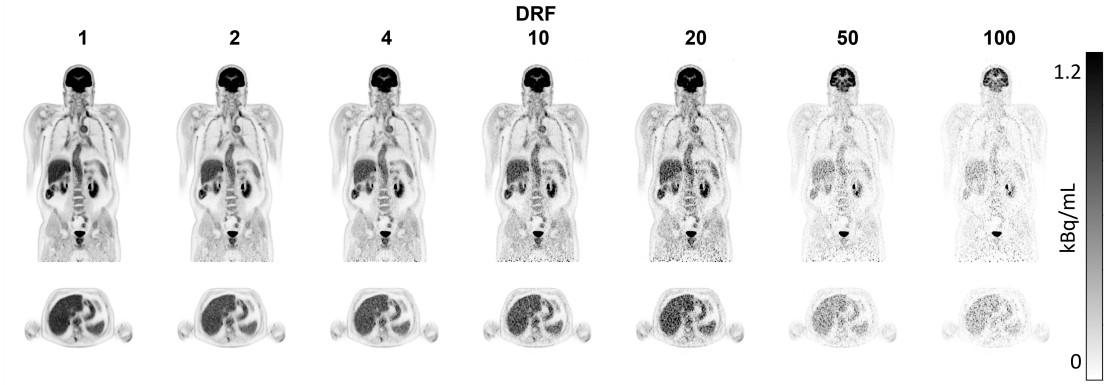

(a)

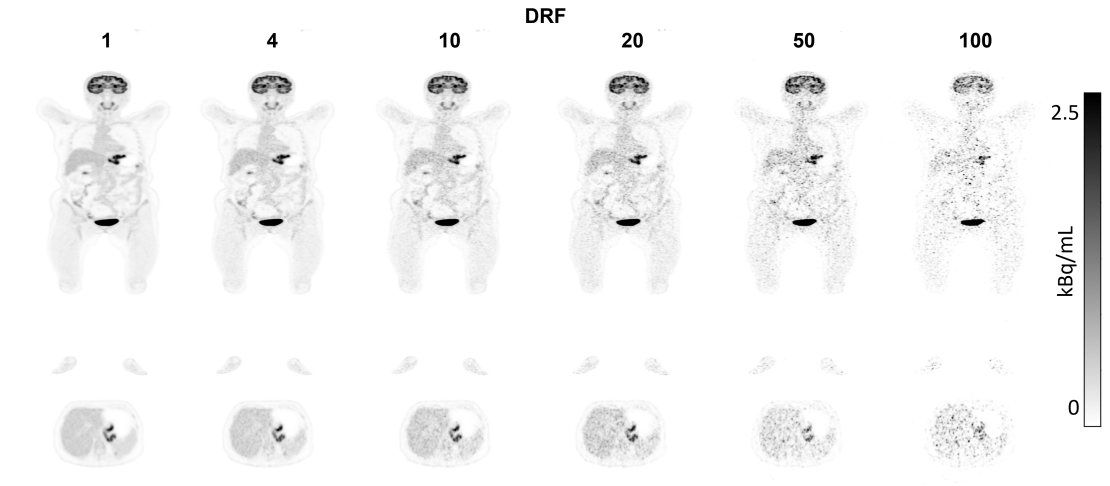

(b)

Fig. 5.1: A sample of $\text{Dataset}_{\text{LD}}$ showing a) Quadra data with DRF1,2,4,10,20,50, and 100 while b) uEXPLORER data with the full dose and starting from DRF4 up to 100.

training process, and (C) low-dose imaging from ^{90}Y phantom images were utilized, and (D) low-dose imaging of the ^{89}Zr IEC printed phantom, as described below. The nomenclature $PETAL\text{-}3D_{[training,test]}$ will be used henceforth, with *training* being ULD or LD, indicating the two possible training datasets, and *test* being ULD, LD, ^{90}Y, or ^{89}Zr.

5.2.2.1 ^{90}Y phantom data

We have tested PETAL-3D, trained with $\text{Dataset}_{\text{LD}}$, in a very different imaging scenario. Namely ^{90}Y PET of the AbdoMan phantom, a 3D printed anthropomorphic AbdoMan phantom containing a warm background and four hot spheres (20 mm,

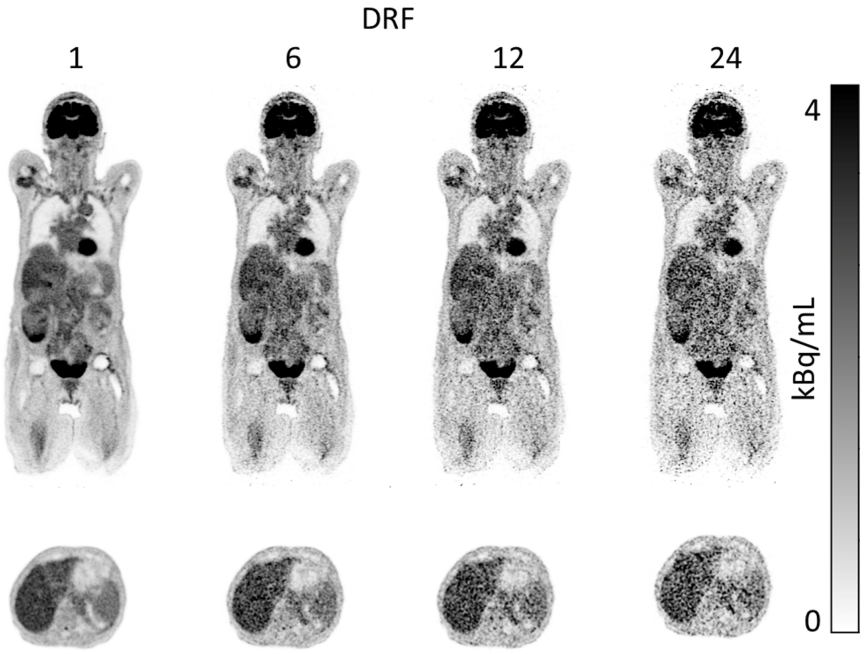

Fig. 5.2: A sample of the $\text{Dataset}_{\text{LD}}$ with DRF 6, 12, and 24 © 2024 IEEE.

30 mm, 40 mm, and 50 mm in diameter) [194]. The activity concentration in the hot spheres was 1103 kBq/mL, while the warm background had a concentration of 299 kBq/mL. The total activity of the phantom was 5.3 GBq, with a SBR of 3.69:1. The scan duration for the high-dose image was 1440 minutes, whereas the low-dose images were obtained after data re-binning and subsequent reconstruction„ with scan durations of 30 minutes and 20 minutes respectively. The 30 minutes and 20 minutes, scans would be equivalent to DRF48 (1440/30), and DRF72 (1440/20), respectively. Further details regarding the phantom and the scanning process can be found in [4]. Figure 5.3 shows the phantom and an obtained PET image.
PETAL-3D was utilized to denoise the phantom images. The objective was to generate reconstructed images equivalent to those obtained from the high-dose 1440-minute scans using low-dose phantom data. This is particularly relevant in ^{90}Y PET, where typical scan durations are limited to around 30 minutes. It is not feasible to subject patients to prolonged scanning periods to achieve high-quality images, especially given the low branching ratio of ^{90}Y [66]. The reconstructed was done as for $\text{Dataset}_{\text{LD}}$. However, the OP-OSEM algorithm was with two iterations and five subsets.

5.2.2.2 ^{89}Zr phantom data

PETAL-3D was also applied to denoise images of the 3D-printed ^{89}Zr IEC spheres. The ^{89}Zr spheres were scanned five times: on day 1 for 12 minutes, day 4 for 24

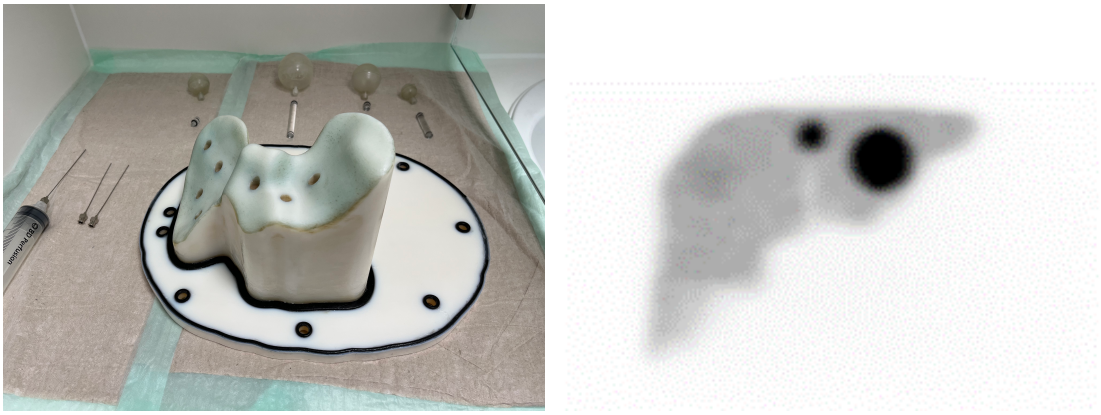

(a) (b)

Fig. 5.3: a) Dissambled 3D printed anthropomorphic AbdoMan phantom, and b) a 1440 min PET scan (DRF1) of the phantom showing the 4-mm and 2-mm spheres © 2024 IEEE.

minutes, day 12 for 128 minutes, day 16 for 301 minutes, and lastly on day 23 for 1440 minutes (see Section 4.2.4 for more details). Starting from day 12, the scans were re-framed for 10 minutes and 30 minutes. The 10-minute duration was used to compare the degradation of image quality over time, while the 30-minute duration represented the standard scanning time for patients injected with such low-activity sources. We applied PETAL-3D for denoising both the 10 and 30 minute scan images to compare them with the Day-4 scan. Furthermore, we examined the performance of PETAL-3D when using a 10 minute scan and assessed its similarity to the results obtained from the 30 minute scan. The data was reconstructed using the *e7 tools* software following the same parameters as mentioned in Section 5.2.1.2 above.

5.2.3 Sampling study with PETAL-3D

As alluded to earlier in Section 2.3.2.2, AI-based supervised learning approaches for denoising require paired data, specifically low-dose/high-dose pairs, to train the network.

Hence, the focus of this study was to assess the effectiveness of the method used for generating low-dose/high-dose pairs for AI training when using $\text{Dataset}_{\text{LD}}$. The Quadra digital twin was utilized to create two datasets containing such pairs, using an XCAT phantom with voxel size of $3.1 \times 3.1 \times 3.1$ mm^3 [176]. The first dataset comprised high-dose images obtained from a 300-second simulated scan of a patient with a standard Body Mass Index (BMI) injected with an activity of 3 MBq/kg. Subsequently, these images were re-binned to generate corresponding low-dose images. Specifically, the low-dose images were generated at DRF6, DRF12, and DRF24, employing the same re-framing technique as described in $\text{Dataset}_{\text{LD}}$ (see 5.2.1.2).

For a patient scan of 160 MBq, the scan time would be 300, 34, 22, and 12 seconds for DRF1, DRF6, DRF12, and DRF24, respectively. We refer to this dataset as the 're-framed low-dose' dataset, which represents the typical data used for training, validation, and testing in image denoising methods. The re-framed data is shown in Figure 5.4.
The second dataset consists of three simulations with low injected activity corresponding to DRF6, DRF12, and DRF24 (0.5 MBq/kg, 0.25 MBq/kg, and 0.125 MBq/kg, respectively). Each simulation was conducted for simulated 300 and 600 seconds scan. This dataset will be referred to as the 'injected low-dose' dataset. This dataset should reflect real-world applications where low-dose imaging is used.
The output of re-framed low-dose and injected low-dose simulated scans were compared by calculating prompts, trues, and randoms ratio for each simulation. Furthermore, the injected low-dose simulations were used to assess the impact of increasing the scan time on mitigating the low image quality resulting from the low-dose scan. The advantage of using the Quadra digital twin lies in the ability to isolate and study the effects of low-dose scanning without the influence of other factors that could degrade image quality, such as CT scan misalignment for scatter correction or motion blur.
Finally, PETAL-3D$_{LD}$ was utilized to denoise the reconstructed images from both datasets. This allowed us to assess the network's performance when applying PETAL-3D to both the injected low-dose and re-framed low-dose simulations. The evaluation was conducted using global metrics and local metrics as discribed in 5.2.5.

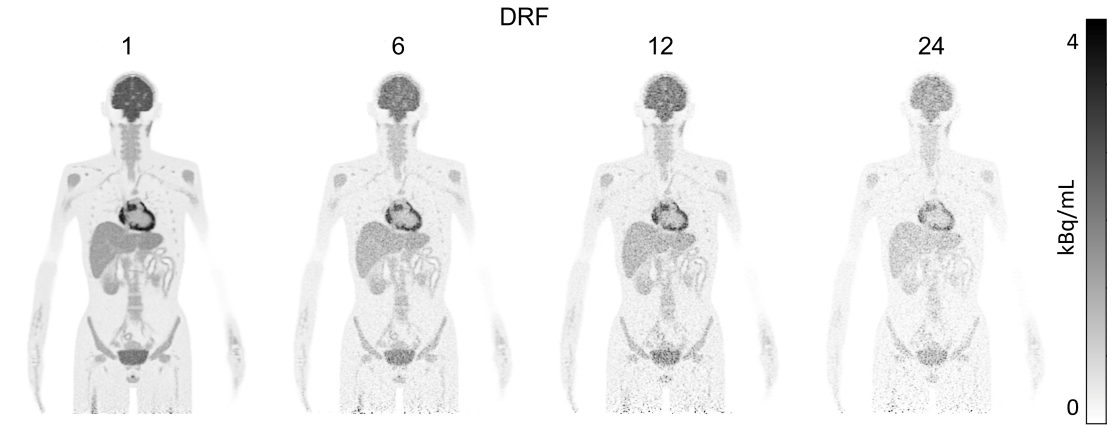

Fig. 5.4: Reconstructed images for the simulation of high-dose XCAT phantom (DRF1) followed by the re-framed data with DRF 6, 12, and 24.

5.2.4 Network Architecture

Drawing inspiration from the diffusion model, PETAL-3D operates by processing the input data through multiple U-Net networks. The hypothesis proposes that this approach facilitates gradual noise reduction in the image, resulting in enhanced performance compared to employing a single 3D U-Net trained solely on a single pair of low-dose/high-dose or mixed-noise data. The selection of a 3D U-Net over 2D or 2.5D U-Net is supported by Lu et al.'s findings, which demonstrate superior image quality relative to Gaussian filtering and CT-guided NLM filtering, as well as reduced SUV bias [199].
PETAL-3D consists of six 3D U-Net convolutional neural networks designed for three-dimensional image denoising. The architecture of the proposed 3D U-Net is shown in Figure 5.5. The network image input was $64 \times 64 \times 64$ voxels. It follows a U-shaped encoder-decoder structure with skip connections, facilitating the capture of both local and global contextual information. The network was implemented using the PyTorch library [200]. In the encoder part, the input volume undergoes a series of convolutional operations with increasing numbers of output channels. To downsample the feature maps after each convolution, max pooling layers were employed for extracting hierarchical features. The decoder section consists of deconvolutional layers for upsampling the feature maps. In addition, subsequent convolutional layers process and concatenate with the corresponding feature maps from the encoder through skip connections. The concatenated feature maps help to maintain spatial information.
The final convolutional layer had the softmax function disabled, as the objective of the network is denoising rather than producing a segmentation mask, as typically done in image segmentation tasks for which the U-Net architecture was originally developed [142, 143]. Each convolutional operation is followed by ReLU activation, and dropout is applied for regularization. Adam optimizer [140] was used for updating the parameters θ of the neural network based on the gradients of the loss function. The learning rate of 0.001 was selected empirically. The initial experiments utilized MSE and L1 loss functions. However, literature has shown that the MSE loss function tends to produce blurry images [141, 201]. Consequently, only the L1 loss function was considered in our subsequent experiments. Padding was applied throughout the forward pass to maintain spatial dimensions after convolutional operations. Our initial results showed that padding with zeros caused streaks in the images at the borders of the patches. To mitigate this artifact, replication padding (RP) was employed in this study. RP was implemented as follows:

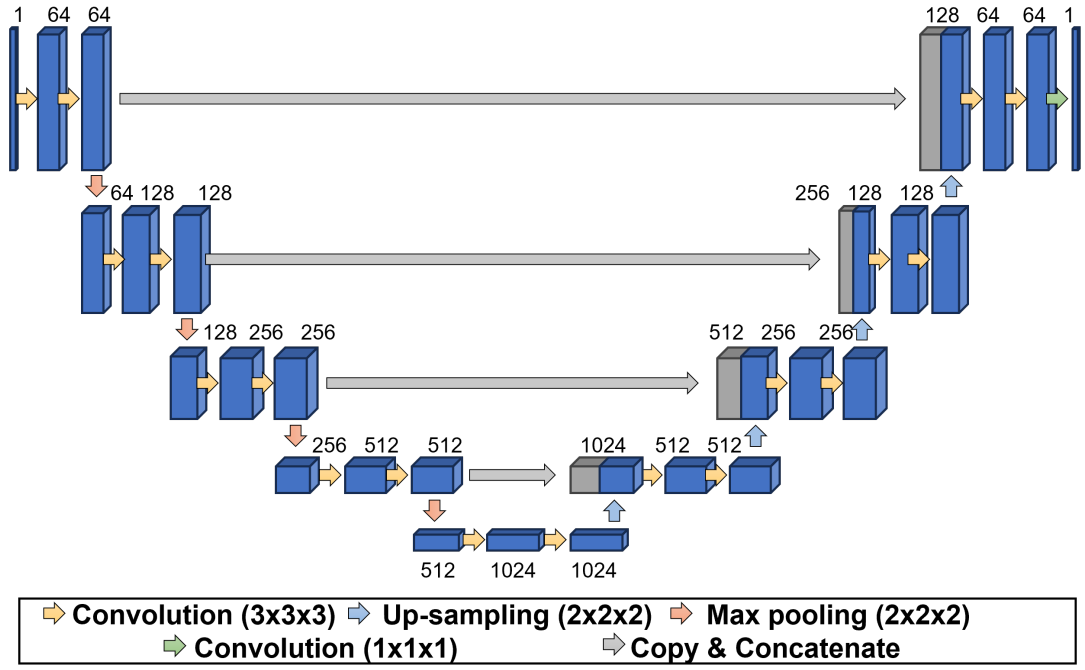

(a)

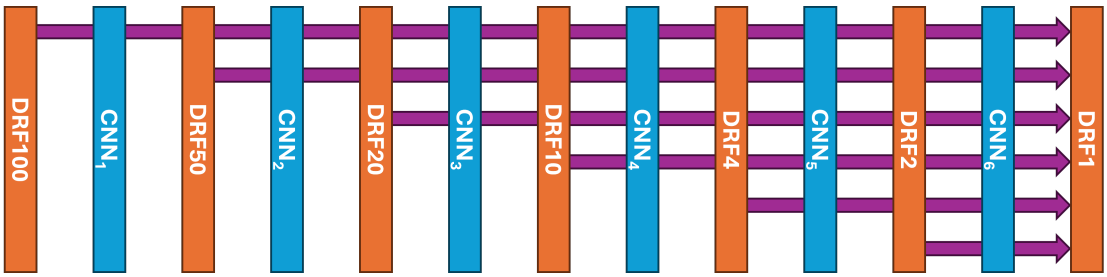

(b)

Fig. 5.5: a) The 3D U-Net architecture used for PETAL-3D. b) From left to right, the six 3D U-Nets marked as CNN_1 to CNN_6. If the input was DRF100, it goes through all the six CNNs, but if the input was DRF4 it goes through only CNN_5 and CNN_6 © 2024 IEEE.

$$O(x,y,z) = \begin{cases} 1 & \text{if } p \leq x < H_i + p \text{ and } p \leq y < W_i + p \\ & \text{and } p \leq z < D_i + p; \\ 0 & \text{otherwise.} \end{cases} \tag{5.1}$$

$$\mathrm{RP}(I,p)_{(x,y,z)} = O(x,y,z) \cdot I_{(x,y,z)} + (1 - O(x,y,z)) \cdot I_{(0,0,0)};$$

where the input tensor I was padded with replicated values along the spatial dimensions to achieve the desired padding size p. The padding was symmetrically applied on both sides of each dimension. If a position fell outside the original input dimensions, the value was replicated from the nearest valid position inside the tensor.

O is the function $O(x, y, z)$, which returns 1 if the voxel is within the range of the original input volume, and 0 otherwise. H_i, W_i, and H_i represent the values in the ith voxel of x, y, and z, respectively.

Since $\text{Dataset}_{\text{ULD}}$ had seven DRF levels, PETAL-3D$_{ULD}$ consisted of six 3D U-Nets, each comprising the 3D U-Net architecture mentioned above. Each network was trained on a pair of specific DRF levels. CNN_1 was trained using data with the highest noise level, DRF100, aiming to denoise it to DRF50. CNN_2 was trained on DRF50 data to achieve a denoised output at DRF20. CNN_3 utilized data pairs of DRF20 and DRF10. CNN_4 was tasked with denoising DRF10 data to DRF4. Subsequently, CNN_5 processed data pairs of DRF4 and DRF2, while the final CNN_6, operating with the least noise, was trained on DRF2 data alongside full-dose images at DRF1. Each network was trained independently, granting us the capability to execute the training process in parallel as illustrated in Figure 5.5.

PETAL-3D was designed to denoise images according to their DRF level by applying the network starting from the corresponding DRF level. For instance, if we have an image with DRF100, the process would start from CNN_1 to CNN_6 sequentially during inference. However, if the image was DRF10, only CNN_4 to CNN_6 would be activated to avoid over-denoising the image. The aforementioned results were obtained through the implementation of denoising based on the correct input DRF. The same approach was applied to $\text{Dataset}_{\text{LD}}$ using three 3D U-Nets. CNN_1 was used to denoise from DRF24 to DRF12, CNN_2 took DRF12 as input to achieve DRF6, and finally, CNN_3 denoised the DRF6 input to full dose.

Furthermore, I trained two additional networks: CNN_{UNet}, and $\text{CNN}_{\text{AG-UNet}}$. CNN_{UNet} is a conventional 3D U-Net designed to denoise images using only DRF100 and DRF1 pairs. $\text{CNN}_{\text{AG-UNet}}$ is an anatomically guided 3D U-Net (AG-UNet) that utilizes both the low-dose PET image and the attenuation map from the CT scan as inputs. Since no CT information was provided for $\text{Dataset}_{\text{ULD}}$, $\text{CNN}_{\text{AG-UNet}}$ was only used for $\text{Dataset}_{\text{LD}}$, which included both PET and CT data, using DRF24 to DRF1 pairs. CNN_{UNet}, and $\text{CNN}_{\text{AG-UNet}}$ were trained to compare the performance of PETAL-3D with traditional AI-based denoising approaches. To achieve optimal denoising results for traditional methods, the networks were trained exclusively for denoising DRF100 on $\text{Dataset}_{\text{ULD}}$ and DRF24 on $\text{Dataset}_{\text{LD}}$, without mixed noise level training. As demonstrated by [202], training with mixed noise levels leads to a decline in network performance.

For comparing PETAL-3D to a classical denoising approach, I have also implemented a 4-mm Gaussian filter. The 4-mm Gaussian filter was a 3D Gaussian filter with a kernel size of 3 voxels and a truncation value of 1.25.

As the $\text{Dataset}_{\text{ULD}}$ included images from both the Quadra and uEXPLORER scanners, there was a mismatch in the 3D image dimensions due to the different voxel sizes of each scanner. To enable the network to handle varying image sizes,

zero padding was applied to augment the image size to $448 \times 448 \times 640$ voxels. Consequently, for the Quadra data, 5 slices were excluded from training, while 33 slices were excluded from uEXPLORER images. These excluded slices, covering the thighs at the edge of the scanner or the fingertips in the case of uEXPLORER images, lacked clinical relevance. Afterward, the original input image size was restored.
For the training dataset, 80% of the data was allocated for training, while the remaining 20% was reserved for validation. After each full epoch, a new shuffle was applied to the data to redistribute the training and validation datasets, preventing the network from overfitting.
The initial development of the networks was carried out using two NVIDIA RTX 3090 GPUs, each with 24 GB of VRAM, interconnected through a NVLink to share VRAM and computational power. Subsequently, training was conducted using the (NHR@ZIB) GPU cluster[2]. Seven A100 GPUs were utilized for training, with each GPU dedicated to training an individual network independently. Each A100 GPU was equipped with 80 GB of VRAM, enabling the use of a large batch size of 80. Each batch comprised 490 image patches with dimensions of $64 \times 64 \times 64$ voxels.
CNN_1 was employed to determine the optimal number of epochs required to train the network. Being the network tasked with handling the highest level of noise, it naturally required the longest time to converge. Consequently, we trained the network until convergence and examined both the training and validation losses. After 1800 epochs, the network reached stability, and further training showed no significant improvement according to the training and validation loss. Therefore, the cutoff was set at 1850 epochs for all networks. Monitoring the behavior of the other networks, it a similar trend was observed , where the networks plateaued after several epochs and remained stable.
During training, a recommended method to reduce training time is to skip patches in regions outside the region of interest [203, 204]. These regions typically have values close to zero and may not contain meaningful information. However, excluding these patches resulted in overestimation in the pixel values when applying the network near the patient's body. Therefore, no filtering for zero patches was applied during training.

5.2.5 Evaluation

To evaluate the performance of the network, I calculated several global metrics, including Peak Signal-to-Noise Ratio (PSNR), Structural Similarity Index Measure (SSIM), and Normalized Root Mean Square Error (NRMSE) [205]. The CV, and tumor-to-background ratio (TBR) were calculated as local metrics. Lastly, a clinical physician assessment was performed.

[2] `https://nhr.zib.de/`

5.2.5.1 Global metrics

PSNR, SSIM, and NRMSE were used to assess the performance of the denoising methods in the ULDPET challenge and are commonly employed for evaluating AI algorithms in denoising tasks.

NRMSE is a commonly employed measure for quantifying the differences between values predicted by a model (in this instance, the denoised image K) and the values observed in reality (the target image I). Unlike the MSE, it offers a normalized scale for comparing errors across various models or datasets, rendering it a valuable metric across multiple domains, including image processing. Lower NRMSE values signify a better fit, contrasting with PSNR and SSIM where higher values are desired. The NRMSE is calculated as:

$$\text{NRMSE} = \frac{\sqrt{\frac{1}{n}\sum_{i=1}^{n}(I_(i) - K_(i))^2}}{I_{\max} - I_{\min}}, \tag{5.2}$$

where $I_{\max}$ and $I_{\min}$ are the maximum and minimum values of I, respectively, and n is the total number of pixels.

PSNR is a commonly used measure for assessing the quality of a reconstructed image compared to the original noise-free image. Given I and its noisy approximation K, MSE is utilized for evaluating the quality of a denoised image [206], as illustrated:

$$\text{PSNR} = 20 \cdot \log_{10}\left(\frac{I_{\max}}{\sqrt{\text{MSE}}}\right), \tag{5.3}$$

$$\text{MSE} = \frac{1}{p \times m \times n}\sum_{i=0}^{p-1}\sum_{j=0}^{m-1}\sum_{k=0}^{n-1}[I_{(i,j,k)} - K_{(i,j,k)}]^2, \tag{5.4}$$

where, i, j, k, m, n, and p represent the dimensions of the target, and denoised images, respectively.

SSIM is another metric for measuring the similarity between two images. The SSIM index is a full reference metric, meaning the measurement or prediction of image quality is based on an initial uncompressed or distortion-free image as reference. The SSIM formula is based on three comparison measurements between the samples of I and K: luminance, contrast, and structure [207] as shown below:

$$\text{SSIM}(I, K) = \frac{(2\mu_I\mu_K + c_1)(2\sigma_{IK} + c_2)}{(\mu_I^2 + \mu_K^2 + c_1)(\sigma_I^2 + \sigma_K^2 + c_2)}; \tag{5.5}$$

where μ_I is the average intensity over all voxels of I, μ_K is the average intensity over all voxels of K, σ_I^2 and σ_K^2 is the variance of I and K respectively while σ_{IK} is the covariance of I and K; $c_1 = (k_1 L)^2$, and $c_2 = (k_2 L)^2$ are two variables to stabilize the division with weak denominator, where L is the dynamic range of the pixel-values and $k_1 = 0.01$ and $k_2 = 0.03$. All of the aforementioned metrics were implemented using the PyTorch and scikit-learn image packages [200, 208].

5.2.5.2 Local metrics

CV was calculated using a 15 cm^3 VOI in the liver as the ratio of the standard deviation (σ_{VOI}) to the mean (μ_{VOI}) as follows:

$$CV_{VOI} = \frac{\sigma_{VOI}}{\mu_{VOI}}. \tag{5.6}$$

CV serves as a valuable measure for comparing the degree of variation between different data series, even when their means differ significantly from each other.
Moreover, a total of 23 lesions of varying sizes were segmented to calculate the tumor-to-background ratio (TBR). The TBR was determined using the maximum value of the lesion ($T_{\max}$) and the mean value of the liver as the background (μ_{VOI}), as shown:

$$\text{TBR} = \frac{T_{\max}}{\mu_{VOI}}. \tag{5.7}$$

In the case of phantom studies, TBR is replaced with the SBR.

5.2.5.3 Clinical physicians assessment

Furthermore, an evaluation of $\text{Dataset}_{\text{LD}}$ was conducted by two experienced resident nuclear medicine physicians[3] for lesion detectability and visual assessment (image quality and image noise) in consensus. The images with and without the application of PETAL-3D$_{[LD,LD]}$ were viewed in a randomized order. In patients with a multifocal disease, a maximum of five lesions per patient were analyzed to reduce over-representation. A 5-point Likert scale was used for the subjective evaluation. The evaluation covers the overall impression of image quality, subjective image noise, and conspicuity of suspected pathological lesions. The criteria for the Likert scoring system are provided in Table 5.2.

Table 5.2: Five-Point Likert scoring system for subjective PET image rating

Score	Image Quality	Lesion Conspicuity	Image Noise
5	state-of-the-art quality	well-defined	near-imperceptible noise
4	superior to the average	fairly defined	lower than regular image of daily practice
3	regular quality of daily practice	hazy, recognizable	similar to regular image of daily practice
2	barely diagnostic	impairing diagnostic confidence	increased noise
1	non-diagnostic	un-recognizable	excessive noise

[3] One of the two physicians is a board-certified radiology physician, and both have long experience in the reading of oncological PET/CT scans at Department of Nuclear Medicine and Clinical Molecular Imaging, University Hospital Tuebingen.

5.3 Results

5.3.1 Dataset$_{\mathrm{ULD}}$

Figure 5.6 presents the denoised DRF100 image obtained using a 4-mm Gaussian filter, CNN$_{\mathrm{UNet}}$, and PETAL-3D$_{[ULD,ULD]}$. Moreover, Figure 5.7 shows an exemplary dataset of the thorax region from the Quadra scanner (raw images, as well as the result of post-reconstruction application of PETAL-3D and a 4-mm Gaussian filter, including zoomed sections). Both denoising techniques effectively reduced image noise; as expected, the Gaussian filter slightly blurred organ contours. Table 5.3 shows the values of the PSNR and NRMSE averaged over all test data used for evaluation, and their standard deviation. In addition, the CV in the liver for the images showed in Fig. 5.7. The global metrics evaluation places PETAL-3D$_{[ULD,ULD]}$ denoised DRF100 images between DRF10 and DRF20 while it further improved with lower noise. PETAL-3D$_{[ULD,ULD]}$ exhibits lower CV values compared to Gaussian filtering. However, for lower noise images, the CV of Gaussian filtering is smoother than the ground truth (6% and 4% for DRF 4 and DRF 2, respectively, compared to 7% for DRF 1). This suggests that Gaussian filtering may result in over-smoothing, potentially removing not only noise but also important image details. In contrast, PETAL-3D$_{[ULD,ULD]}$ achieves a CV that matches the ground truth (7%), indicating a better balance between noise reduction and detail preservation.

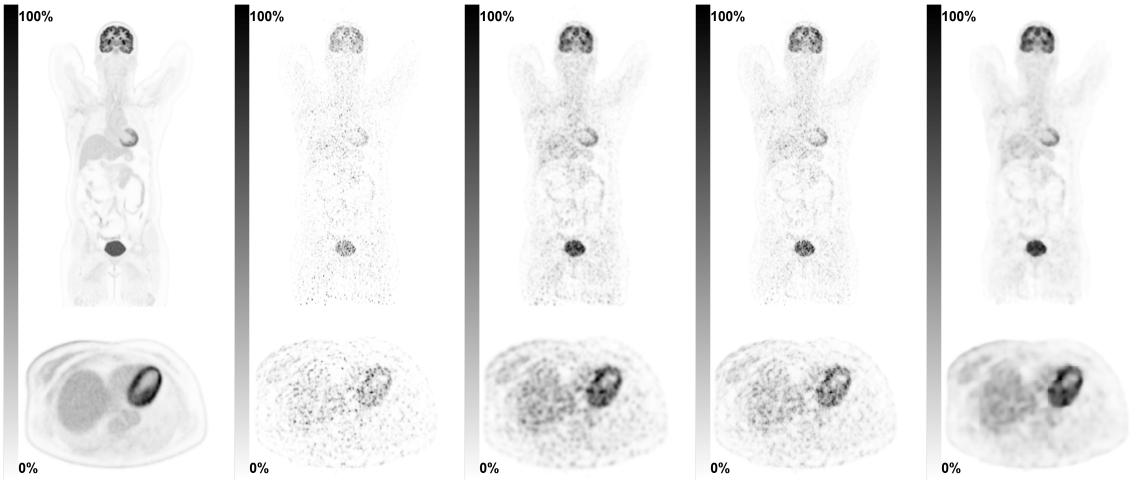

(a) (b) (c) (d) (e)

Fig. 5.6: a) DRF1, b) DRF100, c) DRF100 denoised with a 4-mm Gaussian filter, d) DRF100 denoised with CNN$_{\mathrm{UNet}}$, and e) DRF100 denoised with PETAL-3D$_{[ULD,ULD]}$.

Figure 5.8 displays the global metrics for Dataset$_{\mathrm{ULD}}$, comparing the performance of PETAL-3D$_{[ULD,ULD]}$ on the test dataset to the input images with different DRFs.

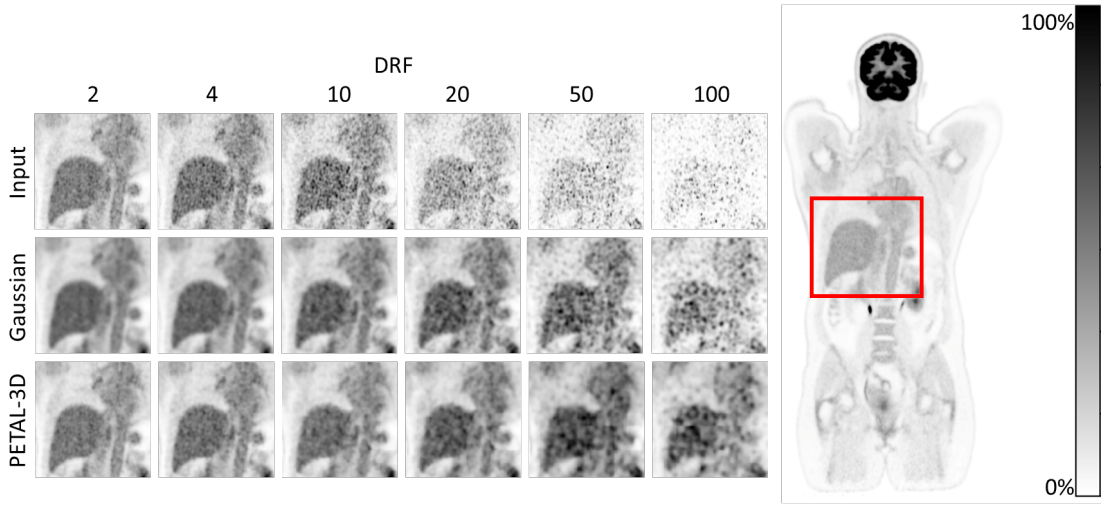

Fig. 5.7: Comparison between PETAL-3D denoising and Gaussian filtering. DRF1 image is shown on the right as a reference. Top row: Original input with the noise level incrementally increasing from left to right. Middle row: Images after 4-mm Gaussian filtering. Bottom row: Images after PETAL-3D denoising. All images are normalized to their own maximum © 2024 IEEE.

Table 5.3: Quantitative assessment of the input dataset, 4-mm Gaussian filter, and PETAL-3D$_{[ULD,ULD]}$ denoised images. The CV value for DRF1 was 7%

	PSNR			NRMSE			CV		
DRF	Input	Gaussian	PETAL-3D	Input	Gaussian	PETAL-3D	Input	Gaussian	PETAL-3D
2	62 ±6	54 ±5	63 ±5	0.08 ±0.04	0.21 ±0.12	0.07 ±0.02	9%	4%	7%
4	57 ±7	48 ±4	60 ±5	0.15 ±0.09	0.27 ±0.10	0.10 ±0.02	13%	6%	8%
10	53 ±9	48 ±4	55 ±6	0.25 ±0.17	0.27 ±0.10	0.18 ±0.06	20%	9%	9%
20	49 ±9	48 ±4	54 ±6	0.40 ±0.23	0.27 ±0.09	0.19 ±0.06	28%	11%	10%
50	45 ±9	47 ±4	52 ±6	0.58 ±0.24	0.29 ±0.08	0.25 ±0.07	47%	18%	12%
100	43 ±8	45 ±3	50 ±6	0.71 ±0.21	0.36 ±0.05	0.32 ±0.13	87%	33%	18%

Additionally, the figure includes the results for CNN$_{\text{UNet}}$ and the application of Gaussian filters. In the case of the noisiest image (DRF100), while CNN$_{\text{UNet}}$ denoised the images and improved PSNR, it was outperformed by the Gaussian filter. The PSNR of the Gaussian-filtered DRF100 image shows improvement in quality metrics but deteriorates for lower DRF values (below DRF 20). PETAL-3D$_{[ULD,ULD]}$ achieves the highest PSNR and SSIM values for all DRF inputs while also minimizing NRMSE. Since the Gaussian filter underperformed compared to PETAL-3D, further evaluations on Dataset$_{\text{LD}}$ will focus exclusively on AI-based methods.
Figure 5.9 illustrates the outcomes of using DRF100 and DRF1 input data for each CNN, instead of using the CNNs designed for their respective DRF input levels. This

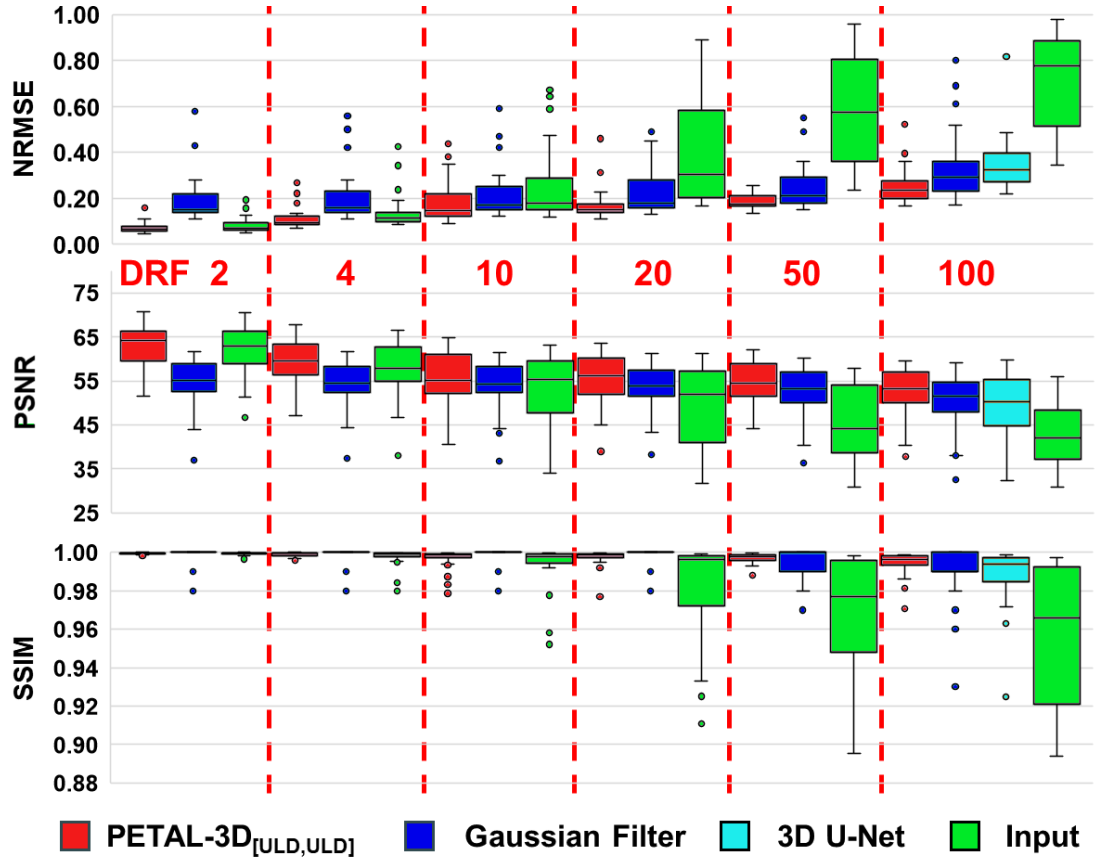

Fig. 5.8: Box plots representing the distribution of NRMSE (top graph), PSNR (center), and SSIM (bottom), across various DRFs. The data shown is for the input image (green), Gaussian filter (blue), PETAL-3D$_{[ULD,ULD]}$ denoised images (red), for DRF values ranging from 2 (left) to 100 (right). For comparison, the results of CNN$_{\text{UNet}}$ for DRF100 are presented (cyan). Each box plot illustrates the interquartile range (IQR), with the median marked by a horizontal line inside the box. The whiskers extend to the minimum and maximum values within 1.5 times the IQR, while outliers beyond this range are shown as individual points. The plots highlight the spread and skewness of the data, with wider boxes indicating greater variability.

approach was employed to assess the impact of DRF input on network performance. The results indicate that DRF1 produces an over-smoothed image when starting from CNN$_1$, while DRF100 results in a properly denoised image. However, lower DRF inputs lead to under-denoised images for DRF100 when not initiated from the appropriate network (CNN$_1$).

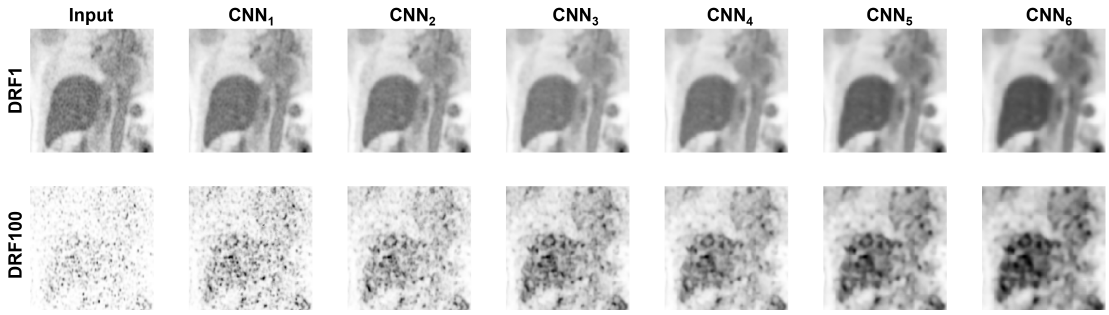

Fig. 5.9: A zoomed in 2D slices from Dataset$_{ULD}$ Quadra example. Top row, applying PETAL-3D$_{[ULD,ULD]}$ on DRF1 image to each level of the CNN. Bottom row, correctly application of PETAL-3D$_{[ULD,ULD]}$ on DRF100.

5.3.2 Dataset$_{\mathbf{LD}}$

Figure 5.10 shows the performance of both PETAL-3D$_{[ULD,LD]}$ and PETAL-3D$_{[LD,LD]}$ along with CNN$_{\text{UNet}}$, and CNN$_{\text{AG-UNet}}$ applied to Dataset$_{\text{LD}}$. PETAL-3D$_{[ULD,LD]}$ application began with CNN$_3$ (trained on DRF20), as it closely corresponds to DRF24. PETAL-3D$_{[ULD,LD]}$ outperformed CNN$_{\text{UNet}}$ trained on the specific noise level. However, CNN$_{\text{AG-UNet}}$ achieved higher PSNR values, while PETAL-3D$_{[LD,LD]}$ (trained on the specific noise level) showed the best results overall. A zoomed-in image of PETAL-3D$_{[LD,LD]}$ denoised images are shown in Figure 5.11.
Figure 5.12 shows the Likert scoring. PETAL-3D improved the overall scoring for DRF24 and DRF12 dataset from non-diagnostic to image quality obtained in regular routine while DRF6 was rated as above average.
The results of the local metrics and the values obtained from the segmented tumors are shown in Table 5.4. The CV, TBR, and Lesion Detectability Rate (LDR) improved with the application of PETAL-3D. However, it is notable that the SUV$_{\text{mean}}$ and SUV$_{\text{max}}$ are slightly reduced compared to the input images. Denoising DRF6 images with PETAL-3D$_{[LD,LD]}$ helped to preserve a SUV$_{\text{mean}}$ of 8.1±4.7 closely matching 8.0±4.8 for the original DRF1 images. The increased noise for DRF6 to DRF24 causes an increase and higher variance in SUV$_{\text{max}}$. In contrast, applying PETAL-3D helped to mitigate this effect while preserving a SUV$_{\text{max}}$ of 13.6±8.0 for DRF6 in comparison to 16.0±9.9 (no denoising) and 14.0±8.2 (DRF1 reference). Akin the TBR of 5.5±4.0 obtained by PETAL-3D reassembled closer the original DRF1 value of 5.9+4.1 than the non-denoised DRF6 image with 7.0±4.8.

5.3.3 ^{90}Y phantom data

The extremely low yield for positron emission of ^{90}Y is responsible for high statistical fluctuations in the data, and subsequenly, very noisy images. Additionally, the

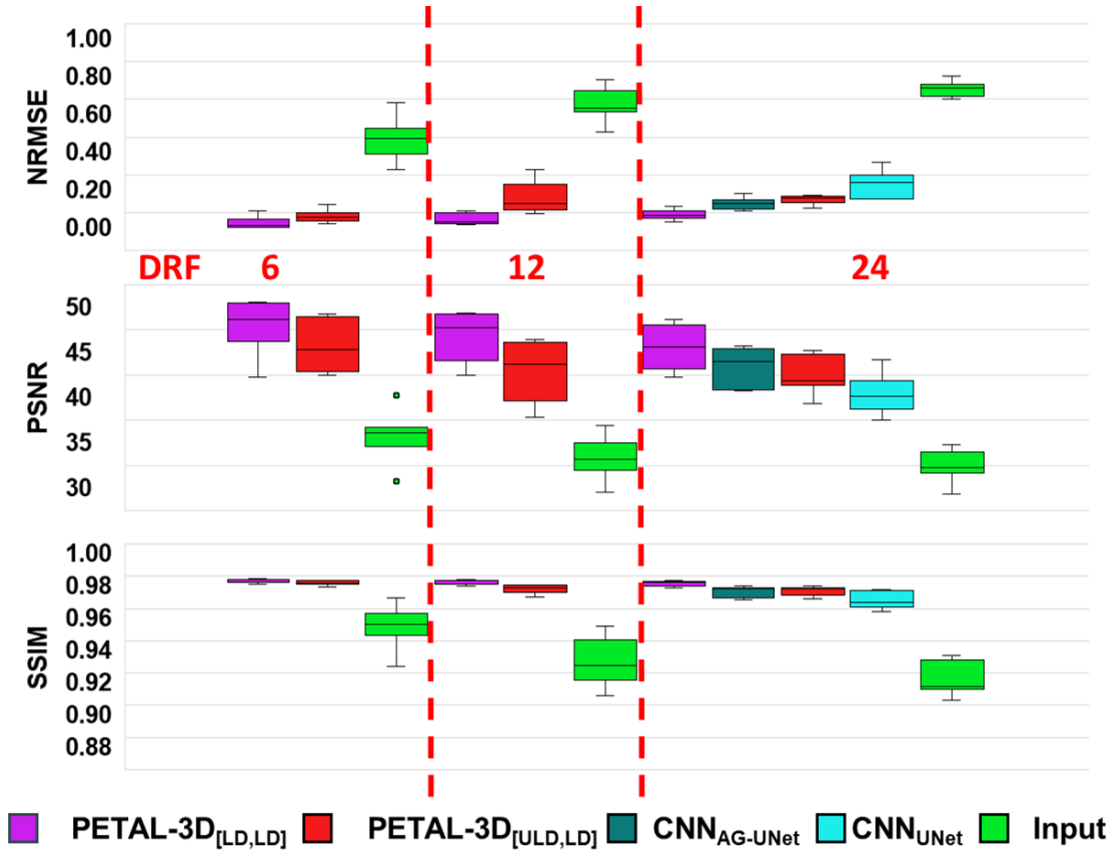

Fig. 5.10: Box plots of the NRMSE (top graph), PSNR (center), and SSIM (bottom), for the input image (green), PETAL-3D$_{[ULD,LD]}$ denoised images (red), and PETAL-3D$_{[LD,LD]}$ denoised images (magenta) for DRF values ranging from 6 (left) to 24 (right). For comparison, the results of CNN$_{\text{UNet}}$ (cyan), and CNN$_{\text{AG-UNet}}$ (teal) for DRF24 are presented (refer to Figure 5.8 for a detailed explanation of the box plot structure).

Table 5.4: Values of the local metrics for PETAL-3D$_{[LD,LD]}$ denoised images

Data	CV(%)	LDR(%)	SUV$_{\text{mean}}$	SUV$_{\text{max}}$	TBR
DRF1	7	100	8.0 ±4.8	14.0 ±8.2	5.9 ±4.1
DRF6	17	96	9.2 ±5.5	16.0 ±9.9	7.0 ±4.8
DRF12	24	65	8.2 ±5.1	14.5 ±9.5	6.0 ±4.7
DRF24	33	52	9.5 ±5.4	17.3 ±10.6	7.4 ±5.2
PETAL-3D					
DRF6	5	100	8.1 ±4.7	13.6 ±8.0	5.5 ±4.0
DRF12	5	91	7.6 ±5.2	11.9 ±8.6	5.0 ±4.1
DRF24	5	78	7.2 ±5.1	11.8 ±8.6	4.4 ±3.9

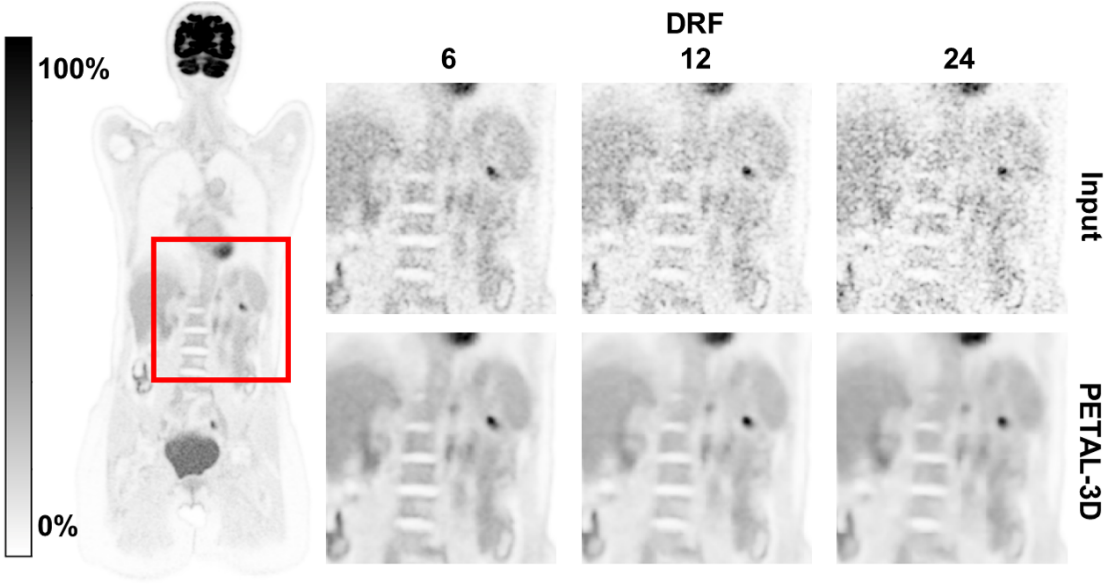

Fig. 5.11: Top row: Original input ($\text{Dataset}_{\text{LD}}$) with the noise level incrementally increasing from left to right. Bottom row: Images after PETAL-3D$_{LD}$ denoising. DRF1 image is shown on the left as a reference. All images are normalized to their own maximum © 2024 IEEE.

emission of Bremsstrahlung radiation in the decay process of ^{90}Y increases the number of random events detected. The latter, if not properly compensated for, might contribute to increasing the background noise of the reconstructed images. Figure 5.13 illustrates the performance of both the Gaussian filter and PETAL-3D$_{[LD,^{90}Y]}$ in denoising ^{90}Y AbdoMan phantom images. PETAL-3D$_{[LD,^{90}Y]}$ improved image quality by enhancing the visibility of the hot spheres and suppressing noise in the warm background. This was confirmed by global metrics as well as local metrics, including CV and SBR values, as shown in Table 5.5. Although the Gaussian filter visually denoised the input images, it was still outperformed by PETAL-3D$_{[LD,^{90}Y]}$ both visually and according to the metrics. Additionally, the SBR reported for the Gaussian filter had an error of 15%, compared to the 4% error for the images denoised with PETAL-3D$_{[LD,^{90}Y]}$. The same behavior was observed with the segmented lesions, where the CV and SBR improved. However, the CRC were reduced by less than 5% in the denoised images, as shown in Figure 5.14.

5.3.4 ^{89}Zr phantom data

The Gaussian filter is expected to perform similar to the ^{90}Y images, as the ^{89}Zr spheres would have similar re-framed DRF values (DRF48 and DRF144 for the 30-minute and 10-minute scan, respectively). Based on the results from the ^{90}Y study, the Gaussian filter was excluded, and only PETAL-3D$_{[LD,^{89}Zr]}$ results will be

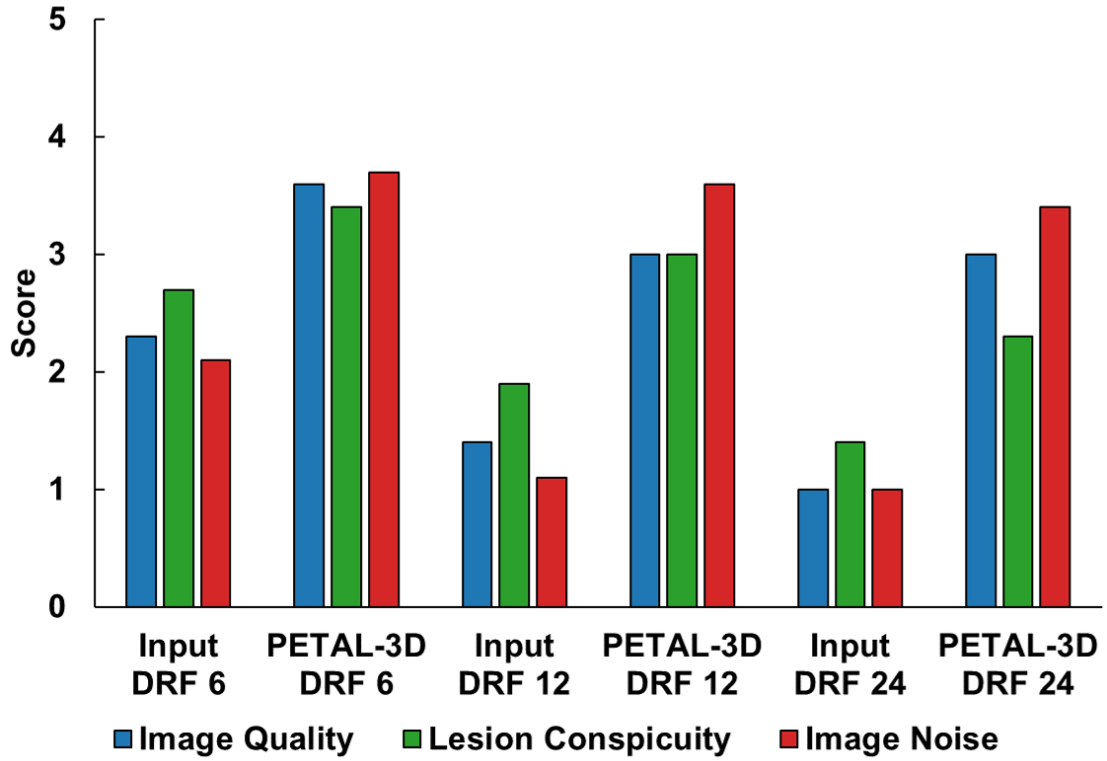

Fig. 5.12: The Likert scoring results for the subjective PET image quality ratings, lesion conspicuity, image Noise for the inputs and the denoised images using PETAL-3D$_{[LD,LD]}$. DRF1 has a perfect score of 5 for each metric © 2024 IEEE.

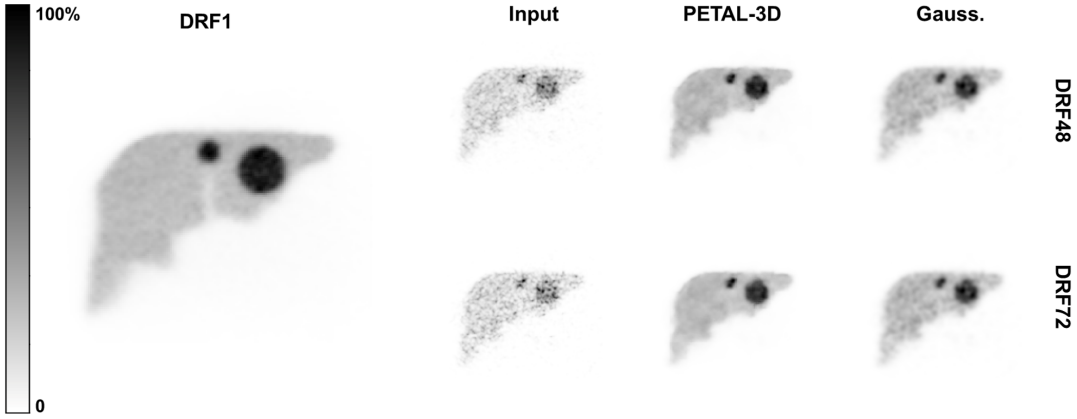

Fig. 5.13: ^{90}Y AbdoMan phantom images. Left: 24-hour scan magnified by a factor of two for better visualization. Top row: 30-minute re-framed (DRF48). Bottom row: 20-minute re-framed (DRF72). Images are presented in the order of input, PETAL-3D$_{[LD,^{90}Y]}$ denoised images, and Gaussian filter denoised images.

Table 5.5: AbdoMan phantom comparison with and without denoising using PETAL-3D$_{[LD,^{90}Y]}$ and a 4-mm Gaussian filter for local metrics (SBR and CV) and global metrics (PSNR, NRMSE, and SSIM). The CV value for DRF1 was 5% with SBR of 3.03

	SBR	CV(%)	PSNR	NRMSE	SSIM
DRF48	2.96	33	28	0.58	0.96
Gauss. DRF48	2.59	17	38	0.19	0.99
PETAL-3D DRF48	2.91	8	41	0.18	0.99
DRF72	3.00	45	27	0.60	0.95
Gauss. DRF72	2.59	19	36	0.22	0.98
PETAL-3D DRF72	2.97	9	39	0.19	0.98

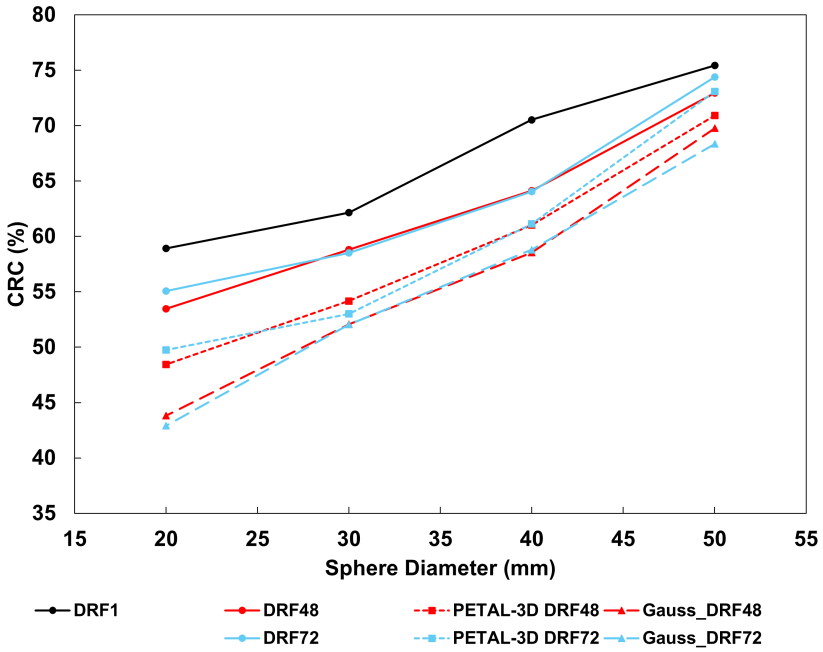

Fig. 5.14: AbdoMan phantom CRCs for different sphere sizes with and without denoising using PETAL-3D$_{[LD,^{90}Y]}$ and a 4-mm Gaussian filter.

reported. The results of PETAL-3D$_{[LD,^{89}Zr]}$ for day4, day12, day16, and day23 are shown in Figure 5.15. The denoised images for days 4, 12, and 16 show suppressed noise levels compared to the input images. However, an artifact is observed at the bottom of the 28-mm sphere that is not present in the input images, even in the 10-minute scan. This artifact appears as the signal is enhanced in the non-active background at the bottom of the sphere, while the upper side, which is surrounded by air, does not exhibit this induced artifact. On day 23, the denoising process primarily smoothed the image, which led to a degradation in image quality in the background of the 10-mm sphere, causing the sphere to appear as if it were fading

into the background. It is noticeable that PETAL-3D did not hallucinate the 10-mm sphere or its background in the 10-minute scan. Moreover, with the reduced signal in the image, the artifact at the 28-mm sphere is diminished and completely absent in the 10-minute scan. The CRC values of the background, 1-mm sphere and 28-mm sphere after denoising the images with PETAL-3D are shown in Table 5.6. Similar to the method used for calculating lung residual error in Section 3.2.3.2, the error for the 28-mm hollow sphere (lung error) was determined by dividing the mean value of the lung VOI by the mean value of the total background VOI, where the ideal value is 0. The denoised images from day 16 (10-minute scan) and day 23 (30-minute scan) show higher lung error values, which are also visible as blurred regions in the images.

Table 5.6: Metrics of the low-dose imaging of the ^{89}Zr spheres with PETAL-3D. For reference, the SBR, lung error, and CV on day 4 were 7.43, 6%, and 0.14, respectively

Images		Input						PETAL-3D					
time (min)	day	SBR	Lung Error	CV	PSNR	SSIM	NRMSE	SBR	Lung Error	CV	PSNR	SSIM	NRMSE
10	12	7.85	6%	50%	29	0.83	0.46	7.75	7%	13%	31	0.91	0.35
10	16	6.63	5%	81%	27	0.75	0.58	7.51	21%	15%	30	0.82	0.41
10	23	-	-	-	23	0.6	0.89	-	-	-	26	0.63	0.63
30	12	7.76	7%	29%	32	0.89	0.32	7.48	5%	13%	31	0.93	0.35
30	16	7.29	6%	46%	29	0.84	0.42	7.33	7%	15%	29	0.88	0.42
30	23	7.94	7%	99%	25	0.72	0.69	7.50	29%	25%	29	0.82	0.45

5.3.5 Sampling study

Table 5.7 presents the random fraction (R) obtained from the sinograms (raw data before image reconstruction). The table also includes the global metric values—COR, PSNR, NRMSE, and SSIM—as well as the CV values at the liver, for both the simulated low-dose and re-framed low-dose datasets. The values for both datasets were very similar, with a slight improvement observed for the re-framed dataset. The amount of trues in the re-framed low-dose dataset was similar to that of the injected low-dose dataset. However, the prompt counts were consistently higher due to increased R.

It is also worth noting that the 10-minute scans for DRF12, DRF24, and DRF48 images resulted in similar values to those of the 5-minute scans for DRF6, DRF12, and DRF24, respectively, in terms of R, PSNR, SSIM, and NRMSE. However, a noticeable difference was observed for CoR (up to 13%) and CV (up to 9%), with these differences becoming more pronounced as the DRF level increases.

Despite these similar metric values, visual inspection of the images depicted in Figure 5.16 reveals small differences in the DRF24 images. Figure 5.16 also displays

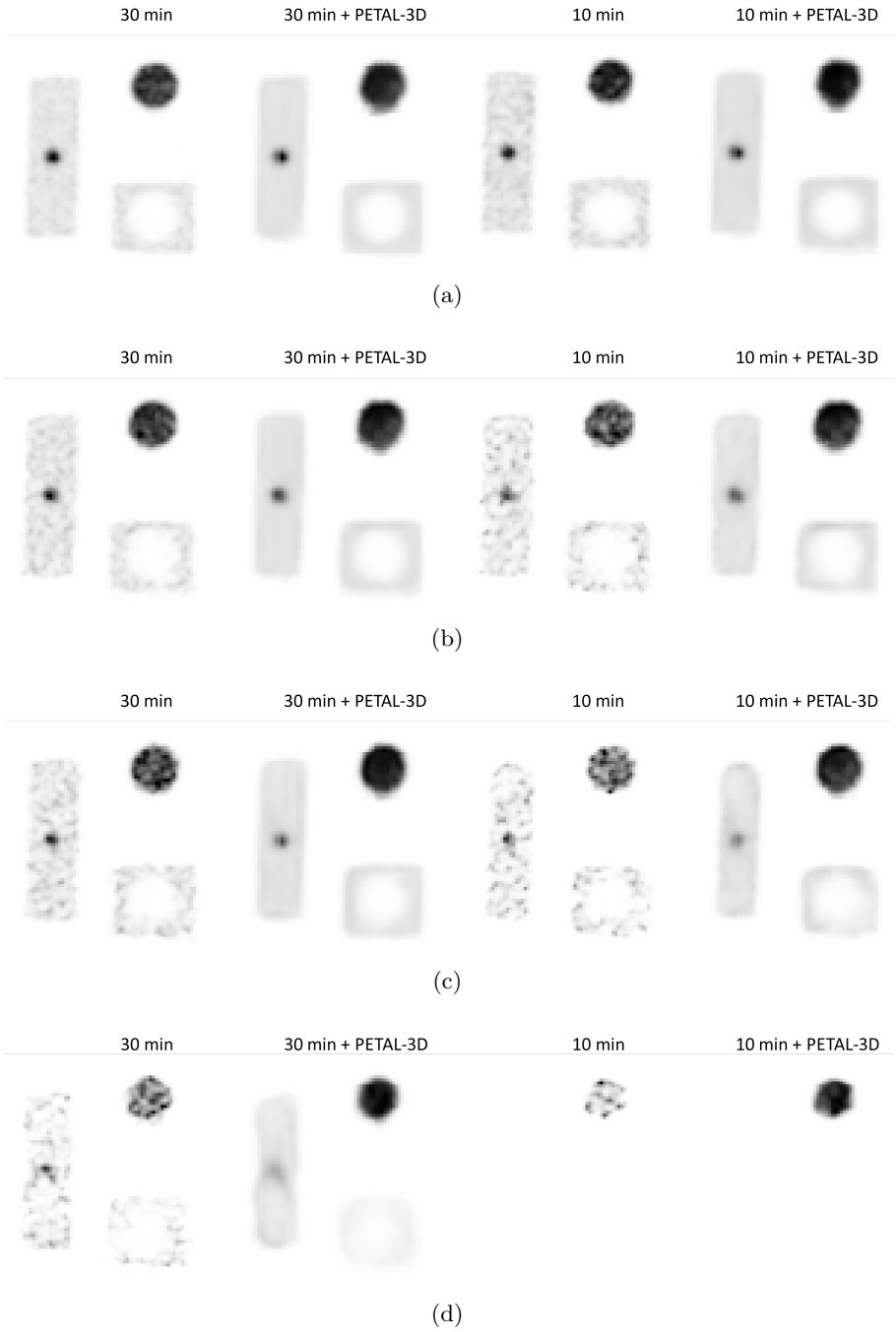

Fig. 5.15: The ^{89}Zr IEC spheres with and without being denoised with PETAL-3D$_{[LD,^{89}Zr]}$ for a) day 4, b) day 12, c) day 16, and d) day 23. Images are shown for both the 30-minutes and 10-minutes scans.

Table 5.7: Comparison of 5-minute scans for the first two groups of re-framed and injected low-dose data, before and after denoising with PETAL-3D$_{LD}$

Data	R%	CoR	CV	PSNR	SSIM	NRMSE
DRF1	46%	0.25	0.07	-	-	-
DRF6 Ref.	46%	0.56	0.17	31	0.92	0.87
DRF6 Inj.	9%	0.60	0.18	31	0.92	0.91
DR12 Ref	46%	0.72	0.24	31	0.92	0.92
DRF12 Inj.	5%	0.69	0.24	31	0.92	0.92
DRF24 Ref.	47%	0.87	0.35	30	0.91	0.96
DRF24 Inj.	2%	0.88	0.35	30	0.91	0.96
DRF6 PETAL-3D Ref.	-	0.21	0.05	35	0.98	0.08
DRF6 PETAL-3D Inj.	-	0.22	0.06	34	0.98	0.09
DRF12 PETAL-3D Ref.	-	0.20	0.05	35	0.98	0.08
DRF12 PETAL-3D Inj.	-	0.17	0.04	34	0.98	0.09
DRF24 PETAL-3D Ref.	-	0.21	0.06	35	0.98	0.08
DRF24 PETAL-3D Inj.	-	0.19	0.06	36	0.97	0.07
DRF12 Inj. 10 min	5%	0.55	0.14	32	0.93	0.91
DRF24 Inj. 10 min	2%	0.59	0.18	31	0.92	0.92
DRF48 Inj. 10 min	1%	0.75	0.26	31	0.92	0.96

the network output when implementing PETAL-3D$_{LD}$ for both the re-framed and low-dose simulated data, again resulting in similar metrics for DRF24 in both the injected and re-framed low-dose datasets. However, a slight degradation in image quality is visually apparent in the re-framed dataset.

5.4 Discussion

The presented results illustrate the efficacy of PETAL-3D across various datasets and scenarios characterized by different levels of noise. The DRF100 images denoised with PETAL-3D$_{[ULD,ULD]}$ demonstrated superior image quality compared to the input DRF20 from DatasetULD, both visually and in terms of global metrics. Additionally, while a basic 3D U-Net model partially denoised DRF100 images, as evidenced by the metrics, it failed to enhance visual quality. This underscores the superior ability of the PETAL-3D network in preserving visual quality during denoising across a wide range of noise levels. Similar trends were observed with Gaussian filter, where global metrics improved but image quality remained insufficient for diagnostic purposes. The Gaussian filter for low-dose showed improvements in the images and metrics but blurred for the low noise images.
The choice of using a 4-mm Gaussian filter followed clinical practice. However, it remains an open question whether narrower Gaussian kernels would improve the results, as a smaller kernel would cause less blurring but achieve less noise reduction compared to the 4-mm filter used in this study. Further studies should be conducted

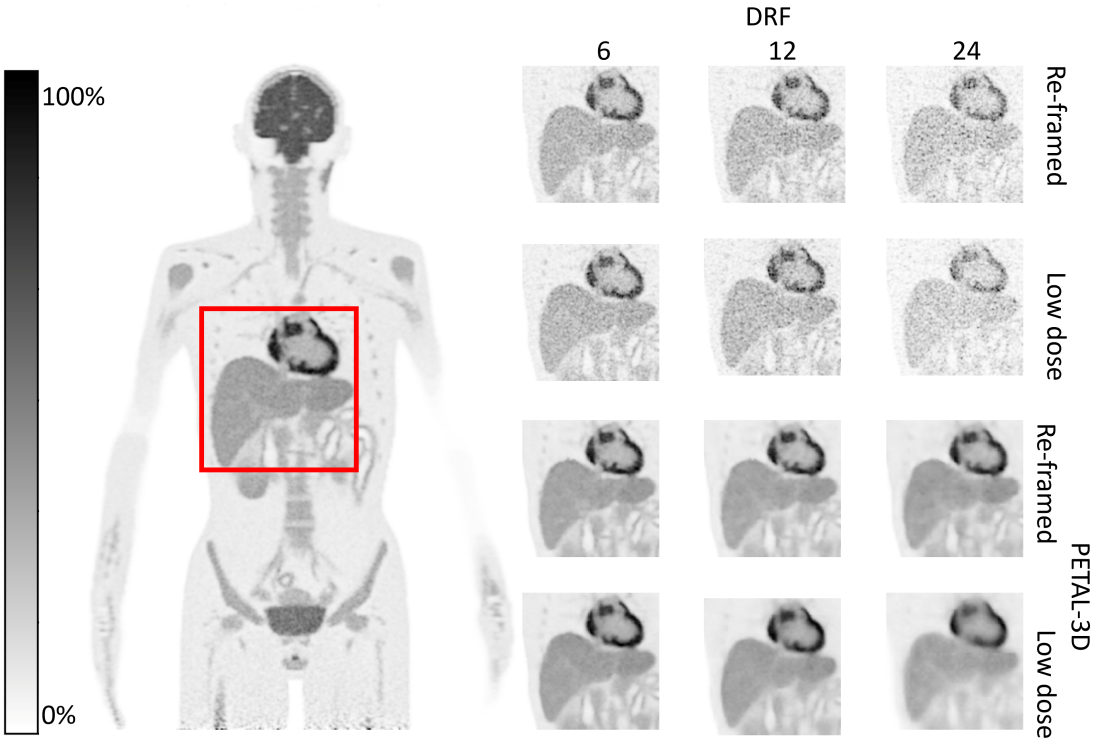

Fig. 5.16: Left: Shows the reference image (DRF1). Right: Comparison between the re-framed and the injected low-dose dataset (top two rows) and the output images after applying PETAL-3D$_{LD}$ for image denoising (bottom two rows) for the liver region. All images were normalized to their own maximum.

with more optimized parameters and alternative filtering methods to better evaluate the performance of PETAL-3D.
The results also improved when utilizing input data with lower noise levels, as it is inherently easier to recover less noisy images. However, it was observed that applying a high level of denoising to an image with low-level noise yielded blurry images, similar to the outcomes seen with classical image filters. This underscores the necessity of knowing the DRF prior to applying PETAL-3D, which is the case in scenarios such as low-dose imaging and re-framing imaging studies.
However, for dynamic scans where the tracer is continuously decaying and moving—altering the activity concentration and varying noise levels in each frame—PETAL-3D, in its current form, may not be suitable. To address this challenge, we propose preprocessing the frames to determine the noise level within each frame and then applying the input through the corresponding CNN designed for that noise level. Alternatively, a method similar to that introduced by Xie et al. [101] could be adopted, where a seventh CNN evaluates the performance of each CNN on the input image and applies a weighting factor accordingly.

Similar to the outcomes observed with $\text{Dataset}_{\text{ULD}}$, PETAL-3D$_{[LD,LD]}$ improved both DRF12 and DRF24, aligning more closely with what physicians evaluate during daily routine in terms of image quality and noise, as demonstrated by both image metrics and physician assessments. Additionally, PETAL-3D enhanced lesion detectability and CV, resulting in more consistent SUV_{mean} values, with a maximum difference of ± 0.8 compared to ± 1.5 for PETAL-3D and the input data, respectively. However, the TBR shows an underestimation of values compared to DRF1, in contrast to the overestimation observed in the noisy input images. This behavior is expected, as the PETAL-3D likely suppresses high-frequency components within the image, resulting in lower values for SUV_{max}.

Moreover, the PETAL-3D$_{ULD}$ network was evaluated on the $\text{Dataset}_{\text{LD}}$ at DRF24. Despite the disparity in noise levels between the training data and the test data, the network demonstrated an ability to enhance image quality compared to a DRF6, albeit not reaching the performance achieved with PETAL-3D$_{LD}$ or the $\text{CNN}_{\text{AG-UNet}}$, but still outperforming a traditional 3D U-Net. This underscores the robustness of the PETAL-3D network to variations in noise levels and its effectiveness across different datasets.

The better performance of PETAL-3D$_{[LD,LD]}$ compared to $\text{CNN}_{\text{AG-UNet}}$ is notable, as it relies solely on PET data without requiring additional input from CT or MR systems. Given that all CNNs implemented use the same U-Net architecture, and that $\text{CNN}_{\text{AG-UNet}}$ outperformed CNN_{UNet}, it is expected that training PETAL-3D$_{[LD,LD]}$ as an anatomically guided U-Net with CT or MR data would lead to even better performance. This demonstrates that PETAL-3D can be applied across different types of scanners. Moreover, this makes PETAL-3D ideal to use for PET systems without anatomical information, such as the newly developed Walk-through flat panel total body PET [128], or Positrigo's NeuroLF Brain PET System [129].

Denoising of ^{90}Y phantom data using PETAL-3D$_{LD}$ demonstrated significant improvement both visually and in terms of metrics, despite the network not being trained with images obtained using ^{90}Y. These results are encouraging, particularly considering that patients imaged with ^{90}Y are sparse, making it challenging to obtain large datasets for training. One aspect that could enhance PETAL-3D performance is using frames consistent with the network's training. The ground truth data were obtained over a period of 1440 minutes, whereas the input data corresponded to 30 minutes and 20 minutes, which would be akin to DRF48 and DRF72, respectively. Adjusting to denoise images that align with the training frames (or adjusting the training to align with the current frames) could potentially yield further improvements in performance.

Applying PETAL-3D on the low-dose PET scan of the ^{89}Zr spheres helped recover the image quailty and CRC to some extent, showcasing the utility of AI denosing for low dose PET imaging once more for a scenario the network was not trained

for. The improvement in recovering lower dose images was notable. However, for low DRF values, the improvement was minor. Additionally, the network appears to struggle with recovering data in hollow regions, as indicated by the lung error results, where PETAL-3D resulted in higher error compared to the input data. This could be due to the network causing a spill-over from the surrounding activity during denoising. This issue could potentially be resolved by either training the network on smaller input samples or integrating CT data, as done with AG-UNet, to indicate to the network that this region should not contain activity since no attenuation medium (organ) is present. Furthermore, since ^{18}F-FDG patient scans show uptake in nearly all regions, this may pose a challenge for the network to effectively denoise areas where no medium or activity is present, especially when surrounded by active regions, as is the case in hollow spheres.

Examining the results obtained from the re-framed low-dose data for the XCAT phantom reveals a notable disparity in the true-to-randoms ratio compared to the injected low-dose simulation. In the re-framed dataset, the random fraction remains nearly constant, while the random fraction in the injected low-dose simulation decreases as the injected dose is reduced. This variation arises from higher activities generating more randoms. Although the increased randoms would typically indicate a noisier image, the image quality for both the re-framed and simulated datasets remained comparable. This can be attributed to the *e7 tools* reconstruction, which includes corrections for randoms. However, this correction is not always perfect, as the noise properties of the resulting images may change. One aspect that warrants attention is the dead time and pile-up modeling of the current simulation setup, which may not accurately reflect the behavior of a real scanner. However, it is noteworthy that the activity levels utilized in this study were below 300 MBq, falling within the validated range for the Quadra digital twin as shown in Section 3.

Qualitatively, the two sets of denoised images were comparable while quantitatively, slight differences in some of the metrics were observed after image denoising. The results of the sampling study indicate that images obtained from the re-framing method to obtain low-dose data from high-dose data are comparable to those directly obtained from a low-dose simulation, as long as random and scatter corrections are applied. The values were within 2% agreement with maximum differences smaller than 5%. This suggests that they can be used interchangeably for training neural networks with a minor difference in the network output. The results are encouraging, as access to injected low-dose scans for training neural networks may not always be feasible. A further study should be conducted to examine noise texture and investigate any changes in its statistical properties, i.e., the statistical properties of the noise distribution.

5.5 Conclusion

With recent advancements in the development of total body PET systems, low-dose PET has become a focal point of research. Additionally, artificial intelligence aids in pushing the boundaries of state-of-the-art PET scanners further to enhance low-dose imaging capabilities.
PETAL-3D emerges as a promising technique for image denoising, particularly in scenarios where the noise level or DRF is predetermined, as in low-dose PET imaging or dynamic PET acquisitions with known frame lengths. Additionally, PETAL-3D demonstrates effectiveness in denoising low-dose imaging of ^{90}Y and ^{89}Zr phantoms, potentially facilitating dose reduction in PET imaging without compromising diagnostic image quality. These advancements in image quality, particularly for DRF24, open up possibilities for leveraging AI in the screening process. However, further research and testing are necessary to address certain limitations of the current study, such as further enhancing the output quality of PETAL-3D. One potential approach involves employing a nested U-Net architecture, where each CNN is concatenated during training, as opposed to the current independent approach for each network. Furthermore, the current study only utilized phantom data for ^{90}Y and ^{89}Zr. To validate the performance of PETAL-3D with other radiotracers, evaluation using patient images is imperative. Future work will concentrate on network optimization and exploring the application of PETAL-3D with other types of PET data, such as sinograms or TOF histograms.
Furthermore, the sampling study allowed us to comprehend the implications of utilizing re-framed high-dose scans for training neural networks in comparison to low-dose scans. Applying PETAL-3D to both datasets yielded comparable results, with no significant degradation in image quality or network performance, as both methods produced comparable image quality. However, caution must be exercised when applying such neural networks to datasets where the true and random rates may exert a more dominant effect. One limitation of this study is the utilization of only one XCAT phantom configuration with a standard BMI, activity concentration injection, and using only ^{18}F-FDG. Future work will entail simulating more scenarios with diverse activity concentrations and phantom configurations. Moreover, incorporating motion into the simulation to degrade image quality could be beneficial, as it mimics real scan conditions. Additionally, introducing hot tumors of various sizes could serve as another metric for lesion detectability.
In conclusion, PETAL-3D enhances diagnostic image quality while reducing radiation dose, presenting a promising future for patient safety and care. However, optimizing this technique and expanding its applicability across various scenarios remains an ongoing effort.

6 Conclusion and Future Work

This thesis main contributions were: development of a digital twin for applications in low-dose PET, improvement of the quantification of ^{89}Zr by preventing its adherence to the walls of phantoms, and development of a neural network, PETAL-3D, as a promising technique for image denoising, particularly in scenarios where the noise level or DRF is known.

The digital twin simulations showed good agreement with the measurements for the NEMA 2018 simulations. Moreover, it demonstrated the ability of simulating with both ^{18}F and ^{90}Y sources where the ground truth provided by the digital twin improved the study accuracy.

Furthermore, 3D printing phantoms have shown effectiveness in preventing the adherence of ^{89}Zr to the phantom walls, making this method suitable for multi-day studies. These findings contribute to enhancing current calibration methods for low-dose immuno-PET, enabling stable phantom scans over several days.

PETAL-3D exhibited better performance compared to traditional denoising methods and simpler neural networks. It was also capable of denoising images using radioisotopes it was not specifically trained or optimized for and images with a variety of DRF levels.

Additionally, the digital twin helped generate the data for the sampling study for injected low-dose and re-framed low-dose data, yielding comparable results with no significant degradation in image quality or network performance.

Moreover, the 3D-printed ^{89}Zr spheres provided low-dose images for applying PETAL-3D denoising, while allowing us to obtain both low-dose and high-dose scans of the phantom without any change in the phantom's activity distribution over 23 days.

Future research will focus on enhancing the digital twin sampling study by simulating additional scenarios and cases involving patients with varying BMIs and different radioisotope studies. Additionally, a deeper investigation into the effect of the LSO

background on low-dose scans could help determine the lowest activity/scan time that can be used with the Quadra before reaching the detection limits imposed by the LSO background or the Quadra detection chain.
Moreover, the expertise gained in 3D printing with ^{18}F, and ^{89}Zr can be applied to other radioisotopes used in low-dose studies, such as ^{90}Y phantoms or longer-lived isotopes like ^{22}Na. Another potential application is translating this approach to SPECT specific tracers, such as ^{57}Co, used for calibration, or ^{177}Lu, used for dosimetry studies.
Further improvements to PETAL-3D could also be envisioned. One approach would be to concatenate different networks to optimize the training parameters more effectively. Another potential enhancement would involve adding a layer or segmentation network capable of automatically detecting the DRF level and assigning the value, eliminating the need to know the DRF level beforehand. These enhancements would broaden the range of applications for PETAL-3D.

Acknowledgments

I would like to thank the following for funding the work that made this thesis possible: the German Federal Ministry for the Environment, Nature Conservation, and Nuclear Safety under grant number BMU 67KI2036C, the German Research Foundation (DFG) Cluster of Excellence EXC 2167 Precision Medicine for Chronic Inflammatory Diseases (PMI) under grant agreement no. 390884018, and the *Norddeutscher Verbund für Hoch- und Höchstleistungsrechnen* (HLRN), project numbers shp00028 and shb00004, for granting computation time on the supercomputer Lise at ZIB, which made this research possible.
Additionally, I would like to acknowledge the assistance of AI tools, including ChatGPT, DeepL, and Copilot, for their help with text editing, grammar, and spelling corrections throughout the writing process.
I would also like to extend my deepest gratitude to everyone who has supported me throughout my PhD journey.
First and foremost, I am profoundly grateful to my advisor, Prof. Dr. rer. nat. Magdalena Rafecas, for her invaluable guidance, unwavering support, and insightful feedback. Your expertise and dedication have been instrumental in shaping my research and this dissertation.
I would also like to thank Fabian Schmidt. It has been a pleasure working with you throughout the years and learning from you. I admire your hard work, ethics, and enthusiasm for research.
I am also grateful to Christian Pommranz for his help and collaborative work in developing the Quadra digital twin. It has been an amazing learning experience spending hours debugging the simulations together.
I would also like to thank Jorge Cabello (Siemens Medical Solutions USA, Inc., USA) for his support with the e7tools and the development of the Quadra digital twin. The work would have lagged without his prompt help and fruitful discussions.
Special thanks to my colleagues at the Institute of Medical Engineering for their support and collaboration. My heartfelt thanks go to my colleagues and friends in the 'Nuclear Imaging group' (NucI) for their camaraderie, intellectual stimulation, and the many discussions that enriched my research experience.
I am immensely grateful to my family for their unconditional love and encouragement. To my parents, for their lifelong support and for always believing in me, and to my siblings, for their encouragement and for always being there for me.
Lastly, to all the friends who have supported me in various ways, your contributions have been invaluable, and I deeply appreciate your presence in my life.
This work represents my own 'Bankai'—the final stage of my academic transformation, where persistence, curiosity, and passion converge. Just as 'Bankai' symbolizes the unlocking of one's true potential after relentless training and overcoming countless

challenges, this thesis embodies the culmination of years of dedication to advancing the field of low-dose PET imaging. May this integrated approach, combining AI denoising, Monte Carlo simulations, and 3D phantom printing, contribute to clearer insights and pave the way for future innovations in medical imaging. Thank you all for being part of this incredible journey.

References

[1] S. Vandenberghe, P. Moskal, and J. S. Karp, "State of the art in total body PET," *EJNMMI Physics*, vol. 7, pp. 1–33, 12 2020.

[2] E. Calderón, F. P. Schmidt, W. Lan, and et al., "Image quality and quantitative PET parameters of low-dose [18F]FDG PET in a long axial field-of-view PET/CT scanner," *Diagnostics*, vol. 13, p. 3240, 10 2023.

[3] L. Melendez-Alafort, G. Ferro-Flores, L. D. Nardo, and et al., "Zirconium immune-complexes for PET molecular imaging: Current status and prospects," *Coordination Chemistry Reviews*, vol. 479, p. 215005, 3 2023.

[4] P. M. Linder, W. Lan, N. F. Trautwein, and et al., "Optimization of Y-90 radioembolization imaging for post-treatment dosimetry on a long axial field-of-view PET/CT scanner," *Diagnostics*, vol. 13, p. 3418, 11 2023.

[5] F. Kiessling, B. Pichler, and P. Hauff, *Small Animal Imaging*, F. Kiessling, B. J. Pichler, and P. Hauff, Eds. Springer International Publishing, 2017.

[6] K. Thielemans, E. ASMA, M. Cook, and et al., "The PET raw data standardization initiative," *Journal of Nuclear Medicine*, vol. 64, no. supplement 1, pp. P687–P687, 2023.

[7] N. Karakatsanis, D. Atkinson, E. Elmoujarkach, and et al., "Usability of petsird, the PET raw data open format of the emission tomography standardization initiative (ETSI): results from ETSIs first hackathon," *Journal of Nuclear Medicine*, vol. 65, no. supplement 2, pp. 241 285–241 285, 2024.

[8] S. R. Cherry, J. A. Sorenson, and M. E. Phelps, *Physics in Nuclear Medicine*. Elsevier, 1 2012.

[9] H. Cember and T. E. Johnson, *Introduction to Health physics*, 2012, vol. 102.

[10] P. Zanzonico, "Positron emission tomography: a review of basic principles, scanner design and performance, and current systems," *Seminars in Nuclear Medicine*, vol. 34, pp. 87–111, 4 2004.

[11] J. Zhang and M. Knopp, *Advances in PET*. Springer International Publishing, 2020.

[12] L. Jodal, C. L. Loirec, and C. Champion, "Positron range in PET imaging: an alternative approach for assessing and correcting the blurring," *Physics in*

Medicine & Biology, vol. 57, p. 3931, 5 2012.

[13] A. T. Soderlund, J. Chaal, G. Tjio, and et al., "Beyond ^{18}F-FDG: characterization of PET/CT and PET/MR scanners for a comprehensive set of positron emitters of growing application — ^{18}F, ^{11}C, ^{89}Zr, ^{124}I, ^{68}Ga, and ^{90}Y," *Journal of Nuclear Medicine*, vol. 56, no. 8, pp. 1285–1291, 2015.

[14] K. N. Maloth, N. Velpula, S. Ugrappa, and et al., "Radioisotopes: An overview," *International Journal of Case Reports and Images*, vol. 5, p. 604, 2014.

[15] R. H. Mach and S. W. Schwarz, "Challenges for developing PET tracers: Isotopes, chemistry, and regulatory aspects," *PET Clinics*, vol. 5, pp. 131–153, 4 2010.

[16] M. Conti and L. Eriksson, "Physics of pure and non-pure positron emitters for PET: A review and a discussion," *EJNMMI Physics*, vol. 3, pp. 1–17, 12 2016.

[17] T. E. Wuensche, S. Lyashchenko, G. A. van Dongen, and et al., "Good practices for 89Zr radiopharmaceutical production and quality control," *EJNMMI Radiopharmacy and Chemistry*, vol. 9, pp. 1–21, 12 2024.

[18] T. Yamada, Y. Kawada, Y. Sato, and et al., "Standardization of 18F using the integral counting technique," *Applied Radiation and Isotopes*, vol. 66, pp. 909–913, 6 2008.

[19] A. Williams, "Measurement of the ratio of electron capture to positon emission in the decay of Na-22," *Nuclear Physics*, vol. 52, pp. 324–332, 3 1964.

[20] K. Vaughan, A. H. Sher, and B. D. Pate, "The decay of 68Cu and 68Ga," *Nuclear Physics A*, vol. 132, pp. 561–570, 8 1969.

[21] E. B. Podgoršak, *Interactions of Charged Particles with Matter*. Cham: Springer International Publishing, 2016, pp. 229–276.

[22] S. I. Eidelman and B. A. Shwartz, *Interactions of Particles and Radiation with Matter*. Cham: Springer International Publishing, 2021, pp. 3–27.

[23] H. Bichsel and H. Schindler, "The interaction of radiation with matter," *Particle Physics Reference Library: Volume 2: Detectors for Particles and Radiation*, vol. 2, pp. 5–44, 1 2020.

[24] G. F. Knoll, *Radiation Detection and Measurement*, 4th ed. John Wiley & Sons, 2010.

[25] J. J. Vaquero and P. Kinahan, "Positron emission tomography: Current challenges and opportunities for technological advances in clinical and preclinical imaging systems," *Annual Review of Biomedical Engineering*, vol. 17, no. 1, pp. 385–414, 2015, pMID: 26643024.

[26] J. Schwenck, D. Sonanini, J. M. Cotton, and et al., "Advances in PET imaging of cancer," *Nature Reviews Cancer 2023 23:7*, vol. 23, pp. 474–490, 5 2023.

[27] H. G. Kang, H. Tashima, H. Wakizaka, and et al., "Submillimeter-resolution PET for high-sensitivity mouse brain imaging," *Journal of Nuclear Medicine*, vol. 64, p. 978, 6 2023.

[28] K. Gong, E. Berg, S. R. Cherry, and et al., "Machine learning in PET: From photon detection to quantitative image reconstruction," *Proceedings of the IEEE*, vol. 108, pp. 51–68, 1 2020.

[29] D. Politte and D. Snyder, "Corrections for accidental coincidences and attenuation in maximum-likelihood image reconstruction for positron-emission tomography," *IEEE Transactions on Medical Imaging*, vol. 10, no. 1, pp. 82–89, 1991.

[30] J. F. Oliver and M. Rafecas, "Modelling random coincidences in positron emission tomography by using singles and prompts: A comparison study," *PLOS ONE*, vol. 11, p. e0162096, 9 2016.

[31] X. Yu, X. Zhang, H. Zhang, and et al., "Requirements of scintillation crystals with the development of PET scanners," *Crystals*, vol. 12, no. 9, 2022.

[32] C. L. Melcher, "Scintillation crystals for PET," *Journal of Nuclear Medicine*, vol. 41, pp. 1051–1055, 6 2000.

[33] P. Lecoq, A. Gektin, and M. Korzhik, "Scintillation and inorganic scintillators," pp. 1–41, 2017.

[34] W. Chewpraditkul, L. Swiderski, M. Moszynski, and et al., "Scintillation properties of LuAG:Ce, YAG:Ce and LYSO:Ce crystals for gamma-ray detection," *IEEE Transactions on Nuclear Science*, vol. 56, no. 6, pp. 3800–3805, 2009.

[35] H. Alva-Sánchez, A. Zepeda-Barrios, V. D. Díaz-Martínez, and et al., "Understanding the intrinsic radioactivity energy spectrum from 176Lu in LYSO/LSO scintillation crystals," *Scientific Reports 2018 8:1*, vol. 8, pp. 1–7, 11 2018.

[36] W. V. Vogel, S. C. van der Marck, and M. W. Versleijen, "Challenges and future options for the production of lutetium-177," *European Journal of Nuclear Medicine and Molecular Imaging*, vol. 48, pp. 2329–2335, 7 2021.

[37] M. I. Freedenberg, R. D. Badawi, A. F. Tarantal, and S. R. Cherry, "Performance and limitations of positron emission tomography (pet) scanners for imaging very low activity sources," *Physica Medica*, vol. 30, no. 1, pp. 104–110, 2014.

[38] S. Usman and A. Patil, "Radiation detector deadtime and pile up: A review of the status of science," *Nuclear Engineering and Technology*, vol. 50, no. 7, pp. 1006–1016, 2018.

[39] E. Berg and S. R. Cherry, "Innovations in instrumentation for positron emission tomography," *Seminars in Nuclear Medicine*, vol. 48, pp. 311–331, 7 2018.

[40] P. Lecoq, C. Morel, J. O. Prior, and et al., "Roadmap toward the 10 ps time-of-flight PET challenge," *Physics in Medicine & Biology*, vol. 65, p. 21RM01, 10 2020.

[41] P. Lecoq, "On the way to the 10 ps time-of-flight PET challenge," *The European Physical Journal Plus 2022 137:8*, vol. 137, pp. 1–7, 8 2022.

[42] D. L. Bailey, D. W. Townsend, P. E. Valk, and M. N. Maisey, Eds., *Positron Emission Tomography*. Springer London, 2005.

[43] G. A. Prenosil, H. Sari, M. F. Urstner, and et al., "Performance characteristics of the biograph vision quadra PET/CT system with a long axial field of view using the NEMA NU 2-2018 standard," *J Nucl Med*, vol. 63, pp. 476–484, 2022.

[44] F. H. Fahey, "Data acquisition in PET imaging," *Journal of Nuclear Medicine Technology*, vol. 30, no. 2, pp. 39–49, 2002.

[45] nema, "NEMA standards publication NU 2-2018 performance measurements of positron emission tomographs (pets)," 2018.

[46] K. Gong, K. Kim, J. Cui, and et al., "The evolution of image reconstruction in PET," *PET Clinics*, vol. 16, pp. 533–542, 10 2021.

[47] C. Comtat, F. Bataille, C. Michel, and et al., "OSEM-3D reconstruction strategies for the ECAT HRRT," in *IEEE Symposium Conference Record Nuclear Science 2004.*, vol. 6, 2004, pp. 3492–3496 Vol. 6.

[48] A. Iriarte, R. Marabini, S. Matej, and et al., "System models for PET statistical iterative reconstruction: A review," *Computerized Medical Imaging and Graphics*, vol. 48, pp. 30–48, 3 2016.

[49] H. Hudson and R. Larkin, "Accelerated image reconstruction using ordered subsets of projection data," *IEEE Transactions on Medical Imaging*, vol. 13, no. 4, pp. 601–609, 1994.

[50] M. Jacobson, R. Levkovitz, A. Ben-Tal, and et al., "Model-based normalization for iterative 3D PET image reconstruction," *Physics in Medicine & Biology*, vol. 47, p. 2773, 7 2002.

[51] E. Vicente, J. J. Vaquero, S. Espana, and et al., "Normalization in 3d pet: Dependence on the activity distribution of the source," in *2006 IEEE Nuclear Science Symposium Conference Record*, vol. 4, 2006, pp. 2206–2209.

[52] A. Alessio, P. Kinahan, and T. Lewellen, "Modeling and incorporation of system response functions in 3-d whole body PET," *IEEE Transactions on Medical Imaging*, vol. 25, no. 7, pp. 828–837, 2006.

[53] V. Panin, F. Kehren, C. Michel, and et al., "Fully 3-d PET reconstruction with system matrix derived from point source measurements," *IEEE Transactions on Medical Imaging*, vol. 25, no. 7, pp. 907–921, 2006.

[54] B. W. Jakoby, Y. Bercier, C. C. Watson, and et al., "Performance characteristics of a new LSO PET/CT scanner with extended axial field-of-view and PSF reconstruction," *IEEE Transactions on Nuclear Science*, vol. 56, no. 3, pp. 633–639, 2009.

[55] A. Rahmim, J. Qi, and V. Sossi, "Resolution modeling in PET imaging: Theory, practice, benefits, and pitfalls," *Medical Physics*, vol. 40, no. 6Part1, p. 064301, 2013.

[56] A. M. Alessio, C. W. Stearns, S. Tong, and et al., "Application and evaluation of a measured spatially variant system model for PET image reconstruction," *IEEE Transactions on Medical Imaging*, vol. 29, pp. 938–949, 3 2010.

[57] D. Brasse, P. E. Kinahan, C. Lartizien, and et al., "Correction methods for random coincidences in fully 3D whole-body PET: Impact on data and image quality," *Journal of Nuclear Medicine*, vol. 46, no. 5, pp. 859–867, 2005.

[58] G. Krokos, J. MacKewn, J. Dunn, and et al., "A review of PET attenuation correction methods for PET-MR," *EJNMMI Physics 2023 10:1*, vol. 10, pp. 1–45, 9 2023.

[59] D. L. Snyder, M. I. Miller, L. J. Thomas, and et al., "Noise and edge artifacts in maximum-likelihood reconstructions for emission tomography," *IEEE Transactions on Medical Imaging*, vol. 6, pp. 228–238, 1987.

[60] Z. Hu, W. Wang, E. E. Gualtieri, and et al., "An LOR-based fully-3D PET image reconstruction using a blob-basis function," in *2007 IEEE Nuclear Science Symposium Conference Record*, vol. 6, 2007, pp. 4415–4418.

[61] E. Guedj, A. Varrone, R. Boellaard, and et al., "EANM procedure guidelines for brain PET imaging using [18F]FDG, version 3," *European Journal of Nuclear Medicine and Molecular Imaging 2021 49:2*, vol. 49, pp. 632–651, 12 2021.

[62] A. Verger, A. Kas, J. Darcourt, and et al., "Pet imaging in neuro-oncology: An update and overview of a rapidly growing area," *Cancers 2022, Vol. 14, Page 1103*, vol. 14, p. 1103, 2 2022.

[63] E. T. Sarcan, M. Silindir-Gunay, A. Y. Ozer, and et al., "89Zr as a promising radionuclide and it's applications for effective cancer imaging," *Journal of Radioanalytical and Nuclear Chemistry 2021 330:1*, vol. 330, pp. 15–28, 8 2021.

[64] A. Polyak and T. L. Ross, "Nanoparticles for SPECT and PET imaging: Towards personalized medicine and theranostics," *Current Medicinal Chemistry*, vol. 25, pp. 4328–4353, 12 2018.

[65] R. L. Montana, I. H. Gonzalez, A. A. Ramirez, and et al., "Yttrium-90 – current status, expected availability and applications of a high beta energy emitter," *Current Radiopharmaceuticals*, vol. 5, pp. 253–263, 11 2012.

[66] R. G. Selwyn, R. J. Nickles, B. R. Thomadsen, and et al., "A new internal pair production branching ratio of 90y: The development of a non-destructive assay for 90y and 90sr," *Applied Radiation and Isotopes*, vol. 65, pp. 318–327, 3 2007.

[67] L. Carrion-Martin, J. O. Rincón, A. Rotger, and et al., "Radioembolization in liver tumors," *Revista Española de Medicina Nuclear e Imagen Molecular (English Edition)*, vol. 38, pp. 370–381, 11 2019.

[68] N. Aide, C. Lasnon, A. Kesner, and et al., "New PET technologies – embracing progress and pushing the limits," *European Journal of Nuclear Medicine and Molecular Imaging*, vol. 48, pp. 2711–2726, 8 2021.

[69] F. Hashimoto, Y. Onishi, K. Ote, and et al., "Deep learning-based PET image denoising and reconstruction: a review," *Radiological Physics and Technology*, vol. 17, pp. 24–46, 2024.

[70] B. A. Spencer, E. Berg, J. P. Schmall, and et al., "Performance evaluation of the uEXPLORER total-body PET/CT scanner based on NEMA NU 2-2018 with additional tests to characterize PET scanners with a long axial field of view," *Journal of Nuclear Medicine*, vol. 62, pp. 861–870, 6 2021.

[71] B. Dai, Z. A. Elcadi, M. Mkimel, and et al., "Performance evaluation of the pennpet explorer with expanded axial coverage," *Physics in Medicine & Biology*, vol. 68, p. 095007, 4 2023.

[72] S. Xue, R. Guo, K. P. Bohn, and et al., "A cross-scanner and cross-tracer deep learning method for the recovery of standard-dose imaging quality from low-dose pet," *European Journal of Nuclear Medicine and Molecular Imaging*, vol. 49, p. 1843, 5 2022.

[73] E. Mumcuoglu, R. Leahy, and S. Cherry, "Bayesian reconstruction of PET images: methodology and performance analysis," *Physics in Medicine & Biology*, vol. 41, no. 9, p. 1777, sep 1996.

[74] A. Buades, B. Coll, and J. M. Morel, "A non-local algorithm for image denoising," *Proceedings - 2005 IEEE Computer Society Conference on Computer Vision and Pattern Recognition, CVPR 2005*, vol. II, pp. 60–65, 2005.

[75] B. T. Christian, N. T. Vandehey, J. M. Floberg, and et al., "Dynamic PET denoising with HYPR processing," *Journal of Nuclear Medicine*, vol. 51, pp. 1147–1154, 7 2010.

[76] K. He, J. Sun, and X. Tang, "Guided image filtering," *IEEE Transactions on Pattern Analysis and Machine Intelligence*, vol. 35, pp. 1397–1409, 2013.

[77] D. L. Snyder and M. I. Miller, "The use of sieves to stabilize images produced with the EM algorithm for emission tomography," *IEEE Transactions on Nuclear Science*, vol. 32, pp. 3864–3872, 1985.

[78] S. Ziegler, B. W. Jakoby, H. Braun, and et al., "Nema image quality phantom measurements and attenuation correction in integrated PET/MR hybrid imaging," *EJNMMI Physics*, vol. 2, pp. 1–14, 12 2015.

[79] I. Rausch, J. G. Mannheim, J. Kupferschläger, and et al., "Image quality assessment along the one metre axial field-of-view of the total-body biograph vision quadra PET/CT system for 18F-FDG," *EJNMMI Physics*, vol. 9, pp. 1–17, 12 2022.

[80] F. Hashimoto, K. Ote, and Y. Onishi, "PET image reconstruction incorporating deep image prior and a forward projection model," *IEEE Transactions on Radiation and Plasma Medical Sciences*, vol. 6, pp. 841–846, 11 2022.

[81] W. Qi, M. Miyahara, L. Yang, and et al., "A robust implementation of non-linear post-filters on PET images," *Journal of Nuclear Medicine*, vol. 62, 2021.

[82] A. J. Reader and B. Pan, "AI for PET image reconstruction," *British Journal of Radiology*, vol. 96, 10 2023.

[83] A. Bousse, V. S. S. Kandarpa, K. Shi, and et al., "A review on low-dose emission tomography post-reconstruction denoising with neural network approaches," *IEEE Transactions on Radiation and Plasma Medical Sciences*, 12 2024.

[84] L. Xiang, Y. Qiao, D. Nie, and et al., "Deep auto-context convolutional neural networks for standard-dose PET image estimation from low-dose PET/MRI," *Neurocomputing*, vol. 267, pp. 406–416, 12 2017.

[85] A. Sanaat, H. Arabi, I. Mainta, and et al., "Projection space implementation of deep learning–guided low-dose brain PET imaging improves performance over implementation in image space," *Journal of Nuclear Medicine*, vol. 61, no. 9, pp. 1388–1396, 2020.

[86] H. Liu, J. Wu, W. Lu, and et al., "Noise reduction with cross-tracer and cross-protocol deep transfer learning for low-dose pet," *Physics in Medicine & Biology*, vol. 65, no. 18, p. 185006, sep 2020.

[87] J. Cui, K. Gong, N. Guo, and et al., "Pet image denoising using unsupervised deep learning," *European journal of nuclear medicine and molecular imaging*, vol. 46, p. 2780, 12 2019.

[88] T. A. Song, F. Yang, and J. Dutta, "Noise2void: unsupervised denoising of PET images," *Physics in medicine and biology*, vol. 66, 11 2021.

[89] G. Schramm, D. Rigie, T. Vahle, and et al., "Approximating anatomically-guided PET reconstruction in image space using a convolutional neural network," *NeuroImage*, vol. 224, p. 117399, 1 2021.

[90] Y. Onishi, F. Hashimoto, K. Ote, and et al., "Anatomical-guided attention enhances unsupervised PET image denoising performance," *Medical Image Analysis*, vol. 74, p. 102226, 12 2021.

[91] Z. Xie, T. Li, X. Zhang, and et al., "Anatomically aided PET image reconstruction using deep neural networks," *Medical Physics*, vol. 48, pp. 5244–5258, 9 2021.

[92] L. Zhou, J. D. Schaefferkoetter, I. W. Tham, and et al., "Supervised learning with cyclegan for low-dose FDG PET image denoising," *Medical image analysis*, vol. 65, 10 2020.

[93] Y. Fu, S. Dong, M. Niu, and et al., "AIGAN: Attention–encoding integrated generative adversarial network for the reconstruction of low-dose CT and low-dose PET images," *Medical Image Analysis*, vol. 86, p. 102787, 5 2023.

[94] J. Ho, A. Jain, and P. Abbeel, "Denoising diffusion probabilistic models," *Advances in Neural Information Processing Systems*, vol. 2020-December, 6 2020.

[95] K. Gong, K. Johnson, G. El Fakhri, and et al., "PET image denoising based on denoising diffusion probabilistic model," *European Journal of Nuclear Medicine*

and Molecular Imaging, vol. 51, no. 2, pp. 358–368, 2024.

[96] N. Kim, D. Jang, S. Lee, and et al., "Unsupervised image denoising with frequency domain knowledge," *32nd British Machine Vision Conference, BMVC 2021*, 11 2021.

[97] X. Chen, Z. Liu, S. Xie, and et al., "Deconstructing denoising diffusion models for self-supervised learning," 1 2024.

[98] V. Antun, F. Renna, C. Poon, and et al., "On instabilities of deep learning in image reconstruction and the potential costs of AI," *Proceedings of the National Academy of Sciences of the United States of America*, vol. 117, pp. 30 088–30 095, 12 2020.

[99] N. Maleki, B. Padmanabhan, and K. Dutta, "AI hallucinations: A misnomer worth clarifying," 1 2024.

[100] S. Pan, E. Abouei, J. Peng, and et al., "Full-dose PET synthesis from low-dose PET using 2D high efficiency denoising diffusion probabilistic model," in *Medical Imaging 2024: Clinical and Biomedical Imaging*, B. S. Gimi and A. Krol, Eds., vol. 12930, International Society for Optics and Photonics. SPIE, 2024, p. 129301Q.

[101] H. Xie, Q. Liu, B. Zhou, and et al., "Unified noise-aware network for low-count PET denoising with varying count levels," *IEEE Transactions on Radiation and Plasma Medical Sciences*, 2023.

[102] J. V. Sluis, J. D. Jong, J. Schaar, and et al., "Performance characteristics of the digital biograph vision PET/CT system," *Journal of Nuclear Medicine*, vol. 60, pp. 1031–1036, 7 2019.

[103] K. K. Ghosh, P. Padmanabhan, C. T. Yang, and et al., "Dealing with pet radiometabolites," *EJNMMI Research*, vol. 10, 2020.

[104] M. Ljungberg, S.-E. Strand, and M. A. King, "Monte carlo calculations in nuclear medicine : applications in diagnostic imaging," p. 337, 2013.

[105] R. L. Harrison, "Simulation of medical imaging systems: Emission and transmission tomography," *Handbook of Particle Detection and Imaging*, pp. 1095–1124, 1 2012.

[106] H. Zaidi, Ed., *Monte Carlo Calculations in Nuclear Medicine (Second Edition)*, ser. 2053-2563. IOP Publishing, 2022.

[107] R. A. Forster and T. N. K. Godfrey, "MCNP - a general monte carlo code for neutron and photon transport," *Monte-Carlo Methods and Applications in Neutronics, Photonics and Statistical Physics*, pp. 33–55, 7 1985.

[108] S. Agostinelli, J. Allison, K. Amako, and et al., "Geant4—a simulation toolkit," *Nuclear Instruments and Methods in Physics Research Section A: Accelerators, Spectrometers, Detectors and Associated Equipment*, vol. 506, pp. 250–303, 7 2003.

[109] S. Espãa, J. L. Herraiz, E. Vicente, and et al., "PeneloPET, a monte carlo PET simulation tool based on penelope: features and validation," *Physics in Medicine & Biology*, vol. 54, p. 1723, 2 2009.

[110] J. Allison, K. Amako, J. Apostolakis, and et al., "Recent developments in Geant4," *Nuclear Instruments and Methods in Physics Research Section A: Accelerators, Spectrometers, Detectors and Associated Equipment*, vol. 835, pp. 186–225, 11 2016.

[111] P. Arce, P. Rato, M. Cañadas, and et al., "GAMOS: A GEANT4-based easy and flexible framework for nuclear medicine applications," *IEEE Nuclear Science Symposium Conference Record*, pp. 3162–3168, 2008.

[112] S. Jan, G. Santin, D. Strul, and et al., "GATE: a simulation toolkit for PET and spect," *Physics in Medicine & Biology*, vol. 49, p. 4543, 9 2004.

[113] S. Jan, D. Benoit, E. Becheva, and et al., "GATE v6: a major enhancement of the GATE simulation platform enabling modelling of ct and radiotherapy," *Physics in Medicine & Biology*, vol. 56, p. 881, 1 2011.

[114] D. Sarrut, M. Bała, M. B. s, and et al., "Advanced monte carlo simulations of emission tomography imaging systems with GATE," *Physics in Medicine & Biology*, vol. 66, p. 10TR03, 5 2021.

[115] L. Lu, H. Zhang, Z. Bian, and et al., "Validation of a monte carlo simulation of the inveon PET scanner using GATE," *Nuclear Instruments and Methods in Physics Research Section A: Accelerators, Spectrometers, Detectors and Associated Equipment*, vol. 828, pp. 170–175, 8 2016.

[116] S. Lee, J. Gregor, and D. Osborne, "Development and validation of a complete GATE model of the siemens inveon trimodal imaging platform," *Molecular Imaging*, vol. 12, p. 7290.2013.00058, 10 2013.

[117] N. Zeraatkar, M. R. Ay, A. R. Kamali-Asl, and et al., "Accurate monte carlo modeling and performance assessment of the XPET subsystem of the flex triumph preclinical PET/CT scanner," *Medical Physics*, vol. 38, pp. 1217–1225, 3 2011.

[118] S. Pells, D. M. Cullen, D. Deidda, and et al., "Quantitative validation of monte carlo SPECT simulation: application to a mediso AnyScan GATE simulation," *EJNMMI Physics*, vol. 10, pp. 1–25, 12 2023.

[119] A. Merlet, B. Presles, K. H. Su, and et al., "Validation of a discovery MI 4-ring model according to the NEMA NU 2-2018 standards: from monte carlo simulations to clinical-like reconstructions," *EJNMMI Physics*, vol. 11, 12 2024.

[120] B. Aklan, B. W. Jakoby, C. C. Watson, and et al., "GATE monte carlo simulations for variations of an integrated PET/MR hybrid imaging system based on the biograph mMR model," *Physics in Medicine & Biology*, vol. 60, p. 4731, 6 2015.

[121] C. M. Pommranz, F. P. Schmidt, J. G. Mannheim, and et al., "Design and performance simulation studies of a breast PET insert integrable into a clinical whole-body PET/MRI scanner," *Physics in Medicine & Biology*, vol. 68, p. 055019, 3 2023.

[122] M. E. Katib, E. M. Chakir, R. Sebihi, and et al., "Validation of a monte carlo model of the uEXPLORER total-body PET scanner using GATE code," *Radiation Physics and Chemistry*, vol. 210, p. 111052, 9 2023.

[123] H. Rezaei, P. Sheikhzadeh, P. Ghafarian, and et al., "Accurate modeling and performance evaluation of a total-body PET scanner using monte carlo simulations," *Medical Physics*, vol. 50, pp. 6815–6827, 11 2023.

[124] V. Viswanath, A. R. Pantel, M. E. Daube-Witherspoon, and et al., "Quantifying bias and precision of kinetic parameter estimation on the pennpet explorer, a long axial field-of-view scanner," *IEEE Transactions on Radiation and Plasma Medical Sciences*, vol. 4, pp. 735–749, 11 2020.

[125] M. M. Peña-Acosta, S. Gallardo, M. Lorduy-Alós, and et al., "Application of NEMA protocols to verify GATE models based on the digital biograph vision and the biograph vision quadra scanners," *Zeitschrift für Medizinische Physik*, 2 2024.

[126] M. Dadgar, S. Parzych, J. Baran, and et al., "Comparative studies of the sensitivities of sparse and full geometries of total-body PET scanners built from crystals and plastic scintillators," *EJNMMI Physics*, vol. 10, p. 62, 10 2023.

[127] M. Abi-Akl, M. Dadgar, Y. Toufique, and et al., "Monte carlo simulation of the system performance of a long axial field-of-view PET based on monolithic lyso detectors," *EJNMMI Physics*, vol. 10, p. 37, 6 2023.

[128] S. Vandenberghe, F. M. Muller, N. Withofs, and et al., "Walk-through flat panel total-body PET: a patient-centered design for high throughput imaging at lower cost using DOI-capable high-resolution monolithic detectors," *European journal of nuclear medicine and molecular imaging*, vol. 50, pp. 3558–3571, 10 2023.

[129] E. Mikhaylova, M. Jehl, D. Deidda, and et al., "Simulated NEMA nu2 performance of the ultra-compact clinical NeuroLF brain PET," in *2022 IEEE Nuclear Science Symposium and Medical Imaging Conference (NSS/MIC)*, 2022, pp. 1–6.

[130] M. Zvolský, S. Seeger, M. Schaar, C. Schmidt, and M. Rafecas, "MERMAID - A PET Prototype for Small Aquatic Animal Imaging," in *2019 IEEE Nuclear Science Symposium and Medical Imaging Conference (NSS/MIC)*, 2019.

[131] R. Brun and F. Rademakers, "ROOT - an object oriented data analysis framework," in *Proceedings AIHENP'96 Workshop*. Lausanne, 1996, pp. 81–86, see also "ROOT" [software], Release v6.24/06, 29/09/2022.

[132] C. Pommranz, "Interdisciplinary applications of automated computational workflows for XMM-newton cross-calibration and monte carlo simulations of eROSITA and a breast PET insert," Ph.D. dissertation, Eberhard Karls Universität Tübingen, September 2024.

[133] A. Pépin, S. Stute, S. Jan, and et al., "Normalization of monte carlo PET data using GATE," *IEEE Nuclear Science Symposium Conference Record*, pp. 4196–4200, 2011.

[134] B. Krose and P. van der Smagt, *An Introduction to Neural Networks*, 01 1996.

[135] H. Kinsley and D. Kukieła, *Neural Networks from Scratch (NNFS)*, 2020.

[136] V. Sze, Y.-H. Chen, T.-J. Yang, and et al., "Efficient processing of deep neural networks: A tutorial and survey," *Proceedings of the IEEE*, vol. 105, no. 12, pp. 2295–2329, 2017.

[137] A. Canziani, A. Paszke, and E. Culurciello, "An analysis of deep neural network models for practical applications," 2017.

[138] J. Gu, Z. Wang, J. Kuen, and et al., "Recent advances in convolutional neural networks," *Pattern Recognition*, vol. 77, pp. 354–377, 5 2018.

[139] Z. Li, F. Liu, W. Yang, and et al., "A survey of convolutional neural networks: Analysis, applications, and prospects," *IEEE Transactions on Neural Networks and Learning Systems*, vol. 33, no. 12, pp. 6999–7019, 2022.

[140] D. P. Kingma and J. L. Ba, "Adam: A method for stochastic optimization," *3rd International Conference on Learning Representations, ICLR 2015 - Conference Track Proceedings*, 12 2014.

[141] S. Y. Yie, K. M. Kim, S. Bae, and et al., "Effects of loss functions and supervision methods on total-body PET denoising," *IEEE Transactions on Radiation and Plasma Medical Sciences*, 2023.

[142] O. Ronneberger, P. Fischer, and T. Brox, "U-Net: Convolutional networks for biomedical image segmentation," *arXiv preprint arXiv:1505.04597*, 2015.

[143] Özgün Çiçek, A. Abdulkadir, S. S. Lienkamp, T. Brox, and O. Ronneberger, "3D U-Net: Learning dense volumetric segmentation from sparse annotation," *Lecture Notes in Computer Science (including subseries Lecture Notes in Artificial Intelligence and Lecture Notes in Bioinformatics)*, vol. 9901 LNCS, pp. 424–432, 6 2016.

[144] "NEMA standards publication NU 4 2008: Performance measurements for small animal positron emission tomographs," *National Electrical Manufacturers Association*, 2008.

[145] J. wu Kang and Q. xian Ma, "The role and impact of 3D printing technologies in casting," *China Foundry*, vol. 14, pp. 157–168, 5 2017.

[146] J. Horvath and R. Cameron, *Mastering 3D Printing: a Guide to Modeling, Printing, and Prototyping, Second Edition.* Apress Media LLC, 1 2020.

[147] S. F. Iftekar, A. Aabid, A. Amir, and et al., "Advancements and limitations in 3D printing materials and technologies: A critical review," *Polymers*, vol. 15, no. 11, 2023.

[148] O. A. Mohamed, S. H. Masood, and J. L. Bhowmik, "Optimization of fused deposition modeling process parameters: a review of current research and future prospects," *Advances in Manufacturing*, vol. 3, pp. 42–53, 3 2015.

[149] E. Elmoujarkach, S. Seeger, C. Schareck, and et al., "Characterization of using infused PLA for 3D printed radiation shielding," *Current Directions in Biomedical Engineering*, vol. 8, no. 2, 2022.

[150] U. Chadha, A. Abrol, N. P. Vora, and et al., "Performance evaluation of 3D printing technologies: a review, recent advances, current challenges, and future directions," *Progress in Additive Manufacturing 2022 7:5*, vol. 7, pp. 853–886, 2 2022.

[151] E. M. Maines, M. K. Porwal, C. J. Ellison, and et al., "Sustainable advances in sla/dlp 3D printing materials and processes," *Green Chemistry*, vol. 23, pp. 6863–6897, 9 2021.

[152] K. Son, J.-H. Lee, K.-B. Lee, and et al., "Comparison of intaglio surface trueness of interim dental crowns fabricated with sla 3D printing, dlp 3D printing, and milling technologies," *Healthcare 2021, Vol. 9, Page 983*, vol. 9, p. 983, 8 2021.

[153] E. Béchet, J. C. Cuilliere, and F. Trochu, "Generation of a finite element MESH from stereolithography (STL) files," *Computer-Aided Design*, vol. 34, pp. 1–17, 1 2002.

[154] J. D. Hiller and H. Lipson, "STL 2.0: A proposal for a universal multi-material additive manufacturing file format," 9 2009.

[155] X. Li, "G-code re-compilation and optimization for faster 3D printing," *Lecture Notes in Computer Science (including subseries Lecture Notes in Artificial Intelligence and Lecture Notes in Bioinformatics)*, vol. 13149 LNCS, pp. 104–116, 2022.

[156] M. M. Prabhakar, A. K. Saravanan, A. H. Lenin, and et al., "A short review on 3D printing methods, process parameters and materials," *Materials Today: Proceedings*, vol. 45, pp. 6108–6114, 1 2021.

[157] Eye Creations, "Eye creations - creative web solutions," 2023.

[158] V. Filippou and C. Tsoumpas, "Recent advances on the development of phantoms using 3D printing for imaging with CT, MRI, PET, SPECT, and ultrasound," *Medical physics*, vol. 45, no. 9, pp. e740–e760, 2018.

[159] R. Tino, A. Yeo, M. Leary, and et al., "A systematic review on 3D-printed imaging and dosimetry phantoms in radiation therapy," *Technology in cancer research & treatment*, vol. 18, p. 1533033819870208, 2019.

[160] "NEMA standards publication NU 2 2018: Performance measurements of positron emission tomographs (pet)," *National Electrical Manufacturers Association*, 2018.

[161] M. F. Bieniosek, B. J. Lee, and C. S. Levin, "3d printing for cost-effective, customized, reusable multi-modality imaging phantoms," *IEEE Nuclear Science Symposium Conference Record*, 2013.

[162] F. Zell, J. Mannheim, M. Grehn, and et al., "3D-printed standardized phantoms for small animal PET and MRI: a comparison study," *Transactions on Additive Manufacturing Meets Medicine*, vol. 1, no. 1, 2019.

[163] A. P. Robinson, J. Tipping, D. M. Cullen, D. Hamilton, R. Brown, A. Flynn, C. Oldfield, E. Page, E. Price, A. Smith, and R. Snee, "Organ-specific SPECT activity calibration using 3D printed phantoms for molecular radiotherapy dosimetry," *EJNMMI Phys.*, vol. 3, no. 1, p. 12, Dec. 2016.

[164] T. Läppchen, L. P. Meier, M. Fürstner, G. A. Prenosil, T. Krause, A. Rominger, B. Klaeser, and M. Hentschel, "3D printing of radioactive phantoms for nuclear medicine imaging," *EJNMMI Physics*, vol. 7, no. 1, Apr. 2020.

[165] J. I. Gear, C. Cummings, J. Sullivan, and et al., "Radioactive 3D printing for the production of molecular imaging phantoms," *Physics in Medicine & Biology*, vol. 65, no. 17, p. 175019, Sep. 2020.

[166] D. Gillett, D. Marsden, S. Ballout, and et al., "3D printing 18F radioactive phantoms for PET imaging," *EJNMMI Physics*, vol. 8, no. 1, Apr. 2021.

[167] L. P. Meier, T. Läppchen, M. Hentschel, and et al., "3D printing of calibrated Germanium-68 PET phantoms without inactive walls," *IEEE Transactions on Radiation and Plasma Medical Sciences*, pp. 1–1, 2023.

[168] M. A. Park, A. Mahmood, R. E. Zimmerman, and et al., "Adsorption of metallic radionuclides on plastic phantom walls," *Medical Physics*, vol. 35, pp. 1606–1610, 4 2008.

[169] T. J. Bradshaw, M. J. Voorbach, D. R. Reuter, and et al., "Image quality of Zr-89 PET imaging in the Siemens microPET Focus 220 preclinical scanner," *Molecular imaging and biology*, vol. 18, pp. 377–385, 2016.

[170] C. M. Pommranz, E. Elmoujarkach, J. Cabello, and et al., "Development and validation of a monte carlo simulation workflow for a total-body PET scanner," *European journal of nuclear medicine and molecular imaging*, vol. 50, pp. 690–691, 9 2023.

[171] C. Pommranz, E. Elmoujarkach, J. Cabello, and et al., "Development and initial validation of two simulation workflows using GATE for a total-body PET/CT scanner," pp. 1–1, 12 2023.

[172] C. M. Pommranz, E. Elmoujarkach, J. Cabello, and et al., "Simulation studies and experimental model validation of the biograph vision quadra," *Nuklearmedizin - NuclearMedicine*, vol. 62, p. V8, 4 2023.

[173] V. Beaudoux, G. Blin, B. Barbrel, and et al., "Geant4 physics list comparison for the simulation of phase-contrast mammography (xpulse project)," *Physica Medica*, vol. 60, pp. 66–75, 2019.

[174] J. E. Breeding, W. F. Jones, J. H. Reed, and et al., "PETLINK™ stream buffer: Using an FPGA-based RAID controller with solid-state drives to achieve lossless, high count-rate 64-bit coincidence event acquisition for 3-D pet," in *2011 IEEE Nuclear Science Symposium Conference Record*, 2011, pp. 3894–3900.

[175] M. Teimoorisichani, V. Panin, H. Rothfuss, and et al., "A CT-less approach to quantitative PET imaging using the LSO intrinsic radiation for long-axial FOV PET scanners," *Medical Physics*, vol. 49, p. 309, 1 2022.

[176] W. P. Segars, B. M. Tsui, J. Cai, and et al., "Application of the 4d xcat phantoms in biomedical imaging and beyond," *IEEE transactions on medical imaging*, vol. 37, p. 680, 3 2018.

[177] S. Zincirkeser, E. Şahin, M. Halac, and et al., "Standardized uptake values of normal organs on 18F-Fluorodeoxyglucose positron emission tomography and computed tomography imaging," *Journal of International Medical Research*, vol. 35, pp. 231–236, 3 2007.

[178] P. Dryák and J. Šolc, "Measurement of the branching ratio related to the internal pair production of Y-90," *Applied Radiation and Isotopes*, vol. 156, p. 108942, 2 2020.

[179] E. Elmoujarkach, S. Seeger, N. Möller, and et al., "Development and characterization of 3D printed radioactive phantoms for high resolution pet," in *2022 IEEE Nuclear Science Symposium and Medical Imaging Conference (NSS/MIC)*, 2022, pp. 1–2.

[180] S. Seeger, E. Elmoujarkach, N. Möller, and et al., "3D printed radioactive phantoms for positron emission tomography," vol. 4, no. S1 (Supplement). Transactions on Additive Manufacturing Meets Medicine, 2022, p. ID 640.

[181] E. Elmoujarkach, S. Seeger, C. Schmidt, and et al., "First 3D printed radioactive ^{89}Zr phantoms for positron emission tomography," vol. 5. Transactions on Additive Manufacturing Meets Medicine, 2023, p. Vol. 5 No. S1 (2023): Trans. AMMM Supplement.

[182] S. Weigel, E. Elmoujarkach, L. Rauscher, and et al., "A moveable 3-D printed phantom setup for evaluation of motion induced artefacts in a total-body PET/CT," *Nuklearmedizin - NuclearMedicine*, vol. 63, p. V69, 2024.

[183] P. M. Linder, E. Elmoujarkach, J. S. L. Koehnlein, and et al., "Feasibility study on late 89Zr-immuno total-body PET based on patient simulation and a customized longterm-stable phantom." Georg Thieme Verlag, 2024.

[184] S. Seeger, H. P. Vo, A. Bolke, and et al., "Characterisation of the upgraded MERMAID prototype, a PET/CT device for small aquatic animals," in

2022 IEEE Nuclear Science Symposium and Medical Imaging Conference (NSS/MIC), 2022, pp. 1–2.

[185] S. Seeger, "Entwicklung und charakterisierung eines dedizierten PET-prototyps fuer die in-vivo bildgebung von adulten zebrafischen und kleinen wassertieren," Ph.D. dissertation, Universität zu Lübeck, October 2024.

[186] S. Seeger, M. Zvolskỳ, S. Melikov, M. Frerkes, and M. Rafecas, "Dedicated chamber for multimodal in vivo imaging of adult zebrafish," *Zebrafish*, vol. 19, no. 2, pp. 67–70, 2022.

[187] L. Nazario, J. Vierstraete, J. Bek, S. Neyt, N. V. Overberghe, R. Dierckx, A. Willaert, R. S. Jeckel, Cristina Maria M.and da Silva, J. Doorduin, and E. de Vries, "In vivo PET/CT imaging in zebrafish using 18F-FDG and 18F-NaF," in *European Molecular Imaging Meeting - EMIM 2019*, European Society of Molecular Imaging, Ed., no. 293, 2019.

[188] M. Zvolský, M. Schaar, S. Seeger, and et al., "Development of a digital zebrafish phantom and its application to dedicated small-fish pet," *Physics in Medicine & Biology*, vol. 67, no. 17, p. 175005, aug 2022.

[189] J. P. Chung, Y. M. Seong, T. Y. Kim, and et al., "Development of a PMMA phantom as a practical alternative for quality control of gamma knife dosimetry," *Radiation Oncology*, vol. 13, no. 1, p. 176, 2018.

[190] J. Seco and P. M. Evans, "Assessing the effect of electron density in photon dose calculations," *Medical Physics*, vol. 33, no. 2, pp. 540–552, 2006.

[191] E. M. Strome, S. Jivan, and D. J. Doudet, "Quantitative in vitro phosphor imaging using [3H] and [18F] radioligands: the effects of chronic desipramine treatment on serotonin 5-HT2 receptors," *Journal of Neuroscience Methods*, vol. 141, no. 1, pp. 143–154, 2005.

[192] S. S. Adler, J. Seidel, and P. L. Choyke, "Advances in preclinical pet," *Seminars in Nuclear Medicine*, vol. 52, no. 3, pp. 382–402, 2022, advancement in Instrumentation for Molecular Imaging.

[193] Q. Bao, D. Newport, M. Chen, and et al., "Performance evaluation of the inveon dedicated PET preclinical tomograph based on the NEMA nu-4 standards," *Journal of Nuclear Medicine*, vol. 50, no. 3, pp. 401–408, 2009.

[194] "Pabdo-man."

[195] M. Goyat, S. Ray, and P. Ghosh, "Innovative application of ultrasonic mixing to produce homogeneously mixed nanoparticulate-epoxy composite of improved physical properties," *Composites Part A: Applied Science and Manufacturing*, vol. 42, no. 10, pp. 1421–1431, 2011.

[196] S. B. Abdul-Fatah, M. Zamburlini, S. G. Halders, B. Brans, G. J. Teule, and G. J. Kemerink, "Identification of a shine-through artifact in the trachea with 124I PET/CT," *Journal of Nuclear Medicine*, vol. 50, no. 6, pp. 909–911, 2009.

[197] A. Kolb, A. W. Sauter, L. Eriksson, and et al., "Shine-through in PET/MR imaging: effects of the magnetic field on positron range and subsequent image artifacts," *Journal of Nuclear Medicine*, vol. 56, no. 6, pp. 951–954, 2015.

[198] Y. Tomita, Y. Ichikawa, and H. Sakuma, "Shine-through artifact due to high-radioactivity bladder and bowel gas in ^{18}F-FDG PET/CT: impact of time-of-flight algorithm and radioactivity concentration of urine in the bladder on the occurrence of the artifacts," *Annals of Nuclear Medicine*, vol. 36, no. 8, pp. 736–745, 2022.

[199] W. Lu, J. A. Onofrey, Y. Lu, and et al., "An investigation of quantitative accuracy for deep learning based denoising in oncological pet," *Physics in Medicine & Biology*, vol. 64, p. 165019, 8 2019.

[200] A. Paszke, S. Gross, F. Massa, and et al., "Pytorch: An imperative style, high-performance deep learning library," *Advances in Neural Information Processing Systems*, vol. 32, 12 2019.

[201] M. Elad, B. Kawar, and G. Vaksman, "Image denoising: The deep learning revolution and beyond—a survey paper," *SIAM Journal on Imaging Sciences*, vol. 16, pp. 1594–1654, 8 2023.

[202] Q. Liu, H. Liu, N. Mirian, and et al., "A personalized deep learning denoising strategy for low-count PET images," *Physics in Medicine & Biology*, vol. 67, p. 145014, 7 2022.

[203] K. Fritscher, P. Raudaschl, P. Zaffino, and et al., "Deep neural networks for fast segmentation of 3D medical images," *Lecture Notes in Computer Science (including subseries Lecture Notes in Artificial Intelligence and Lecture Notes in Bioinformatics)*, vol. 9901 LNCS, pp. 158–165, 2016.

[204] Z. Wang, Y. Jiang, H. Zheng, and et al., "Patch diffusion: Faster and more data-efficient training of diffusion models," 4 2023.

[205] A. Kaur and G. Dong, "A complete review on image denoising techniques for medical images," *Neural Processing Letters*, vol. 55, pp. 7807–7850, 12 2023.

[206] F. A. Fardo, V. H. Conforto, F. C. de Oliveira, and et al., "A formal evaluation of PSNR as quality measurement parameter for image segmentation algorithms," 5 2016.

[207] Z. Wang, A. C. Bovik, H. R. Sheikh, and et al., "Image quality assessment: From error visibility to structural similarity," *IEEE Transactions on Image Processing*, vol. 13, pp. 600–612, 4 2004.

[208] F. Pedregosa, G. Varoquaux, A. Gramfort, and et al., "Scikit-learn: Machine learning in Python," *Journal of Machine Learning Research*, vol. 12, pp. 2825–2830, 2011.